WOMEN IN LANTHANIDE-BASED LUMINESCENCE RESEARCH: FROM BASIC RESEARCH TO APPLICATIONS

EDITED BY: Qianqian Su, Lining Sun, Eva Hemmer and Ho Seong Jang
PUBLISHED IN: Frontiers in Chemistry

frontiers Research Topics

ISSN 1664-8714
ISBN 978-2-88966-772-7
DOI 10.3389/978-2-88966-772-7

About Frontiers

Frontiers is more than just an open-access publisher of scholarly articles: it is a pioneering approach to the world of academia, radically improving the way scholarly research is managed. The grand vision of Frontiers is a world where all people have an equal opportunity to seek, share and generate knowledge. Frontiers provides immediate and permanent online open access to all its publications, but this alone is not enough to realize our grand goals.

Frontiers Journal Series

The Frontiers Journal Series is a multi-tier and interdisciplinary set of open-access, online journals, promising a paradigm shift from the current review, selection and dissemination processes in academic publishing. All Frontiers journals are driven by researchers for researchers; therefore, they constitute a service to the scholarly community. At the same time, the Frontiers Journal Series operates on a revolutionary invention, the tiered publishing system, initially addressing specific communities of scholars, and gradually climbing up to broader public understanding, thus serving the interests of the lay society, too.

Dedication to Quality

Each Frontiers article is a landmark of the highest quality, thanks to genuinely collaborative interactions between authors and review editors, who include some of the world's best academicians. Research must be certified by peers before entering a stream of knowledge that may eventually reach the public - and shape society; therefore, Frontiers only applies the most rigorous and unbiased reviews.
Frontiers revolutionizes research publishing by freely delivering the most outstanding research, evaluated with no bias from both the academic and social point of view. By applying the most advanced information technologies, Frontiers is catapulting scholarly publishing into a new generation.

What are Frontiers Research Topics?

Frontiers Research Topics are very popular trademarks of the Frontiers Journals Series: they are collections of at least ten articles, all centered on a particular subject. With their unique mix of varied contributions from Original Research to Review Articles, Frontiers Research Topics unify the most influential researchers, the latest key findings and historical advances in a hot research area! Find out more on how to host your own Frontiers Research Topic or contribute to one as an author by contacting the Frontiers Editorial Office: frontiersin.org/about/contact

WOMEN IN LANTHANIDE-BASED LUMINESCENCE RESEARCH: FROM BASIC RESEARCH TO APPLICATIONS

Topic Editors:
Qianqian Su, Shanghai University, China
Lining Sun, Shanghai University, China
Eva Hemmer, University of Ottawa, Canada
Ho Seong Jang, Korea Institute of Science and Technology, South Korea

Citation: Su, Q., Sun, L., Hemmer, E., Jang, H. S., eds. (2021). Women in Lanthanide-based Luminescence Research: From Basic Research to Applications. Lausanne: Frontiers Media SA. doi: 10.3389/978-2-88966-772-7

Table of Contents

frontiers in Chemistry

EDITORIAL
published: 23 March 2021
doi: 10.3389/fchem.2021.667672

Editorial: Women in Lanthanide-Based Luminescence Research: From Basic Research to Applications

Qianqian Su[1], Lining Sun[2]*, Eva Hemmer[3]* and Ho Seong Jang[4]**

[1]Institute of Nanochemistry and Nanobiology, Shanghai University, Shanghai, China, [2]Research Center of Nano Science and Technology, College of Sciences, Shanghai University, Shanghai, China, [3]Department of Chemistry and Biomolecular Sciences, University of Ottawa, Ottawa, ON, Canada, [4]Materials Architecturing Research Center, Korea Institute of Science and Technology, Seoul, South Korea

Keywords: lanthanide, luminescence, upconversion (UC) luminescence, downshifting, nanomaterials

Editorial on the Research Topic

Women in Lanthanide-Based Luminescence Research: From Basic Research to Applications

Lanthanide-based luminescence nanomaterials have attracted considerable attention in the last 2 decades because of the unique optical properties of lanthanides. Given their 4f electronic configuration, these nanomaterials exhibit unique emission spectra, including tunable emissions spanning the ultraviolet (UV) to near-infrared (NIR) regions, long excited-state lifetime, high resistance to optical photobleaching, no optical blinking, superior photostability, as well as large Stoke or anti-Stoke shifts. This set of outstanding features makes the study of lanthanide-based luminescence nanomaterials a subject of fundamental and technological importance (Auzel, 2004; Wang et al., 2010; Bettinelli et al., 2015; Li et al., 2015; Jalani et al., 2018). Indeed, encouraged by recent advances in the controllable synthesis and optical tuning of lanthanide-based nanomaterials, there are high expectations for the lanthanide research field to shape a wider attention on the emerging applications, including bioimaging, multiplexing sensing, super-resolution imaging, opto-genetics, volumetric display, photovoltaics, and more (Chen et al., 2014; Chen et al., 2015; Zhou et al., 2015; Liu et al., 2017; Su et al., 2017; Chen et al., 2018; Gai et al., 2018; Ma et al., 2019).

Among, many inspiring female researchers have made great contributions to the lanthanide research field. These contributions drove forward the understanding of the underlying mechanisms of lanthanide luminescence and pushed the exploration of manifold possible applications. Moreover, the spirit of the recent "Research Topic on Women in Science: Chemistry" motivated us to initiate a research topic focusing on the contributions of female researchers in lanthanide research. We, the editors of this special issue hope to help with "Women in Lanthanide-based Luminescence Research: From Basic Research to Applications" to motivate closure of the gender gap in this field, which—despite all stories of success—is still present. As such, the aim of this research topic is to promote the excellent female researchers' work in theory, experimental methodology, as well as emerging applications of lanthanide-based nanomaterials.

A key challenge in lanthanide-based upconversion nanoparticles is the low quantum efficiency of the upconversion process. While promising proof-of-concepts have demonstrated the great application potential for lanthanide-based nanomaterials in e.g., photodynamic therapy, light-triggered drug release, photocatalysis or (solar) energy conversion technologies, the success of these approaches in real life depends on the community's capability to overcome the limitations of low upconversion quantum efficiency. Consequently, great efforts are undertaken by researchers around the globe to tackle this challenge.

For example, Pei et al. surveyed examples of recent optical enhancement strategies on upconversion and even downshifting luminescence by metal ions doping strategy. Special

OPEN ACCESS

Edited and reviewed by:
Nasir Mahmood,
RMIT University, Australia

****Correspondence:***
Qianqian Su
chmsqq@shu.edu.cn
Lining Sun
lnsun@shu.edu.cn
Eva Hemmer
ehemmer@uottawa.ca
Ho Seong Jang
msekorea@kist.re.kr

Specialty section:
This article was submitted to Nanoscience, a section of the journal Frontiers in Chemistry

Received: *14 February 2021*
Accepted: *19 February 2021*
Published: *23 March 2021*

Citation:
Su Q, Sun L, Hemmer E and Jang HS (2021) Editorial: Women in Lanthanide-Based Luminescence Research: From Basic Research to Applications. Front. Chem. 9:667672. doi: 10.3389/fchem.2021.667672

attention is paid to the related mechanism of enhancement, involving host lattice asymmetry increase and energy transfer pathway optimization. Another strategy to boost upconversion efficiency is broadband dye-sensitization to partially overcome the limitation of the small absorption cross-sections and fixed excitation wavelength of the lanthanides. Agbo et al. reported the ultraviolet ligand decorated core-shell lanthanide nanoparticles, resulting in a large spectral shift, shifting the excitation wavelength to the UV range and resulting in the enhancement of NIR emission.

With respect to optical and biomedical applications, the assemblies of luminescence nanoparticles with unique structures hold great promise. Herein, merging several materials classes has the power to leverage the desirable features of each moiety into one hybrid system of superior performance. However, alignment of isotropic nanoparticles into anisotropic superstructures is a fundamental challenge in nanochemistry. Hence, the controllable assembly of isotropic nanocrystals into anisotropic structures by mediating inter-particle interactions as demonstrated by Su et al. constitutes an excellent example for the successful integration of lanthanide-based nanoparticles into a polymeric structure. In their contribution, the authors developed an amphiphilic block copolymer coating approach for the preparation of the belt-like assemblies of upconversion nanoparticles with length up to micro-scale.

With features of environment-sensitive, selective and bio-compatible spectroscopic characteristics, lanthanide-doped nanoparticles are ideal for optical trapping. So-called optical tweezers are of great promise for applications ranging from single-particle spectroscopy and tailored particle assembly to high-resolution surface studies, surface-enhanced spectroscopy, and controlled investigation of biological processes. In their contribution, Ortiz-Rivero et al. highlighted recent strategies to increase the optical forces in the manipulation of lanthanide-doped nanoparticles, for example, surface modification of these nanoparticles and optimization of the optical tweezer setup to ease access of lanthanide-based nanoparticles to these exciting applications.

The environment-sensitive spectroscopic characteristics of the lanthanides further render them ideal candidates for use in chemical and biological sensing. In this context, the lanthanide nanoparticles should exhibit good water dispersibility. However, most lanthanide-doped nanocrystals are prepared by synthetic methods that involve the use of capping hydrophobic, long alkyl chain ligands. Consequently, controlled and application-oriented surface modifications are essential to improve the sensitivity and versatility of upconversion probes. Burgess et al. reported a robust and versatile method for the covalent attachment of a wide variety of molecules including organic dyes, enzymes and proteins to the surface of upconversion nanophosphors. Su et al. focused on the detection of Cu^{2+} by using water-dispersible poly(acrylic acid) (PAA)-coated upconversion nanoparticles. Wang et al. utilized the ultra-weak chemiluminescence of lanthanide nanoparticles to demonstrate the potential use in nitrite detection.

In the context of biomedicine, the use of NIR light as an excitation source, but also the emission of NIR photons, is particularly appealing. Encouraged by the deeper penetration depth, minimized background fluorescence interference and less photo-damage to normal tissues offered by NIR-excited and -emitting lanthanide-based nanoparticles, researchers have paid considerable attention to their biomedical applications. For instance, Chen et al. explored recent advances in the development of photoimmuno-therapeutic agents activated by multifunctional upconversion nanoparticles. The fascinating long lifetime of lanthanides can create a temporal coding dimension for biomedical applications. In another excellent contribution, Qin et al. illustrated the aspects of synthesis of lanthanide-doped persistent luminescence phosphors with NIR emissions and exemplify the potential impact of this research area on biomedical science, including biosensing, bioimaging, drug delivery, as well as phototherapy.

We deeply appreciate our contributors for their dedication and the reviewers for their constructive comments and suggestions. We would like to thank all the editorial staff of Frontiers in Chemistry for valuable assistance in organizing this issue. Last but not least, we hope that this themed issue will not only provide a timely overview of current developments in the field of lanthanide-based luminescence nanomaterials, offering an enjoyable and enlightening lecture to our readership, but will also encourage the career developments of female researchers in this exciting field of research.

AUTHOR CONTRIBUTIONS

All authors listed have made a substantial, direct, and intellectual contribution to the work and approved it for publication.

REFERENCES

Auzel, F. (2004). Upconversion and anti-Stokes processes with f and d ions in solids. *Chem. Rev.* 104, 139–173. doi:10.1021/cr020357g

Bettinelli, M., Carlos, L., and Liu, X. (2015). Lanthanide-doped upconversion nanoparticles. *Phys. Today* 68, 38–44. doi:10.1063/PT.3.2913

Chen, G., Ågren, H., Ohulchanskyy, T. Y., and Prasad, P. N. (2015). Light upconverting core-shell nanostructures: nanophotonic control for emerging applications. *Chem. Soc. Rev.* 44, 1680–1713. doi:10.1039/c4cs00170b

Chen, G., Qiu, H., Prasad, P. N., and Chen, X. (2014). Upconversion nanoparticles: design, nanochemistry, and applications in theranostics. *Chem. Rev.* 114, 5161–5214. doi:10.1021/cr400425h

Chen, S., Weitemier, A. Z., Zeng, X., He, L., Wang, X., Tao, Y., et al. (2018). Near-infrared deep brain stimulation via upconversion nanoparticle-mediated optogenetics. *Science* 359, 679–684. doi:10.1126/science.aaq1144

Gai, S., Yang, G., Yang, P., He, F., Lin, J., Jin, D., et al. (2018). Recent advances in functional nanomaterials for light-triggered cancer therapy. *Nano Today* 19, 146–187. doi:10.1016/j.nantod.2018.02.010

Jalani, G., Tam, V., Vetrone, F., and Cerruti, M. (2018). Seeing, targeting and delivering with upconverting nanoparticles. *J. Am. Chem. Soc.* 140, 10923–10931. doi:10.1021/jacs.8b03977

Li, X., Zhang, F., and Zhao, D. (2015). Lab on upconversion nanoparticles: optical properties and applications engineering via designed nanostructure. *Chem. Soc. Rev.* 44, 1346–1378. doi:10.1039/c4cs00163j

Liu, Y., Lu, Y., Yang, X., Zheng, X., Wen, S., Wang, F., et al. (2017). Amplified stimulated emission in upconversion nanoparticles for super-resolution nanoscopy. *Nature* 543, 229–233. doi:10.1038/nature21366

Ma, Y., Bao, J., Zhang, Y., Li, Z., Zhou, X., Wan, C., et al. (2019). Mammalian near-infrared image vision through injectable and self-powered retinal nanoantennae. *Cell* 177, 243–255.e15. doi:10.1016/j.cell.2019.01.038

Su, Q., Feng, W., Yang, D., and Li, F. (2017). Resonance energy transfer in upconversion nanoplatforms for selective biodetection. *Acc. Chem. Res.* 50, 32–40. doi:10.1021/acs.accounts.6b00382

Wang, F., Han, Y., Lim, C. S., Lu, Y., Wang, J., Xu, J., et al. (2010). Simultaneous phase and size control of upconversion nanocrystals through lanthanide doping. *Nature* 463, 1061–1065. doi:10.1038/nature08777

Zhou, J., Liu, Q., Feng, W., Sun, Y., and Li, F. (2015). Upconversion luminescent materials: advances and applications. *Chem. Rev.* 115, 395–465. doi:10.1021/cr400478f

Conflict of Interest: The authors declare that the research was conducted in the absence of any commercial or financial relationships that could be construed as a potential conflict of interest.

frontiers in Chemistry

ORIGINAL RESEARCH
published: 07 August 2020
doi: 10.3389/fchem.2020.00639

Ultra-Weak Chemiluminescence Enhanced by Cerium-Doped LaF_3 Nanoparticles: A Potential Nitrite Analysis Method

Yufei Wang[1], *Yanran Wang*[1], *Chunxia Huang*[1], *Tianyou Chen*[1] *and Jing Wu*[1,2]*

[1] School of Science, China University of Geosciences, Beijing, China, [2] Key Laboratory of Optic-electric Sensing and Analytical Chemistry for Life Science, MOE, Qingdao University of Science and Technology, Qingdao, China

In this work, cerium-doped LaF_3 nanoparticles (LaF_3:Ce NPs) were successfully synthesized and characterized. Its chemiluminescence (CL) property was studied, and it was amazingly found that it intensely enhanced the ultra-weak CL of the $NaNO_2$-H_2O_2 system. The CL mechanism was systematically investigated and suggested to be the recombination of electron-injected and hole-injected LaF_3:Ce NPs. The new CL system was developed to be a facile, original, and direct method for nitrite analysis. Experimental conditions were optimized and then a satisfactory linear relationship between CL intensity and nitrite concentration was obtained. This work introduced a new pathway for the research and application of traditional fluoride NPs doped with RE^{3+}.

Keywords: chemiluminescence, cerium, fluoride, nitrite, nanoparticles

OPEN ACCESS

Edited by:
Qianqian Su,
Shanghai University, China

Reviewed by:
Xiaoji Xie,
Nanjing Tech University, China
Suli Wu,
Dalian University of Technology, China

***Correspondence:**
Jing Wu
wujing@cugb.edu.cn

Specialty section:
This article was submitted to Nanoscience, a section of the journal Frontiers in Chemistry

Received: *28 May 2020*
Accepted: *19 June 2020*
Published: *07 August 2020*

Citation:
Wang Y, Wang Y, Huang C, Chen T and Wu J (2020) Ultra-Weak Chemiluminescence Enhanced by Cerium-Doped LaF_3 Nanoparticles: A Potential Nitrite Analysis Method. Front. Chem. 8:639. doi: 10.3389/fchem.2020.00639

INTRODUCTION

Fluoride is utilized as an ideal and appealing host for phosphors doped with rare earth ions (RE^{3+}) owing to its adequate thermal and environmental stability as well as large solubility for RE^{3+} ions (Li et al., 2012). Compared with oxide systems, vibrational energies in fluorides is low and therefore trigger scarce quenching of the excited states of the RE^{3+} ions (Bender et al., 2000). Furthermore, RE^{3+}-doped fluorides exhibit characteristic properties, such as high ionicity, low refractive index, wide band gap, and low phonon energy. $KMgF_3$ (Schuyt and Williams, 2018), $NaYF_4$ (Wu et al., 2019, 2020), $NaGdF_4$ (Yi et al., 2019), and LaF_3 (Bekah et al., 2016; Nampoothiri et al., 2017) have been investigated and exhibit high quantum yields and long luminescent lifetimes. RE^{3+}-doped fluorides have been attracting attentions for several years due to the wide variety of technological applications including biomedical researches (All et al., 2019; Yan et al., 2019), biosensors (Vijayan et al., 2019), bioimaging (Hu et al., 2016; Han et al., 2017; Zeng et al., 2019), radiation detection (Ju et al., 2017), optoelectronic devices (Wu et al., 2018), and so on. However, to the best of our knowledge, the performance of RE^{3+}-doped fluorides toward chemiluminescence (CL) has not been explored.

Nitrite is widely used in food manufacture as preservatives and fertilizing reagents. As an essential precursor of carcinogenic *N*-nitrosamine, excess intake of nitrite is harmful for human beings. Nitrite can cause irreversible conversion of hemoglobin to methemoglobin in the bloodstream and then bring detrimental effect for the oxygen transport in the whole body. In addition, nitrogen-based fertilizers and industrial wastewater pollute groundwater resources by nitrites. Thus, nitrite detection is of significant importance for food safety, public health, and environment protection (Wang et al., 2017; Zhang Y. et al., 2018; Cao et al., 2019).

Various principle-based analytical methods have been devised for nitrite detection, such as electrochemical sensors (Ma et al., 2018; Wang et al., 2018; Zhou et al., 2019; Madhuvilakku et al., 2020), microplasma emission (Zheng et al., 2018), absorption spectrophotometry (Zhang L. et al., 2018), fluorescence (Dai et al., 2017; Jana et al., 2019; Pires et al., 2019), and CL (Lu et al., 2002, 2004; Lin et al., 2011; Wu et al., 2016). Electrodes are modified with complex strategies in electrochemical analysis. Special molecules need to be designed for spectrophotometric detections in order to amplify signal and reduce the background interferences. CL detections require simple instruments, interfere with low background, and are compatible with gas or aqueous phases. CL intensity was reported to be significantly enhanced by nanomaterials that gave promise for developing sensitive and convenient CL analytical methods. In 2011, carbon dots were firstly demonstrated to enhance the CL signal of the $NaNO_2$-H_2O_2 system because of peroxynitrous acid generation (Lin et al., 2011). Nitrogen-rich quantum dots (QDs) were facilely synthesized and intensely enhanced the ultra-weak CL reaction of the $NaIO_4$-H_2O_2 system through electron hole injection and CL resonance energy transfer (Zheng et al., 2017). In particular, molybdenum sulfide QDs were proved to give rise to the generation of reactive oxygen species from hydrogen peroxide (H_2O_2) in alkaline solution and gave a promise for CL emission (Dou et al., 2019). However, fluoride-based nanomaterials were scarcely utilized and the developed CL analysis was rarely applied in nitrite detection. Original CL detections for nitrites are worth giving research to pursue better performance.

In this work, cerium-doped LaF_3 nanoparticles (LaF_3:Ce NPs) were synthesized and firstly demonstrated to enhance the CL signal of the $NaNO_2$-H_2O_2 system. Reactive oxygen species generation that was triggered by LaF_3:Ce NPs was proved to be the main reason for CL enhancement. A linear relationship between the CL signal and nitrite concentration was found and implied that the LaF_3:Ce NPs-$NaNO_2$-H_2O_2 system could be applied in the determination of nitrite.

MATERIALS AND METHODS

Reagents and Materials

Sodium nitrite ($NaNO_2$) was purchased from Sinopharm Chemical Reagent Co., Ltd. (Shanghai, China). Sulfuric acid (H_2SO_4, 98%), H_2O_2 (35%), hydrochloric acid, and ethanol (98%) were brought from Beijing Chemical Reagent Co. (Beijing, China). Sodium fluoride (NaF, >98%), heptahydrate lanthanum chloride ($LaCl_3{\cdot}7H_2O$, 99.9%), heptahydrate cerium chloride ($CeCl_3{\cdot}7H_2O$, 99.9%), oleic acid (90%), 5,5-dimethyl-1-pyrroline *N*-oxide (DMPO), and ascorbic acid (AA) were all purchased from Sigma-Aldrich. Unless otherwise noted, all the chemicals were used without further purification.

Abbreviations: AA, ascorbic acid; LaF_3:Ce NPs, cerium-doped LaF_3 nanoparticles; CL, chemiluminescence; EPR, electron paramagnetic resonance; FT-IR, Fourier transform infrared; PL, photoluminescent; PMT, photomultiplier tube; QDs, quantum dots; RE^{3+}, rare earth ions.

Apparatus

UV-vis absorption spectra were performed on a PerkinElmer Lambda 950 spectrophotometer. The photoluminescent (PL) spectra were collected on an Agilent Cary Eclipse spectrofluorometer. Fourier transform infrared (FT-IR) spectra were obtained on a PerkinElmer Frontier FT-IR spectrometer. CL experiments were conducted with an ultra-weak CL analyzer (IFFM-E, Xi'an Remex Analytical Instrument Co., Ltd, China). Transmission electron microscopy images were obtained on a JEOL-1400 transmission electron microscope (JEOL, Tokyo, Japan). Electron paramagnetic resonance (EPR) spectra were measured on a Bruker E500 spectrometer.

LaF_3:Ce NPs Synthesis

Hydrothermal reaction was utilized to synthesize LaF_3:Ce NPs. 2.25 ml of $LaCl_3$ solution (0.20 M), 1.00 ml of $CeCl_3$ solution (0.05 M), 2.00 ml of NaF solution (1.00 M), 20 ml of ethanol, and 10 ml of oleic acid were mixed and stirred for 0.5 h in reaction kettle. The mixture was heated in an oven and kept at 200°C for 8 h. After reaction, the supernatant was removed. The remnant suspension was centrifuged at 6,000 rpm for 5 min and then the supernatant was also removed. The resultant solid was dispersed in 2.00 M hydrochloric acid. After ethanol addition, the mixture was centrifuged at 6,000 rpm for 5 min to remove the supernatant. The product was stored in 4 ml H_2O for further use. The exact doping percentage of cerium was calculated to be 10%.

CL Study of the LaF_3:Ce NPs-$NaNO_2$-H_2O_2 System

At first, CL intensities of the $NaNO_2$-H_2O_2 system with and without LaF_3:Ce NPs were compared. Fifty microliters of H_2O_2 (3.00 M), which was acidified by 0.04 M H_2SO_4, was injected into the mixture of 50 μl of LaF_3:Ce NPs and 50 μl of $NaNO_2$ (10 μM). In the control experiment, 50 μl of LaF_3:Ce NPs was replaced by 50 μl of H_2O. CL intensities of both the two conditions were recorded and compared. CL profiles were integrated at intervals of 0.1 s. Voltage of the photomultiplier tube (PMT) was set at 1.2 kV. CL spectrum was measured with high-energy cutoff filters (400–640 nm), which were set between the quartz cuvette and PMT as described in Cui et al. (2003). Additional orders of the reagents were investigated to collect CL kinetic curves. EPR measurements were operated at an X-band frequency of 9.85 GHz. Irradiation was performed by using a 300-W Xe lamp (300 nm $< \lambda <$ 1,100 nm) with the output radiation focused on the samples in the cavity by an optical fiber (50 cm length, 0.3 cm diameter). All spectra were acquired at 298 K. DMPO (12.4 μl in 1 ml of H_2O) was taken as the specific detection reagent for ·OH. AA (0.1 mM) was used as a scavenger for $O_2^{\cdot-}$. CL intensities of the LaF_3:Ce NPs-$NaNO_2$-H_2O_2 system with and without AA were recorded.

Nitrite Analysis

Experimental conditions were optimized with different H_2SO_4 concentrations (0, 0.02, 0.03, 0.04, 0.05, and 0.06 M), H_2O_2 concentrations (0.00, 1.00, 2.00, 3.00, 4.00, and 5.00 M), and additional volumes of LaF_3:Ce NPs (0, 10, 20, 30, 40, 50, 60, and 70 μl). The univariate method was adopted in systematically

optimizing experimental parameters through changing one parameter at a time while keeping others constant. At the optimal experimental conditions, calibration curve was recorded by detecting CL intensities vs. different nitrite concentrations.

RESULTS

Characterization of LaF_3:Ce NPs

LaF_3:Ce NPs obtained in this work exhibited hexagonal phase and their average sizes were about 80 × 20 nm (**Figure 1A**). 4*f* shells of lanthanides are partially filled and are effectively shielded by outer 5s and 5p shells leading to satisfactory emissions. The prepared LaF_3:Ce NPs gave a bright blue color under ultraviolet radiation (λ_{ex} = 254 nm) (**Figure 1B**, inset). The emission of LaF_3:Ce NPs shifted to longer wavelength with the increase of excitation wavelength revealing the distribution of different surface energy traps of the LaF_3:Ce NPs (**Figure 1B**). UV-vis absorption spectra of the LaF_3:Ce NPs-$NaNO_2$-H_2O_2 system were collected and are shown in **Figure 1C**. $NaNO_2$ gave an absorption peak at 354 nm, which decreased when acidified H_2O_2 was added. Another absorption peak located at 301 nm appeared due to the isomerization of ONOOH, which was generated in the mixture of acidified H_2O_2 and $NaNO_2$ (Lin et al., 2011), while no new absorption peaks were found when acidified H_2O_2 mixed with LaF_3:Ce NPs. Except the absorption peak of ONOOH, no other new absorption peak was found in the LaF_3:Ce NPs-$NaNO_2$-H_2O_2 system, indicating that no new compound was formed. UV-vis absorption spectra gave some indications for the CL mechanism of this system, which was illustrated in detail in the subsequent section. FT-IR spectrum of LaF_3:Ce NPs indicated that there were O-H groups on the surface of LaF_3:Ce NPs (**Figure 1D**).

CL of the LaF_3:Ce NPs-$NaNO_2$-H_2O_2 System

CL intensities of the $NaNO_2$-H_2O_2 system with and without LaF_3:Ce NPs were sharply different. LaF_3:Ce NPs addition intensely enhanced CL intensity (**Figure 2A**). As shown in **Figure 2B**, the CL spectrum for the LaF_3:Ce NPs-$NaNO_2$-H_2O_2 system was wide ranging from 375 to 500 nm and was centered

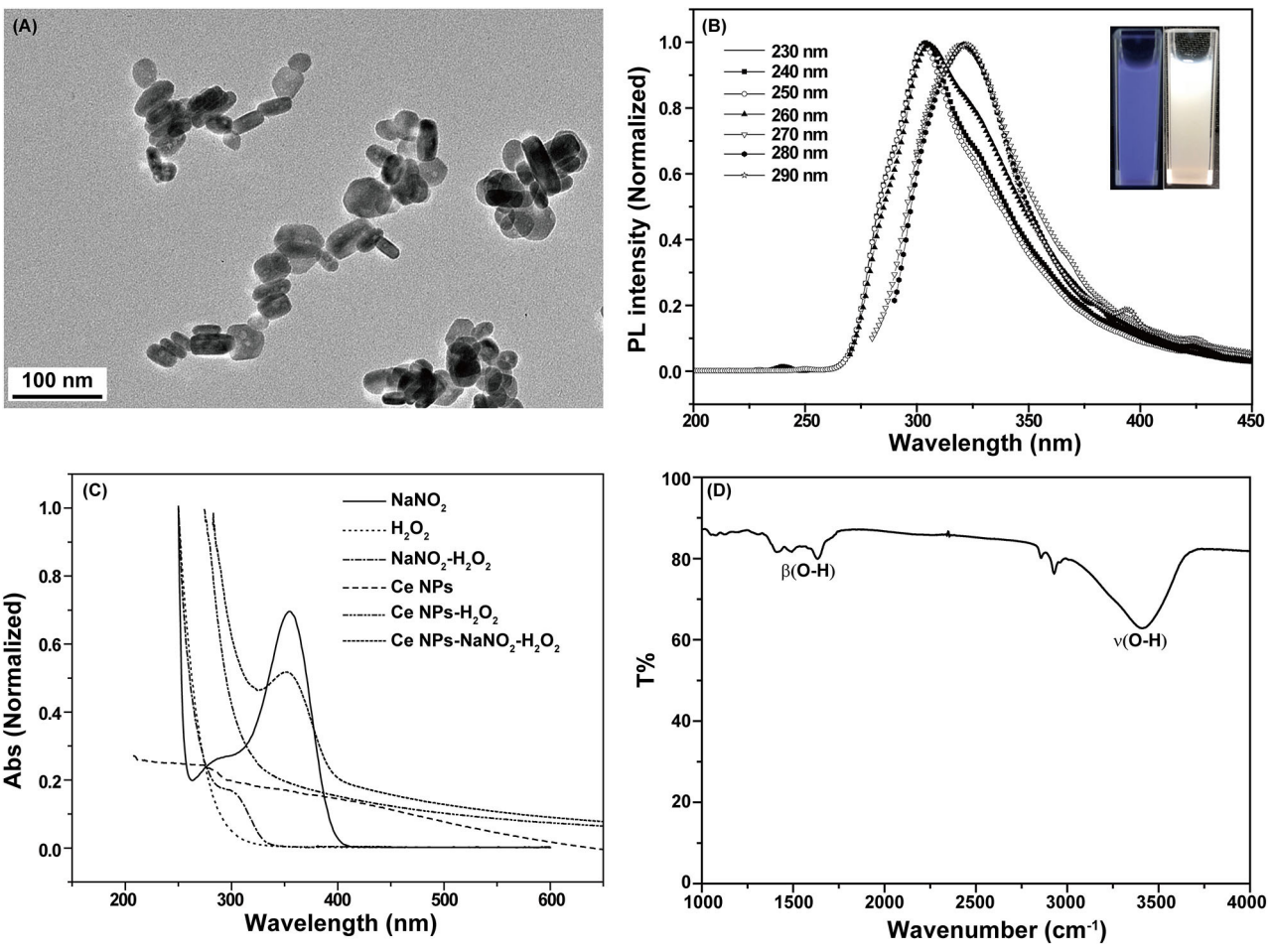

FIGURE 1 | Characterization of LaF_3:Ce NPs. **(A)** Transmission electron microscopy images of LaF_3:Ce NPs. **(B)** PL spectra of LaF_3:Ce NPs. The inset is the photograph of LaF_3:Ce NPs under a UV lamp (λ_{ex} = 254 nm). **(C)** UV-vis absorption spectra of the reagent in the CL reaction. **(D)** FT-IR spectra of LaF_3:Ce NPs.

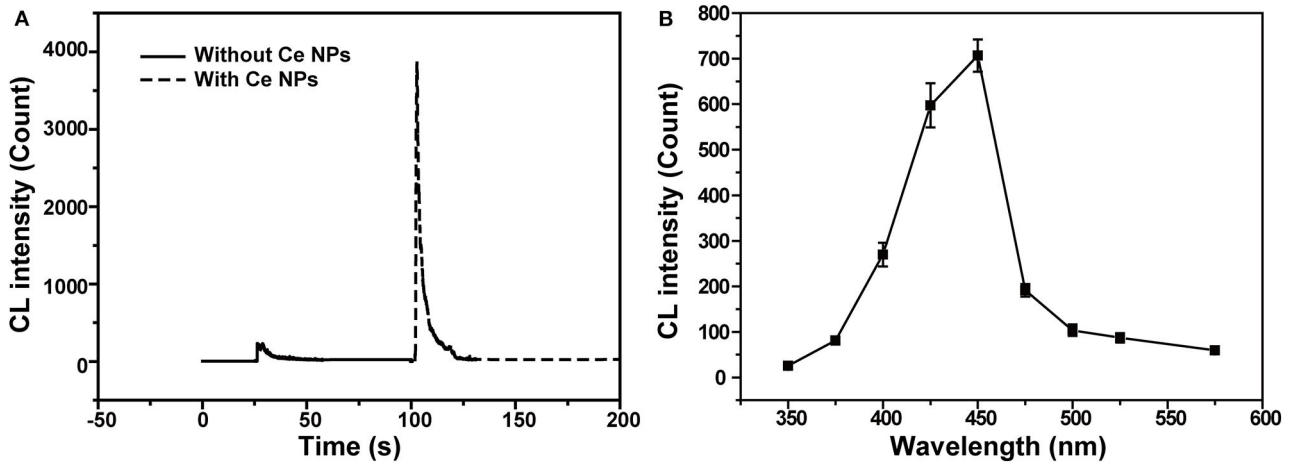

FIGURE 2 | CL profiles of the LaF_3:Ce NPs-$NaNO_2$-H_2O_2 system. **(A)** Comparison of CL intensities of the $NaNO_2$-H_2O_2 system with and without LaF_3:Ce NPs. **(B)** CL spectrum of the LaF_3:Ce NPs-$NaNO_2$-H_2O_2 system. The standard error bars mean the variation of three individual experiments. Conditions: 3.00 M H_2O_2 in 0.04 M H_2SO_4, 50 μl of LaF_3:Ce NPs and 10 μM $NaNO_2$ solution. Voltage of the PMT was set at 1.2 kV.

at 450 nm. The fluorescent emission of LaF_3:Ce NPs is also wide, which is similar to the CL spectrum of the LaF_3:Ce NPs-$NaNO_2$-H_2O_2 system. As a result, it is reasonable to refer that the CL originates from the various surface energy traps existing on the LaF_3:Ce NPs. Compared with the PL peak of LaF_3:Ce NPs, the CL spectrum is red-shifted due to the energy separations of LaF_3:Ce NPs surface states. PL was generated through excitation and emission within the core of the LaF_3:Ce NPs and the energy gap between them is larger than the energy separations on NPs surface (Ding et al., 2002; Myung et al., 2002).

CL Kinetic Study

As described in UV-vis absorption spectra, ONOOH was generated when $NaNO_2$ was mixed with acidified H_2O_2 (Equation 1) (Anbar and Taube, 1954). ONOOH easily transforms to be nitrate via the stage of HOONO* and give emissions during the process (Equation 2) (Houk et al., 1996). The emission locates at 350–450 nm, which overlaps the absorption spectrum of LaF_3:Ce NPs. Hence, LaF_3:Ce NPs can be excited by the energy of transformation and cause CL emission. However, the maximum of the transformation-derived CL was obtained at the pH value of 6.5–7.0 while the maximum CL of the LaF_3:Ce NPs-$NaNO_2$-H_2O_2 system was recorded in a severe acidic solution (Starodubtseva et al., 1999). As a consequence, the transformation energy only partially contributed to the CL of the LaF_3:Ce NPs-$NaNO_2$-H_2O_2 system. Various mixing orders of reagents influenced the reactions between LaF_3:Ce NPs and ONOOH and then affected the CL intensities (**Figure 3A**). The highest CL was obtained when acidified H_2O_2 was injected into the mixture of LaF_3:Ce NPs and $NaNO_2$. At this condition, the generated ONOOH adequately reacted with LaF_3:Ce NPs and gave enhanced CL. Mixing of $NaNO_2$ with acidified H_2O_2 without LaF_3:Ce NPs gave weak and lasting CL while mixing of LaF_3:Ce NPs with acidified H_2O_2 without $NaNO_2$ gave weak and rapid CL (**Figure 3B**).

$$\mathbf{HNO_2 + H_2O_2 \rightarrow ONOOH + H_2O} \quad (1)$$

$$\mathbf{ONOOH \rightarrow ONOOH^* \rightarrow NO_3^- + H^+} \quad (2)$$

CL Mechanism

According to the CL kinetic study, it demonstrated that the reactions between LaF_3:Ce NPs and ONOOH or its related species were the main cause accounting for the enhanced CL. ONOOH was reported to be capable of producing reactive oxygen species (Equations 3–5) (Alvarez et al., 1995; Gunaydin and Houk, 2008; Lin et al., 2011). It was obvious that ONOOH-produced reactive oxygen species include ·OH, $O_2^{\cdot-}$, and $^1O_2$ in this system. EPR was performed and DMPO was utilized as the specific detection reagent for ·OH to directly examine the variation of ·OH after LaF_3:Ce NPs addition. Although CL intensity of the LaF_3:Ce NPs-$NaNO_2$-H_2O_2 system was greatly enhanced, the production of ·OH was almost not increased (**Figure 4A**). $^1O_2$ was derived from ·OH so it could refer that there was no increase in $^1O_2$ quantity. Ethanol was reported to react with ·OH and yield an octet spectrum that was completely distinct from the DMPO-OH spectrum (Finkelstein et al., 1980). The octet spectrum in the LaF_3:Ce NPs-$NaNO_2$-H_2O_2 system rooted in the reaction between ·OH and residual ethanol from treatment process of LaF_3:Ce NPs. Furthermore, AA, which was a scavenger for $O_2^{\cdot-}$, obviously inhibited the CL of the LaF_3:Ce NPs-$NaNO_2$-H_2O_2 system (**Figure 4B**). All the results indicated that $O_2^{\cdot-}$ was the critical reason for the enhanced CL instead of ·OH and $^1O_2$. $O_2^{\cdot-}$ acting as an electron donor reacted with LaF_3:Ce NPs to produce LaF_3:Ce $NPs^{\cdot-}$ (Equation 6) (Poznyak et al., 2004). ONOOH serving as a hole injector converted LaF_3:Ce NPs to LaF_3:Ce $NPs^{\cdot+}$ (Equation 7). Electron–hole annihilation between LaF_3:Ce $NPs^{\cdot-}$ and LaF_3:Ce $NPs^{\cdot+}$ resulted in CL emission (Equation 8) (**Figure 5**; Ding et al., 2002;

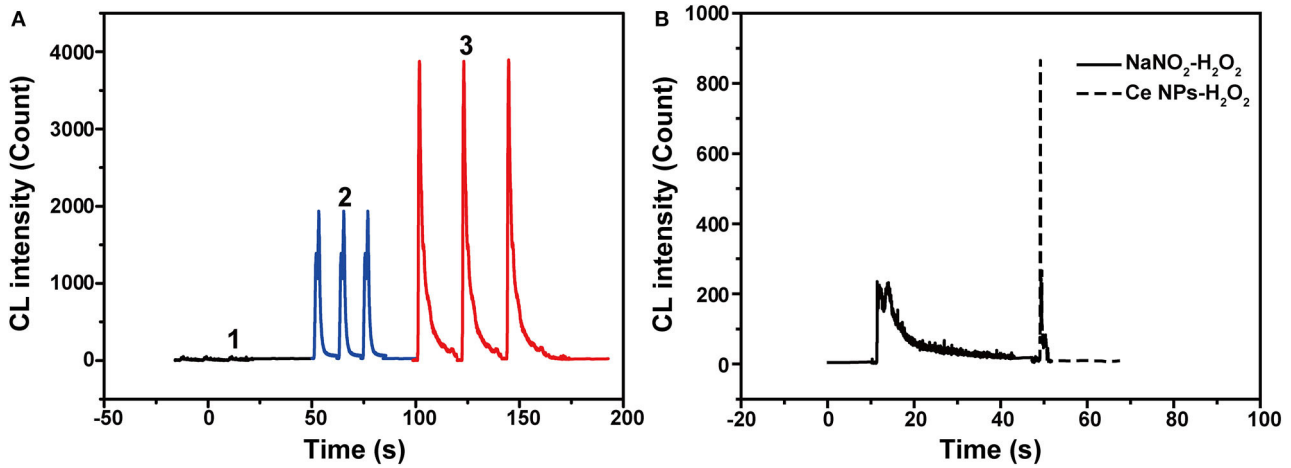

FIGURE 3 | CL kinetic study of the LaF_3:Ce NPs-$NaNO_2$-H_2O_2 system. **(A)** CL kinetic curves of the LaF_3:Ce NPs-$NaNO_2$-H_2O_2 system with different reagent mixing orders: **1**. injecting LaF_3:Ce NPs into the mixture of $NaNO_2$ and acidified H_2O_2; **2**. injecting $NaNO_2$ into the mixture of LaF_3:Ce NPs and acidified H_2O_2; **3**. injecting acidified H_2O_2 into the mixture of LaF_3:Ce NPs and $NaNO_2$. CL signals of three repeated experiments were given. **(B)** CL kinetic curves of the $NaNO_2$-H_2O_2 system and the LaF_3:Ce NPs-H_2O_2 system. Conditions: 3.00 M H_2O_2 in 0.04 M H_2SO_4, 50 μl of LaF_3:Ce NPs and 10 μM $NaNO_2$ solution. Voltage of the PMT was set at 1.2 kV.

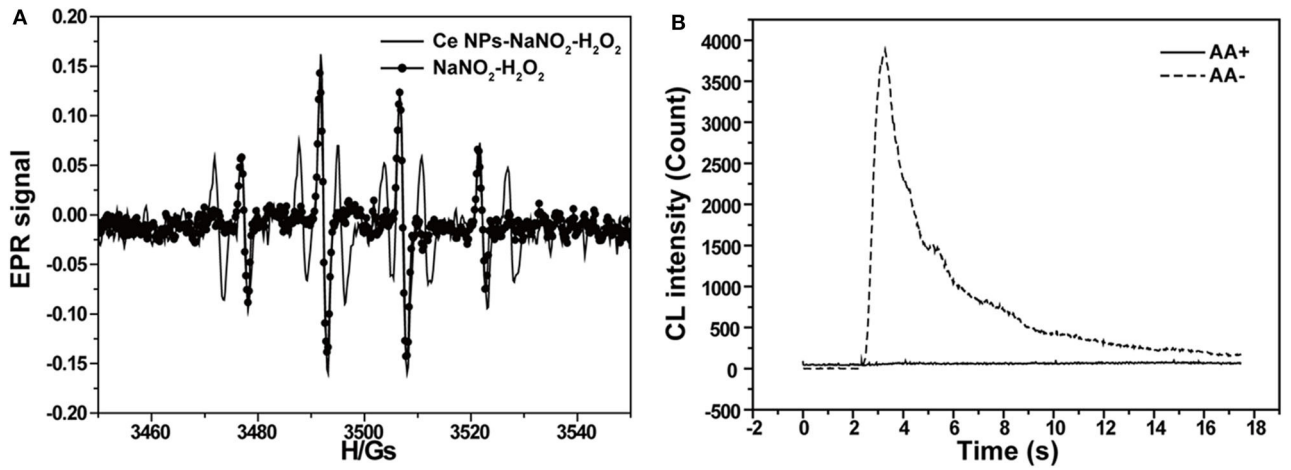

FIGURE 4 | CL mechanism study of the LaF_3:Ce NPs-$NaNO_2$-H_2O_2 system. **(A)** EPR spectra of ·OH generated via the reaction of DMPO probe in the LaF_3:Ce NPs-$NaNO_2$-H_2O_2 and $NaNO_2$-H_2O_2 systems. **(B)** CL profiles of the LaF_3:Ce NPs-$NaNO_2$-H_2O_2 system with and without AA. Conditions: 3.00 M H_2O_2 in 0.04 M H_2SO_4, 50 μl of LaF_3:Ce NPs, 10 μM $NaNO_2$ solution, 12.4 μl of DMPO in 1 ml of H_2O, and 0.1 mM AA. Voltage of the PMT was set at 1.2 kV.

Poznyak et al., 2004; Zheng et al., 2009; Dong et al., 2010).

$$ONOOH \rightarrow \cdot NO_2 + \cdot OH \quad (3)$$

$$ONOOH + H_2O_2 \rightarrow O_2^{\cdot -} + \cdot NO_2 + H^+ + H_2O \quad (4)$$

$$O_2^{\cdot -} + \cdot OH \rightarrow {}^1O_2 + OH^- \quad (5)$$

$$LaF_3{:}Ce\ NPs + O_2^{\cdot -} \rightarrow LaF_3{:}Ce\ NPs^{\cdot -} + O_2 \quad (6)$$

$$LaF_3{:}Ce\ NPs + ONOOH \rightarrow LaF_3{:}Ce\ NPs^{\cdot +} + \cdot NO_2 + H_2O \quad (7)$$

$$LaF_3{:}Ce\ NPs^{\cdot +} + LaF_3{:}Ce\ NPs^{\cdot -} \rightarrow LaF_3{:}Ce\ NPs^* + LaF_3{:}Ce\ NPs \rightarrow 2LaF_3{:}Ce\ NPs + hv \quad (8)$$

Nitrite Analysis

To establish the optimal conditions for nitrite analysis, the volume of LaF_3:Ce NPs added into the CL system and concentrations of H_2SO_4 and H_2O_2 were investigated, respectively. As shown in **Figure 6A**, 50 μl of LaF_3:Ce NPs was added into the CL system and provided the highest CL emission. Less LaF_3:Ce NPs inadequately reacted with ONOOH while surplus LaF_3:Ce NPs also consumed energy. Reactive substance ONOOH was the product of $NaNO_2$ and H_2O_2 in acid medium, so H_2SO_4 was indispensable for the CL system. No CL signals could be observed in the absence of H_2SO_4. The most intense

CL signal was obtained with the H_2SO_4 concentration of 0.04 M (**Figure 6B**). CL signal increased with the concentration of H_2O_2 in the range from 0 to 3.00 M (**Figure 6C**). Hence, the optimal analytical conditions for nitrite analysis were 3.00 M H_2O_2 in 0.04 M H_2SO_4 injected into the mixture of 50 μl of LaF_3:Ce NPs and nitrite solution.

Under the optimal conditions, CL signals for different nitrite concentrations were recorded and shown in **Figure 7**. Good linear relationship between CL intensity and nitrite concentration was obtained in the range from 1 to 100 μM with a correlation coefficient of 0.9981 ($y = 256.3x + 42.72$). The relative standard deviation values of the analysis were 8.7, 1.2, and 4.8% for nitrite concentrations of 1, 10, and 100 μM, respectively. Relative standard deviation values demonstrated the satisfactory reproducibility. The limit of detection ($S/N = 3$) for nitrite was 0.33 μM.

DISCUSSION

The eternal goals and challenges of analytical chemistry are developing accurate, automated, selective, stable, sensitive, high-speed, high-throughput, and *in situ* analytical methods and protocols (Ju, 2013). The combination of analytical chemistry with new materials, especially nanomaterials, is the current frontier research topics and exhibits greatly improved analytical capacities. CL analysis is a traditional analytical technology and possesses outstanding advantages, such as low cost, simple instrument, fast response, and high compatibility. The application of nanomaterials in CL analysis leads to new CL sensing disciplines and offers a broad palette of opportunities for analytical chemists. In 2004, Poznyak et al. (2004) firstly reported the nanocrystal band gap CL derived from CdSe/CdS core-shell QDs that acted as a novel class of luminophores with the emission state originated from quantum-confined orbitals. Superior emission properties in QDs gave promises for developing QD-based nanoprobes for CL analysis. Besides traditional semiconductor QDs, some novel nanomaterials, such as carbon nanodots (Lin et al., 2011), graphene QDs (Hassanzadeh and Khataee, 2018), graphitic carbon nitride QDs (Zhu et al., 2019), and N-dots (Zheng et al., 2017), were developed to be potential platforms for CL

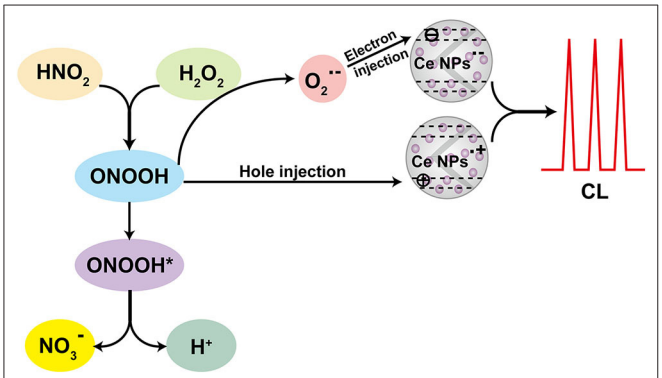

FIGURE 5 | Schematic illustration of the CL mechanism of the LaF_3:Ce NPs-$NaNO_2$-H_2O_2 system.

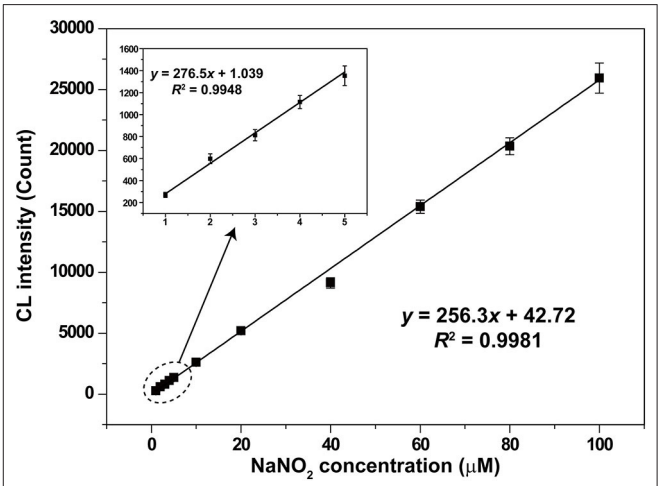

FIGURE 7 | Calibration curve for nitrite analysis based on the LaF_3:Ce NPs-enhanced CL. The standard error bars mean the variation of three individual experiments. Conditions: 3.00 M H_2O_2 in 0.04 M H_2SO_4 and 50 μl of LaF_3:Ce NPs. Voltage of the PMT was set at 1.2 kV.

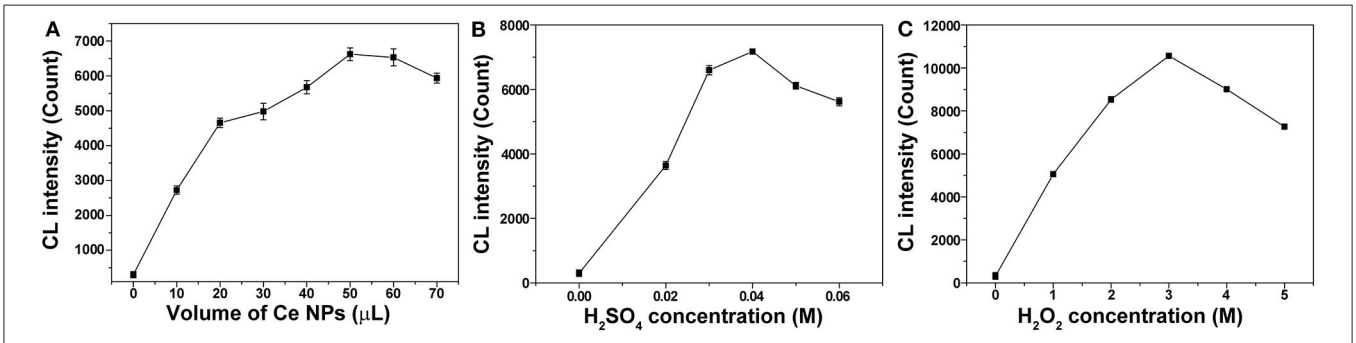

FIGURE 6 | Optimization of experimental conditions for nitrite analysis. **(A)** Volume of LaF_3:Ce NPs added into the CL system was optimized. **(B)** Concentration of H_2SO_4 used to acidify H_2O_2 was optimized. **(C)** Concentration of H_2O_2 was optimized. The standard error bars mean the variation of three individual experiments.

sensing. These nanomaterials are superior in terms of robust chemical inertness, low toxicity, good aqueous solubility, high resistance to photobleaching, and satisfactory biocompatibility. Our work is an endeavor step during the development process of nanomaterial-sensitized CL analysis methods. In this study, LaF_3:Ce NPs were successfully synthesized and applied in nitrite detection based on CL signals. The synthetic process of LaF_3:Ce NPs was simple and the products were fully characterized to give indications for the CL mechanism study. The enhancement of LaF_3:Ce NPs for the $NaNO_2$-H_2O_2 CL system was efficient and the mechanism was systematically and scientifically explained. The linear relationship between CL intensity and nitrite concentration was found, although there were spaces for improving the limit of detection. This work tried to explore new CL nanoprobes and gave a new route for fluoride applications. In the future, there is still a great demand for developing novel CL nanoprobes especially metal-free QDs and two-dimensional QDs.

CONCLUSIONS

In summary, LaF_3:Ce NPs were successfully synthesized and demonstrated to intensely enhance ultra-weak CL of the $NaNO_2$-H_2O_2 system. The CL mechanism was suggested to be the electron–hole annihilation between hole-injected and electron-injected LaF_3:Ce NPs. The new CL system was developed to be a novel, simple, and straightforward analytical method for nitrite. All the experimental conditions were optimized and a satisfactory linear relationship between CL intensity and nitrite concentration was obtained. This work shed a new light on the research and application of traditional fluoride NPs doped with RE^{3+}.

DATA AVAILABILITY STATEMENT

The raw data supporting the conclusions of this article will be made available by the authors, without undue reservation, to any qualified researcher.

AUTHOR CONTRIBUTIONS

YuW organized and conducted all the experiments, analyzed data, and wrote the manuscript. JW coordinated the project, supervised all the experiments, analyzed data, and wrote, edited, and reviewed the manuscript. YaW assisted the experiments of nitrite analysis. CH synthesized and characterized LaF_3:Ce NPs. TC performed experiments of the CL study of the LaF_3:Ce NPs-$NaNO_2$-H_2O_2 system. All authors contributed to the article and approved the submitted version.

FUNDING

This work was supported by the National Natural Science Foundation of China (No. 21874120) and the Fundamental Research Funds for the Central Universities (No. 2652018004). During the revision process, support was supplied by the Fundamental Research Funds for the Central Universities (No. 2652019112) and the open fund of Key Laboratory of Optic-electric Sensing and Analytical Chemistry for Life Science, MOE, Qingdao University of Science and Technology (No. OESACLS202004).

ACKNOWLEDGMENTS

Ms. Mengnan Rao is acknowledged for conducting some preparation works.

REFERENCES

All, A. H., Zeng, X., Teh, D. B. L., Yi, Z., Prasad, A., and Ishizuka, T., et al. (2019). Expanding the toolbox of upconversion nanoparticles for *in vivo* optogenetics and neuromodulation. *Adv. Mater.* 31:1803474. doi: 10.1002/adma.201803474

Alvarez, B., Denicola, A., and Radi, R. (1995). Reaction between peroxynitrite and hydrogen peroxide: formation of oxygen and slowing of peroxynitrite decomposition. *Chem. Res. Toxicol.* 8, 859–864. doi: 10.1021/tx00048a006

Anbar, M., and Taube, H. (1954). Interaction of nitrous acid with hydrogen peroxide and with water. *J. Am. Chem. Soc.* 76, 6243–6247. doi: 10.1021/ja01653a007

Bekah, D., Cooper, D., Kudinov, K., Hill, C., Seuntjens, J., and Bradforth, S., et al. (2016). Synthesis and characterization of biologically stable, doped LaF_3 nanoparticles co-conjugated to PEG and photosensitizers. *J. Photochem. Photobiol. A Chem.* 329, 26–34. doi: 10.1016/j.jphotochem.2016.06.008

Bender, C. M., Burlitch, J. M., Barber, D., and Pollock, C. (2000). Synthesis and fluorescence of neodymium-doped barium fluoride nanoparticles. *Chem. Mater.* 12, 1969–1976. doi: 10.1021/cm9904741

Cao, R., Huang, H., Liang, J., Wang, T., Luo, Y., and Asiri, A. M., et al. (2019). A MoN nanosheet array supported on carbon cloth as an efficient electrochemical sensor for nitrite detection. *Analyst* 144, 5378–5380. doi: 10.1039/C9AN01270B

Cui, H., Zou, G., and Lin, X. (2003). Electrochemiluminescence of luminol in alkaline solution at a paraffin-impregnated graphite electrode. *Anal. Chem.* 75, 324–331. doi: 10.1021/ac0201631

Dai, C., Wang, J., Fu, Y., Zhou, H., and Song, Q. (2017). Selective and real-time detection of nitric oxide by a two-photon fluorescent probe in live cells and tissue slices. *Anal. Chem.* 89, 10511–10519. doi: 10.1021/acs.analchem.7b02680

Ding, Z., Quinn, B. M., Haram, S. K., Pell, L. E., Korgel, B. A., and Bard, A. J. (2002). Electrochemistry and electrogenerated chemiluminescence from silicon nanocrystal quantum dots. *Science* 296, 1293–1297. doi: 10.1126/science.1069336

Dong, Y., Zhou, N., Lin, X., Lin, J., Chi, Y., and Chen, G. (2010). Extraction of electrochemiluminescent oxidized carbon quantum dots from activated carbon. *Chem Mater.* 22, 5895–5899. doi: 10.1021/cm1018844

Dou, X., Zhang, Q., Shah, S. N. A., Khan, M., Uchiyama, K., and Lin, J. (2019). MoS_2-quantum dot triggered reactive oxygen species generation and depletion, responsible for enhanced chemiluminescence. *Chem. Sci.* 10, 497–500. doi: 10.1039/C8SC03511C

Finkelstein, E., Rosen, G. M., and Rauckman, E. J. (1980). Spin trapping kinetics of the reaction of superoxide and hydroxyl radicals with nitrones. *J. Am. Chem. Soc.* 102, 4994–4999. doi: 10.1021/ja00535a029

Gunaydin, H., and Houk, K. N. (2008). Molecular dynamics simulation of the HOONO decomposition and the HO•/NO_2• caged radical pair in water. *J. Am. Chem. Soc.* 130, 10036–10037. doi: 10.1021/ja711365e

Han, S., Samanta, A., Xie, X., Huang, L., Peng, J., and Park, S. J., et al. (2017). Gold and hairpin DNA functionalization of upconversion nanocrystals for imaging and *in vivo* drug delivery. *Adv. Mater.* 29:1700244. doi: 10.1002/adma.201700244

Hassanzadeh, J., and Khataee, A. (2018). Ultrasensitive chemiluminescent biosensor for the detection of cholesterol based on synergetic peroxidase-like activity of MoS_2 and graphene quantum dots. *Talanta* 178, 992–1000. doi: 10.1016/j.talanta.2017.08.107

Houk, K. N., Condroski, K. R., and Pryor, W. A. (1996). Radical and concerted mechanisms in oxidations of amines, sulfides, and alkenes by peroxynitrite, peroxynitrous acid, and the peroxynitrite–CO_2 adduct: density functional theory transition structures and energetics. *J. Am. Chem. Soc.* 118, 13002–13006. doi: 10.1021/ja9619521

Hu, Y., Wu, B., Jin, Q., Wang, X., Li, Y., and Sun, Y., et al. (2016). Facile synthesis of 5 nm $NaYF_4$:Yb/Er nanoparticles for targeted upconversion imaging of cancer cells. *Talanta* 152, 504–512. doi: 10.1016/j.talanta.2016.02.039

Jana, J., Lee, H. J., Chung, J. S., Kim, M. H., and Hur, S. H. (2019). Blue emitting nitrogen-doped carbon dots as a fluorescent probe for nitrite ion sensing and cell-imaging. *Anal. Chim. Acta* 1079, 212–219. doi: 10.1016/j.aca.2019.06.064

Ju, H. (2013). Grand challenges in analytical chemistry, towards more bright eyes for scientific research, social events and human health. *Front. Chem.* 1:5. doi: 10.3389/fchem.2013.00005

Ju, J., Won, H., Jung, J., Yeo, J., Van Cuong, P., and Kim, D. (2017). Enhanced X-ray excited luminescence of LaF_3:Ce/CdSeS nanocomposites by resonance energy transfer for radiation detection. *J. Electron. Mater.* 46, 5319–5323. doi: 10.1007/s11664-017-5548-z

Li, S., Zhang, X., Hou, Z., Cheng, Z., Ma, P., and Lin, J. (2012). Enhanced emission of ultra-small-sized LaF_3:RE^{3+} (RE = Eu, Tb) nanoparticles through 1,2,4,5-benzenetetracarboxylic acid sensitization. *Nanoscale* 4, 5619–5626. doi: 10.1039/c2nr31206a

Lin, Z., Xue, W., Chen, H., and Lin, J. (2011). Peroxynitrous-acid-induced chemiluminescence of fluorescent carbon dots for nitrite sensing. *Anal. Chem.* 83, 8245–8251. doi: 10.1021/ac202039h

Lu, C., Lin, J., Huie, C. W., and Yamada, M. (2004). Chemiluminescence study of carbonate and peroxynitrous acid and its application to the direct determination of nitrite based on solid surface enhancement. *Anal. Chim. Acta* 510, 29–34. doi: 10.1016/j.aca.2003.12.057

Lu, C., Qu, F., Lin, J., and Yamada, M. (2002). Flow-injection chemiluminescent determination of nitrite in water based on the formation of peroxynitrite from the reaction of nitrite and hydrogen peroxide. *Anal. Chim. Acta* 474, 107–114. doi: 10.1016/S0003-2670(02)01010-3

Ma, Y., Wang, Y., Xie, D., Gu, Y., Zhang, H., and Wang, G., et al. (2018). NiFe-Layered double hydroxide nanosheet arrays supported on carbon cloth for highly sensitive detection of nitrite. *ACS Appl. Mater. Inter.* 10, 6541–6551. doi: 10.1021/acsami.7b16536

Madhuvilakku, R., Alagar, S., Mariappan, R., and Piraman, S. (2020). Glassy carbon electrodes modified with reduced graphene oxide-MoS_2-poly (3, 4-ethylene dioxythiophene) nanocomposites for the non-enzymatic detection of nitrite in water and milk. *Anal. Chim. Acta* 1093, 93–105. doi: 10.1016/j.aca.2019.09.043

Myung, N., Ding, Z., and Bard, A. J. (2002). Electrogenerated chemiluminescence of CdSe nanocrystals. *Nano Lett.* 2, 1315–1319. doi: 10.1021/nl0257824

Nampoothiri, P. K., Gandhi, M. N., and Kulkarni, A. R. (2017). Elucidating the stabilizing effect of oleic acid coated LaF_3: Nd^{3+} nanoparticle surface in the thermal degradation of PMMA nanocomposites. *Mater. Chem. Phys.* 190, 45–52. doi: 10.1016/j.matchemphys.2016.12.075

Pires, N. M. M., Dong, T., and Yang, Z. (2019). A fluorimetric nitrite biosensor with polythienothiophene-fullerene thin film detectors for on-site water monitoring. *Analyst* 144, 4342–4350. doi: 10.1039/C8AN02441C

Poznyak, S. K., Talapin, D. V., Shevchenko, E. V., and Weller, H. (2004). Quantum dot chemiluminescence. *Nano Lett.* 4, 693–698. doi: 10.1021/nl049713w

Schuyt, J. J., and Williams, G. V. M. (2018). Photoluminescence, radioluminescence and optically stimulated luminescence in nanoparticle and bulk $KMgF_3$(Eu). *J. Lumin.* 204, 472–479. doi: 10.1016/j.jlumin.2018.08.056

Starodubtseva, M. N., Cherenkevich, S. N., and Semenkova, G. N. (1999). Investigation of the interaction of sodium nitrite with hydrogen peroxide in aqueous solutions by the chemiluminescence method. *J. Appl. Spectrosc.* 66, 473–476. doi: 10.1007/BF02676785

Vijayan, A. N., Liu, Z., Zhao, H., and Zhang, P. (2019). Nicking enzyme-assisted signal-amplifiable Hg^{2+} detection using upconversion nanoparticles. *Anal. Chim. Acta* 1072, 75–80. doi: 10.1016/j.aca.2019.05.001

Wang, Q., Yu, L., Liu, Y., Lin, L., Lu, R., and Zhu, J., et al. (2017). Methods for the detection and determination of nitrite and nitrate: A review. *Talanta* 165, 709–720. doi: 10.1016/j.talanta.2016.12.044

Wang, R., Wang, Z., Xiang, X., Zhang, R., Shi, X., and Sun, X. (2018). MnO_2 nanoarrays: an efficient catalyst electrode for nitrite electroreduction toward sensing and NH_3 synthesis applications. *Chem. Commun.* 54, 10340–10342. doi: 10.1039/C8CC05837G

Wu, J., Wang, X., Lin, Y., Zheng, Y., and Lin, J. (2016). Peroxynitrous-acid-induced chemiluminescence detection of nitrite based on Microfluidic chip. *Talanta* 154, 73–79. doi: 10.1016/j.talanta.2016.03.062

Wu, J., Yang, Z., Qiu, C., Zhang, Y., Wu, Z., and Yang, J., et al. (2018). Enhanced performance of a graphene/GaAs self-driven near-infrared photodetector with upconversion nanoparticles. *Nanoscale* 10, 8023–8030. doi: 10.1039/C8NR00594J

Wu, N., Gu, Y., Kong, M., Liu, Q., Cheng, S., and Yang, Y., et al. (2020). Yb-based nanoparticles with the same excitation and emission wavelength for sensitive *in vivo* biodetection. *Anal. Chem.* 92, 2027–2033. doi: 10.1021/acs.analchem.9b04448

Wu, Y., Xu, J., Poh, E. T., Liang, L., Liu, H., and Yang, J. K. W., et al. (2019). Upconversion superburst with sub-2 μs lifetime. *Nat. Nanotechnol.* 14, 1110–1115. doi: 10.1038/s41565-019-0560-5

Yan, S., Zeng, X., Tang, Y., Liu, B., Wang, Y., and Liu, X. (2019). Activating antitumor immunity and antimetastatic effect through polydopamine-encapsulated core-shell upconversion nanoparticles. *Adv. Mater.* 31:1905825. doi: 10.1002/adma.201905825

Yi, Z., Luo, Z., Barth, N. D., Meng, X., Liu, H., and Bu, W., et al. (2019). *In vivo* tumor visualization through MRI Off-On switching of $NaGdF_4$-$CaCO_3$ nanoconjugates. *Adv. Mater.* 31, 1901851. doi: 10.1002/adma.201901851

Zeng, X., Chen, S., Weitemier, A., Han, S., Blasiak, A., and Prasad, A., et al. (2019). Visualization of intra-neuronal motor protein transport through upconversion microscopy. *Angew. Chem. Int. Edit.* 58, 9262–9268. doi: 10.1002/anie.201904208

Zhang, L., Wu, X., Yuan, Z., and Lu, C. (2018). Π-Conjugated thiolate amplified spectrophotometry nitrite assay with improved sensitivity and accuracy. *Chem. Commun.* 54, 12178–12181. doi: 10.1039/C8CC06477F

Zhang, Y., Nie, J., Wei, H., Xu, H., Wang, Q., and Cong, Y., et al. (2018). Electrochemical detection of nitrite ions using Ag/Cu/MWNT nanoclusters electrodeposited on a glassy carbon electrode. *Sens. Actuator B Chem.* 258, 1107–1116. doi: 10.1016/j.snb.2017.12.001

Zheng, H., Guan, X., Mao, X., Zhu, Z., Yang, C., and Qiu, H., et al. (2018). Determination of nitrite in water samples using atmospheric pressure glow discharge microplasma emission and chemical vapor generation of NO species. *Anal. Chim. Acta* 1001, 100–105. doi: 10.1016/j.aca.2017.11.060

Zheng, L., Chi, Y., Dong, Y., Lin, J., and Wang, B. (2009). Electrochemiluminescence of water-soluble carbon nanocrystals released electrochemically from graphite. *J. Am. Chem. Soc.* 131, 4564–4565. doi: 10.1021/ja809073f

Zheng, Y., Zhang, D., Shah, S. N. A., Li, H., and Lin, J. (2017). Ultra-weak chemiluminescence enhanced by facilely synthesized nitrogen-rich quantum dots through chemiluminescence resonance energy transfer and electron hole injection. *Chem. Commun.* 53, 5657–5660. doi: 10.1039/C7CC02041D

Zhou, Y., Ma, M., He, H., Cai, Z., Gao, N., and He, C., et al. (2019). Highly sensitive nitrite sensor based on AuNPs/RGO nanocomposites modified graphene electrochemical transistors. *Biosens. Bioelectron.* 146, 111751. doi: 10.1016/j.bios.2019.111751

Zhu, R., Zhang, Y., Fang, X., Cui, X., Wang, J., and Yue, C., et al. (2019). *In situ* sulfur-doped graphitic carbon nitride nanosheets with

enhanced electrogenerated chemiluminescence used for sensitive and selective sensing of l-cysteine. *J. Mater. Chem. B.* 7, 2320–2329. doi: 10.1039/C9TB00301K

Conflict of Interest: The authors declare that the research was conducted in the absence of any commercial or financial relationships that could be construed as a potential conflict of interest.

frontiers in Chemistry

ORIGINAL RESEARCH
published: 16 September 2020
doi: 10.3389/fchem.2020.00836

Microscale Self-Assembly of Upconversion Nanoparticles Driven by Block Copolymer

Qianqian Su[1,2*†], *Meng-Tao Zhou*[1†], *Ming-Zhu Zhou*[1], *Qiang Sun*[3], *Taotao Ai*[4] *and Yan Su*[5*]

[1] *Institute of Nanochemistry and Nanobiology, Shanghai University, Shanghai, China,* [2] *Department of Chemistry, National University of Singapore, Singapore, Singapore,* [3] *Center for Functional Materials, NUS (Suzhou) Research Institute, Suzhou, China,* [4] *National and Local Joint Engineering Laboratory for Slag Comprehensive Utilization and Environmental Technology, School of Materials Science and Engineering, Shaanxi University of Technology, Hanzhong, China,* [5] *Genome Institute of Singapore, Agency of Science Technology and Research, Singapore, Singapore*

OPEN ACCESS

Edited by:
Feng Wang,
City University of Hong Kong, Hong Kong

Reviewed by:
Xiaoji Xie,
Nanjing Tech University, China
Yu Wang,
Shenzhen University, China

****Correspondence:***
Qianqian Su
chmsqq@shu.edu.cn
Yan Su
suy1@gis.a-star.edu.sg

† These authors have contributed equally to this work

Specialty section:
This article was submitted to Nanoscience, a section of the journal Frontiers in Chemistry

Received: *14 July 2020*
Accepted: *10 August 2020*
Published: *16 September 2020*

Citation:
Su Q, Zhou M-T, Zhou M-Z, Sun Q, Ai T and Su Y (2020) Microscale Self-Assembly of Upconversion Nanoparticles Driven by Block Copolymer. Front. Chem. 8:836. doi: 10.3389/fchem.2020.00836

Lanthanide-based upconversion nanoparticles can convert low-energy excitation to high-energy emission. The self-assembled upconversion nanoparticles with unique structures have considerable promise in sensors and optical devices due to intriguing properties. However, the assembly of isotropic nanocrystals into anisotropic structures is a fundamental challenge caused by the difficulty in controlling interparticle interactions. Herein, we report a novel approach for the preparation of the chain-like assemblies of upconversion nanoparticles at different scales from nano-scale to micro-scale. The dimension of chain-like assembly can be fine-tuned using various incubation times. Our study observed Y-junction aggregate morphology due to the flexible nature of amphiphilic block copolymer. Furthermore, the prepared nanoparticle assemblies of upconversion nanoparticles with lengths up to several micrometers can serve as novel luminescent nanostructure and offer great opportunities in the fields of optical applications.

Keywords: lanthanide-doped nanoparticles, upconversion nanoparticle, self-assembly, micro-scale, nanoparticles belt

INTRODUCTION

In the last decade, lanthanide-doped upconversion nanoparticles have been widely studied because of their unique optical properties including narrow emission bandwidth, large Stokes shift, long luminescence lifetime and high photostability (Auzel, 2004; Lu et al., 2013; Bettinelli et al., 2015; Li et al., 2015, 2017; Jalani et al., 2018; Liu et al., 2018; Wang et al., 2018). These nanoparticles have the potential to be used in diverse applications such as biomedicine, data storage, solar energy conversion (Chen et al., 2015, 2019; Tsang et al., 2015; Zhou B. et al., 2015; Qi et al., 2017; Su et al., 2017; Zhu et al., 2017; Chen B. et al., 2018; Chen S. et al., 2018; Gai et al., 2018; Zheng et al., 2018; Ma et al., 2019). Particularly, the growing demand of lanthanide-doped nanoparticles using in various applications has in turn greatly stimulated basic research to develop novel nanoparticles with controlled size, shape, phase and desired properties (Wang et al., 2010, 2019; Du et al., 2016; Liu D. et al., 2016; Shi et al., 2017; Kang et al., 2019; Sun et al., 2019; Wang, 2019; Wu et al., 2019; Zhao et al., 2019; Zheng et al., 2019; Chen and Wang, 2020).

The assemblies of colloidal nanoparticles with unique structure and optical properties have considerable promise in various applications (Nie et al., 2010; Singamaneni et al., 2011; Boles et al., 2016; Ariga et al., 2019; Grzelczak et al., 2019; Runowski et al., 2019). However, the assembly of isotropic nanocrystals into anisotropic structures is a fundamental challenge in nanochemistry (Liu et al., 2010; Chen and Wang, 2019). Methods have been developed for organizing inorganic nanomaterials based on inherent anisotropy of magnetic (Zhang and Wang, 2008) or electric dipoles (Si et al., 2007), external magnetic (Hu et al., 2011) or electric field-induction (Rozynek et al., 2017), spatial confinement using hard or soft templates. Specific examples of templates include linear biomacromolecules (Braun et al., 1998; Tseng et al., 2006), block copolymers (Li et al., 2011; Kim et al., 2020), carbon nanotubes (Wang et al., 2006), and so on. Despite the considerable progress made in the past several years, self-assembly of nanoparticles into an anisotropic structure is still a daunting challenge because subtle variations in interparticle interactions can cause prominent morphology changes (Su et al., 2018). Moreover, anisotropic upconversion nanoparticle self-assemblies have been rarely reported (Liu X. et al., 2016; Ren et al., 2018; Yuan et al., 2018).

Here, we report a self-assembly method of upconversion nanoparticles mediated by amphiphilic block copolymer (**Scheme 1**). This approach can obtain chain-like assemblies that span multiple length scales from nanometers to micrometers. Our study reveals a time-dependent chain-like self-assembly process. Besides, we observe Y-junction aggregate morphology due to the flexible nature of amphiphilic block copolymer. Importantly, this study provides a new route to prepare anisotropic structures materials and offer exciting opportunities for optical applications.

MATERIALS AND METHODS

Materials

Yttrium(III) acetate hydrate (99.9%), ytterbium(III) acetate hydrate (99.9%), thulium(III) acetate hydrate (99.9%), oleic acid (technical grade, 90%), 1-octadecene (technical grade, 90%), Igepal CO-520, tetraethyl orthosilicate (TEOS, >99.0%), ammonium fluoride (98%) sodium hydroxide (>98%), and Pluronic F127 were purchased from Sigma-Aldrich. Methanol (99.5%), cyclohexane (analytical grade), and ammonia solution (25–28%) were obtained from Aladdin. All chemicals were used as received without further purification.

Characterization

Low-resolution transmission electron microscopy (TEM) measurements were carried out on a JEOL-JEM 2010F field emission transmission electron microscopy operated at an acceleration voltage of 200 kV. Powder X-ray diffraction (XRD) data were recorded on a Bruker D8 Advance diffractometer with a graphite monochromatized CuKα radiation (1.5406 Å). Luminescence spectra were recorded at room temperature with a DM150i monochromator equipped with an R928 photon-counting photomultiplier tube (PMT), in conjunction with a 980-nm diode laser. Upconversion luminescence microscopy imaging was performed on an Olympus BX51 microscope with the xenon lamp adapted to a diode laser. Luminescence micrographs were recorded with a Nikon DS-Ri1 imaging system. Digital photographs were taken with a Nikon D700 camera.

Synthesis of $NaYF_4$:Yb,Tm Nanoparticles

In a typical procedure, a solution of $Ln(CH_3CO_2)_3$ (0.2 M, Ln = Y, Yb, Tm) in water (2 mL), and oleic acid (4 mL) were added to a 50 mL two-neck flask and then heated to 150°C for 30 min to remove the water content from the mixture. Then 1-octadecene (6 mL) was quickly added to the flask and the resulting mixture was maintained at 150°C for another 30 min before cooling down to 50°C. Shortly thereafter, 5 mL of a methanol solution containing NH_4F (1.36 mmol) and NaOH (1 mmol) was added and the resultant mixture was stirred for 30 min at this temperature. After the methanol was evaporated, the solution was heated to 300°C under argon for 1.5 h and then cooled down to room temperature. The resulting nanoparticles were precipitated by the addition of excess ethanol, collected by centrifugation at 6,000 rpm for 5 min, and washed with ethanol several times before dispersing them in 2 mL of cyclohexane for optical and TEM measurements.

Synthesis of $NaYF_4$:Yb,Tm$NaYF_4$ ($UCNP_{Tm}$) Nanoparticles

The as-synthesized $NaYF_4$:Yb,Tm core nanoparticles were used as seeds to epitaxial overgrowth of $NaYF_4$ layer. For the preparation of shell precursors, 0.4 mmol of $Y(CH_3CO_2)_3$ was used. The synthetic procedure is similar to the synthesis of core nanoparticles.

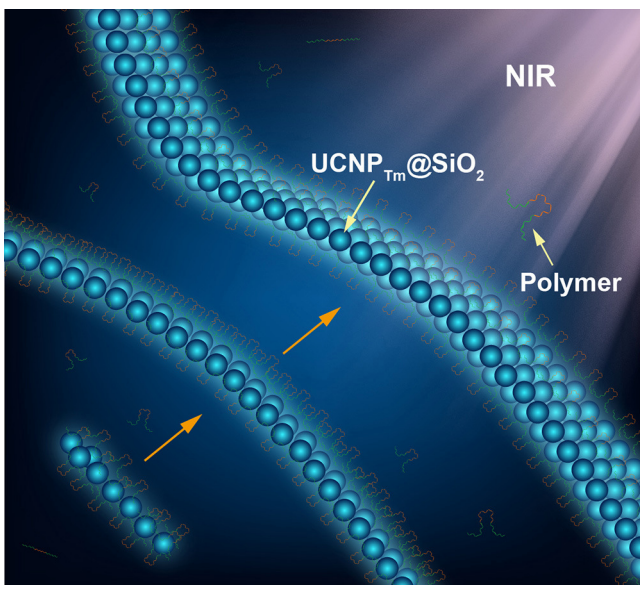

SCHEME 1 | Schematic illustration of amphiphilic copolymer mediated self-assembly of silica-coated upconversion nanoparticles.

Preparation of Hydrophilic Ligand-Free $UCNP_{Tm}$ Nanoparticles

Ligand-free nanoparticles were prepared following a literature procedure (Su et al., 2012). The as-synthesized oleic acid-capped $UCNP_{Tm}$ nanoparticles were dispersed in a mixed solution of HCl (1 mL; 0.2 M) and ethanol (1 mL) and then sonicated for 5 min to remove the surface-capped ligands. The resulting ligand-free nanoparticles were centrifuged at 16,500 rpm for 20 min. The products were finally washed with ethanol and DI water several times and then re-dispersed in DI water.

Synthesis of $NaYF_4$:Yb,Tm@$NaYF_4$@SiO_2 ($UCNP_{Tm}$@SiO_2) Nanoparticles

The synthesis of silica-coated $UCNP_{Tm}$ nanoparticles was carried out following a literature procedure (Han et al., 2017). One milliliter of Igepal CO-520 was mixed with 20 mL cyclohexane in a flask and stirred for 1 h. As-synthesized ligand-free $UCNP_{Tm}$ nanoparticles (1.5 mL) was then added into the mixture and stirred for 3 h at room temperature. After that, $NH_3 \cdot H_2O$ (150 μL, 30%) was added into the resulting mixture and stirred for another 2 h. A solution composed of TEOS (0.2 mL) and cyclohexane (0.8 mL) was introduced into the flask within 1 h by using a syringe pump. Subsequently, the mixture was hermetically stirred for 24 h at room temperature. The as-prepared products were precipitated by methanol and then centrifuged at 12,000 rpm for 10 min. The nanoparticles were then washed with a mixture of ethanol and cyclohexane three times. Finally, the nanoparticles were dispersed in deionized water.

Self-Assembly of Upconversion Nanoparticles by F127

In a typical experiment, 100 μL $UCNP_{Tm}$@SiO_2 aqueous solution (1 mg mL^{-1}) was diluted in 3 mL DI water. 0.6 mg F127 was added to the solution and then heated to 60°C. After stirring for 1 h, the resultant suspension was incubated at 60°C for a certain time (12, 24, 48 h, and 7 days) without agitation. A few drops of nanoparticle solution were dropped onto the glass slide. Subsequently, the luminescence micrographs were captured under a recorded with a Nikon DS-Ri1 color imaging system.

RESULTS AND DISCUSSION

Characterization of Upconversion Nanoparticles

In terms of efficient upconversion luminescence, the inherent property of host materials and crystal nanostructure play key roles (Chen et al., 2014; Zhou J. et al., 2015). Hexagonal

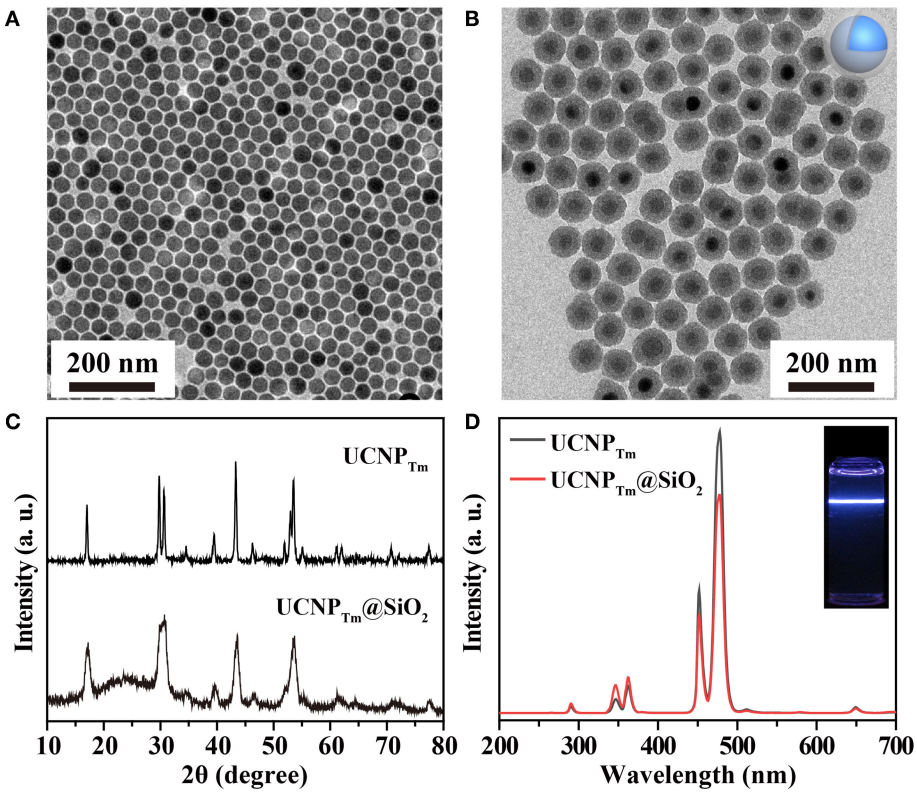

FIGURE 1 | (A) TEM image of $NaYF_4$:Yb,Tm nanoparticles in cyclohexane. **(B)** TEM image of $NaYF_4$:Yb,Tm@SiO_2 nanoparticles in water. **(C)** XRD patterns of $NaYF_4$:Yb,Tm and $NaYF_4$:Yb,Tm@SiO_2 nanoparticles. **(D)** The corresponding emission spectrum of the as-prepared nanoparticles and their silica-coated counterpart. Inset: luminescence photograph of SiO_2 coated-nanoparticles in water under irradiation of a 980 nm laser.

$NaYF_4$ is regarded as ideal host materials because of the low phonon energy and high photochemical stability (Wang et al., 2010). Additionally, optical inert $NaYF_4$ host materials can avoid unwanted energy consumption, i.e., surface quenching of the fluorescence (Su et al., 2012). Therefore, Hexagonal $NaYF_4$ was chosen as the host matrix to obtain efficient upconversion luminescence. To realize good water solubility, we coated a layer of SiO_2 onto the surface of upconversion nanoparticles and use them as an experimental model for the self-assembly demonstration.

We began with the synthesis of oleic acid-capped $NaYF_4$:Yb,Tm@$NaYF_4$ ($UCNP_{Tm}$) and $NaYF_4$:Yb,Er@$NaYF_4$ ($UCNP_{Er}$) core-shell nanospheres through an epitaxial growth method (Abel et al., 2009; Wang and Chen, 2019). The as-synthesized nanospheres were characterized using a transmission electron microscope (TEM). Uniform $UCNP_{Tm}$ nanoparticles

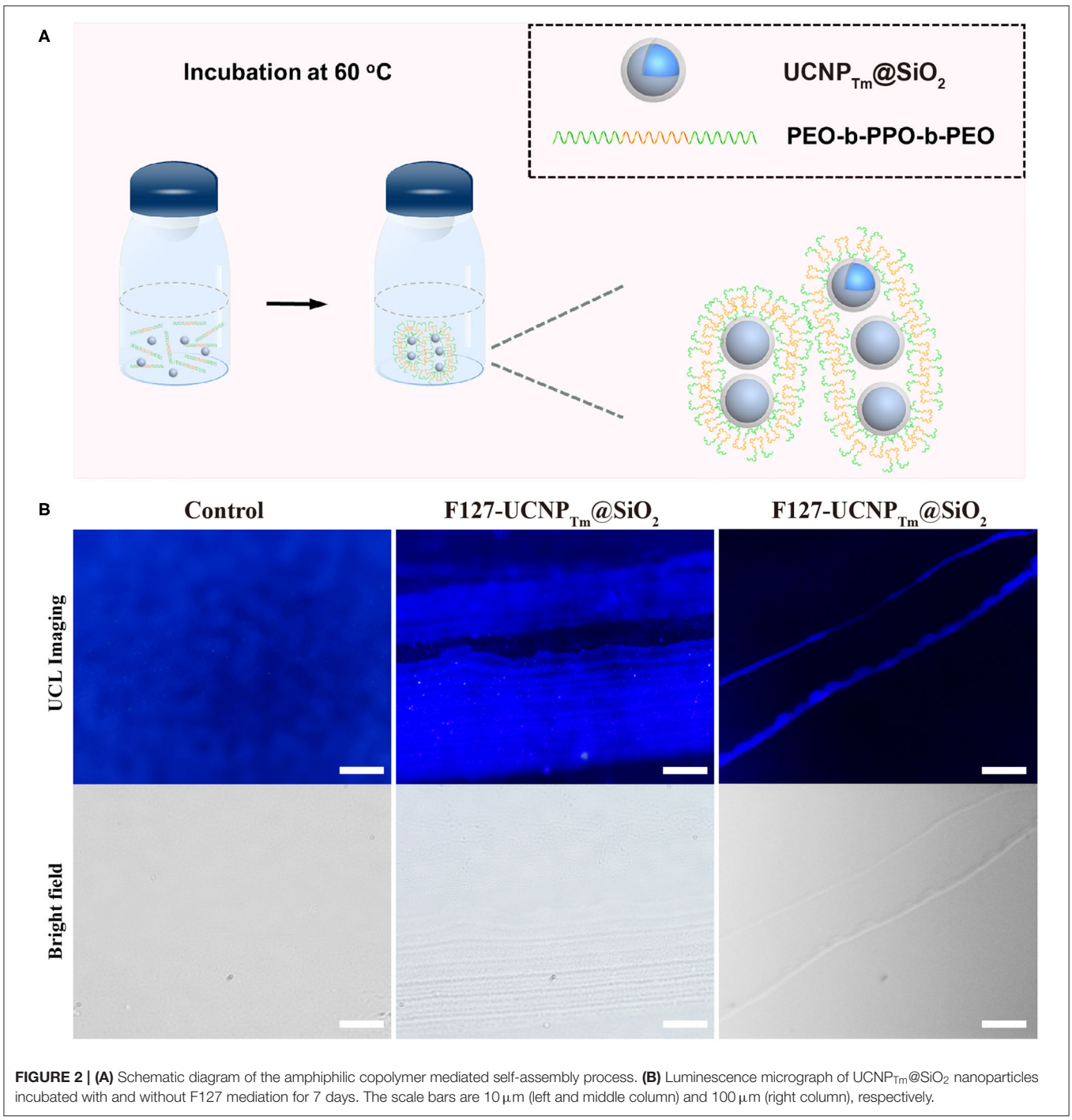

FIGURE 2 | (A) Schematic diagram of the amphiphilic copolymer mediated self-assembly process. **(B)** Luminescence micrograph of $UCNP_{Tm}$@SiO_2 nanoparticles incubated with and without F127 mediation for 7 days. The scale bars are 10 μm (left and middle column) and 100 μm (right column), respectively.

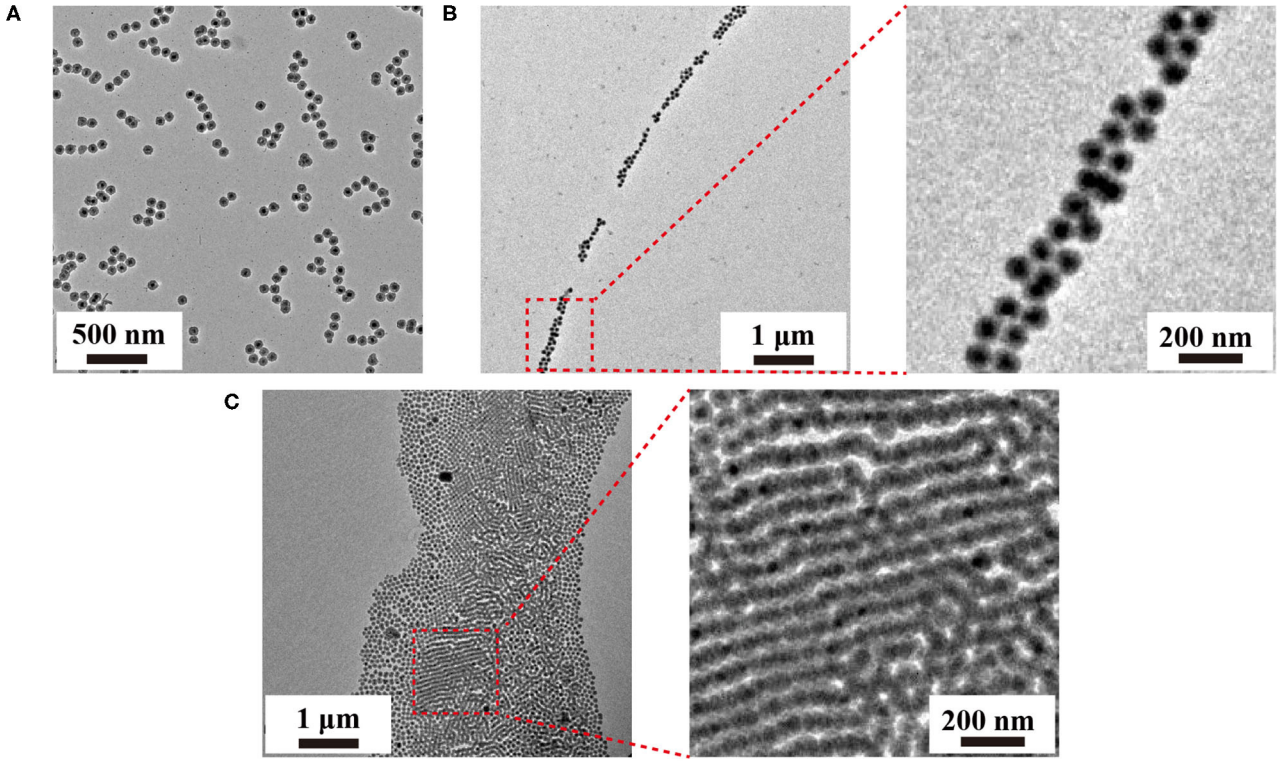

FIGURE 3 | TEM images of the as-prepared upconversion nanoparticle assemblies mediated by F127 under varied incubation time, 12 h **(A)**, 24 h, **(B)**, 48 h **(C)**, respectively.

with an average diameter of about 36 nm for $UCNP_{Tm}$ were obtained and shown in **Figure 1A** and **Supplementary Figure 1**. After silica coating on the surface of $UCNP_{Tm}$ nanospheres, the size of the nanoparticles reached about 76 nm (**Figure 1B** and **Supplementary Figure 2**). The dynamic light scattering (DLS) measurement show that the hydrodiameter of $UCNP_{Tm}@SiO_2$ nanoparticles was around 90 nm (PDI = 0.13), demonstrating their mono-dispersion in water (**Supplementary Figure 3**). X-ray powder diffraction (XRD) analysis was conducted to confirm the phase-purity of $UCNP_{Tm}$ nanoparticles, which can be indexed as a hexagonal phase of $NaYF_4$ (JCPDS file number 16-0334) (**Figure 1C**). A broad diffraction peak at $2\theta = 22^{\circ}$ appeared in $UCNP_{Tm}@SiO_2$ nanoparticles pattern, which can be ascribed to the peak of amorphous silica (Zhou et al., 2019).

We next studied the optical properties of as-prepared upconversion nanoparticles. Upon 980 nm excitation, Tm^{3+} ions in $UCNP_{Tm}$ nanoparticles exhibit a characteristic emission at 290 nm ($^1I_6 \rightarrow {}^3H_6$), 345 nm ($^1I_6 \rightarrow {}^3H_5$), 360 nm ($^1D_2 \rightarrow {}^3H_6$), 450 nm ($^1D_2 \rightarrow {}^3F_4$), 475 nm ($^1G_4 \rightarrow {}^3H_6$), 511 nm ($^1D_2 \rightarrow {}^3H_5$) and 650 nm ($^1G_4 \rightarrow {}^3F_4$) from ultraviolent to visible region (Wang and Liu, 2008), respectively (**Figure 1D**). After silica coating, the luminescent intensity was slightly weaker compared to oleic acid-coated nanoparticles. The resulting nanoparticles were dispersed in DI water prior to being used for self-assembly demonstration (**Figure 1D**, inset).

As a proof-of-concept experiment, the amphiphilic copolymer F127 was employed as a surfactant to mediate the self-assembly process of $UCNP_{Tm}@SiO_2$ nanoparticles. The procedure the $UCNP_{Tm}@SiO_2$ nanoparticles self-assembly was shown in **Figure 2A**. In a typical experiment, we simply mixed $UCNP_{Tm}@SiO_2$ and amphiphilic copolymer F127 in aqueous solution and then heated to 60°C. Upon aging the nanoparticles in amphiphilic copolymer aqueous solution for 7 days without agitation, upconversion nanoparticles long belts gradually generated. As shown in **Figure 2B** (middle and right column), long upconversion nanoparticles belts composed by horizontally arranged nanoparticle chains were clearly observed and the nanoparticle belts reach to micro-scale. However, we didn't observe any organized structure without the addition of copolymer F127 (**Figure 2B**, left column). To our knowledge, this is the first observation of a micrometer scale upconversion nanoparticles belts by solution self-assembly of amphiphilic block copolymers.

The formation of the upconversion nanoparticle chains was then studied using TEM as shown in **Figure 3A**. The nanoparticles connected in a one-dimensional tendency upon short incubation time (12 h) with amphiphilic copolymer F127. TEM images revealed the presence of the short chains composed by several to a dozen nanoparticles. The interparticle separations between $UCNP_{Tm}@SiO_2$ nanoparticles in the chain

were observed (**Supplementary Figure 4**), indicating that the obtained nanoparticle chains are connected by the molecular linker. Noted that hot water can etch away the SiO_2 shell by breaking the internal Si-O-Si bonds (Liu et al., 2014). Our nanoparticles were slightly etched due to the protection of F127 copolymer. When the incubation time was prolonged to 24 h, we observed long chains of $UCNP_{Tm}@SiO_2$ nanoparticles which reached microscale in length (**Figure 3B**). The nanoparticles

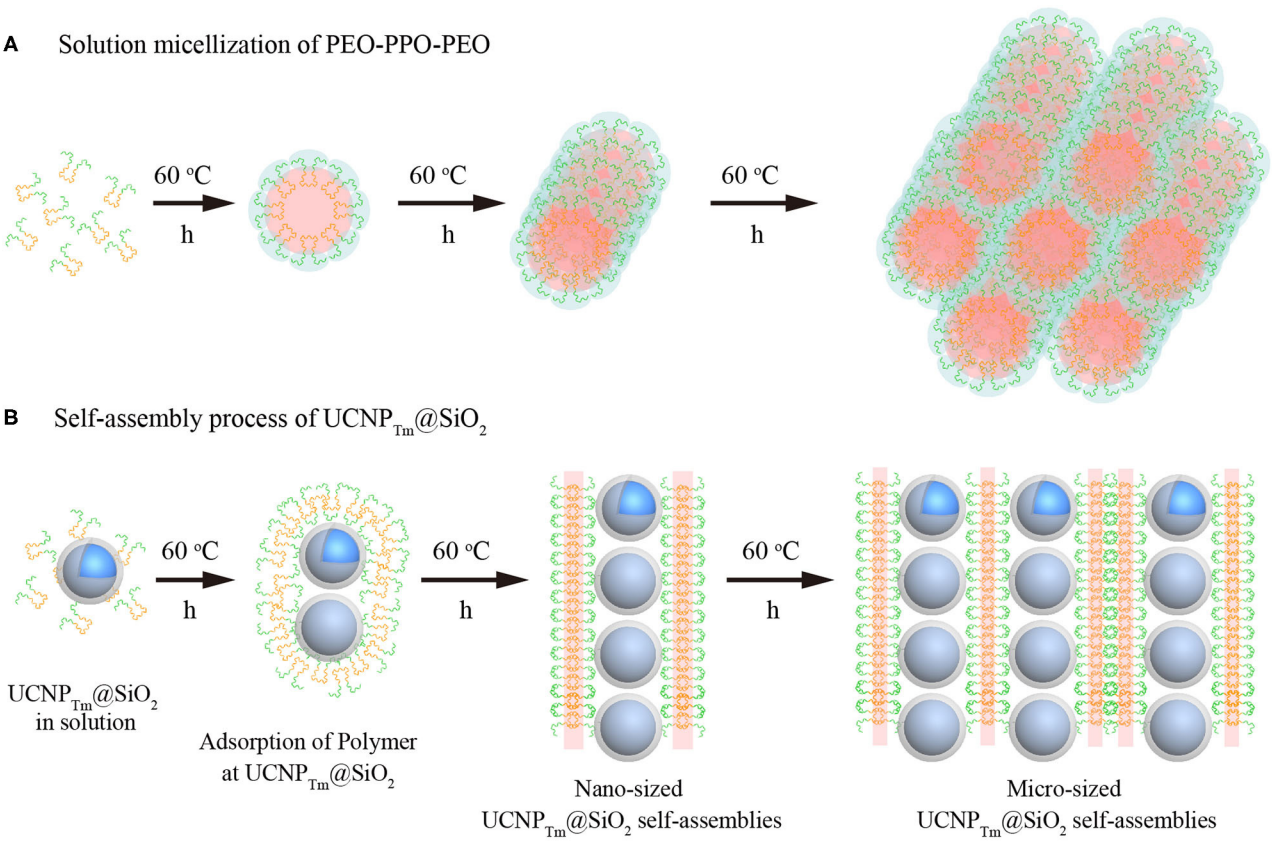

FIGURE 4 | (A) Morphological transitions of amphiphilic block copolymers F127 as a function of time. **(B)** Schematic illustration of the self-assembly process for SiO_2-coated upconversion nanoparticles. Note that the green chain denotes hydrophilic segment PEO, and the orange chain represents hydrophobic segment PPO of F127, respectively.

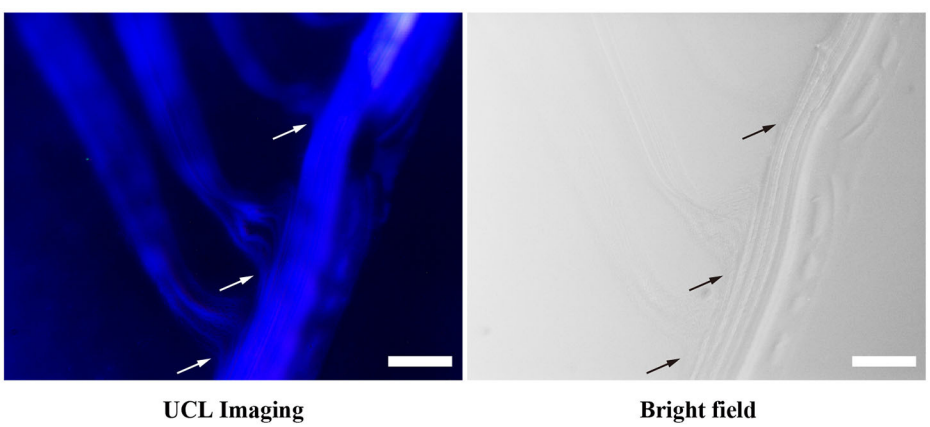

FIGURE 5 | Luminescence micrograph demonstrates the existence of Y-junctions of $UCNP_{Tm}@SiO_2$ assemblies incubated with F127 mediation for 7 days. Arrows indicate examples of Y-junctions. The scale bars are 10 μm.

chains have an average width of 1–3 nanoparticles. Interestingly, further prolonging the incubation time resulted in the formation of upconversion nanoparticle belts. As shown in **Figure 3C**, TEM images revealed the presence of the belts with an average belt length of 40–50 nanoparticles and as wide as about 2.5–4 μm. Furthermore, these nanoparticles under the drive of interfacial energy would spontaneously assemble in close-packed arrangements during the extended incubation period. This result is also consistent with the luminescence micrographs of $UCNP_{Tm}@SiO_2$ nanoparticle showing horizontally arranged nanoparticle chains. By contrast, we observe a random pattern of $UCNP_{Tm}@SiO_2$ nanoparticles without the addition of copolymer F127 (**Supplementary Figure 5**).

The ability of amphiphilic block copolymers to drive $UCNP_{Tm}@SiO_2$ nanoparticles self-assemble into chain-like nanostructures when dissolved in water is based on the specific amphiphilic character of this block copolymer F127. These amphiphilic block copolymers consist of a polar, hydrophilic polymer block (PEO) and a non-polar, lipophilic polymer block (PPO). In water, which is a thermodynamically good solvent for the PEO block but a poor solvent for the PPO block, the "insoluble" PPO block aggregates and forms a core while the "soluble" PEO block forms a corona that interacts with the water and stabilizes the polymer self-assembly (Alexandridis et al., 1994; Liu and Li, 2015). As shown in **Figure 4A**, the formation of one-dimensional chains may be induced by the transition from spherical to long cylindrical micelles of the amphiphilic block copolymer. It should be noted that the self-assembly of amphiphilic block copolymers in specific block-selective solvents generates morphologies such as spheres, cylindrical micelles, and a variety of other architectures (Kang et al., 2005; Gilroy et al., 2010).

SiO_2 coated upconversion nanoparticles exhibited durable super-hydrophilic surface properties due to that the surface of silica particles is covered with SiOH groups. The PEO-PPO-PEO block copolymer can be absorbed on the hydrophilic surfaces. On hydrophilic surfaces, these block copolymer surfactants adsorb with their hydrophilic tail (PEO) toward the SiO_2 surface, resulting in double-layer adsorption (Malmsten et al., 1992). Furthermore, when the incubation time was prolonged, the size of the cylindrical micelles became larger in width and length, and thus micro-scaled nanoparticle assembly was formed (**Figure 4B**). It should be noted that our results are also consistent with the previous experimental evidence showing that the length of cylindrical block copolymer micelles could reach up to ∼200 nm to 2 μm (Gilroy et al., 2010). Taken together, we suggest that $UCNP_{Tm}@SiO_2$ nanoparticles prefer to assemble in a chain manner might be caused by the mutual attraction between the hydrophilic-hydrophilic interactions (Fukao et al., 2009) and cylindrical micelles formed by the self-assembly process of block copolymers F127.

In addition to chain-like assemblies spanning from the nanometer to the micrometer length scale, we also observed occasional Y-junctions of $UCNP_{Tm}@SiO_2$ assemblies incubated with F127 mediation for 7 days by using the luminescence microscope and the image was shown in **Figure 5**. To further demonstrate the existence of Y-junctions, we carefully examined the 24 h-incubation samples of $UCNP_{Tm}@SiO_2$ by TEM image.

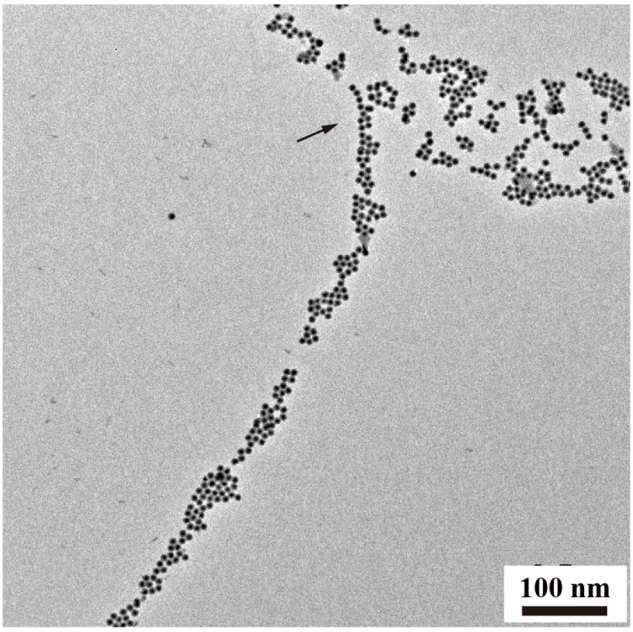

FIGURE 6 | TEM analysis of Y-junctions of $UCNP_{Tm}@SiO_2$ assemblies incubated with F127 mediation for 24 h. Arrows indicate examples of Y-junctions.

As expected, we observed the formation of Y-junctions, and TEM images were shown in **Figure 6**. This morphology may be ascribed to typical structural defects associated with the formation of the cylindrical micelle (Fenyves et al., 2014). It was reported that the formation of structural defects (i.e., Y-junctions) becomes prevalent when micellization kinetics slow down (Tlusty and Safran, 2000). We observed some Y-junctions (**Supplementary Figure 6**). We hypothesized that such a behavior can be ascribed to the flexible nature of F127 copolymer, which can accommodate packing frustrations in structures that have significant deviations from the mean curvature. This explanation was consistent with the previous report indicating that the packing frustrations associated with deviations from the mean curvature in the Y-junctions would be alleviated by chain stretching of polymers with high molecular weight (Jain and Bates, 2003). Moreover, our mechanism is different from the DNA mediated self-assembly mechanism reported by Jin and coworkers, which involves anisotropic surface functionalization of upconversion nanoparticle that directs the anisotropic pattern of upconversion nanoparticle self-assembly (Ren et al., 2018).

CONCLUSIONS

In conclusion, we have presented a novel approach for controlling the one-dimensional assemblies of upconversion nanoparticles at different scales from nano-scale to micro-scale. The results revealed time-dependent morphology, producing chain-like and belt-like structures. Our study suggests that the morphology is depending on the morphology of micelles of amphiphilic block copolymers in specific conditions. And the

driving force for the self-assembly of upconversion nanoparticles is particle surface hydrophobic and hydrophilic force offered by amphiphilic polymers. Furthermore, this work may lead to new applications for upconversion nanoparticles and may provide insightful ideas for the design of other functional nanomaterials.

DATA AVAILABILITY STATEMENT

All datasets generated for this study are included in the article/**Supplementary Material**.

AUTHOR CONTRIBUTIONS

QSu and YS conceived the project. QSu, M-TZ, YS, M-ZZ, and QSun were primarily responsible for the experiments of nanoparticle synthesis and characterization. QSu, M-TZ, YS, and TA contributed to the data analyses and discussion. QSu, YS, and TA prepared figures and wrote the paper with input from other authors. All authors contributed to the article and approved the submitted version.

ACKNOWLEDGMENTS

We are thankful for financial support from the National Natural Science Foundation of China (Nos. 21701109 and 21701119) and the National Basic Research Program of China (No. 2016YFA0201600). The content of this manuscript has been published in part as part of the thesis of Su Qianqian (Su, 2013).

SUPPLEMENTARY MATERIAL

The Supplementary Material for this article can be found online at: https://www.frontiersin.org/articles/10.3389/fchem.2020.00836/full#supplementary-material

REFERENCES

Abel, K. A., Boyer, J. C., and van Veggel, F. C. J. M. (2009). Hard proof of the $NaYF_4$/$NaGdF_4$ nanocrystal core/shell structure. *J. Am. Chem. Soc.* 131, 14644–14645. doi: 10.1021/ja906971y

Alexandridis, P., Holzwarth, J. F., and Hatton, T. A. (1994). Micellization of poly(ethylene oxide)-poly(propylene oxide)-poly(ethylene oxide) triblock copolymers in aqueous solutions: thermodynamics of copolymer association. *Macromolecules* 27, 2414–2425. doi: 10.1021/ma00087a009

Ariga, K., Nishikawa, M., Mori, T., Takeya, J., Shrestha, L. K., and Hill, J. P. (2019). Self-assembly as a key player for materials nanoarchitectonics. *Sci. Technol. Adv. Mater.* 20, 51–95. doi: 10.1080/14686996.2018.1553108

Auzel, F. (2004). Upconversion and anti-Stokes processes with f and d ions in solids. *Chem. Rev.* 104, 139–173. doi: 10.1021/cr020357g

Bettinelli, M., Carlos, L. D., and Liu, X. (2015). Lanthanide-doped upconversion nanoparticles. *Phys. Today* 68, 38–44. doi: 10.1063/PT.3.2913

Boles, M. A., Engel, M., and Talapin, D. V. (2016). Self-assembly of colloidal nanocrystals: from intricate structures to functional materials. *Chem. Rev.* 116, 11220–11289. doi: 10.1021/acs.chemrev.6b00196

Braun, E., Eichen, E., Sivan, U., and Ben-Yoseph, G. (1998). DNA-templated assembly and electrode attachment of a conducting silver wire. *Nature* 391, 775–778. doi: 10.1038/35826

Chen, B., Su, Q., Kong, W., Wang, Y., Shi, P., and Wang, F. (2018). Energy transfer-based biodetection using optical nanomaterials. *J. Mater. Chem. B* 6, 2924–2944. doi: 10.1039/c8tb00614h

Chen, B., and Wang, F. (2019). Combating concentration quenching in upconversion nanoparticles. *Acc. Chem. Res.* 53, 358–367. doi: 10.1021/acs.accounts.9b00453

Chen, B., and Wang, F. (2020). Emerging frontiers of upconversion nanoparticles. *Trends Chem.* 2, 427. doi: 10.1016/j.trechm.2020.01.008

Chen, G., Agren, H., Ohulchanskyy, T. Y., and Prasad, P. N. (2015). Light upconverting core-shell nanostructures: nanophotonic control for emerging applications. *Chem. Soc. Rev.* 44, 1680–1713. doi: 10.1039/c4cs00170b

Chen, G., Qiu, H., Prasad, P. N., and Chen, X. (2014). Upconversion nanoparticles: design, nanochemistry, and applications in theranostics. *Chem. Rev.* 114, 5161–5214. doi: 10.1021/cr400425h

Chen, L., Su, B., and Jiang, L. (2019). Recent advances in one-dimensional assembly of nanoparticles. *Chem. Soc. Rev.* 48, 8–21. doi: 10.1039/c8cs00703a

Chen, S., Weitemier, A. Z., Zeng, X., He, L., Wang, X., Tao, Y., et al. (2018). Near-infrared deep brain stimulation via upconversion nanoparticle-mediated optogenetics. *Science* 359, 679–683. doi: 10.1126/science.aaq1144

Du, P., Luo, L., Park, H. K., and Yu, J. S. (2016). Citric-assisted sol-gel based $Er3^{+}$/Yb^{3+}-codoped $Na_{0.5}Gd_{0.5}MoO_4$: A novel highly-efficient infrared-to-visible upconversion material for optical temperature sensors and optical heaters. *Chem. Eng. J.* 306, 840–848. doi: 10.1016/j.cej.2016.08.007

Fenyves, R., Schmutz, M., Horner, I. J., Bright, F. V., and Rzayev, J. (2014). Aqueous self-assembly of giant bottlebrush block copolymer surfactants as shape-tunable building blocks. *J. Am. Chem. Soc.* 136, 7762–7770. doi: 10.1021/ja503283r

Fukao, M., Sugawara, A., Shimojima, A., Fan, W., Arunagirinathan, M. A., Tsapatsis, M., et al. (2009). One-dimensional assembly of silica nanospheres mediated by block copolymer in liquid phase. *J. Am. Chem. Soc.* 131:16344. doi: 10.1021/ja907013u

Gai, S., Yang, G., Yang, P., He, F., Lin, J., Jin, D., et al. (2018). Recent advances in functional nanomaterials for light-triggered cancer therapy. *Nano Today* 19, 146–187. doi: 10.1016/j.nantod.2018.02.010

Gilroy, J. B., Gadt, T., Whittell, G. R., Chabanne, L., Mitchels, J. M., Richardson, R. M., et al. (2010). Monodisperse cylindrical micelles by crystallization-driven living self-assembly. *Nat. Chem.* 2, 566–570. doi: 10.1038/nchem.664

Grzelczak, M., Liz-Marzan, L. M., and Klajn, R. (2019). Stimuli-responsive self-assembly of nanoparticles. *Chem. Soc. Rev.* 48, 1342–1361. doi: 10.1039/c8cs00787j

Han, S., Samanta, A., Xie, X., Huang, L., Peng, J., Park, S. J., et al. (2017). Gold and hairpin DNA functionalization of upconversion nanocrystals for imaging and in vivo drug delivery. *Adv. Mater.* 29:1700244. doi: 10.1002/adma.201700244

Hu, Y., He, L., and Yin, D. (2011). Magnetically responsive photonic nanochains. *Angew. Chem. Int. Ed.* 50, 3747–3750. doi: 10.1002/anie.201100290

Jain, S., and Bates, F. S. (2003). On the origins of morphological complexity in block copolymer surfactants. *Science* 300, 460–464. doi: 10.1126/science.1082193

Jalani, G., Tam, V., Vetrone, F., and Cerruti, M. (2018). Seeing, targeting and delivering with upconverting nanoparticles. *J. Am. Chem. Soc.* 140, 10923–10931. doi: 10.1021/jacs.8b03977

Kang, M., Kang, H., Park, S., and Jang, H. S. (2019). Facile synthesis of sub-10 nm-sized bright red-emitting upconversion nanophosphors via tetrahedral YOF: Yb, Er seed-mediated growth. *Chem. Commun.* 55, 13350–13353. doi: 10.1039/c9cc06797c

Kang, Y., Erickson, K. J., and Taton, T. A. (2005). Plasmonic nanoparticle chains via a morphological, sphere-to-string transition. *J. Am. Chem. Soc.* 127, 13800–13801. doi: 10.1021/ja055090s

Kim, J. H., Jin, H. M., Yang, G. G., Han, K. H., Yun, T., Shin, J. Y., et al. (2020). Smart nanostructured materials based on self-assembly of block copolymers. *Adv. Funct. Mater.* 30:1902049. doi: 10.1002/adfm.201902049

Li, W., Liu, S., Deng, R., and Zhu, J. (2011). Encapsulation of nanoparticles in block copolymer micellar aggregates by directed supramolecular assembly. *Angew. Chem. Int. Ed.* 50, 5865–5868. doi: 10.1002/anie.201008224

Li, X., Zhang, F., and Zhao, D. (2015). Lab on upconversion nanoparticles: optical properties and applications engineering via designed nanostructure. *Chem. Soc. Rev.* 44, 1346–1378. doi: 10.1039/c4cs00163j

Li, Z., Yuan, H., Yuan, W., Su, Q., and Li, F. (2017). Upconversion nanoprobes for biodetections. *Coord. Chem. Rev.* 354, 155–168. doi: 10.1016/j.ccr.2017.06.025

Liu, D., Xu, X., Du, Y., Qin, X., Zhang, Y., Ma, C., et al. (2016). Three-dimensional controlled growth of monodisperse sub-50 nm heterogeneous nanocrystals. *Nat. Commun.* 7, 10254. doi: 10.1038/ncomms10254

Liu, J., Bu, J., Bu, W., Zhang, S., Pan, L., Fan, W., et al. (2014). Real-time in vivo quantitative monitoring of drug release by dual-mode magnetic resonance and upconverted luminescence imaging. *Angew. Chem. Int. Ed.* 53, 4551–4555. doi: 10.1002/anie.201400900

Liu, K., Nie, Z., Zhao, N., Li, W., Rubinstein, M., and Kumacheva, E. (2010). Step-growth polymerization of inorganic nanoparticles. *Science* 329, 197–200. doi: 10.1126/science.1189457

Liu, L., Wang, S., Zhao, B., Pei, P., Fan, Y., Li, X., et al. (2018). Er^{3+} sensitized 1530 nm to 1180 nm second near-infrared window upconversion nanocrystals for in vivo biosensing. *Angew. Chem. Int. Ed.* 57, 7518–7522. doi: 10.1002/anie.201802889

Liu, S., and Li, L. (2015). Molecular interactions between PEO-PPO-PEO and PPO-PEO-PPO triblock copolymers in aqueous solution. *Colloid Surf. A Physicochem. Eng. Asp.* 484, 485–497. doi: 10.1016/j.colsurfa.2015.08.034

Liu, X., Ni, Y., Zhu, C., Fang, L., Kou, J., Lu, C., et al. (2016). Controllable self-assembly of $NaREF_4$ upconversion nanoparticles and their distinctive fluorescence properties. *Nanotechnology* 27:295605. doi: 10.1088/0957–4484/27/29/295605

Lu, Y., Zhao, J., Zhang, R., Liu, Y., Liu, D., Goldys, E. M., et al. (2013). Tunable lifetime multiplexing using luminescent nanocrystals. *Nat. Photonics* 8, 33–37. doi: 10.1038/nphoton.2013.322

Ma, Y., Bao, J., Zhang, Y., Li, Z., Zhou, X., Wan, C., et al. (2019). Mammalian near-infrared image vision through injectable and self-powered retinal nanoantennae. *Cell* 177, 243. doi: 10.1016/j.cell.2019.01.038

Malmsten, M., Linse, P., and Cosgrove, T. (1992). Adsorption of PEO-PPO-PEO block copolymers at silica. *Macromolecules* 25, 2474–2481.

Nie, Z., Petukhova, A., and Kumacheva, E. (2010). Properties and emerging applications of self-assembled structures made from inorganic nanoparticles. *Nat. Nanotechnol.* 5, 15–25. doi: 10.1038/nnano.2009.453

Qi, Q., Li, C., Liu, X., Jiang, S., Xu, Z., Lee, R., et al. (2017). Solid-state photoinduced luminescence switch for advanced anticounterfeiting and super-resolution imaging applications. *J. Am. Chem. Soc.* 139, 16036–16039. doi: 10.1021/jacs.7b07738

Ren, W., Wen, S., Tawfik, S. A., Lin, G., Ford, M. J., Jin, D., et al. (2018). Anisotropic functionalization of upconversion nanoparticles. *Chem. Sci.* 9, 4352–4358. doi: 10.1039/c8sc01023d

Rozynek, Z., Han, M., Dutka, F., Garstecki, P., Jozefczak, A., and Luijten, E. (2017). Formation of printable granular and colloidal chains through capillary effects and dielectrophoresis. *Nat. Commun.* 8:15255. doi: 10.1038/ncomms15255

Runowski, M., Stopikowska, N., Szeremeta, D., Goderski, S., Skwierczynska, M., and Lis, S. (2019). Upconverting lanthanide fluoride core@shell nanorods for luminescent thermometry in the first and second biological windows: beta-$NaYF_4$: Yb^{3+}-Er^{3+}@SiO_2 temperature sensor. *ACS Appl. Mater. Interfaces* 11, 13389–13396. doi: 10.1021/acsami.9b00445

Shi, R., Ling, X., Li, X., Zhang, L., Lu, M., Xie, X., et al. (2017). Tuning hexagonal $NaYbF_4$ nanocrystals down to sub-10 nm for enhanced photon upconversion. *Nanoscale* 9, 13739–13746. doi: 10.1039/c7nr04877g

Si, S., Kotal, A., and Mandal, T. K. (2007). One-dimensional assembly of peptide-functionalized gold nanoparticles: an approach toward mercury ion sensing. *J. Phys. Chem. C* 111, 1248–1255. doi: 10.1021/jp066303i

Singamaneni, S., Bliznyuk, V. N., Binek, C., and Tsymbal, E. Y. (2011). Magnetic nanoparticles: recent advances in synthesis, self-assembly and applications. *J. Mater. Chem.* 21, 16819–16845. doi: 10.1039/c1jm11845e

Su, Q. (2013). *Luminescent Nanocrystals: Synthesis, Characterization and Optical Tuning*. [Ph.D. thesis]. [Singapore]: National University of Singapore.

Su, Q., Feng, W., Yang, D., and Li, F. (2017). Resonance energy transfer in upconversion nanoplatforms for selective biodetection. *Acc. Chem. Res.* 50, 32–40. doi: 10.1021/acs.accounts.6b00382

Su, Q., Han, S., Xie, X., Zhu, H., Chen, H., Chen, C., et al. (2012). The effect of surface coating on energy migration-mediated upconversion. *J. Am. Chem. Soc.* 134, 20849–20857. doi: 10.1021/ja3111048

Su, Q., Zou, R., Su, Y., and Fan, S. (2018). Morphology control and growth mechanism study of quantum-sized ZnS nanocrystals from single-source precursors. *J. Nanosci. Nanotechnol.* 18:6850. doi: 10.1166/jnn.2018.15516

Sun, T., Li, Y., Ho, W. L., Zhu, Q., Chen, X., Jin, L., et al. (2019). Integrating temporal and spatial control of electronic transitions for bright multiphoton upconversion. *Nat. Commun.* 10:1811. doi: 10.1038/s41467-019-09850-2

Tlusty, T., and Safran, S. A. (2000). Microemulsion networks: the onset of bicontinuity. *J. Phys.: Condens. Matter* 12, A253–A262. doi: 10.1088/0953-8984/12/8a/332

Tsang, M. K., Bai, G., and Hao, J. (2015). Stimuli responsive upconversion luminescence nanomaterials and films for various applications. *Chem. Soc. Rev.* 44, 1585–1607. doi: 10.1039/c4cs00171k

Tseng, R. J., Tsai, C. L., Ma, L. P., and Ouyang, J. Y. (2006). Digital memory device based on tobacco mosaic virus conjugated with nanoparticles. *Nat. Nanotechnol.* 1, 72–77. doi: 10.1038/nnano.2006.55

Wang, D., Li, Z. C., and Chen, L. (2006). Templated synthesis of single-walled carbon nanotube and metal nanoparticle assemblies in solution. *J. Am. Chem. Soc.* 128, 15078–15079. doi: 10.1021/ja066617j

Wang, F., Han, Y., Lim, C. S., Lu, Y., Wang, J., Xu, J., et al. (2010). Simultaneous phase and size control of upconversion nanocrystals through lanthanide doping. *Nature* 463, 1061–1065. doi: 10.1038/nature08777

Wang, F., and Liu, X. (2008). Upconversion multicolor fine-tuning:visible to near-infrared emission from lanthanide-doped $NaYF_4$ nanoparticles. *J. Am. Chem. Soc.* 130:5642. doi: 10.1021/ja800868a

Wang, S., Shen, B., Wei, H. L., Liu, Z., Chen, Z., Zhang, Y., et al. (2019). Comparative investigation of the optical spectroscopic and thermal effect in Nd^{3+}-doped nanoparticles. *Nanoscale* 11, 10220–10228. doi: 10.1039/c9nr02493j

Wang, X., and Chen, G. (2019). A strategy for prompt phase transfer of upconverting nanoparticles through surface oleate-mediated supramolecular assembly of amino-beta-cyclodextrin. *Front. Chem.* 7:161. doi: 10.3389/fchem.2019.00161

Wang, Y. (2019). The role of an inert shell in improving energy utilization in lanthanide-doped upconversion nanoparticles. *Nanoscale* 11, 10852–10858. doi: 10.1039/c9nr03205c

Wang, Y., Zheng, K., Song, S., Fan, D., Zhang, H., and Liu, X. (2018). Remote manipulation of upconversion luminescence. *Chem. Soc. Rev.* 47, 6473–6485. doi: 10.1039/c8cs00124c

Wu, Y., Xu, J., Poh, E. T., Liang, L., Liu, H., Wang, J. K. W., et al. (2019). Upconversion superburst with sub-2 μm lifetime. *Nat. Nanotechnol.* 14, 1110–1115. doi: 10.1038/s41565-019-0560-5

Yuan, Z., Zhang, L., Li, S., Zhang, W., Lu, M., Pan, Y., et al. (2018). Paving metal-organic frameworks with upconversion nanoparticles via self-assembly. *J. Am. Chem. Soc.* 140, 15507–15515. doi: 10.1021/jacs.8b10122

Zhang, F., and Wang, C. C. (2008). Fabrication of one-dimensional iron oxide/silica nanostructures with high magnetic sensitivity by dipole-directed self-assemble. *J. Phys. Chem. C* 112, 15151–15156. doi: 10.1021/jp804452r

Zhao, J., Chen, X., Chen, B., Luo, X., Sun, T., Zhang, W., et al. (2019). Accurate control of core-shell upconversion nanoparticles through anisotropic strain engineering. *Adv. Funct. Mater.* 29:1903295. doi: 10.1002/adfm.201903295

Zheng, K., Han, S., Zeng, X., Wu, Y., Song, S., Zhang, H., et al. (2018). Rewritable optical memory through high-registry orthogonal upconversion. *Adv. Mater.* 30:1801726. doi: 10.1002/adma.201801726

Zheng, K., Loh, K. Y., Wang, Y., Chen, Q., Fan, J., Jung, T., et al. (2019). Recent advances in upconversion nanocrystals: expanding the kaleidoscopic toolbox for emerging applications. *Nano Today* 29:100797. doi: 10.1016/nantod.2019.100797

Zhou, B., Shi, B., Jin, D., and Liu, X. (2015). Controlling upconversion nanocrystals for emerging applications. *Nat. Nanotechnol.* 10, 924–936. doi: 10.1038/nnano.2015.251

Zhou, J., Liu, Q., Feng, W., Sun, Y., and Li, F. (2015). Upconversion luminescent materials: advances and applications. *Chem. Rev.* 115, 395–465. doi: 10.1021/cr400478f

Zhou, M., Ge, X., Ke, D. M., Tang, H., Zhang, J. Z., Calvaresi, M., et al. (2019). The bioavailability, biodistribution, and toxic effects of silica-coated upconversion nanoparticles *in vivo*. *Front. Chem.* 7:218. doi: 10.3389/fchem.2019.00218

Zhu, X., Su, Q., Feng, W., and Li, F. (2017). Anti-stokes shift luminescent materials for bio-application. *Chem. Soc. Rev.* 46, 1025–1039. doi: 10.1039/c6cs00415f

Conflict of Interest: The authors declare that the research was conducted in the absence of any commercial or financial relationships that could be construed as a potential conflict of interest.

frontiers in Chemistry

ORIGINAL RESEARCH
published: 04 November 2020
doi: 10.3389/fchem.2020.579942

Infrared Photon Pair-Production in Ligand-Sensitized Lanthanide Nanocrystals

Peter Agbo[1], *Jacob S. Kanady*[2] *and Rebecca J. Abergel*[1,3]*

[1] Chemical Sciences Division, Lawrence Berkeley National Laboratory, Berkeley, CA, United States, [2] Department of Chemistry, University of California, Berkeley, Berkeley, CA, United States, [3] Department of Nuclear Engineering, University of California, Berkeley, Berkeley, CA, United States

This report details spectroscopic characterizations of rare-earth, core-shell nanoparticles decorated with the *f*-element chelator 3,4,3-LI(1,2-HOPO). Evidence of photon downconversion is corroborated through detailed power dependence measurements, which suggest two-photon decay paths are active in these materials, albeit only representing a minority contribution of the sum luminescence, with emission being dominated by normal, Stokes' shifted fluorescence. Specifically, ultraviolet ligand photosensitization of Nd^{3+} ions in a $NaGdF_4$ host shell results in energy transfer to a Nd^{3+}/Yb^{3+}-doped $NaGdF_4$ nanoparticle core. The population and subsequent decay of core, Yb^{3+} $^2F_{5/2}$ states result in a spectral shift of 620 nm, manifested in a NIR emission displaying luminescence profiles diagnostic of Yb^{3+} and Nd^{3+} excited state decays. Emphasis is placed on the generality of this material architecture for realizing ligand-pumped, multi-photon downconversion, with the Nd^{3+}/Yb^{3+} system presented here functioning as a working prototype for a design principle that may be readily extended to other lanthanide pairs.

Keywords: sensitization, lanthanide, two-photon, downconversion, energy transfer

OPEN ACCESS

Edited by:
Qianqian Su,
Shanghai University, China

Reviewed by:
Guanying Chen,
Harbin Institute of Technology, China
Limin Jin,
Harbin Institute of Technology, Shenzhen, China

***Correspondence:**
Rebecca J. Abergel
abergel@berkeley.edu

Specialty section:
This article was submitted to Nanoscience, a section of the journal Frontiers in Chemistry

Received: *03 July 2020*
Accepted: *08 October 2020*
Published: *04 November 2020*

Citation:
Agbo P, Kanady JS and Abergel RJ (2020) Infrared Photon Pair-Production in Ligand-Sensitized Lanthanide Nanocrystals. Front. Chem. 8:579942. doi: 10.3389/fchem.2020.579942

INTRODUCTION

Broadening the spectral bandwidth of conventional photovoltaics remains one of the chief avenues for generating photocurrent at the detailed-balance limit described by Shockley and Queisser (1961). Realization of such advanced single-junction devices mandates the address of spectral mismatching between semiconductor absorption profiles and the terrestrial solar spectrum. Despite a sizable body of scholarship devoted to light upconversion (UC), comparatively little work has addressed the challenge of ultraviolet (UV) downconversion (DC) toward the low-energy visible and near-infrared (NIR) regimes, where the photocurrent response for bulk Si is highest. Currently, the practical implementation of downconverting lanthanide (Ln) materials in solar arrays has largely been limited by the low absorption intensities typical of *f-f* transitions ($\sim$ 10 M^{-1} cm^{-1}), resulting in low external quantum efficiencies (Shavaleev et al., 2005; Werts, 2005; Zhang et al., 2007; Charbonnière et al., 2008; Moore et al., 2008, 2009; Van Der Ende et al., 2009; Bünzli and Eliseeva, 2010; Janssens et al., 2011; Li S. et al., 2012; Gauthier et al., 2013; Bünzli and Chauvin, 2014; Li S. W. et al., 2014; Binnemans, 2015; Irfanullah et al., 2015, 2016; Goetz et al., 2016; Song et al., 2016). Methods previously explored include the relaxation of Laporte selection rules through the embedding of Ln ions in low-symmetry crystal hosts, and the photosensitization of *f*-states through the

use of either ligand-to-metal charge transfer transitions in transition metal ions, or inter-band (*d-f*) charge transfer in Ln such as Ce^{3+} or Eu^{2+} (Sun et al., 2017). By contrast, the possibility of assisting spectral conversion yields in Ln nanoparticles (NPs) through the use of organic ligands remains a relatively novel method of enhancing f-block NP light absorption (Garfield et al., 2018). Recent work by Meijerink et al. described a dye-sensitized NP system showing successful Pr^{3+}/Yb^{3+} energy transfer, but excluded explicit proof of two-photon production through power dependence or quantum yield determinations (Wang and Meijerink, 2018). As a complement to an earlier patent application disclosure (Agbo and Abergel, 2017), this report relates the concept of UV-NIR nanocrystals featuring the hydroxypyridinone-derived, metal chelator 3,4,3-LI(1,2-HOPO) (**343**) as a UV photosensitizer of $NaGd_{1-x-y}Nd_xYb_yF_4$ | $NaGd_{1-x}Nd_xF_4$ core|shell NPs. Our previous work demonstrated the utility of sensitizing Ln excited states in nanocrystals through energy transfer from the **343** triplet state following UV ligand absorption. Aside from a demonstration of dramatic wavelength shifts from the UV to the NIR, the material described here achieves this spectral transformation through partial utilization of decay channels that permit the production of two NIR photons per UV photon absorbed, as illustrated by a detailed power dependence study.

RESULTS AND DISCUSSION

Preparation of these core-shell structures proceeded through the stepwise synthesis of doubly-doped Nd^{3+}/Yb^{3+} nanocrystal cores from Ln acetate precursors (Wang et al., 2014), followed by a second synthetic round using only Nd^{3+} dopant to yield the corresponding $NaGd_{1-x-y}Nd_xYb_yF_4$ | $NaGd_{1-x}Nd_xF_4$ NPs. Successful synthesis was inferred from the results of transmission electron microscopy (TEM) and powder x-ray diffraction (XRD). Diffraction showed persistence of a single crystal phase consistent with the Bragg diffraction lines expected for the hexagonal-form, β-$NaGdF_4$ (**Figure 1**). NP morphologies interrogated through TEM revealed monodisperse nanocrystals roughly 10 nm in diameter. High resolution imaging and electron diffraction permitted resolution of lattice plane spacings consistent with those observed in $NaGdF_4$ hosts (**Supplementary Figures 1–5**). Modification of NP surfaces with **343** was found to promote aggregation among NPs (**Supplementary Figures 1–4**), consistent with earlier observations (Agbo and Abergel, 2016; Agbo et al., 2016). and was also demonstrated by UV-vis absorption (**Figure 2A**, inset). Absorption measurements of the unmodified particles are characterized solely by Rayleigh scatter. **343** surface chelation of these NPs results in the evolution of a broad $\pi \rightarrow \pi^*$ ($\varepsilon \sim 17,000\ M^{-1}cm^{-1}$) transition between ca. 300 and 360 nm, with a maximum at 325 nm (Abergel et al., 2009).

NP luminescence reveals a ligand-sensitized emission in the NIR that is a composite of Yb^{3+} ($^2F_{5/2} \rightarrow {}^2F_{7/2}$) and Nd^{3+} ($^4F_{3/2} \rightarrow {}^4I_{J=9/2,11/2}$) transitions (**Figure 2B**). Specifically, excitation spectra of these materials indicate their irradiation between ca. 300 and 360 nm results in an IR emission representing a superposition of Yb^{3+} radiative decay and peaks diagnostic of Nd^{3+} transitions at 860 nm ($^4F_{3/2} \rightarrow {}^4I_{9/2}$) and 1059 nm ($^4F_{3/2} \rightarrow {}^4I_{11/2}$). Varying Yb^{3+} content results in an increased Yb^{3+} luminescence until a 20% dopant concentration is reached (**Figure 2B**) (Lakshminarayana et al., 2008a; Li L. et al., 2012; Wang et al., 2015), which was therefore used for all subsequent measurements in this study.

These results are consistent with a deliberate nanocrystal design where **343** functions as a terminal light absorber, transmitting energy exclusively to Nd^{3+} ions in the adjacent NP shell via Dexter transfer, followed by an energy migration step between shell Nd^{3+} ions and the nanocrystalline core. Partial energy localization in the core is presumed to result in the reversible energy transfer between Nd^{3+} $^4F_{3/2}$ ($\sim$11,460 cm^{-1}) and Yb^{3+} $^2F_{5/2}$ (10,400 cm^{-1}), populating an equilibrium mixture of Yb^{3+} excited states under steady-state illumination; radiative deactivation of these states produces an NIR luminescence centered around 979 nm. Inspection of control data bolsters this narrative: NPs featuring a Nd^{3+}/Yb^{3+}-doped core and an undoped shell ($NaGd_{1-x-y}Nd_xYb_yF_4$ | $NaGdF_4$ -**343**) display no NIR emission (**Figure 2B**, inset). Yb^{3+}-free controls ($NaGd_{1-x}Nd_xF_4$ | $NaGd_{1-x}Nd_xF_4$ -**343**) yield the intuitive result of an IR emission defined solely by Nd^{3+} transitions. UV illumination in the absence of the **343** ligand yields no detectable luminescence under identical conditions from either Nd^{3+} or Yb^{3+} lumiphores. Furthermore, ligand incorporation is shown to significantly increase luminescence yield upon excitation at 350 nm, with a resulting signal intensity at 979 nm approximately 1100-fold greater for the **343**-decorated particles than observed for the unmodified nanostructures (**Figure 3**). It is noteworthy that none of the higher energy emissions that typically result from transitioning between Nd^{3+} stark levels are found in the visible range between 360 and 860 nm (Koningstein and Geusic, 1964; Zhang et al., 2007, 2015; Chen et al., 2012; Li X. et al., 2013; Wang et al., 2015), a surprising fact, given the high density of energetic states in Nd^{3+} electronic structure, and a standing precedent in the literature of Nd^{3+}-doped, rare-earth hosts yielding emission spectra reflective of the ion's several *f-f* transitions (Li X. et al., 2013; Mimun et al., 2013; Wang et al., 2015). One, or a combination, of four likely possibilities may explain such phenomena: (1) the overall equilibrium between Yb^{3+} $^2F_{5/2}$ and the Nd^{3+} states serving as acceptor states from the **343** triplet manifold favors production of Yb^{3+} excited states; (2) The resonant exchange between Yb^{3+} $^2F_{5/2}$ and Nd^{3+} donor states largely favors Yb^{3+} $^2F_{5/2}$ production; (3) Nd^{3+} states are rapidly quenched by phonon-coupled effects involving either ligand or host lattice vibrational states; (4) Rates of energy migration between Nd^{3+} ions significantly outpace the rates of radiative decay from individual Nd^{3+} stark levels. The scope of data acquired in this current study make assertions (1) and (4) difficult to confirm, as it demands a comprehensive knowledge of the rates and efficiency of all steps from the initial point of photon absorption by the ligand to Yb^{3+} ion emission. However, the nature of energy exchange between Nd^{3+} and Yb^{3+} is moderately exothermic, with an energy gap that is sufficiently large to possibly make phonon-assisted, energetic back-transfer from Yb^{3+} ($^2F_{5/2}$) $\rightarrow$ Nd^{3+} ($^4F_{3/2}$) kinetically prohibitive in $NaGd(Y)F_4$ hosts (1060

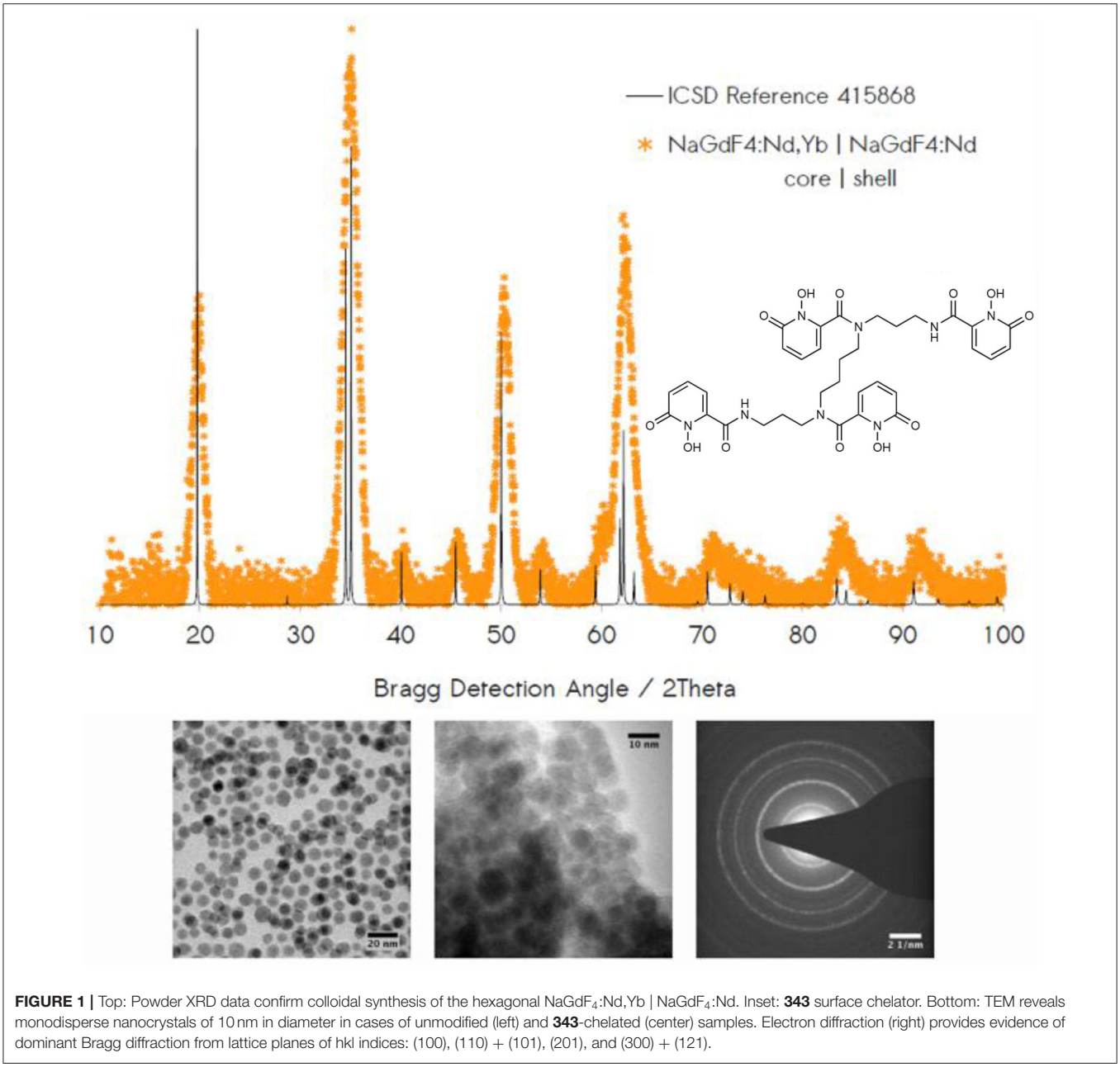

FIGURE 1 | Top: Powder XRD data confirm colloidal synthesis of the hexagonal $NaGdF_4$:Nd,Yb | $NaGdF_4$:Nd. Inset: **343** surface chelator. Bottom: TEM reveals monodisperse nanocrystals of 10 nm in diameter in cases of unmodified (left) and **343**-chelated (center) samples. Electron diffraction (right) provides evidence of dominant Bragg diffraction from lattice planes of hkl indices: (100), (110) + (101), (201), and (300) + (121).

cm^{-1} energy gap vs. $\sim 400\ cm^{-1}$ phonon energy), suggesting (2) as a partial explanation. Finally, (3) also seems possible. Despite numerous reports of Nd^{3+} visible-frequency luminescence in rare-earth fluoride particles featuring surface ligands bound via Ln coordination by oxygen donors (Li X. et al., 2013; Wang et al., 2015), such studies are generally conducted in nonpolar solvents. In this work, the ethanol solvent needed for stabilizing particles with **343** contain OH oscillators that are likely conduits for non-radiative decays that may result in quenched visible emission form Nd^{3+}. Such a possibility is also consistent with previous findings that the **343**-Nd^{3+} molecular complex dissolved in aqueous buffer only yields NIR Nd^{3+} luminescence (Sturzbecher-Hoehne et al., 2011).

Excited State Dynamics and Energy Transfer

Extraction of **343**-Nd^{3+}, Nd^{3+}-Yb^{3+} energy transfer rates and Nd^{3+}/Yb^{3+} excited state lifetimes were achieved through time-resolved luminescence measurements. Rates of energy transfer between the ligand and shell-confined Nd^{3+} were found through

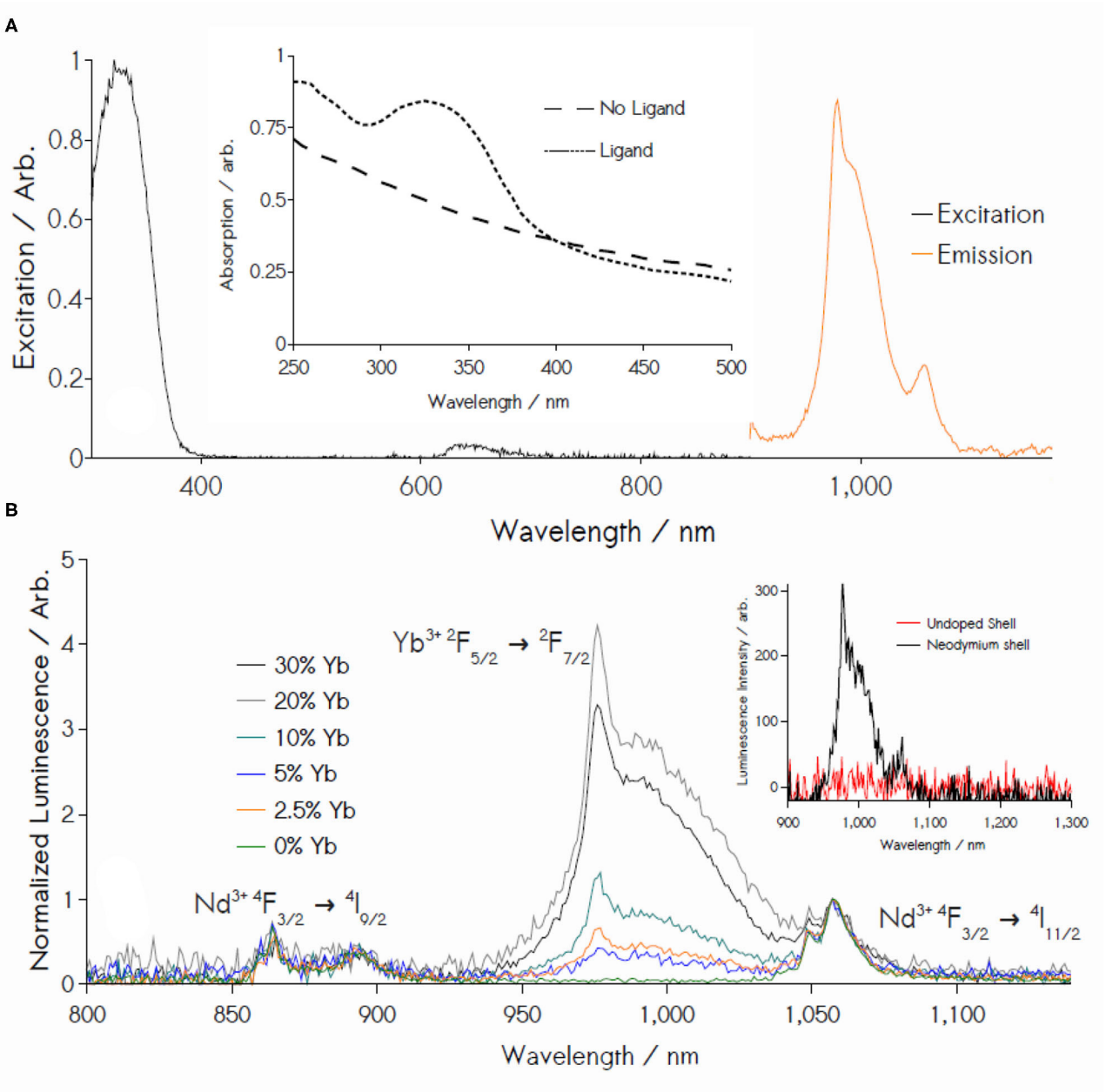

FIGURE 2 | (A) *Black:* Excitation spectrum of 3% Nd^{3+}/20% Yb^{3+}-doped NPs monitoring 980 nm Yb^{3+} emission. *Orange trace:* NIR emission under 355 nm excitation. Inset: UV-vis absorption in ethanol. **(B)** Luminescence from Nd^{3+}, Yb^{3+} core-shell NPs upon excitation at 355 nm, showing increasing Yb^{3+} emission (normalized relative to Nd^{3+} emission at 1059 nm) as Yb^{3+} content increases (0 to 20 mol %). Nd^{3+} content is held constant at 3 mol %. Inset: Removal of Nd^{3+} from the shell blocks energy transfer to terminal Yb^{3+} acceptor ions, arresting photoemission.

cryogenic (77 K) monitoring of the **343** triplet luminescence at 525 nm (**Supplementary Figure 6**). Mean decay times for the ligand triplet state in the presence of Nd^{3+} quenching were calculated according to Equation (**1**) (where I(t) is the time-dependent emission intensity, and I_0 is its initial value), yielding values of 626 ± 48 μs. **343** triplet deactivation displayed tri-exponential behavior, occurring in decay phases with rates of 2197 ± 392 s^{-1}, 382 ± 42 s^{-1}, and 25.5 ± 19 s^{-1} at respective amplitudes of 0.60, 0.34, and 0.06, consistent with data previously reported for a **343**-sensitized, Eu^{3+}-doped system (Agbo and Abergel, 2016; Agbo et al., 2016). Extracting mean lifetimes by calculating the weighted sum of these decay rates (Equation **2**) according to their respective contributions toward the measured decay spectrum yields a similar lifetime

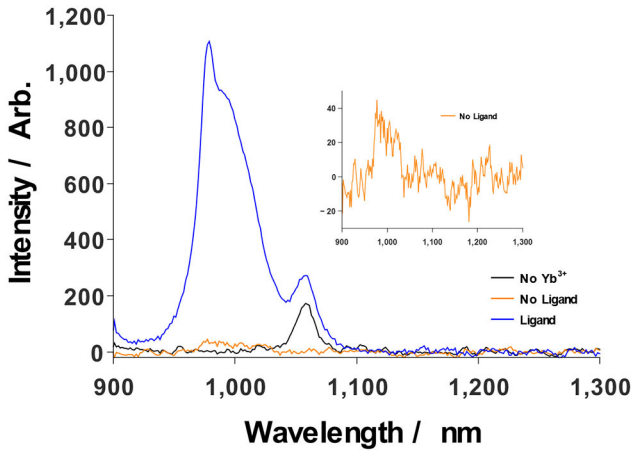

FIGURE 3 | Ligand sensitization significantly enhances Yb^{3+} luminescence upon excitation at 350 nm (blue), relative to the case of NP illumination in the absence of photosensitization by **343** (orange, inset). Sensitized NPs without Yb^{3+} only show Nd^{3+} emission at 1057 nm (black).

of 694 ± 127 μs, a value within error of the integral method. Ligand-Nd^{3+} energy transfer efficiencies were then determined according to Equation (**3**), where τ_{DA} is the measured **343** donor lifetime in the presence of Nd^{3+} acceptor ions and τ_D is the measured **343** donor lifetime in the absence of acceptor quenching. Values for τ_D were determined previously (1.61 ms) (Agbo and Abergel, 2016; Agbo et al., 2016). Accordingly, energy transfer between ligands on the NP surface and Nd^{3+} atoms in the nanocrystalline shell was found to proceed with an efficiency of 61 ± 3%.

$$< \tau > = \frac{1}{I_0} \int_{I_0} I\,(t)\,dt \quad (1)$$

$$< \tau > = \frac{1}{\sum_j k_j c_j} \quad (2)$$

$$< \eta > = 1 - \frac{\tau_{DA}}{\tau_D} \quad (3)$$

Quenching of Nd^{3+} excited states by Yb^{3+} ions was resolved through monitoring of Nd^{3+} transitions at 860 nm ($^4F_{3/2} \rightarrow {}^4I_{9/2}$) and 1057 nm ($^4F_{3/2} \rightarrow {}^4I_{11/2}$), as the $^4F_{3/2}$ state in Nd^{3+} lies at a similar energy to the $^2F_{5/2}$ state of Yb^{3+} (**Figure 4C**). Transient luminescence of the 860 nm transition proceeds in two phases, with treatments showing rates of 2.13 x 10^5 ± 6150 s^{-1} and 798 ± 67.7 s^{-1}; $^4F_{3/2} \rightarrow {}^4I_{11/2}$ decay at 1057 nm displays quenching rates of 1.56 x 10^5 ± 2760 s^{-1} and 4940 ± 140 s^{-1} (**Figures 4A,B**). Controls containing no core Yb^{3+} ($NaGdF_4$: Nd|$NaGdF_4$:Nd-**343** core|shell NPs) yielded Nd^{3+} decay rates of 4.14 x 10^5 s^{-1} at 860 nm and 1.43 x 10^5 s^{-1} at 1057 nm. These data permit the calculation of Nd^{3+}-Yb^{3+} energy transfer efficiencies (Equation **3**) of 86.8 ± 2.0 and 82.4 ± 1.4%, using the respective 860 nm and 1057 nm transitions as spectroscopic handles (**Supplementary Figure 7**).

Downconversion Order *via* Power Dependence

Luminescence measurements as a function of incident light power were conducted to determine the order of photon production by the coated nanocrystals featuring Nd^{3+} and Yb^{3+} doping levels of 3 and 20%, respectively (**Figure 5**) (Suyver et al., 2005; Zou et al., 2012; Lin et al., 2015). Luminescence measured at light intensities over the range of 6.2–2.1 mW cm^{-2} (3.0 μW to 1.0 μW as measured at the fiber optic) displays linear correlations between the source power logarithms and integrated emission intensity in the NIR regime, with an average slope of 0.86 ± 0.04 (**Supplementary Figures 8–9**). Notably, this behavior occurs under diffuse illumination conditions relevant to the terrestrial solar spectrum (∼100 mW cm^{-2} total), a stark contrast to the high excitation powers generally required for Ln luminescence. Furthermore, the excitation powers used here are far below the regimes for power saturation that are generally observed in these and related materials (Suyver et al., 2005; Chen G, et al., 2009; Lin et al., 2015; Loiko et al., 2016; Chen et al., 2017), demonstrating that our reported power dependencies are not mere artifacts of excited state saturation. The observed sub-unity slopes are diagnostic of a multi-photon production process involving direct transitions from the $^4G_{9/2}$ donor level in Nd^{3+} to the $^2F_{5/2}$ level in Yb^{3+}. Generally, an idealized two-photon DC process yields a theoretical slope of $n = 0.5$, in contrast to the slope of 1 found in the power dependence for a typical, 1:1 Stokes-shifted emission and the $n = 2$ slope for two-photon UC (Suyver et al., 2005; Chen G, et al., 2009; Zou et al., 2012; Lin et al., 2015; Loiko et al., 2016; Chen et al., 2017). Here, the intermediate slope observed in the NIR luminescence suggests a photoemission that is a function of both 1:1 Stokes-shifted luminescence and 1:2 photon DC pathways. Furthermore, while our slopes values are far from the ideal two-photon slope, the small measurement error strongly suggests the measured effect is a statistically significant one, and that the multi-photon effect is therefore genuine (if minor); this is bolstered by control power dependencies conducted with Nd^{3+}-only, **343** NPs, which yield a slope value of 1, for Nd^{3+} luminescence detected at 1057 nm (**Supplementary Figure 10**). The relative contributions of these various decay channels to the overall photoluminescence are difficult to precisely quantify but are estimated with the system described in Equation (4), where terms a_k are weights representing the respective contributions of the k^{th} unique decay channel (i.e., 1:1 photon emission, 2-photon DC), m_k are the theoretical slopes for a photon DC process of order $1/m_k$ and m is the total slope derived from power dependence, a value in which the contributions of all active luminescent decay channels are implicit. For our particular case, where only two unique processes (one-photon, $m = 1$ luminescence and $m = 0.5$, two-photon conversion) are present, solving for the coefficients for $m = 0.86$ yields $a_1 = 0.72$ and $a_2 = 0.28$, suggesting that, while two-photon mechanisms are operative (28%), luminescence in the NIR

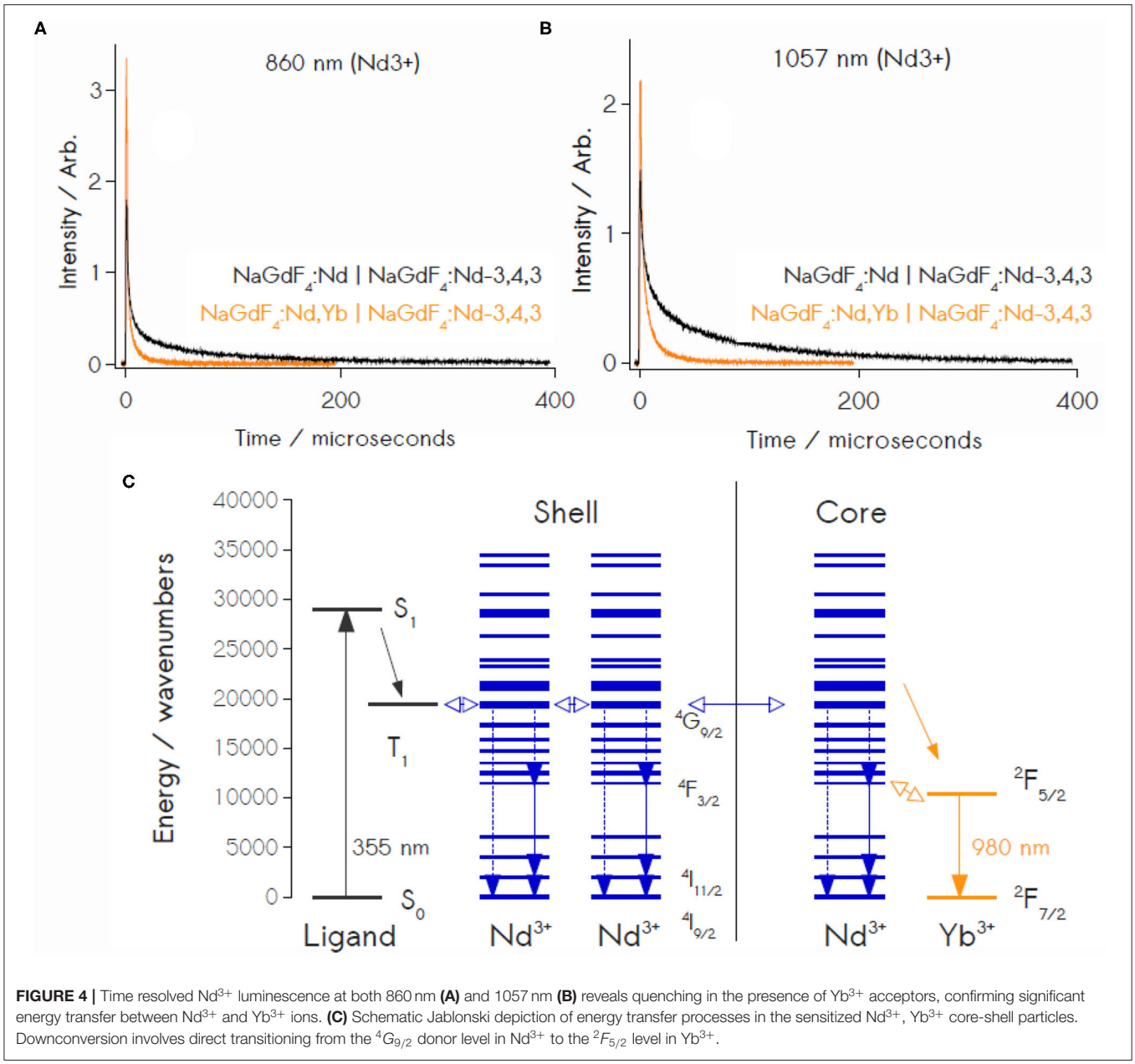

FIGURE 4 | Time resolved Nd^{3+} luminescence at both 860 nm **(A)** and 1057 nm **(B)** reveals quenching in the presence of Yb^{3+} acceptors, confirming significant energy transfer between Nd^{3+} and Yb^{3+} ions. **(C)** Schematic Jablonski depiction of energy transfer processes in the sensitized Nd^{3+}, Yb^{3+} core-shell particles. Downconversion involves direct transitioning from the $^4G_{9/2}$ donor level in Nd^{3+} to the $^2F_{5/2}$ level in Yb^{3+}.

remains dominated by single-photon processes (72%) (Strek et al., 2001). These results are notable, as a handful of previous reports had pointed to claims of ligand-sensitized, Stokes-shifted luminescence in nanocrystals, however these studies had not produced any explicit evidence of multi-photon DC (Charbonnière et al., 2008; Cross et al., 2010; Chen et al., 2013; Li S. et al., 2013, 2014; Irfanullah et al., 2015; Goetz et al., 2016).

$$m = \sum_k a_k m_k; 1 = \sum_k a_k \quad (4)$$

Quantum Efficiency of Sensitized Emission

343's efficacy as a photosensitizer was further evaluated by determining the internal quantum yields observed for Yb^{3+} infrared emission. Direct Nd^{3+} excitation was achieved through laser excitation at 456 nm ($^4I_{9/2} \rightarrow {}^4G_{9/2}$, SI). Direct excitation pathways display the low external quantum yields that are a natural consequence of the low *f-f* absorptivities of Ln transitions, with direct generation of Nd^{3+} excited states yielding an average efficiency of 0.15, 0.14, and 0.34% (0.21 ± 0.11%) for Yb^{3+} luminescence integrated over the range 940–1040 nm. Using the relation $\Phi_{343-Yb} = \Phi_{Nd-Yb}\eta_{sens}$, where η_{sens} is the ligand-Nd^{3+} sensitization efficiency, allows

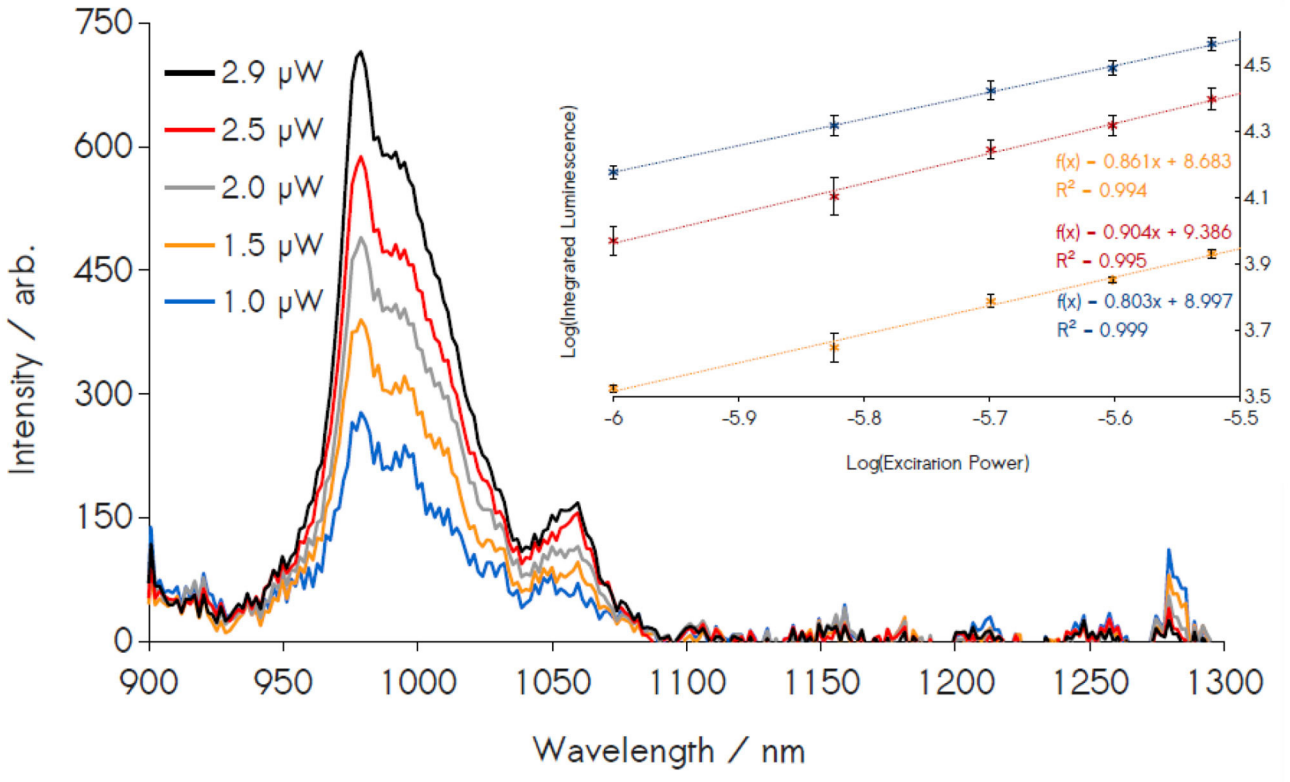

FIGURE 5 | Power dependence study of 3/20% doped Nd^{3+}/Yb^{3+} NPs. Emission spectra are integrated in the region of Yb^{3+} luminescence (940–1040 nm) and plotted against the excitation power (inset). The power dependence of these material exhibits a sub-linear slope, with a total of 10 independent measurements yielding an average slope of 0.86 ± 0.04 among three replicates, confirming the presence of two-photon emissions.

for determination of an approximate quantum yield of 0.13% for Yb^{3+} emission originating from 355 nm ligand excitation. In addition to our measured quantum yields, we compare these results to a treatment for calculating DC quantum yields commonly employed throughout photon DC literature (Vergeer et al., 2005; Lakshminarayana et al., 2008a,b; Ye et al., 2008, 2011; Chen X, et al., 2009; Van Der Ende et al., 2009; Li K.-Y. et al., 2014; Zhu et al., 2014). As defined in Equation (**5**), QY_{Nd-Yb} is the quantum efficiency of DC from a Nd^{3+} donor to an Yb^{3+} acceptor, whereas η_{Nd} is the Nd^{3+} donor quantum efficiency and is generally assumed to be 100% (no non-radiative losses); (Vergeer et al., 2005; Lakshminarayana et al., 2008a,b; Ye et al., 2008, 2011; Chen X, et al., 2009; Van Der Ende et al., 2009; Li K.-Y. et al., 2014; Zhu et al., 2014). *ETE* is the Nd^{3+}-Yb^{3+} energy transfer efficiency (0.87). Here, such approach yields a maximum two-photon quantum yield of 182% for these nanocrystals in the case of luminescence driven by photoexcitation of the Nd^{3+} absorption band at 456 nm. Determination of the ligand-sensitized Yb^{3+} quantum yields are found by factoring in the additional ligand-Nd^{3+} energy transfer step according to Equation (6). Applying our experimentally determined value of 61% for the ligand-Nd^{3+} sensitization efficiency yields a maximum quantum yield of 114% for a two-photon Yb^{3+} emission in these crystals, where the ligand is the terminal light absorber, rather than Nd^{3+}. It must be stressed that such values of two-photon emission that are calculated using Equations (**5**, **6**) only represent theoretical upper limits on the two-photon quantum yields, as they assume the absence of non-radiative decay paths (Vergeer et al., 2005; Lakshminarayana et al., 2008a,b; Ye et al., 2008, 2011; Chen X, et al., 2009; Van Der Ende et al., 2009; Li K.-Y. et al., 2014; Zhu et al., 2014). Here, we have provided the actual quantum yields of these materials as a comparison, with the substantial gap between the calculated and experimental values reflecting the considerable degree of non-radiative losses that exist in these nanocrystals. This observation should prompt a conservative interpretation of any two-photon quantum efficiencies determined through calculated methods assuming an absence of non-radiative decays. Such approaches run in stark contrast to physical measurements of two-photon production, where an accounting of non-radiative excited-state deactivation is necessarily an implicit feature of acquired experimental data.

$$QY_{Nd-Yb} = \eta_{Nd}\,(1 - ETE) + 2(ETE) \quad (5)$$

$$QY_{343-Yb} = \eta_{sens} \times QY_{Nd-Yb} \quad (6)$$

CONCLUSION

This work demonstrates the value in considering not only the respective energies of Ln donor/acceptor levels in the design of multi-photon emitters, but also the role that core-shell structures can play. Specifically, the use of layered crystal domains permits the critical segregation of ligand absorber and metal donors/acceptors (Nd^{3+}/Yb^{3+}), enabling an efficient, stepwise ligand-donor-acceptor energy transfer that mitigates the possibility of quantum efficiency losses arising from the direct sensitization of Yb^{3+} by **343** (Sturzbecher-Hoehne et al., 2011). Though availability of a resonant $^4F_{3/2}$ donor level in Nd^{3+} facilitates energy transfer to the Yb^{3+} excited state, the high density of Nd^{3+} f-states falling between energies of the **343** triplet (21,500 cm^{-1}) and the Nd^{3+} $^4F_{3/2}$ donor (11,460 cm^{-1}) allows for significant losses through multi-phonon relaxation during **343** $\rightarrow$ Nd^{3+} sensitization, a physical basis for the low contribution of two-photon emission to the overall Yb^{3+} luminescence (while the measured energy transfer efficiency for this step is 0.61, this is only a remark on the total energy siphoned from **343** phosphors by Nd^{3+} acceptor levels; it provides no information on non-radiative losses incurred by excited Nd^{3+} ions during internal conversion to yield the $^4F_{3/2}$ intermediate). These results build on our initial studies of ligand sensitization of Eu^{3+} in $NaGd(Y)F_4$ crystals (Agbo et al., 2016), extending the general principle of sensitized Ln NP luminescence to the particular case of two-photon generation in the NIR. The present findings detail a material capable of shifting luminescence over a range of 600 nm, from UV to IR, with a NIR emission profile that is a partial function of two-photon processes. These results bear significance to the challenge of addressing energetic mismatches between terrestrial solar illumination and the spectral response of commercial photovoltaics.

DATA AVAILABILITY STATEMENT

All datasets generated for this study are included in the article/ **Supplementary Material**.

AUTHOR CONTRIBUTIONS

PA and RA designed the research. PA performed experimental work. All authors performed data analysis and contributed to the writing of the manuscript.

FUNDING

This work was supported by the Director, Office of Science, Office of Basic Energy Sciences, and the Division of Chemical Sciences, Geosciences, and Biosciences of the U.S. Department of Energy at the Lawrence Berkeley National Laboratory under Contract No. DE-AC02-05CH11231.

ACKNOWLEDGMENTS

We thank Dr. S. Fischer and J. Swabeck for help acquiring quantum yield data on a custom system in the laboratory of Prof. P. Alivisatos at UC Berkeley.

SUPPLEMENTARY MATERIAL

The Supplementary Material for this article can be found online at: https://www.frontiersin.org/articles/10.3389/fchem.2020.579942/full#supplementary-material

Supporting Information: Experimental procedures, quantum yield data, time-resolved luminescence, energy transfer calculations, and Eu^{3+}-Cm^{3+} excitation spectra are included in the Supporting Information. This material is available free of charge via the internet at http://pubs.acs.org.

REFERENCES

Abergel, R. J., D'Aléo, A., Ng Pak Leung, C., Shuh, D. K., and, Raymond, K. N. (2009). Using the antenna effect as a spectroscopic tool: photophysics and solution thermodynamics of the model luminescent hydroxypyridonate complex $[Eu^{III}$ (3, 4, 3-LI (1, 2-HOPO))$]^-$. *Inorg. Chem.* 48, 10868–10870. doi: 10.1021/ic9013703

Agbo, P., and Abergel, R. J. (2016). Ligand-sensitized lanthanide nanocrystals: merging solid-state photophysics and molecular solution chemistry. *Inorg. Chem.* 55, 9973–9980. doi: 10.1021/acs.inorgchem.6b00879

Agbo, P., and Abergel, R. J. (2017). *Ligand-Sensitized Lanthanide Nanocrystals as Ultraviolet Downconverters*. U.S. Patent.

Agbo, P., Xu, T., Sturzbecher-Hoehne, M., and Abergel, R. J. (2016). Enhanced ultraviolet photon capture in ligand-sensitized nanocrystals. *ACS Photon.* 3, 547–552. doi: 10.1021/acsphotonics.6b00118

Binnemans, K. (2015). Interpretation of europium (III) spectra. *Coord. Chem. Rev.* 295, 1–45. doi: 10.1016/j.ccr.2015.02.015

Bünzli, J.-C. G., and Chauvin, A.-S. (2014). "Lanthanides in solar energy conversion," in *Handbook on the Physics and Chemistry of Rare Earths. Vol. 44*, eds J.-C. G. Bünzli and V. K. Pecharsky (Amsterdam: Elsevier Science B.V.), 169–281. doi: 10.1016/B978-0-444-62711-7.00261-9

Bünzli, J.-C. G., and Eliseeva, S. V. (2010). "Basics of lanthanide photophysics," in *Lanthanide Luminescence*, eds P. Hänninen and H. Härmä (Berlin; Heidelberg: Springer), 1–45. doi: 10.1007/4243_2010_3

Charbonnière, L. J., Rehspringer, J.-L., Ziessel, R., and Zimmermann, Y. (2008). Highly luminescent water-soluble lanthanide nanoparticles through surface coating sensitization. *New. J. Chem.* 32, 1055–1059. doi: 10.1039/b719700d

Chen, G., Liang, H., Liu, H., Somesfalean, G., and Zhang, Z. (2009). Near vacuum ultraviolet luminescence of Gd^{3+} and Er^{3+} ions generated by super saturation upconversion processes. *Opt. Express.* 17, 16366–16371. doi: 10.1364/OE.17.016366

Chen, G., Ohulchanskyy, T. Y., Liu, S., Law, W.-C., Wu, F., Swihart, M. T., et al. (2012). Core/shell $NaGdF_4$: $Nd^{3+}/NaGdF_4$ nanocrystals with efficient near-infrared to near-infrared downconversion photoluminescence for bioimaging applications. *ACS nano.* 6, 2969–2977. doi: 10.1021/nn2042362

Chen, J., Meng, Q., May, P. S., Berry, M. T., and Lin, C. (2013). Sensitization of Eu^{3+} luminescence in Eu: YPO_4 nanocrystals. *J. Mat. Chem.* 117, 5953–5962. doi: 10.1021/jp3109072

Chen, X., Huang, X., and Zhang, Q. (2009). Concentration-dependent near-infrared quantum cutting in $NaYF_4$: Pr^{3+}, Yb^{3+} phosphor. *J. Appl. Phys.* 106:063518. doi: 10.1063/1.3224906

Chen, X., Zhu, Y., Zhou, D., Xu, W., Zhu, J., Pan, G., et al. (2017). Size-dependent downconversion near-infrared emission of $NaYF_4$: Yb^{3+}, Er^{3+} nanoparticles. *J. Mat. Chem.* 5, 2451–2458. doi: 10.1039/C7TC00267J

Cross, A. M., May, P. S., Veggel, F. C., and v., Berry, M. T. (2010). Dipicolinate sensitization of europium luminescence in dispersible 5%

Eu: LaF_3 nanoparticles. *J. Mat. Chem*. 114, 14740–14747. doi: 10.1021/jp103366j

Garfield, D. J., Borys, N. J., Hamed, S. M., Torquato, N. A., Tajon, C. A., Tian, B., et al. (2018). Enrichment of molecular antenna triplets amplifies upconverting nanoparticle emission. *Nat. Photon*. 12, 402–407. doi: 10.1038/s41566-018-0156-x

Gauthier, N., Raccurt, O., Imbert, D., and Mazzanti, M. (2013). Efficient sensitization of Ln^{3+}-doped $NaYF_4$ nanocrystals with organic ligands. *J. Nanoparticle Res*. 15:1723. doi: 10.1007/s11051-013-1723-1

Goetz, J., Nonat, A., Diallo, A., Sy, M., Sera, I., Lecointre, A., et al. (2016). Ultrabright lanthanide nanoparticles. *ChemPlusChem*. 81, 526–534. doi: 10.1002/cplu.201600007

Irfanullah, M., Bhardwaj, N., and Chowdhury, A. (2016). Sensitized luminescence from water-soluble LaF_3: Eu nanocrystals via partially-capped 1, 10-phenanthroline: time-gated emission and multiple lifetimes. *Dalton Trans*. 45, 12483–12495. doi: 10.1039/C6DT01917J

Irfanullah, M., Sharma, D. K., Chulliyil, R., and Chowdhury, A. (2015). Europium-doped LaF_3 nanocrystals with organic 9-oxidophenalenone capping ligands that display visible light excitable steady-state blue and time-delayed red emission. *Dalton Trans*. 44, 3082–3091. doi: 10.1039/C4DT03249G

Janssens, S., Williams, G., and Clarke, D. (2011). Systematic study of sensitized LaF_3: Eu^{3+} nanoparticles. *J. Appl. Phys*. 109, 023506. doi: 10.1063/1.3531994

Koningstein, J., and Geusic, u. J. (1964). Energy levels and crystal-field calculations of neodymium in yttrium aluminum garnet. *Phys. Rev*. 136, A711. doi: 10.1103/PhysRev.136.A711

Lakshminarayana, G., Yang, H., Ye, S., Liu, Y., and Qiu, J. (2008a). Cooperative downconversion luminescence in Pr^{3+}/Yb^{3+}: SiO_2-Al_2O_3-BaF_2-GdF_3 glasses. *J. Mater. Res*. 23, 3090–3095. doi: 10.1557/JMR.2008.0372

Lakshminarayana, G., Yang, H., Ye, S., Liu, Y., and Qiu, J. (2008b). Co-operative downconversion luminescence in Tm^{3+}/Yb^{3+}: SiO_2-Al_2O_3-LiF-GdF_3 glasses. *J. Phys. D*. 41:175111. doi: 10.1088/0022-3727/41/17/175111

Li, K.-Y., Liu, L.-Y., Wang, R.-Z., Xiao, S.-G., Zhou, H., and Yan, H. (2014). Broadband sensitization of downconversion phosphor YPO_4 by optimizing TiO_2 substitution in host lattice co-doped with Pr^{3+}-Yb^{3+} ion-couple. *J. Appl. Phys*. 115:123103. doi: 10.1063/1.4869659

Li, L., Xiantao, W., Yonghu, C., Changxin, G., and Min, Y. (2012). Energy transfer in Tb^{3+}, Yb^{3+} codoped Lu_2O_3 near-infrared downconversion nanophosphors. *J. Rare Earths*. 30, 197–201. doi: 10.1016/S1002-0721(12)60022-2

Li, S., Hou, Z., Cheng, Z., Lian, H., Li, C., and Lin, J. (2013). Enhanced near-infrared quantum cutting luminescence in 1, 2, 4, 5-benzenetetracarboxylic acid/$NaYF_4$: Tb^{3+}, Yb^{3+} hybrid nanoparticles. *RSC Adv*. 3, 5491–5497. doi: 10.1039/c3ra23439h

Li, S., Li, X., Jiang, Y., Hou, Z., Cheng, Z., Ma, P., et al. (2014). Highly luminescent lanthanide fluoride nanoparticles functionalized by aromatic carboxylate acids. *RSC Adv*. 4, 55100–55107. doi: 10.1039/C4RA09266J

Li, S., Zhang, X., Hou, Z., Cheng, Z., Ma, P., and Lin, J. (2012). Enhanced emission of ultra-small-sized LaF_3: RE^{3+}(RE= Eu, Tb) nanoparticles through 1, 2, 4, 5-benzenetetracarboxylic acid sensitization. *Nanoscale*. 4, 5619–5626. doi: 10.1039/c2nr31206a

Li, S. W., Ren, H. J., and Ju, S. G. (2014). Sensitized Luminescence of LaF_3: Eu^{3+} Nanoparticles through Pyromellitic Acid. *J. Nanosci. Nanotech*. 14, 3677–3682. doi: 10.1166/jnn.2014.7968

Li, X., Wang, R., Zhang, F., Zhou, L., Shen, D., Yao, C., et al. (2013). Nd^{3+} sensitized up/down converting dual-mode nanomaterials for efficient *in-vitro* and *in-vivo* bioimaging excited at 800 nm. *Sci. Rep*. 3:3536. doi: 10.1038/srep03536

Lin, J., Fujita, Y., and Neogi, A. (2015). Saturation of two photon emission in ZnO nanoparticles with second order nonlinearity. *RSC Adv*. 5, 10921–10926. doi: 10.1039/C4RA08380F

Loiko, P., Khaidukov, N., Méndez-Ramos, J., Vilejshikova, E., Skoptsov, N., and Yumashev, K. (2016). Up-and down-conversion emissions from Er^{3+} doped K2YF5 and K2YbF5 crystals. *J. Luminesc*. 170, 1–7. doi: 10.1016/j.jlumin.2015.10.016

Mimun, L. C., Ajithkumar, G., Pokhrel, M., Yust, B. G., Elliott, Z. G., Pedraza, F., et al. (2013). Bimodal imaging using neodymium doped gadolinium fluoride nanocrystals with near-infrared to near-infrared downconversion luminescence and magnetic resonance properties. *J. Mater. Chem. B*. 1, 5702–5710. doi: 10.1039/c3tb20905a

Moore, E. G., Samuel, A. P., and Raymond, K. N. (2009). From antenna to assay: lessons learned in lanthanide luminescence. *Acc. Chem. Res*. 42, 542–552. doi: 10.1021/ar800211j

Moore, E. G., Szigethy, G., Xu, J., and Pålsson, L.-O. (2008). 3, 2-HOPO Complexes of Near Infra-Red (NIR) Emitting Lanthanides: sensitization of Ho^{III} and Pr^{III} in Aqueous Solution. *Angew. Chem*. 47:9500. doi: 10.1002/anie.200802337

Shavaleev, N. M., Accorsi, G., Virgili, D., Bell, Z. R., Lazarides, T., Calogero, G., et al. (2005). Syntheses and crystal structures of dinuclear complexes containing d-block and f-block luminophores. Sensitization of NIR luminescence from Yb (III), Nd (III), and Er (III) centers by energy transfer from Re (I)– and Pt (II)– bipyrimidine metal centers. *Inorg. Chem*. 44, 61–72. doi: 10.1021/ic048875s

Shockley, W., and Queisser, H. J. (1961). Detailed balance limit of efficiency of p-n junction solar cells. *J. Appl. Phys*. 32, 510–519. doi: 10.1063/1.1736034

Song, Y., Shao, B., Feng, Y., Ľu, W., Huo, J., Zhao, S., et al. (2016). Emission enhancement and color tuning for $GdVO_4$: Ln^{3+} (Ln= Dy, Eu) by surface modification at single wavelength excitation. *Inorg. Chem*. 56, 282–291. doi: 10.1021/acs.inorgchem.6b02125

Strek, W., Bednarkiewicz, A., and Dere,ń, P. (2001). Power dependence of luminescence of Tb^{3+}-doped KYb $(WO_4)_2$crystal. *J. Luminesc*. 92, 229–235. doi: 10.1016/S0022-2313(00)00263-5

Sturzbecher-Hoehne, M., Ng Pak Leung, C., D'Aléo, A., Kullgren, B., Prigent, A.-L., Shuh, D. K., et al. (2011). 3,4,3-LI(1,2-HOPO): *In vitro* formation of highly stable lanthanide complexes translates into efficacious in vivo europium decorporation. *Dalton Trans*. 40, 8340–8346. doi: 10.1039/c1dt10840a

Sun, T., Chen, X., Jin, L., Li, H.-W., Chen, B., Fan, B., et al. (2017). Broadband Ce (III)-sensitized quantum cutting in core-shell nanoparticles: mechanistic investigation and photovoltaic application. *J. Phys. Chem. Lett*. 8, 5099–5104. doi: 10.1021/acs.jpclett.7b02245

Suyver, J., Aebischer, A., García-Revilla, S., Gerner, P., and Güdel, H. (2005). Anomalous power dependence of sensitized upconversion luminescence. *Phys. Rev. B*. 71:125123. doi: 10.1103/PhysRevB.71.125123

Van Der Ende, B. M., Aarts, L., and Meijerink, A. (2009). Lanthanide ions as spectral converters for solar cells. *Phys. Chem. Chem. Phys*. 11, 11081–11095. doi: 10.1039/b913877c

Vergeer, P., Vlugt, T., Kox, M., Den Hertog, M., Van der Eerden, J., and Meijerink, A. (2005). Quantum cutting by cooperative energy transfer in Yb_x Y_{1-x} P O_4: Tb^{3+}. *Phys. Rev. B*. 71:014119. doi: 10.1103/PhysRevB.71.014119

Wang, F., Deng, R., and Liu, X. (2014). Preparation of core-shell $NaGdF_4$ nanoparticles doped with luminescent lanthanide ions to be used as upconversion-based probes. *Nat. Prot*. 9:1634. doi: 10.1038/nprot.2014.111

Wang, K., Qincheng, W., Zhang, Y., Qiao, R., Li, S., and Li, Z. (2015). Synthesis of Nd^{3+}/Yb^{3+} sensitized upconversion core-shell nanocrystals with optimized hosts and doping concentrations. *RSC Adv*. 5, 62899–62904. doi: 10.1039/C5RA09873D

Wang, Z., and Meijerink, A. (2018). Dye-sensitized downconversion. *J. Phys. Chem. Lett*. 9, 1522–1526. doi: 10.1021/acs.jpclett.8b00516

Werts, M. H. (2005). Making sense of lanthanide luminescence. *Sci. Prog*. 88, 101–131. doi: 10.3184/003685005783238435

Ye, S., Katayama, Y., and Tanabe, S. (2011). Down conversion luminescence of Tb^{3+}-Yb^{3+} codoped SrF_2 precipitated glass ceramics. *J. Non-Cryst. Solids*. 357, 2268–2271. doi: 10.1016/j.jnoncrysol.2010.11.083

Ye, S., Zhu, B., Luo, J., Chen, J., Lakshminarayana, G., and Qiu, J. (2008). Enhanced cooperative quantum cutting in Tm^{3+}-Yb^{3+} codoped glass ceramics containing LaF_3 nanocrystals. *Opt. Express*. 16, 8989–8994. doi: 10.1364/OE.16.008989

Zhang, J., Shade, C. M., Chengelis, D. A., and Petoud, S. (2007). A strategy to protect and sensitize near-infrared luminescent Nd^{3+} and Yb^{3+}: organic tropolonate ligands for the sensitization of Ln^{3+}-doped

$NaYF_4$ nanocrystals. *J. Am. Chem. Soc.* 129, 14834–14835. doi: 10.1021/ja074564f

Zhang, X., Zhao, Z., Zhang, X., Cordes, D. B., Weeks, B., Qiu, B., et al. (2015). Magnetic and optical properties of $NaGdF_4$: Nd^{3+}, Yb^{3+}, Tm^{3+} nanocrystals with upconversion/downconversion luminescence from visible to the near-infrared second window. *Nano Res.* 8, 636–648. doi: 10.1007/s12274-014-0548-2

Zhu, W., Chen, D., Lei, L., Xu, J., and Wang, Y. (2014). An active-core/active-shell structure with enhanced quantum-cutting luminescence in Pr-Yb co-doped monodisperse nanoparticles. *Nanoscale*. 6, 10500–10504. doi: 10.1039/C4NR02785J

Zou, W., Visser, C., Maduro, J. A., Pshenichnikov, M. S., and Hummelen, J. C. (2012). Broadband dye-sensitized upconversion of near-infrared light. *Nat. Photon.* 6:560. doi: 10.1038/nphoton.2012.158

Conflict of Interest: RA and PA are listed as inventors on a patent application filed by the Lawrence Berkeley National Laboratory and describing inventions related to the research results presented here.

The remaining author declares that the research was conducted in the absence of any commercial or financial relationships that could be construed as a potential conflict of interest.

frontiers in Chemistry

REVIEW
published: 06 November 2020
doi: 10.3389/fchem.2020.596658

Recent Advances on Rare Earth Upconversion Nanomaterials for Combined Tumor Near-Infrared Photoimmunotherapy

Weilin Chen†, *Yulin Xie*†, *Man Wang and Chunxia Li**

Institute of Frontier and Interdisciplinarity Science, Institute of Molecular Sciences and Engineering, Shandong University, Qingdao, China

Cancer has been threatening the safety of human life. In order to treat cancer, many methods have been developed to treat tumor, such as traditional therapies like surgery, chemotherapy, radiotherapy, as well as new strategies like photodynamic therapy, photothermal therapy, sonodynamic therapy, and other emerging therapies. Although there are so many ways to treat tumors, these methods all face the dilemma that they are incapable to cope with metastasis and recurrence of tumors. The emergence of immunotherapy has given the hope to conquer the challenge. Immunotherapy is to use the body's own immune system to stimulate and maintain a systemic immune response to form immunological memory, resist the metastasis and recurrence of tumors. At the same time, immunotherapy can combine with other treatments to exhibit excellent antitumor effects. Upconversion nanoparticles (UCNPs) can convert near-infrared (NIR) light into ultraviolet and visible light, thus have good performance in bioimaging and NIR triggered phototherapy. In this review paper, we summarize the design, fabrication, and application of UCNPs-based NIR photoimmunotherapy for combined cancer treatment, as well as put forward the prospect of future development.

Keywords: upconversion nanoparticles, near infrared, immunotherapy, phototherapy, combined therapy

OPEN ACCESS

Edited by:
Qianqian Su,
Shanghai University, China

Reviewed by:
Piaoping Yang,
Harbin Engineering University, China
Zhanjun Gu,
Chinese Academy of Sciences, China

***Correspondence:**
Chunxia Li
cxli@sdu.edu.cn

†*These authors have contributed equally to this work*

Specialty section:
This article was submitted to Nanoscience, a section of the journal Frontiers in Chemistry

Received: *20 August 2020*
Accepted: *07 October 2020*
Published: *06 November 2020*

Citation:
Chen W, Xie Y, Wang M and Li C (2020) Recent Advances on Rare Earth Upconversion Nanomaterials for Combined Tumor Near-Infrared Photoimmunotherapy. Front. Chem. 8:596658. doi: 10.3389/fchem.2020.596658

INTRODUCTION

Malignant tumor is one of the major diseases that seriously threaten human health. Because of the metastasis and recurrence of tumor, it is still a great challenge to eliminate cancer completely. The outcome of the persisting declination in cancer death rates since 1991 was an over drop of 27% (Siegel et al., 2019). In the next 20 years, new cancer cases and deaths are expected to increase to 22 million and 13 million, respectively. Thus, great efforts have been devoted to developing new approaches for the diagnosis and treatment of tumors. Modern oncology researches show that tumor is not a simple local disease, but a local manifestation of systemic disease. It is difficult to remove all tumor cells in the body by the existing tumor treatment methods. The conventional strategies including chemotherapy and radiotherapy often lead to the tolerance of tumor cells to the treatment. Consequently, the recurrence and metastasis of tumors are inevitable after treatment.

Immunotherapy has recently become an effective cancer treatment strategy. In 2018 the Nobel Prize in Physiology or Medicine was awarded to the field of cancer for the discovery of cancer therapy by inhibition of negative immune regulation (Hokland et al., 2018). The purpose of

immunotherapy is to use the body's own immune system to stimulate and activate systemic immune response, specifically eliminate minimal residual disease, resulting in inhibiting tumor growth and breaking the immune tolerance (Shekarian et al., 2015; Hu et al., 2019b; Chang et al., 2020). In other ways, tumor immunotherapy is to overcome the mechanism of tumor immune escape, so as to re-awake immune cells to clear cancer cells. Because of its slight side effects and obvious therapeutic effect, immunotherapy has gradually become the development direction of tumor treatment in the future, which is regarded as the fourth major tumor treatment technology after surgery, radiotherapy and chemotherapy (Yang et al., 2016).

Although immunotherapy has made considerable progress, the effect of immunotherapy is challenged by the immune escape mechanism of tumor, which brings the establishment of immunosuppressive microenvironment through the loss of antigenicity and immunogenicity (Beatty and Gladney, 2015). Moreover, immunotherapy has a wide range of targets, and side effects are inevitable. For example, immune checkpoint blockade raises the immune system to a high level while also attacking normal cells (Sang et al., 2019). Therefore, immunotherapy is generally used as an adjuvant therapy in combination with other traditional therapies to improve the comprehensive therapeutic effect and prevent recurrence and metastasis of the tumor. In this case, the integrated cancer therapy will be the new development direction of immunotherapy.

Phototherapy including photodynamic therapy (PDT) and photothermal therapy (PTT) has always been a research hotspot (Gai et al., 2018). PTT could employ PTT agents to convert light energy into hyperthermia to precisely "cook" cancer cells (Zhang et al., 2016; Ding et al., 2017; Gao et al., 2017; Wang et al., 2017). The three elements of PDT are photosensitizer (PS), oxygen, and light. The principle of PDT is to irradiate the tumor site with a specific wavelength to activate the photosensitive drugs that selectively gather in the tumor tissue, and induce the production of cytotoxic reactive oxygen species (ROS) by luminescent chemical reaction, and induce tumor death (Henderson and Dougherty, 1992; Sharman et al., 1999; Juarranz et al., 2008; Lan et al., 2019). The process of phototherapy can induce the antitumor immune response by inducing apoptosis or necrosis of cancer cells to induce immunogenic cell death (ICD) and release tumor associated antigen (TAA). This "*in situ* vaccine" strategy can stimulate "cold" tumor microenvironment (TME) to become "hot" immunogenic TME (Wang et al., 2018b, 2020a; Duan et al., 2019; Deng et al., 2020). Thus, the marrying of immunotherapy and phototherapy provides new opportunities for the treatment of tumors with high efficacy (Chang et al., 2019; Kobayashi and Choyke, 2019; Ma et al., 2019).

However, the traditional PDT PSs are usually excited by ultraviolet (UV) or visible light. In view of the challenges of these wavelengths such as lower penetration depth of biological tissue, higher background luminescence interference, and stronger light damage to normal tissues, the application of PDT in biomedical field is limited to some extent (Wang et al., 2004; Quail and Joyce, 2013; Zhou et al., 2016). In contrast, NIR light can address these problems and be used as a good minimally invasive manner and external stimulation style for light triggered delivery of various therapeutic agents for the diagnosis and treatment of tumors (Gai et al., 2014; Zheng et al., 2015; Guryev et al., 2018; Wang et al., 2018a, 2020b; Chen et al., 2019). Rare earth UCNPs can effectively convert NIR light into UV, visible light even NIR light under the excitation of 980/808 nm NIR as excitation light source (Sun et al., 2014; Zhong et al., 2014; Dong et al., 2015; Liu et al., 2017; Gu et al., 2019; Rabie et al., 2019). In light of the special advantages of NIR light, UCNPs can serve as optical probe for the tracking of *in vivo* treatment, but also as energy transducers to indirectly activate PS to generate ROS for PDT (Liu et al., 2014; Yang et al., 2015; Hou et al., 2016, 2019; Xu et al., 2018a; Feng et al., 2019; Tang et al., 2019). In addition, UCNPs make it possible to modulate photosensitive switches by NIR light due to their unique upconversion luminescence (UCL) ability (Zou et al., 2012). The modulation of photosensitive switches with UCNPs could overcome the penetration depth and photoactivation efficiency challenged by UV and visible light. Thus, NIR light has become an attractive tool for precisely regulating the time and space of chemical and biological activities (Kowalik and Chen, 2017; Ankenbruck et al., 2018).

Although PDT could generate certain levels of immune responses, the immune effects from PDT alone are not enough for inhibiting the remaining tumor growth (Castano et al., 2006). Thus, the combined PDT and immunotherapy would achieve an enhanced cancer treatment outcome (Xu et al., 2020). This is also consistent with the idea of multi-synergistic therapy, that is, the use of two toxic drugs will lead to superadditive effect, and the total effect of drugs (R_{ab}) is greater than the arithmetic sum of constituent toxic effects (R_a, R_b), making $R_{ab} > R_a + R_b$ (Gordon Steel and Peckham, 1979; Seiwert et al., 2007). Although there exist pharmacokinetic inconsistencies, long-term studies on combination therapy have confirmed its effect (Wang et al., 2019b). In this review, focusing on the combination between UCNPs mediated phototherapy and immunotherapy, the current advancements and latest breakthroughs have been summarized. Furthermore, the major challenges in the combinatorial strategies and the future prospects are also highlighted. The composition of UCNPs combined with immunotherapy was summarized in **Table 1**. Though the combination of phototherapy and immunotherapy emerged early, the use of UCNPs with immunotherapy is just springing up. In particular, we hope that this review could shed light on the development of the combination between UCNPs mediated phototherapy and immunotherapy for high performance tumor therapy.

CLASSIFICATION OF IMMUNOTHERAPY

Concomitant with the development of the immunotherapy, it has five kinds of representative treatment modalities.

First of all, antibody therapy has gradually become one of the standard regimens for cancer treatment, which mainly includes tumor targeted antibody drug therapy and immunomodulatory antibody therapy based on the different ways of activating the antitumor immune response. The mechanism of the former is to target the cellular growth factor receptors and cell surface

TABLE 1 | Summary of UCNPs combined with immunotherapy.

Nanocarrier	UCNPs	Immunotherapy agents	References
UCNP-PEG-PEI	NaY/GdF_4 (Y:Gd:Yb:Er = 58%:20%:20%:2%)	OVA	Xiang et al., 2015
Monodispersed macroporous mesoporous silica-coated upconversion nanoparticles (UCMSs)	β-$NaYF_4$:20%Yb,2%Er	OVA/tumor cell fragment (TF)	Ding et al., 2018
SA-PEG-TK-PLGA (SPTP)	β-$NaYF_4$:20%Yb,2%Er	DOX and RB	Jin et al., 2020
UCNPs	$NaYF_4$:20%Yb,2%Er	R837 and CTLA-4 immune checkpoint inhibitors	Xu et al., 2017a
UCNP@SiO_2	$NaYF_4$:Yb,Er	Anti-CTLA-4	Lin et al., 2020
UCNPs	$NaYF_4$:48%Yb/2%Er@$NaYF_4$:30%Nd Core/Shell Nanoparticles	Anti-CTLA-4	Wang et al., 2019a
PDA@UCNP-PEG	NaGdF4:Yb/Er	α-PD-1	Yan et al., 2019
AIE luminogen (AIEgen)–coupled UCNPs (AUNPs)	$NaYF_4$:Yb/Tm@$NaYF_4$	α-PD-1	Mao et al., 2020
UCNPs@porphyrin MOFs (UCSs)	$NaGdF_4$:Yb,Er@$NaGdF_4$	α-PD-L1	Shao et al., 2020
UCNPs	$NaGdF_4$:Yb,Er@$NaYF_4$@$NaYF_4$:Yb,Tm@$NaYbF_4$:Nd@$NaYF_4$	α-PD-L1	Di et al., 2020
UCNPs	$NaGdF_4$:70%Yb,1%Tm@$NaGdF_4$ core-shell UCNPs	CpG ODNs	Chu et al., 2019
UCNPs@mesoporous silica	$NaYF_4$:Er/Yb	CCL21	Lee et al., 2013
UCNs-MnO_2	$NaYF_4$:Yb/Tm/Nd (30/0.5/1%)@$NaYF_4$:Nd (20%)	HA	Ai et al., 2018
Bi doped mesoporous upconversion nanophosphor (UCNP)	$Na_{0.2}Bi_{0.8}O_{0.35}F_{1.91}$:20%Yb,2%Er	DOX and X-ray	Qin et al., 2020

antigens, etc. At present, many tumor targeting antibodies have been approved by Food and Drug Administration (FDA). For example, Avastin can effectively block the binding of vascular endothelial growth factor and receptor, inhibit the formation of tumor blood vessels, and achieve antitumor effect (Sullivan and Brekken, 2010). In contrast, the targets of immunomodulatory antibodies are immune cells rather than tumor cells, which can augment the antitumor immune response of the body by blocking the immunosuppressive pathway or directly playing the role of immune stimulation. Among various immunomodulatory antibodies, antibody blockers for inhibitory receptors mainly act on the immune checkpoints, which have shown encouraging therapeutic effects (Pardoll, 2012). Cytotoxic T-lymphocyte-associated protein 4 (CTLA-4) and programmed death 1 (PD-1) are two kinds of crucial inhibitory regulatory receptor that are overexpressed on the activated T cells (Dariavach et al., 1988; Francisco et al., 2010). Activation of T lymphocytes requires two signals: the major histocompatibility complex (MHC) peptide signal and costimulatory molecule signal. Costimulatory molecules mainly include positive costimulatory CD27, CD28, and CD137 pathways as well as negative costimulatory CTLA-4 and PD-1/programmed death 1 ligand (PD-L1) pathways to prevent T cells from being over stimulated. This inhibition pathway can be hijacked by tumor to fight the immune system. Therefore, the use of positive costimulatory factor agonists or negative costimulatory factor antagonists can improve the immune killing effect of T cells on tumor. Ipilimumab is the first checkpoint antibody was approved by the FDA in 2011 for treatment of melanoma (Cameron et al., 2011). Ipilimumab can block the action of CTLA-4 molecules on the surface of activated T cells, so that T cells can maintain sustained antitumor activity. At present, antibody therapy has become a mature and widely used cancer treatment method.

The second kind of immunotherapy therapy is biological response modulators (BRMs), also known as immunomodulators or immunopotentiators, which involves those components that can improve the activity level of the immune system, thus enhancing the effect of immunotherapy. BRMs include a variety of cytokines, toll like receptor (TLR) signaling and non-coding RNAs. Cytokine is one of the typical non-specific BRMs. Some cytokines have been approved by FDA for cancer treatment. For example, Interleukin 2 (IL-2) is a kind of representative cytokines, which could regulate the survival, proliferation, and differentiation of T cell and natural killer (NK) cell, which could be put to use in the treatment of malignant melanoma and renal cell carcinoma (Dranoff, 2004). In addition to cytokines, TLR signaling is also an important biological response regulator, which can be activated by pathogen-associated molecular patterns or similar agonists, and then activate downstream signaling to induce immune response to eliminate pathogens (Kawasaki and Kawai, 2014). TLR agonists have been used in different cancers. For example, in breast cancer, colorectal cancer, and lung cancer, TLR3 agonists could induce tumor cell apoptosis through caspase (Salaun et al., 2006). Non-coding RNA plays a regulatory role in the development, differentiation, and activation of infiltrating leukocytes in tumor tissue (Desgranges et al., 2019). Non-coding RNA based therapy can regulate the TME to improve the effect of tumor therapy. At present, MRX34, the first miRNA-based tumor therapeutic agent, has entered phase I clinical trials (Bouchie, 2013).

Tumor vaccine is also one of the methods of tumor immunotherapy, which can be divided into preventive tumor

vaccine and therapeutic tumor vaccine. Among them, the therapeutic vaccine for tumor antigen has been developed rapidly. The common tumor vaccines include protein/peptide vaccines, cell vaccines, DNA vaccines, and so on (Hu et al., 2018b). Protein/peptide vaccines are the most common kinds, which could be recognized by antigen-presenting cells (APCs) and activate T cells to kill cancer cells expressing antigen proteins. Cell vaccines could activate the immune response by injecting inactivated tumor cells or dendritic cells (DCs) expressing tumor antigens. DNA vaccines are prepared by injecting DNA into cells by gene technology, which makes cells produce antigen directly and cause immune protection. After years of development, many therapeutic tumor vaccines have been put into clinical practice and even to the market. For example, provenge vaccine and M-vax vaccine have been approved for marketing and have achieved good results in clinical applications (Berd, 2004; Anassi and Ndefo, 2011).

Adoptive cell therapy is a new type of immunotherapy, which depends on tumor specific T cells. The T cells cultured and activated *in vitro* can be reinfused into the body to kill the tumor (Kalos and June, 2013). Previously, adoptive cell therapy also included the use of NK cells, cytokine induced killer cells, and tumor infiltrating lymphocytes, and so on. The earliest adoptive cell therapy strategy employed lymphokine-activated killer cells, which use IL-2 to stimulate and activate peripheral blood mononuclear cells *in vitro*. This method was approved by FDA as early as 1984 (Mazumder and Rosenberg, 1984). With the continuous development and innovation of cell engineering technology, T cells improved by cell engineering have gradually become the focus of adoptive cell therapy. T-cell receptor engineered T-Cell (TCR-T) can improve the recognition and clearance of cancer cells with the antigen which express the designed T cell receptor. Chimeric antibody receptor engineered T Cell (CAR-T) could recognize a specific protein expressed on the surface of tumor cells and lead to rapid activation and tumor cell killing (Ikeda, 2016; June et al., 2018). Both of these cell-engineered modified T cells have achieved good results in clinical trials (Robbins et al., 2011; Maude et al., 2014).

Oncolytic immunotherapy is a newly developing kind of tumor immunotherapy. Significant success has been achieved through the use of oncolytic immunotherapy, which could cause virus-induced tumor cell death and release of relevant antigens. Oncolytic immunotherapy could induce of long-term immune response formation, especially in combination with other immunotherapies (Beug et al., 2014; Workenhe et al., 2014). At present, there are 67 studies about oncolytic virus on the official website of clinical trials (clinicaltrials.gov), indicating that oncolytic virus has potential as one of the treatment methods for cancer.

FABRICATION AND DESIGN OF UCNPs-BASED PHOTOIMMUNOTHERAPY PALTFORM

In this review, all of the UCNPs are synthesized by thermal decomposition method or urea coprecipitation method. In general, the keys to a successful synthesis are carefully choosing precursors, tuning of the coordinating behavior of the solvents using coordinating and non-coordinating surfactants, and maintaining balance between nucleation and growth stages (Mai et al., 2006). Thermal decomposition method is to obtain UCNPs by cracking rare earth salt precursors in high temperature and shielding gas. While urea coprecipitation method could obtain crystalline UCNPs directly by coprecipitation nanoparticles within fluid solvent. These issues requiring attention could be controlled by both of them to obtain nanocrystalline materials with uniform, controllable, and single dispersion.

The design of the UCNP-based therapeutic nanoplatform should give full play to the unique characteristics of UCNPs, and combine multiple functional modules to achieve treatment and diagnosis. How to realize the effective connection of functional modules and maximize the role of functional groups is a challenge (Yang et al., 2015). First of all, the synthesized UCNPs should be well-shaped, monodisperse and homogeneous. High quality UCNPs are essential for the synthesis of high-efficiency therapeutic platform. Secondly, as kind of nanocomposites, UCNP-based therapeutic nanoplatform needs to connect different substances, which could be achieved through a variety of ways, such as electrostatic force, hydrophobic force, and chemical bond formation. Meanwhile, UCNPs need to be modified according to the properties of immune functional modules, so as to realize the construction of photoimmunotherapy nanoplatform. Thirdly, the key to reasonable design is to perform each function module. UCNPs can be used as carriers to carry photothermal agents, chemotherapy drugs, immune adjuvants, etc., and can also be used as activators to convert near-infrared light into ultraviolet and visible light to activate PS. Finally, UCNPs-based nanoplatforms need good biocompatibility and targeting to achieve good results.

THE CORPRATION OF UCNPs AND IMMUNOTHERAPY

In this section, we summarized the design strategy of UCNPs-based nanomaterials in combination with immunotherapy for synergistic therapy of tumors, as indicated in the **Figure 1**.

UCNPs With Vaccine and Vaccine-Like Therapy

DCs are powerful antigen presenting cells *in vivo*. With surface expressing MHC class I/II molecules and T-cells activation costimulatory molecules, etc., DCs have antigen uptake, processing, and presentation functions (Kapsenberg, 2003; Steinman, 2012). DCs can be divided into immature DCs and mature DCs according to their functions. When antigen was presented to DCs, immature DCs differentiated into mature DCs. Then, DCs loaded with antigen peptide migrated to lymph nodes and activated T cells (Banchereau et al., 2000; Randolph et al., 2005). The migration process is the key process to DC vaccine. However, traditional imaging methods cannot achieve real-time imaging of DC migration. Xiang et al. used UCNPs to load antigens to label and stimulate DCs (Xiang

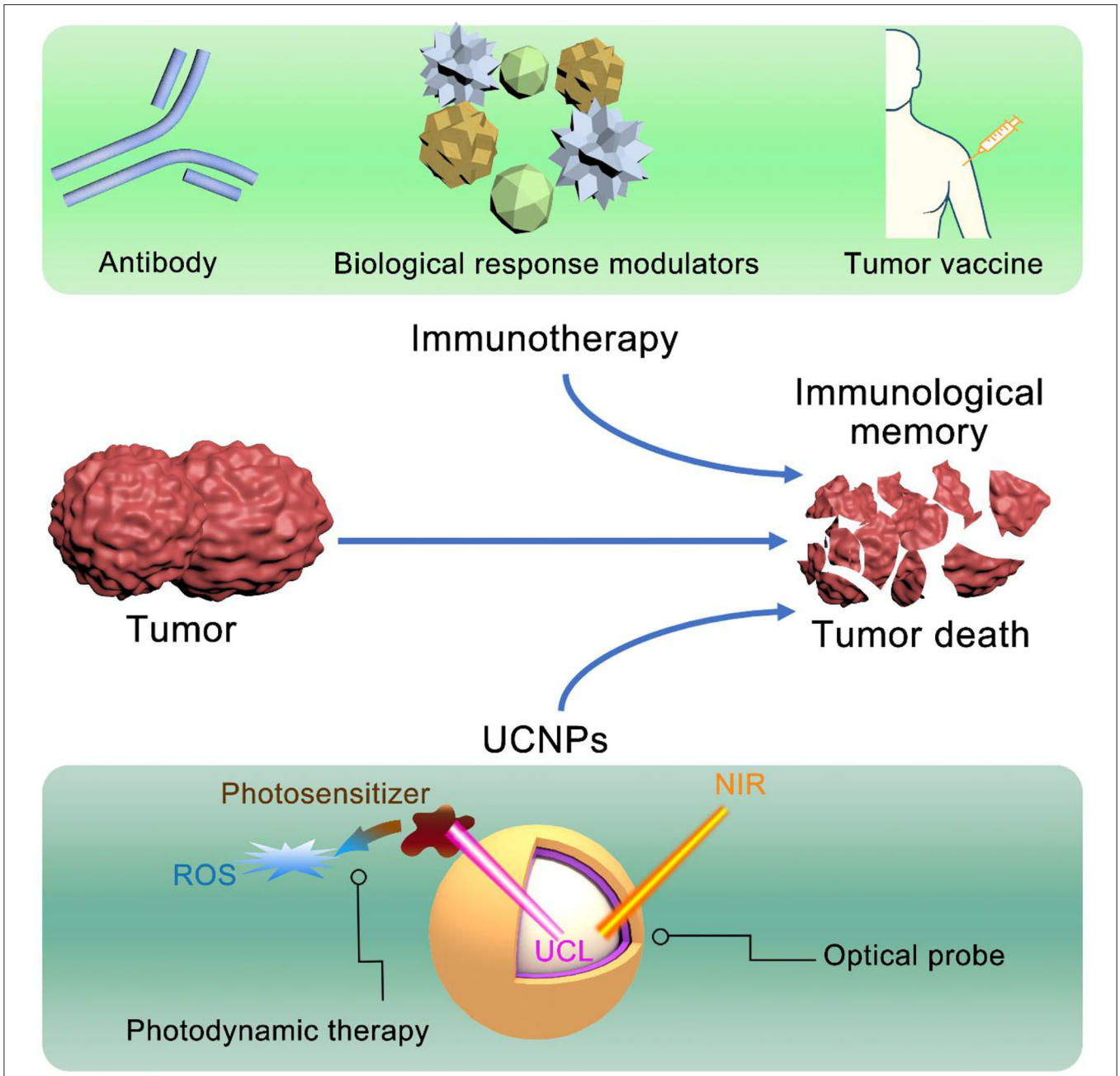

FIGURE 1 | The combination of UCNPs and immunotherapy.

et al., 2015). The location of DC vaccine can be traced through UCL imaging *in vivo* during DC immunotherapy. Firstly, they modified UCNPs (NaY/GdF_4:Yb,Er) with polyethylene glycol (PEG) and polyethyleneimine (PEI) to prepare UCNP-PEG-PEI (UPP). Then, the antigen model OVA was loaded onto UPP (UPP@OVA) by electrostatic interaction (**Figure 2A**). Mature DCs were injected into tumor-bearing mice, and the location of DCs could be traced by UCL imaging *in vivo*, revealing the homing process of DCs from peripheral tissues to draining lymph nodes (**Figures 2B,C**). Compared with OVA-treated DC vaccine, the UPP@OVA treated DC vaccine elicited strong antigen-specific immune responses (**Figure 2D**), such as enhanced T cell proliferation, IFN-gamma (IFN-γ) production, and cytotoxic T lymphocyte (CTL)-mediated responses. This work is the first to achieve highly sensitive *in vivo* DC tracing and prepare DC vaccines with strong immune function using antigen-loaded UCNPs, which is of great significance in the development of traceable DC immunotherapy.

As mentioned above, phototherapy can induce anti-tumor immune response by inducing apoptosis or necrosis of tumor

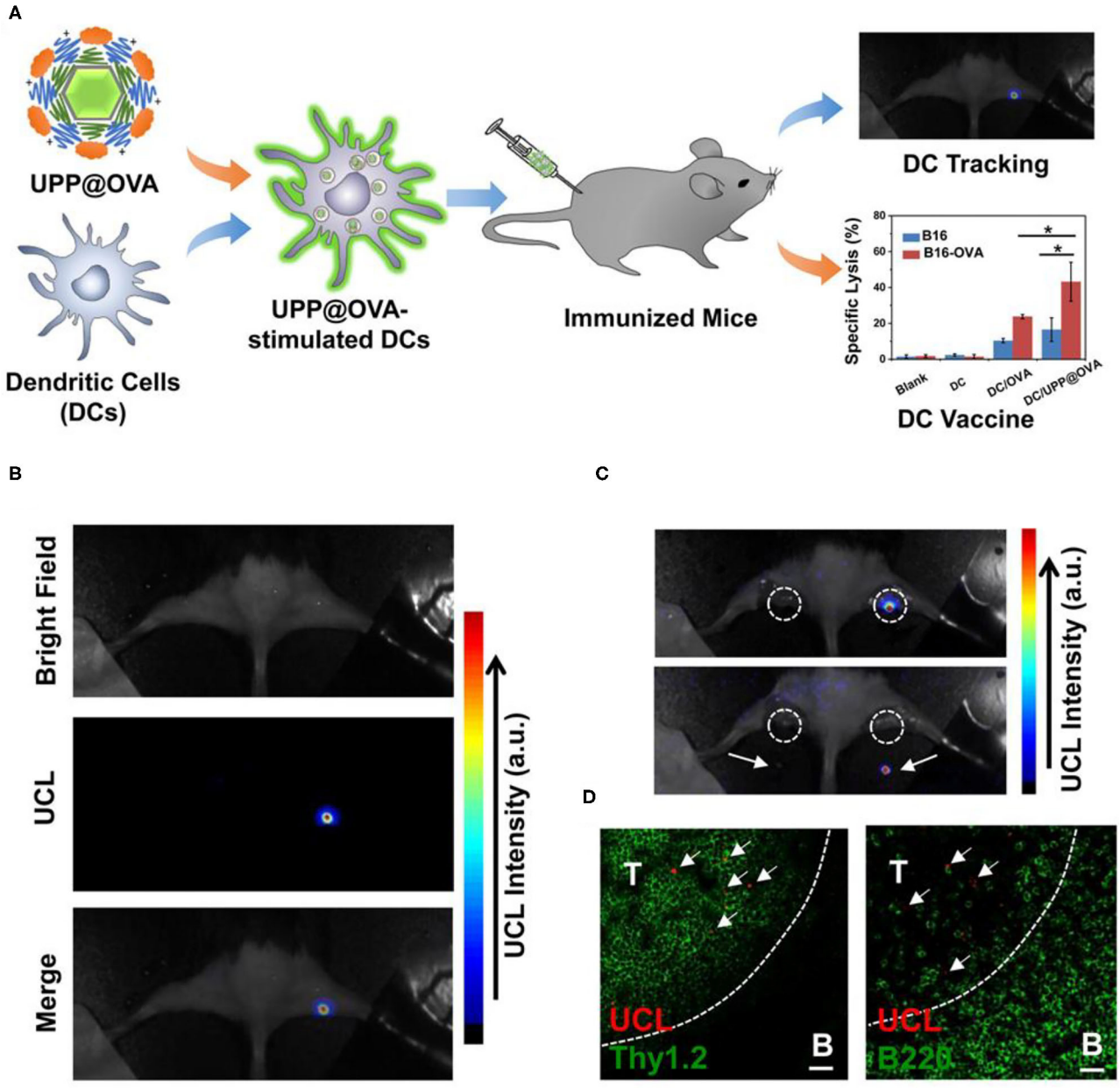

FIGURE 2 | (A) Schematic illustration of antigen-loaded UCNPs for DC stimulation, tracking, and vaccination in DC-based immunotherapy. **(B)** Labeled DCs were injected into the right footpad of a mouse; 48 h after injection, strong UCL signals from the draining lymph node were seen under *in vivo* UCL imaging. **(C)** *Ex vivo* imaging of popliteal lymph nodes (white circles) before (top) and after (bottom) being dissected from the mouse. **(D)** Immunofluorescence images of the lymph nodes dissected from the mouse injected with UPP@OVA-labeled DCs. T, T-cell zone (Thy1.2þ); B, B-cell zone (B220þ). Scale bar = 20 μm. Arrows point to UCL signals from labeled DCs. Copyright 2015, American Chemical Society (Xiang et al., 2015). *$P < 0.05$.

cells to release TAA. It can be used as *in situ* therapeutic tumor vaccine to activate immune response at the same time of phototherapy. This kind of *in situ* vaccine often needs some help to strengthen the immune response to ensure the effect of immunotherapy. Immune adjuvant can improve the adaptive immune response of the body to the antigen. It can make up for the weak immunogenicity of tumor antigen and enhance the immune response of tumor antigen (Vermaelen, 2019). In order to achieve strong and lasting antitumor effects in cancer immunotherapy, it is very important to select appropriate immune adjuvants (Shao et al., 2015). Mesoporous silica materials have attracted extensive attention from researchers because of their high surface area, adjustable pore size, and good biocompatibility (Lee et al., 2011). Recent studies have

shown that mesoporous silica materials can be used as immune adjuvants to enhance the host's antitumor immune effects (Wang et al., 2016a,b). Based on the above studies, Ding et al. prepared monodispersed macroporous mesoporous silica-coated upconversion nanoparticles (UCMSs) with particle size <100 nm and applied them as an immune adjuvant for the first time in antitumor studies (**Figure 3A**) (Ding et al., 2018). Because of the pore size structure of silica, UCMSs were loaded with PS merocyanine 540 (MC540), chicken OVA or tumor cell fragments simultaneously. Under 980 nm light irradiation, upconverted green light activated MC540 to produce ROS. Furtherly, TAA produced by PDT and released from nanovaccines can stimulate DC maturation, resulting in effector T cell release from lymph node. Finally, T cell activation and proliferation and relevant cytokines release can dramatically kill tumor cells. *In vivo* experiments demonstrated that UCMSs-MC540-OVA exhibited the strongest Th1 and Th2 immune responses and the highest frequencies of $CD4^+$, $CD8^+$, and effector memory T cells (**Figures 3B–D**). In addition, UCMSs-MC540-TF could more effectively inhibit the tumor growth and prolong the life span of CT26 tumor-bearing BALB/c mice. The successful construction of this multifunctional UCMSs immune adjuvant opens the way for the development of smart nanomedicines.

Both PDT and drug doxorubicin (DOX) can activate T cell immune responses in TME by activating the ICD process, which make it possible for PDT to be combined with chemotherapy to activate immune response (Garg and Agostinis, 2014; Kuai et al., 2018). The ICD process mainly has adenosine triphosphate (ATP) secretion, heat shock protein (HSP)-antigen peptide complex, calreticulin (CRT) surface exposure, and release of high migration protein B1 (HMGB1) (Garg et al., 2013). Jin et al. loaded chemotherapy DOX and photosensitive rose-bengal (RB) into ROS response micelles based on UCNPs (β-$NaYF_4$:Yb,Er), and constructed the treatment nanoplatform (Jin et al., 2020). The ROS response micelles were constructed from biocompatible sialic acid (SA), PEG, thioketone (TK), and poly(lactic-co-glycolic acid) (PLGA). TK is a sulfhydryl-based ROS reactive bond that can trigger rapid drug release through PDT. In addition, SA is a type of N-Acetylneuraminic acid that effectively attaches to E-selectin highly expressed on the cell membrane surface of tumor cells (Xu et al., 2018b), which can dramatically enhance cellular and tumoral uptake of nanoparticles. The micelles (SA-PEG-TK-PLGA, SPTP) loaded with UCNPs, DOX, RB would specifically target overexpressed E-selectin on tumor cells and produced cytotoxic singlet oxygen ($^1O_2$) from RB activated by UCNPs under the irradiation of 980 nm. Furtherly, $^1O_2$ can destroy the TK linkers and decompose the SPTP micelles system, thus achieving the release of controllable chemotherapy drugs (DOX). The mechanism of the antitumor immunity *in vivo* demonstrated that the synergistic effect of chemo-PDT could induce strong antitumor immune response by the ICD process with enhanced CRT expression, HMGB1 secretion, and sequential activation of T lymphocytes especially $CD8^+$ T cells infiltrated in tumors (**Figure 4**). This process has no addition of immune checkpoint inhibitors or immunoadjuvants, resulting in effective antitumor effects and inhibition of tumor metastasis.

UCNPs and Tumor Antibody Therapy

In many cases, the immune effect induced by PDT is not enough to inhibit the growth of residual tumor. The use of immunomodulatory antibodies such as anti-CTLA-4 and anti-PD-1 has high significance in enhancing such immune response. This *in situ* vaccine combined with immunomodulatory antibody can produce immune memory effect and obtain better therapeutic effect. Xu et al. constructed a therapeutic nanoplatform loaded with PS chlorin e6 (Ce6) and immune adjuvant R837 based on UCNPs [$NaYF_4$ (Y/Yb/Er = 78:20:2)] (Xu et al., 2017a). As shown in **Figure 5A**, under 980 nm NIR light irradiation, UCNPs destroyed primary tumors by activating the PS Ce6 to produce cytotoxic singlet oxygen. After PDT treatment, TAA released from tumor residues can effectively promote the maturation of DCs and activate antitumor specific immune responses with the assistance of immune adjuvant R837. After PDT treatment, the levels of immune-related cytokines (IL-12p40, IFN-γ, and TNF-alpha) were significantly increased in UCNPs-Ce6-R837 group. CTLA-4 checkpoint inhibitors can inhibit the immunosuppressive regulatory capacity of regulatory T cells (Wing et al., 2008). UCNPs-Ce6-R837 combined with CTLA-4 immune checkpoint inhibitors not only inhibited the growth of primary tumors, but also had therapeutic effects on distal untreated tumors. It is well-known that immune memory response plays an important role in protecting the body from the second attack of pathogens such as tumor cells (Teixeiro et al., 2009; Kinjyo et al., 2015). The experiment proved that UCNPs-Ce6-R837 combined with CTLA-4 immune checkpoint inhibitor had good long-term immune memory protection.

Besides, UCNPs often face serious problems of low emission efficiency due to the characteristics of low absorption cross-section, inherent structural defects, and prohibition of dipole transition of rare earth ions (Bigall et al., 2012; Bao et al., 2019). UCL can be effectively enhanced by surface plasmon resonance effect by combining gold or silver nanoparticles with UCNPs (Cheng et al., 2017; Sharma et al., 2020). Lin et al. prepared a spindle-like UCNP@SiO_2@Au mitochondrial imaging probe (Lin et al., 2020). As shown in **Figure 5B**, the spindle structure made it easier for the probe to enter the cytoplasm. Gold nanoparticles coated on the surface of layer-by-layer enabled the probe to enhance red UCL under NIR excitation. Spindle@SiO_2@Au had good biocompatibility and could realize real-time dynamic imaging of mitochondria. Under NIR irradiation, UCNP@SiO_2@AuNPs combined with ZnPc (labeled as SPSZ) showed good UCL imaging ability as well as PDT effect. In addition, SPSZ combined with anti-CTLA-4 effectively inhibited tumor growth through the synergistic effect of PDT and immunotherapy. The resulting immune memory effect protects the body from tumor reinvasion and inhibits tumor recurrence.

Immune checkpoint inhibitors could also cooperate with PDT and PTT to assemble multifunctional therapeutic nanoplatform. *In situ* capture of TAA by nanoplatforms can greatly promote the recognition and uptake of antigens by APCs and enhance the tumor immune response. At the same time, dual modal photothermal and photodynamic agents could be triggered by

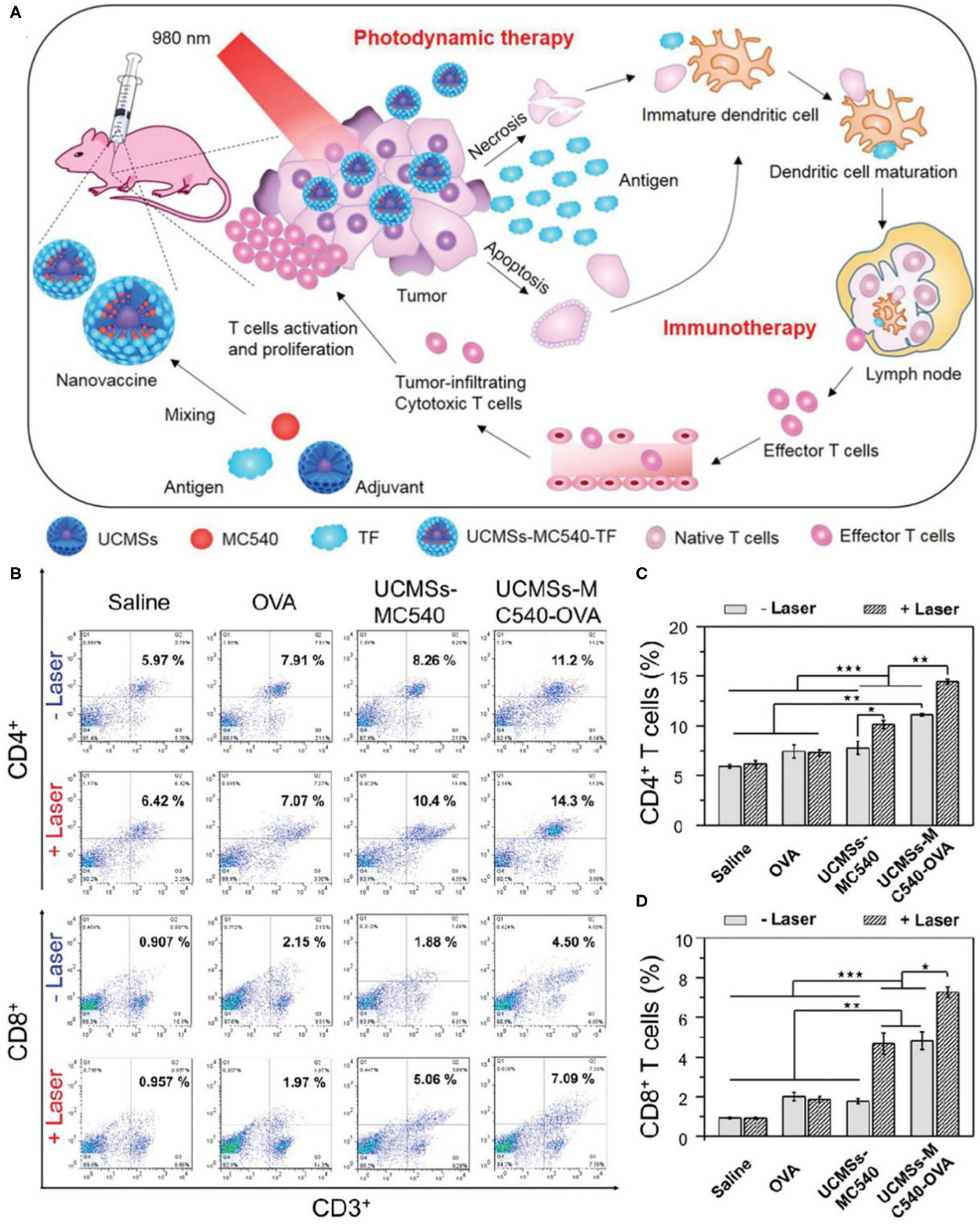

FIGURE 3 | (A) Schematic illustration of fabrication and mechanism of UCMSs-MC540-TF nanovaccines for PDT and immunotherapy. **(B)** Flow cytometric analyses of the populations of $CD4^+$ ($CD3^+$ $CD4^+$ as the marker) and $CD8^+$ ($CD3^+$ $CD8^+$ as the marker) T cells in splenocytes of mice immunized by various vaccine formulation. **(C)** The populations of $CD4^+$ after different treatments. **(D)** The populations of $CD8^+$ after different treatments. Copyright 2018, Wiley-VCH (Ding et al., 2018). $^*P < 0.5$, $^{**}P < 0.01$, $^{***}P < 0.001$.

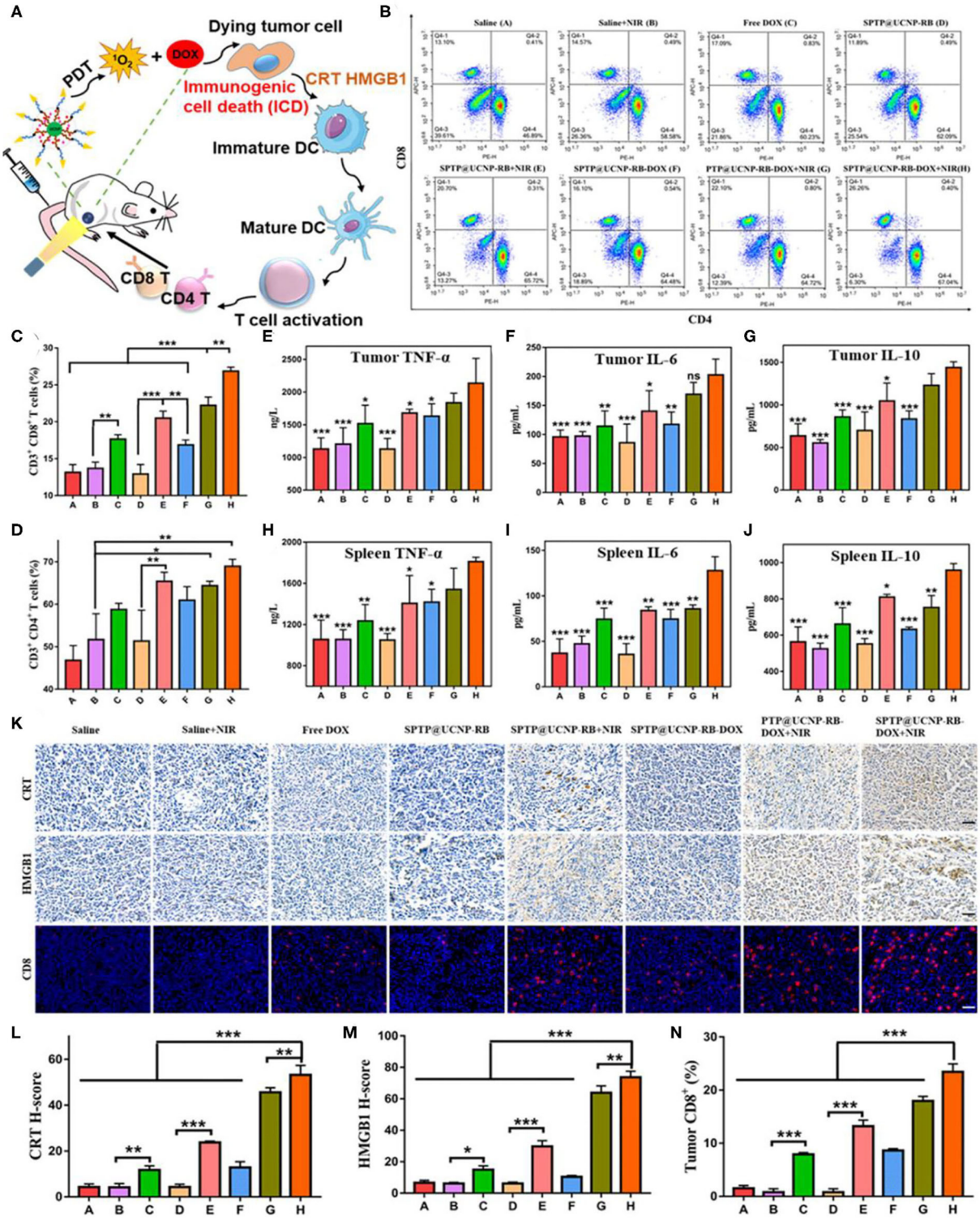

FIGURE 4 | Detection of antitumor immunity *in vivo*. **(A)** Illustration of the ICD-associated DAMP process. **(B–D)** Flow cytometry analysis of $CD4^+$ T cells ($CD3^+$ $CD4^+$) and $CD8^+$ T cells ($CD3^+$ $CD8^+$) proliferation in spleen tissues collected from all mice groups. **(E–G)** Quantitative analysis of TNF-α, IL-6, and IL-10 from tumor lysis solution and **(H–J)** in spleen lysis solution by the Elisa kit. Symbols on columns represent statistic difference vs. the SPTP@UCNP-RB-DOX + NIR group ($n = 6$). **(K)** CRT exposure and HMGB1 secretion in tumor tissues were observed by immunohistochemistry. The infiltration of immune cells in tumors was detected by immunofluorescence dyeing of CD8 T cells (scale bar = 20 μm). **(L–N)** Quantitative analysis of CRT exposure, HMGB1 secretion, and CD8 infiltration in tumor tissues by image J. $^*p < 0.05$; $^{**}p < 0.01$; $^{***}p < 0.001$. Copyright 2020, American Chemical Society (Jin et al., 2020).

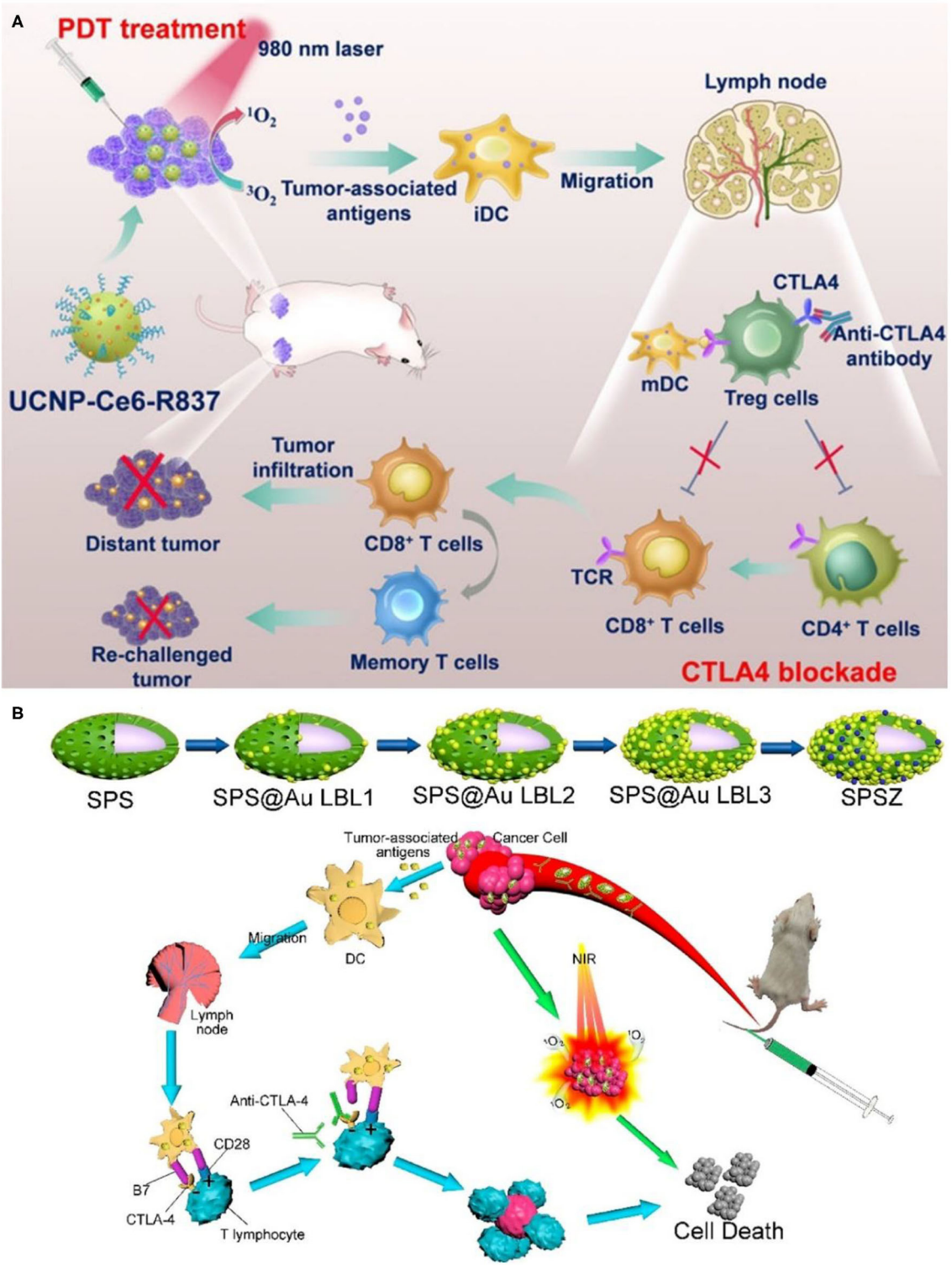

FIGURE 5 | (A) Scheme summarizing the mechanisms of combining NIR-mediated PDT with CTLA-4 checkpoint blockade for cancer immunotherapy. UCNP-Ce6-R837 nanoparticles under NIR light would enable effective photodynamic destruction of tumors. The generated TAA in the presence of those nanoparticles as the adjuvant are able to promote strong antitumor immune responses, which with the help of a CTLA-4 checkpoint blockade would eliminate primary tumors under direct NIR exposure, inhibit the growth of distant tumors left behind after PDT, and further yield a long-term immune memory to prevent tumor reoccurrence. Copyright 2017, American Chemical Society (Xu et al., 2017a). **(B)** Schematic diagram of spindle-like of UCNP@SiO_2@Au synthesis and anticancer therapy. Copyright 2020, American Chemical Society (Lin et al., 2020).

single wavelength laser to trigger PTT and PDT simultaneously so as to shorten the treatment time (Wang et al., 2013; Yang et al., 2017). Based on this, Wang et al. constructed a multifunctional nanotherapeutic platform using UCNPs ($NaYF_4$:Yb,Er@$NaYF_4$:Nd) as carriers, loaded with photothermal agents indocyanine green (ICG) and PS RB, and surface-modified lipid molecules (DSPE-PEG-mal) for functionalization (Wang et al., 2019a). Unlike the combination therapy strategy described earlier, the therapeutic nanoplatform UCNP/ICG/RB-mal can capture tumor antigens *in situ* and promote the recognition and uptake of APCs. Due to the large absorption cross-section of ICG, UCNP/ICG/RB-mal produced significant $^1O_2$ and heat, which could enhance phototherapy and cause more tumor-derived protein antigens (TDPAs) released by ICD (**Figures 6A,B**). TDPAs captured by UCNP/ICG/RB-mal are taken up by APCs to activate tumor-specific immune responses. Experiments demonstrated that UCNP/ICG/RB-mal+anti-CTLA-4+L treatment significantly inhibited the growth of primary tumors and slowed the growth of distant tumors (**Figures 6C,D**). UCNP/ICG/RB-mal combined with anti-CTLA-4 synergistically enhanced the antitumor immune response, regulated the tumor immunosuppressive microenvironment, and effectively prevented tumor metastasis. UCNP/ICG/RB-mal multifunctional nanoplatform realized the synergistic effect of PTT, PDT and immunotherapy. This nanoplatform, which selectively destroys primary tumors, increases the immune response rate and eliminates metastatic lesions.

Besides CTLA-4, PD-1 is another crucial inhibitory regulatory receptor that overexpressed on the activated T cells. Anti-PD-1, or anti-PD-L1 are also familiarly used in enhancing the immune effect of ICD derived from phototherapy. Yan et al. prepared polydopamine (PDA) nanoparticles with $NaGdF_4$:Yb,Er upconversion shell coated on the surface and then grafted Ce6 molecules to obtain PDA@UCNP-PEG/Ce6 nanoparticles (Yan et al., 2019). As shown in **Figure 7A**, under single 980 nm NIR light irradiation, PS Ce6 and photothermal agent PDA in nanocomposites were activated to produce excellent PDT and PTT effects (**Figures 7B,C**), thereby killing tumor cells. Controlled trials showed that the primary tumor was eliminated by PDA@UCNP-PEG/Ce6 with light (**Figures 7D–F**). In addition, PDT and PTT can induce ICD and activate tumor-specific immune response. PDA@UCNP-PEG/Ce6 combined with immune checkpoint inhibitor α-PD-1 synergistically enhanced the antitumor immune response, not only eliminating primary tumors, but also inhibiting the growth of distal tumors. At the same time, the nanotherapeutics promoted the activation of memory T cells and effectively prevented the recurrence of tumors. The synergistic effect of PDT, PTT and immunotherapy greatly enhances the antitumor effect and is of great significance for the elimination of tumors. In a further work, the same group designed a multifunctional immunostimulant by combining aggregation-induced emission (AIE) PS TPEBTPy with UCNPs to realize the controllable ROS production for PDT and immunotherapy, as shown in **Figure 8B** (Mao et al., 2020). TPEBTPy with AIE properties showed strong fluorescence and ROS production in the state of aggregation (Qian and Tang, 2017; Hu et al., 2018a). As a NIR antenna, UCNPs can transmit the energy of NIR photons to AIE PS, thus producing a large amount of ROS in deep tissues. In addition, the design of positively charged PS not only facilitated close contact between oxygen and PS, and promoted the rapid diffusion of ROS, but also ensured the subsequent antigen capture through electrostatic interaction. AIE luminogen (AIEgen)–coupled UCNPs (AUNPs) can regulate intracellular ROS levels by controlling NIR irradiation. As shown in **Figure 8A**, on the one hand, under high power NIR irradiation, a large amount of ROS can effectively kill tumor cells and release TAAs. On the other hand, under low power NIR irradiation, a small amount of ROS activated local DCs and effective cross-presentation, thus inducing the proliferation of stronger $CD8^+$ T cells. AUNPs further combined immune checkpoint blockade therapy αPD-1 to improve immune memory, kill the primary tumor cells, and inhibit the growth of the distant tumors (**Figures 8C–G**). The dual-mode activated ROS strategy provided a reference for the development of tumor immunotherapy.

In some PDT-based systems with porphyrin derivatives and their analogs as PS, the lack of hydrophobicity and tumor selectivity of porphyrin derivatives limits the clinical application of PDT (Cheng et al., 2014). The porphyrin-based metal-organic frameworks (MOFs) have periodic structural ordering, which makes PS molecules in the state of mutual separation, thus avoiding the self-quenching caused by the molecular aggregation of PS (Lu et al., 2014, 2015). In addition, the rich pore structure of MOFs provides a channel for ROS production to spread rapidly, which is conducive to improving the tumor killing effect of PDT (Park et al., 2016). Since the effective energy transfer from UCNP to PS is necessary to achieve NIR photoinduced PDT (Xu et al., 2017b), the attachment of a sufficient number of PSs near UCNP is crucial for the effective generation of $^1O_2$. Shao et al. designed the core-shell UCNPs@porphyrin MOFs (UCSs) for the combined treatment of hypoxia tumors, as shown in **Figure 9A** (Shao et al., 2020). High yield synthesis of UCSs was achieved through conditional surface engineering of UCNPs ($NaGdF_4$:Yb,Er@$NaGdF_4$) and seed-mediated growth strategy. The final structure TPZ/UCSs was obtained by encapsulating the hypoxic activated prodrug tirapazamine (TPZ) in the nanopores of the heterostructure MOF shell. They demonstrated that TPZ/UCSs was a promising system for *in vivo* and *in vitro* cancer treatment through NIR light induced PDT and hypoxic-activated chemotherapy. In addition, the nanoplatform combined with α-PD-L1 immunotherapy promoted complete inhibition of the growth of the distal untreated tumor by producing specific tumor-infiltrating cytotoxic T cells (**Figures 9B,C**). Compared with the PBS control group, the proportion of $CD4^+$ and $CD8^+$ T cells was significantly increased after TPZ/UCSs (+) + α-PD-L1 treatment (**Figures 9D,E**). TPZ/UCSs combined with α-PD-L1 therapy not only inhibited the growth of primary tumors but also slowed the growth of distant tumors.

Immune checkpoint inhibitors could also corporate with light controlled molecular nanodevices to enhance antitumor efficacy. Di et al. designed an orthogonal upconversion nanoplatform, which achieves NIR light deep tissue penetration and specific target recognition of tumors by DNA nanodevices (Di et al., 2020). Therein, DNA is a highly programmable component

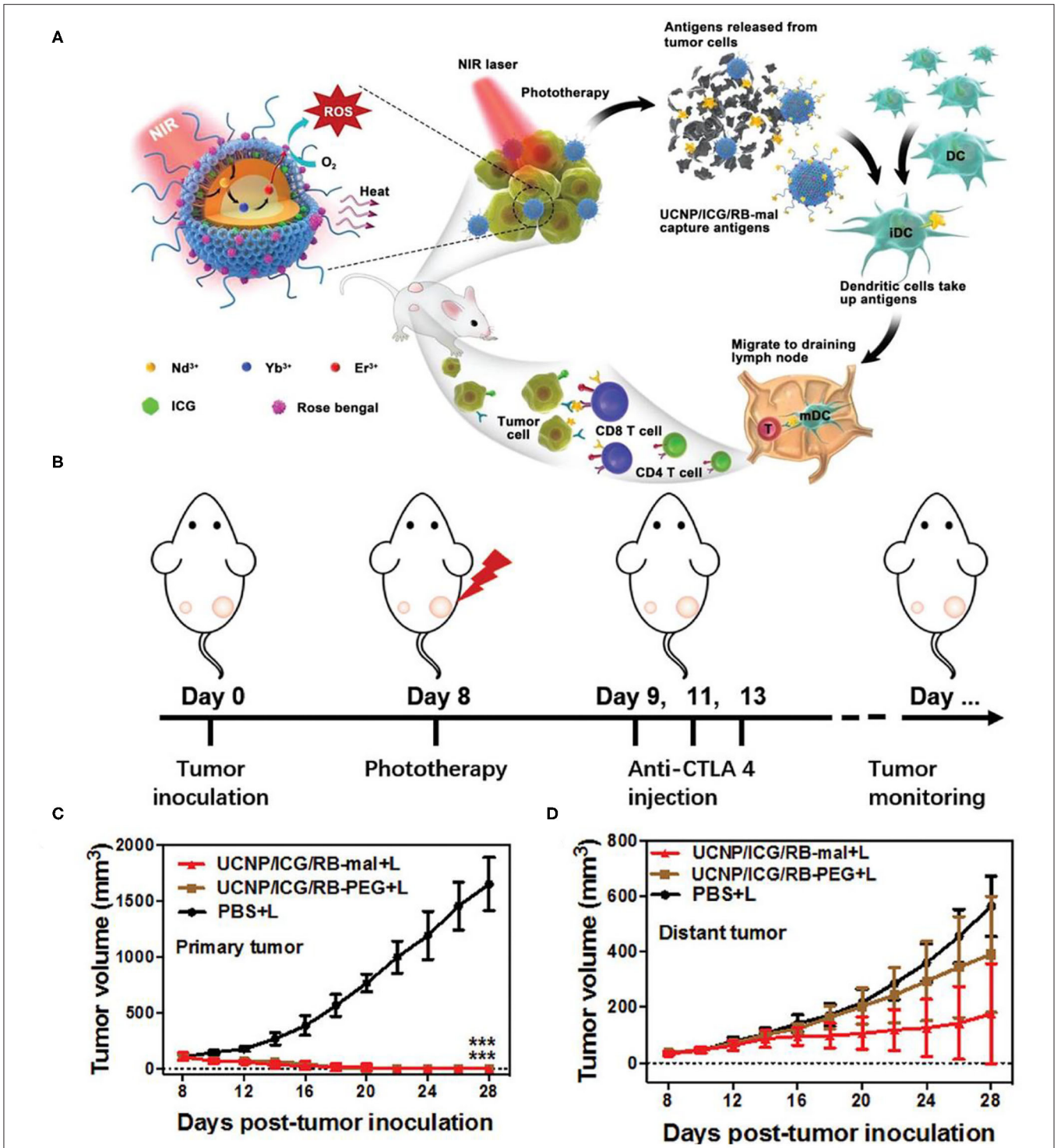

FIGURE 6 | (A) Schematic illustration of both fabrication and mechanism of NIR-triggered antigen-capturing nanoplatform for synergistic photo-immunotherapy. Abscopal effect of UCNP/ICG/RB-mal based phototherapy in combination with checkpoint inhibition for simultaneously inoculated tumors. **(B)** Schematic depiction of the experimental approach for the evaluation of the abscopal effect induced by UCNP/ICG/RB-mal based phototherapy. **(C)** Growth curves of primary tumors of mice after various treatments (***$P < 0.001$ vs. PBS + L group) **(D)** Growth curves of distant tumors on mice in different treated groups. Data are expressed as mean ± SD ($n = 5$). Copyright 2019, Wiley-VCH (Wang et al., 2019a).

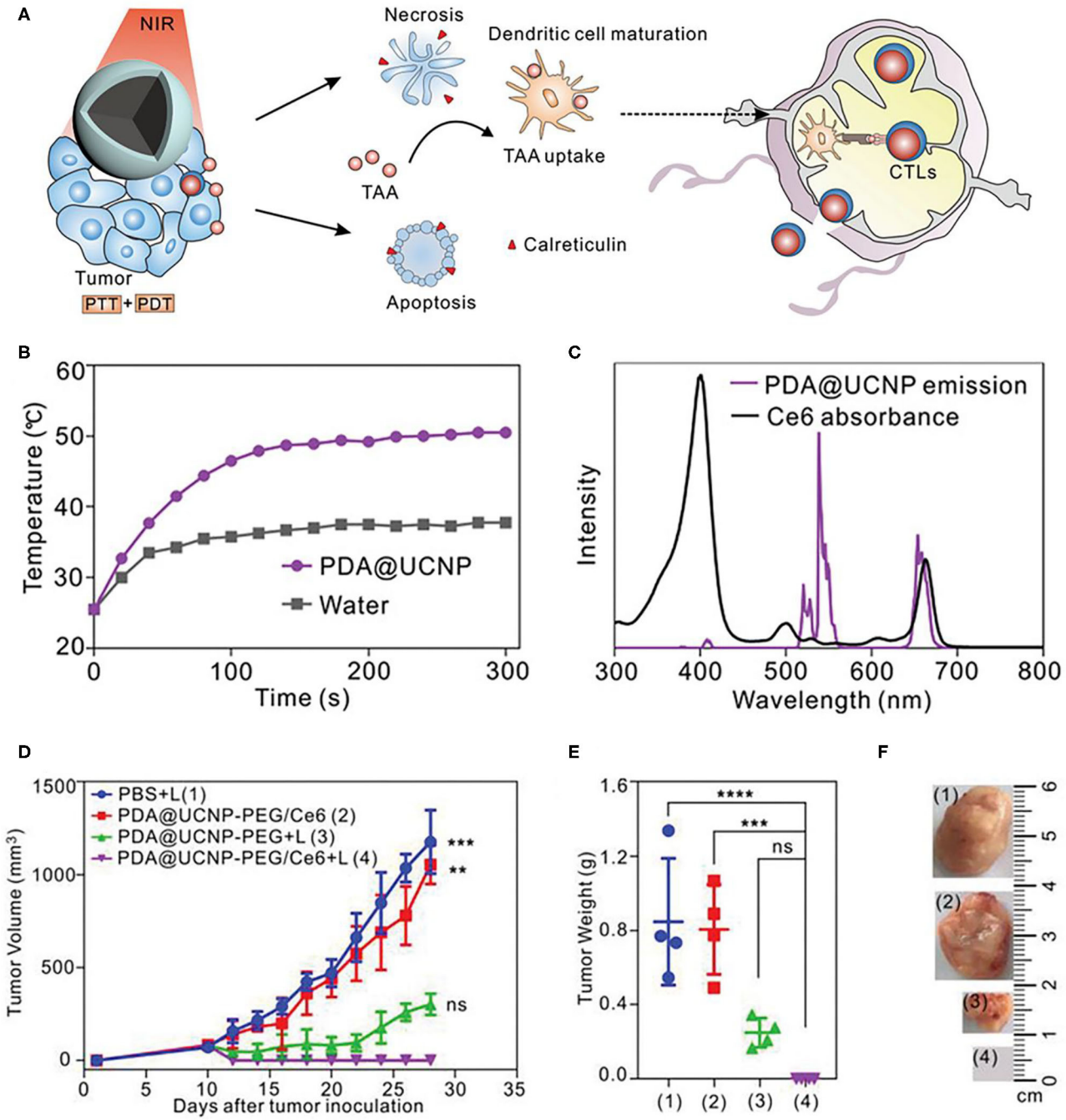

FIGURE 7 | (A) Scheme of synergistic phototherapy for augmentation of antitumor immunity. Upon laser irradiation, designed nanoparticles can ablate the primary tumor through synergistic phototherapy, and the released TAA tend to trigger the antitumor immunity which contributes to the inhibition of tumor metastasis and relapse. **(B)** Temperature profiles of pure water and aqueous dispersions of PDA@UCNP nanoparticles (2 mg mL^{-1}) as a function of irradiation time (0–5 min). **(C)** The spectrum profiles of Ce6 absorption and PDA@UCNP emission excited with a 980 nm laser. **(D)** Tumor growth curve of 4T1 tumor-bearing mice with various treatments. Weight **(E)** and representative images **(F)** of the tumor from each group after euthanizing the animal on day 28. Copyright 2019, Wiley-VCH (Yan et al., 2019). $^{**}P < 0.01$, $^{***}P < 0.001$, $^{****}P < 0.0001$ and ns: not significant ($P > 0.05$).

that can be used to design molecular nanodevices with specific functions, such as biosensing and imaging (Chen et al., 2015), molecular information calculation (Amir et al., 2014), and controlled drug delivery and release (Brodin et al., 2015; Hu et al., 2019a). The adaptor module L-Apt (UV light–activatable aptamer modules) can be activated by UV light, releasing

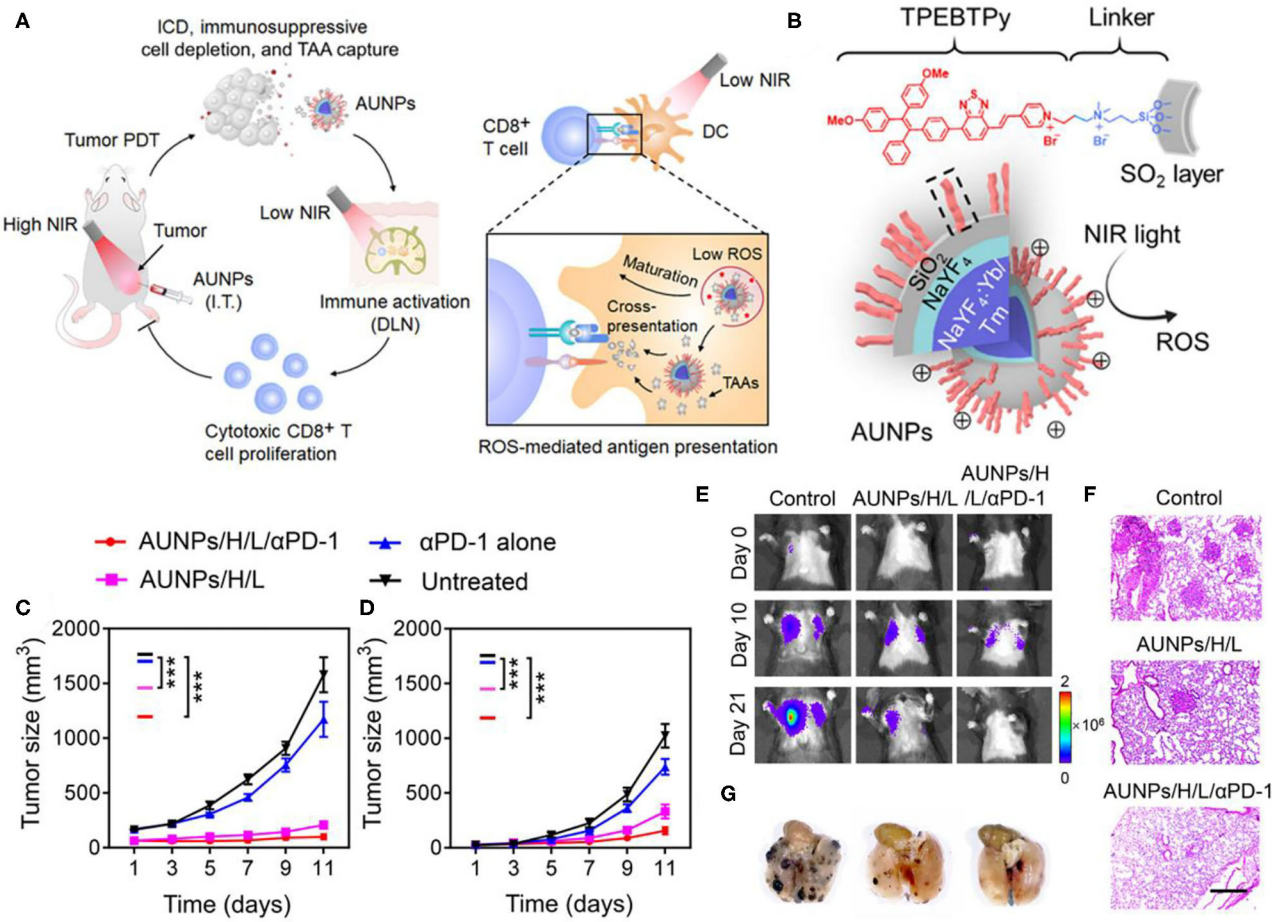

FIGURE 8 | (A) Proposed scheme of dual-mode ROS-driven tumor immunotherapy. **(B)** Structure of TPEBTPy and AUNPs. Dashed box indicates a linked TPEBTPy molecule on the AUNPs. **(C)** Primary and **(D)** distant tumor growth curves of the B16F10 tumor–bearing mice with different treatments ($n = 5$). **(E)** Bioluminescence images of mice after rechallenging with intravenous injection of B16F10 tumor cells. **(F)** Representative lung photographs (21 days) and **(G)** hematoxylin and eosin (F&G) images of lung tissue slices from control (naïve mice), AUNPs/H/L, and AUNPs/H/L/αPD-1 groups. Scale bar, 100 μm. Copyright 2020, American Association for the Advancement of Science (Mao et al., 2020). $^{*}P < 0.05$, $^{**}P < 0.01$, and $^{***}P < 0.001$.

an adaptor that can recognize the overexpressed recognizes nucleolin on the surface of cancer cells (Reyes-Reyes et al., 2010; Li et al., 2014). Nanodevices (PT-UN) with orthogonal UCL are constructed from PS on the surface of UCNPs ($NaGdF_4$:Yb,Er@$NaYF_4$@$NaYF_4$:Yb,Tm@$NaYbF_4$:Nd@$NaYF_4$) and L-Apt. With the light regulators UCNPs, UV UCLs obtained under 808 nm irradiation could cleave photocleavage bonds and release aptamers at the required time and guide nanoparticles to target tumor cells. And green UCLs obtained under 980 nm irradiation can stimulate PS to produce cytotoxic ROS, thereby killing tumor cells (**Figures 10A,B**). Under 808 nm NIR illumination, the characteristic Tm^{3+} emissions located at UV (347 and 363 nm) and blue (452 and 475 nm) regions were observed (**Figure 10D**). In contrast, visible green (522 and 541 nm) and red (656 nm) emission of Er^{3+} occupied the spectra under NIR excitation at 980 nm (**Figure 10C**). PT-UN-mediated PDT combined with α-PD-L1 elicited a strong systemic antitumor immune response by promoting the infiltration of effector T cells. The combination of nanodevices with targeted and killing effects and immune checkpoint inhibitors α-PD-L1 not only eliminated the primary tumors, but also inhibited the growth of distal tumors (**Figures 10E–G**).

Of course, the application of rare earth nanomaterials in second NIR window (NIR-II, 1,000–1,700 nm) is also involved. Different from the upconversion luminescence of NIR region, NIR-II region is usually down-shifting luminescence, which is used for biological imaging research. In recent years, more and more attention has been paid to the study of molecular probes imaging in the NIR-II window (Hong et al., 2014; Antaris et al., 2017). Imaging at the long wavelength end of the NIR-II window (NIR-IIb, 1,500–1,700 nm) has been reported to increase the penetration depth to subcentimeter and completely eliminate self-fluorescence (Diao et al., 2015a,b; Zhang et al., 2018). At present, clinical *in vitro* immunodiagnosis relies on biopsy to analyze the expression status of tumor cells PD-L1 and the presence/proportion of tumor-infiltrating immune

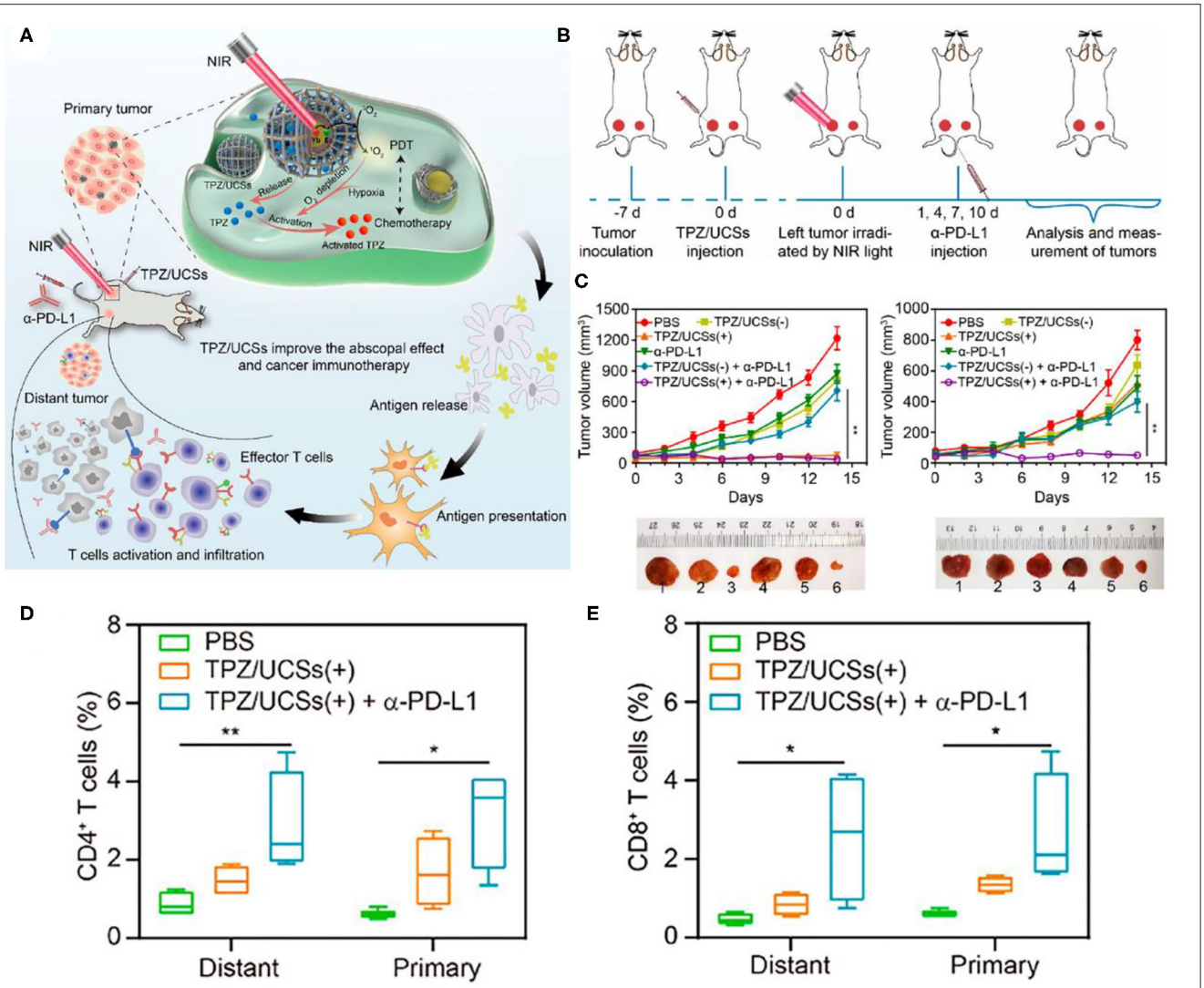

FIGURE 9 | (A) Schematic illustration of the structure of TPZ/UCSs and their application to tumor treatment through a combination of NIR light-triggered PDT and hypoxia-activated chemotherapy with immunotherapy. **(B)** Schematic illustration of NIR light-triggered combinational therapy. **(C)** Growth curves of primary tumors (left) and distant tumors (right) in CT26 tumor-bearing mice after different treatments. Photographs of primary tumors and distant tumors collected from mice 14 days after treatments: (1) PBS, (2) TPZ/UCSs(–), (3) TPZ/ UCSs(+), (4) α-PD-L1, (5) TPZ/UCSs(–) + α-PD-L1, and (6) TPZ/UCSs(+) + α-PD-L1. Percentage of tumor-infiltrating **(D)** $CD4^+$ T cells, **(E)** $CD8^+$ T cells in total tumor cells. Data are means ± SD; $N = 4$. $^*P < 0.05$, $^{**}P < 0.01$. Copyright 2020, American Chemical Society (Shao et al., 2020).

cells. *In vivo* imaging relies on positron emission tomography to solve the problem of uneven distribution of PD-L1 (Mall et al., 2016; Chatterjee et al., 2017). However, no technology had been developed to detect two or more immune-related factors simultaneously *in vivo* with NIRII. Zhong et al. developed the anti-PD-L1 mAb-labeled α-phase Er nanoparticles (ErNPs) with zinc doping (Zhong et al., 2019). Compared with the brightest β-Phase ErNPs before (Zhong et al., 2017), the down-shifting luminescence is enhanced by about 11 times through enhancing the relaxation of multiple phonons in α-phase ErNPs over β-phase, and the symmetry of the crystal field is reduced by doping Zn^{2+}. In addition, the designed hydrophilic polymeric cross-linking network endows ErNPs excellent water solubility and biocompatibility. They combined anti-PD-L1 mAb-labeled ErNPs (targeted at PD-L1) and anti-CD8 mAb-labeled PbS quantum dots (targeted at $CD8^+$ T cells) for bi-channel molecular imaging to monitor two immune-related molecular targets in real time within the same NIR-IIb emission window (∼1,600 nm). Both ErNPs-aPD-L1 excited by 980 nm and PbS-aCD8 excited by 808 nm can emit fluorescence at the NIR-IIb emission window (about 1,600 nm) (**Figure 11C**). The difference is that the fluorescence lifetime of ErNPs is millisecond and that of PbS quantum dots is microsecond. Two fluorescent signals can be captured by setting the delay in the InGaAs CCD camera. In addition, the PbS-aCD8 channel had higher peripheral signals in the tumor and extends inwards. It was

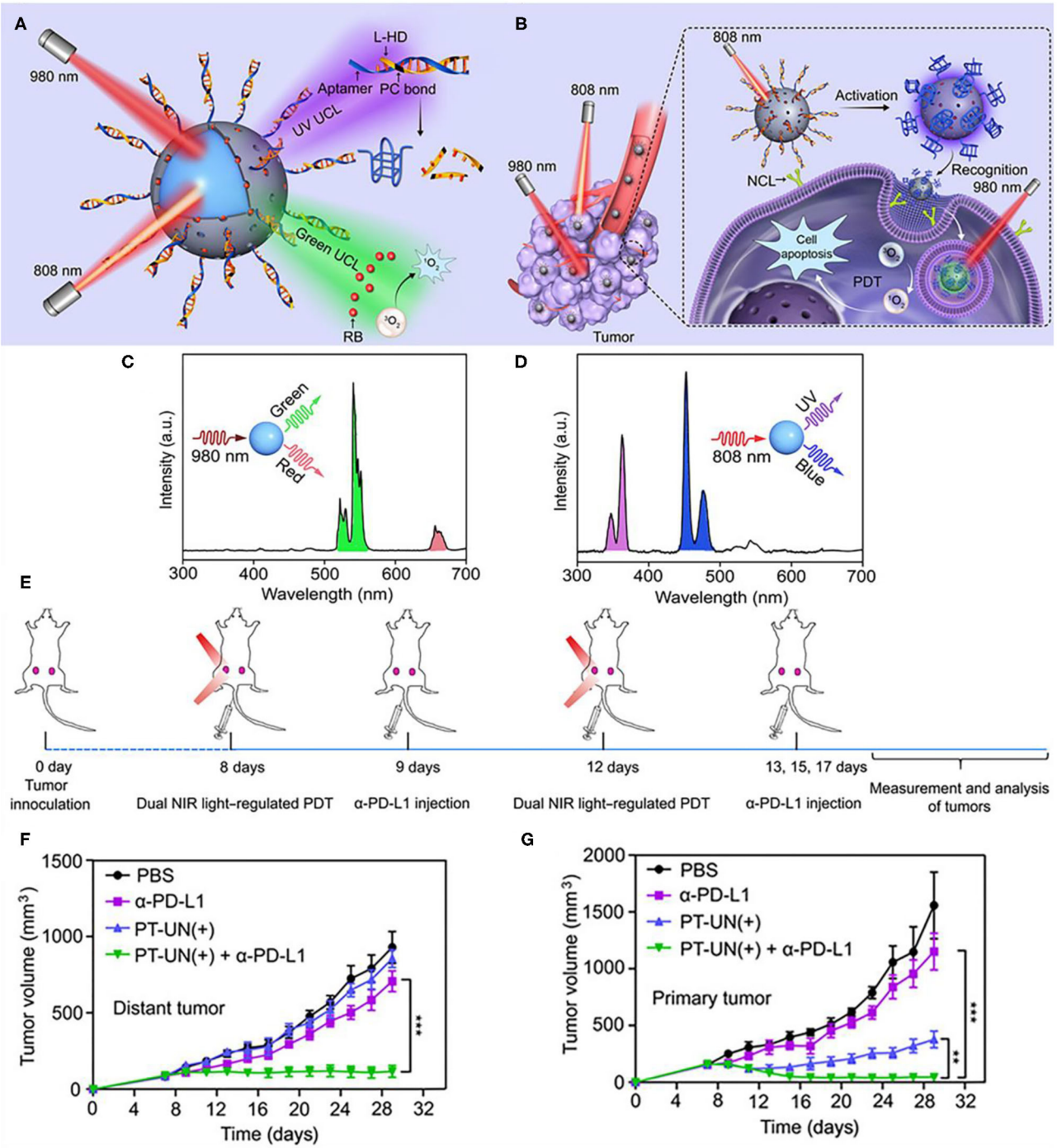

FIGURE 10 | Schematic showing the orthogonal regulation of DNA nanodevice for programmed tumor cell recognition and treatment. **(A)** The orthogonal photoactivation behavior of the DNA nanodevice in response to two NIR light of different wavelengths. **(B)** Sequential activation of the nanodevice with orthogonal UCL for programmed tumor recognition and PDT. UCL spectra of the core-multishell UCNPs upon excitation of 808 **(C)** and 980 nm **(D)**. **(E)** Schematic illustration of combining PT-UN(+) with α-PD-L1 therapy to inhibit tumor growth at both primary and distant sites. Tumor growth curves of primary tumors **(F)** and distant tumors **(G)** of bilateral tumor-bearing mice with different treatments. Data are means ± SD ($n = 5$). Copyright 2020, American Association for the Advancement of Science (Di et al., 2020). $^{**}P < 0.01$, $^{***}P < 0.001$.

demonstrated that tumors treated with anti-PD-L1 monoclonal antibody produced a strong antitumor immune response and had a high (T/spleen)_CD8 ratio. The assessment of the *in vivo* non-invasive biological distribution of tumor cells and immune cells throughout the body can complement *ex vivo* biopsy-based diagnostic methods.

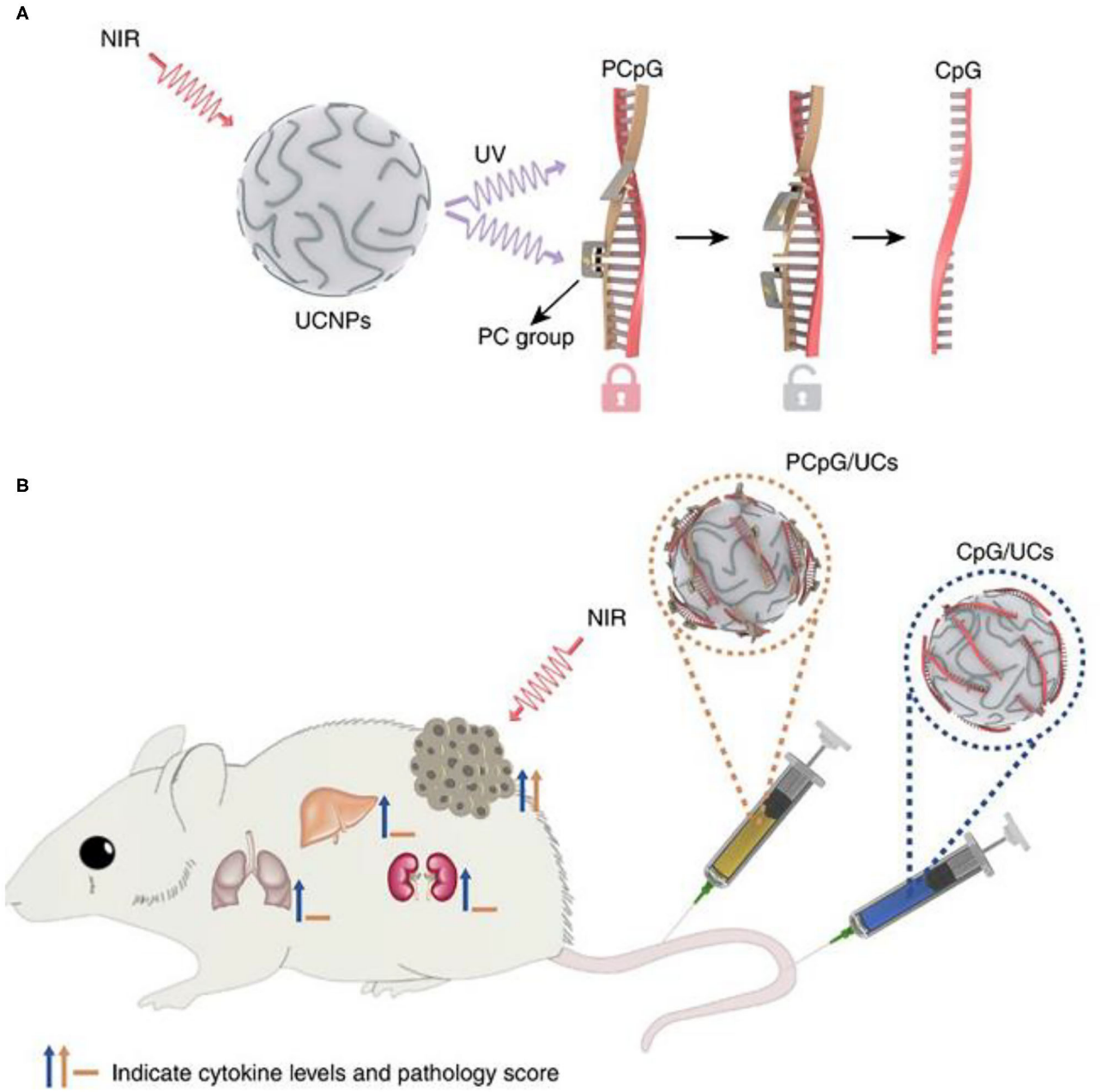

FIGURE 11 | Programming of photoactivatable immunodevice. **(A)** Schematic of the design of photoactivatable immunodevice through the integration of UCNPs with the UV light-responsive PCpG. UCNPs act as transducer to upconvert NIR light into UV light locally, thus liberate CpG ODN from PCpG to achieve the refined temporal control on its immunoactivity. **(B)** Illustration of the photoactivatable immunodevice, PCpG/UCs, for spatially selective triggering of immunoactivity through NIR light irradiation. In contrast to traditional CpG delivery system (CpG/UCs), PCpG/UCs is amenable to personalizing the antitumor modality with reduced systemic toxicity. Copyright 2019, Nature Publishing Group (Chu et al., 2019).

UCNPs and Biological Response Modulators

In immunotherapy based on BRMs, systemic injection of immunostimulants is usually required. However, systemic injection of immunostimulants requires precise control of the injection dose, otherwise it will cause serious side effects, such as excessive immune response and excessive release of cytokines (Morgan et al., 2010; Sharma and Allison, 2015). Therefore, it is of great significance to develop a highly spatiotemporal control immune response strategy for tumor

site. Chu et al. designed and constructed a NIR light-controlled immunotherapy nanomaterial, which can remotely control the activation of immunotherapy *in vivo* and reduce the systemic toxicity of the nanomaterials (Chu et al., 2019). CpG-ODNs (CpG oligonucleotides, an immunotherapeutic agent) are hybridized with complementary ssDNA (PcDNA) containing photocleavable (PC) bonds to form PCpG, which prevents CpG-ODNs from binding to TLR9. They combined UCNPs ($NaGdF_4$:Yb/Tm@$NaGdF_4$) with PCpG to construct light activated immune devices. Under the NIR light irradiation, the NIR light of UCNPs was transformed into ultraviolet. As shown in **Figure 11A**, UV light can photolysis PC bond and release CpG ODNs, thus achieving NIR light controlled immune response. CpG binds to TLR9 in APCs, thus promoting the maturation of DC and the production of inflammatory cytokines, leading to T cell-mediated antitumor immune response (Adamus and Kortylewski, 2018). Compared with the traditional CpG delivery system (CpG/UCS), PCpG/UCS is more suitable for individualized antitumor methods and reduces systemic toxicity (**Figure 11B**).

In immunotherapy, the use of exogenous chemokines to induce the infiltration of immune cells into tumor can improve the antitumor activity (Homey et al., 2002; Lechner et al., 2011). C-C Motif Chemokine Ligand 21 (CCL21) can stimulate the expansion of $CD4^+$ and $CD8^+$ T cells and promote the polarization of Th1 cells (Flanagan et al., 2004). In addition, the specific binding of CCL21 to C-C chemokine receptor type 7 (CCR7) expressed on the surface of tumor cells can promote lymph node metastasis of tumor cells (Mashino et al., 2002; Takeuchi et al., 2004). Zhang's group developed a therapeutic nanoplatform to induce the migration of immune cells to tumor lesions and trigger antitumor immune response (Lee et al., 2013). They used UCNPs ($NaYF_4$:Yb,Er) as carriers and coated mesoporous silica shell on the surface. Meanwhile, UCNPs@mesoporous silica loads chemokine CCL21. To improve the targeting of UCNPs@mesoporous silica to tumor cells, folic acid (FA) was modified on the surface of the core-shell structure. They developed an *in vitro* endothelial-tumor cell bilayer model and demonstrated that CCL21-FA-UCNPs@mesoporous silica could selectively target folate receptor (FR)-expressing OVCAR-3 cells. In addition, it was confirmed CCL21-FA-UCNPs@mesoporous silica effectively induced T cell migration to tumor cell sites using the Transwell system. On this basis, Zhang's group used microfluidic system to further study the effect of CCL21-FA-UCNPs@mesoporous silica in simulating 3D tumor tissue (Wimalachandra et al., 2019). *In vitro* imaging CCL21-FA-UCNPs@mesoporous silica can be selectively absorbed by FR expressed OVCAR-3 cells. Accumulating in the tumor, CCL21-FA-UCNPs@mesoporous silica induced the migration of $CCR7^+$ DCs and Jurkat T cells. This work proved that it is feasible for UCNPs loaded with chemokines to regulate T cell migration.

In addition to the common BRMs such as cytokines, there are also some chemically synthesized molecules with drug properties, which can also be classified as BRMs because of their potential immunomodulatory functions. Tumor-associated macrophages (TAMs) play an important role in tumor recurrence, invasion, angiogenesis, and metastasis (Quail and Joyce, 2013; Georgoudaki et al., 2016). Tumor-associated macrophages are mainly classified into antitumor and immune-enhancing M1 type macrophages and M2 type macrophages which inhibit immune response, promote angiogenesis, tissue repair, and promote tumor growth (Mosser, 2003). The two phenotypes of TAMs, M1 and M2, will undergo a transition, and their M2 type can be reversely polarized into M1 type TAM, thus triggering the body to produce a specific antitumor immune response, the polarization process is reversible and adjustable (Gordon and Martinez, 2010). The addition of BRMs can affect the polarization process and regulate the immune process. Ai et al. constructed a therapeutic nanoplatform to alleviate tumor hypoxia and synergistically reprogram TAMs population (Ai et al., 2018). They first synthesized UCNPs [$NaYF_4$:Yb/Tm/Nd (30/0.5/1%)@$NaYF_4$:Nd (20%)], and then prepared UCNs-MnO_2-Ce6-HA (PUN) nanoparticles using manganese dioxide (MnO_2), PS Ce6 and hyaluronic acid (HA) for surface functionalization. Under the acidic TME, MnO_2 can react with endogenous H_2O_2 to produce sufficient oxygen, which is conducive to alleviating the hypoxic state of tumors. As shown in **Figure 12A**, HA can reverse TAM-polarized tumor-promoting M2 phenotype to antitumor M1 phenotype after PDT treatment, which could stimulate tumor-specific immune response and effectively inhibit tumor recurrence, shows the performance of immune regulation (Tran et al., 2015). After PDT treatment, the tumor cells continued to be cultured with PUN, and their cell activity was significantly reduced. This work has reference significance for improving the efficiency of PDT treatment and solving the problem of tumor recurrence after PDT treatment.

On the other hand, TAMs have been reported to make tumors resistant to radiotherapy with a poor prognosis (Barker et al., 2015). After radiotherapy, increased TAMs and secreted growth factors can enhance tumor cell proliferation, invasion, and metastasis (Tsai et al., 2007). The results have shown that nanodrugs can repolarization TAMs and reverse polarize protumor M2-type TAMs into antitumor M1-type TAMs (Rodell et al., 2018). Qin et al. constructed a Bi doped mesoporous upconversion nanophosphor ($Na_{0.2}Bi_{0.8}O_{0.35}F_{1.91}$:20%Yb,2%Er), which were simultaneously loaded with DOX, a chemotherapy drug, and combined with radiotherapy for the treatment of tumors (**Figure 12B**) (Qin et al., 2020). Co-doping of bismuth ions (Bi ions) in UCNP can enhance UCL, thus Bi-doped UCNP can be used for *in vivo* computed tomography/positron emission tomography/upconversion fluorescence three-mode imaging and radiosensitizer (Lei et al., 2017; Li et al., 2019b; Liu et al., 2019). The radiosensitizer UCNP is combined with chemotherapy drug DOX to enhance the radiation effect, induce tumor ICD, and make protumor M2-type macrophages polarized to antitumor M1-type macrophages. In addition, after UCNP-DOX and X-ray treatment, tumor tissue CD4/CD8 markers showed a large number of CD8 positive T killer cells by immunofluorescence, again confirming the activation of immune effects. The combination of UCNP-DOX and X-ray with three modes of imaging and three treatment methods showed a strong tumor

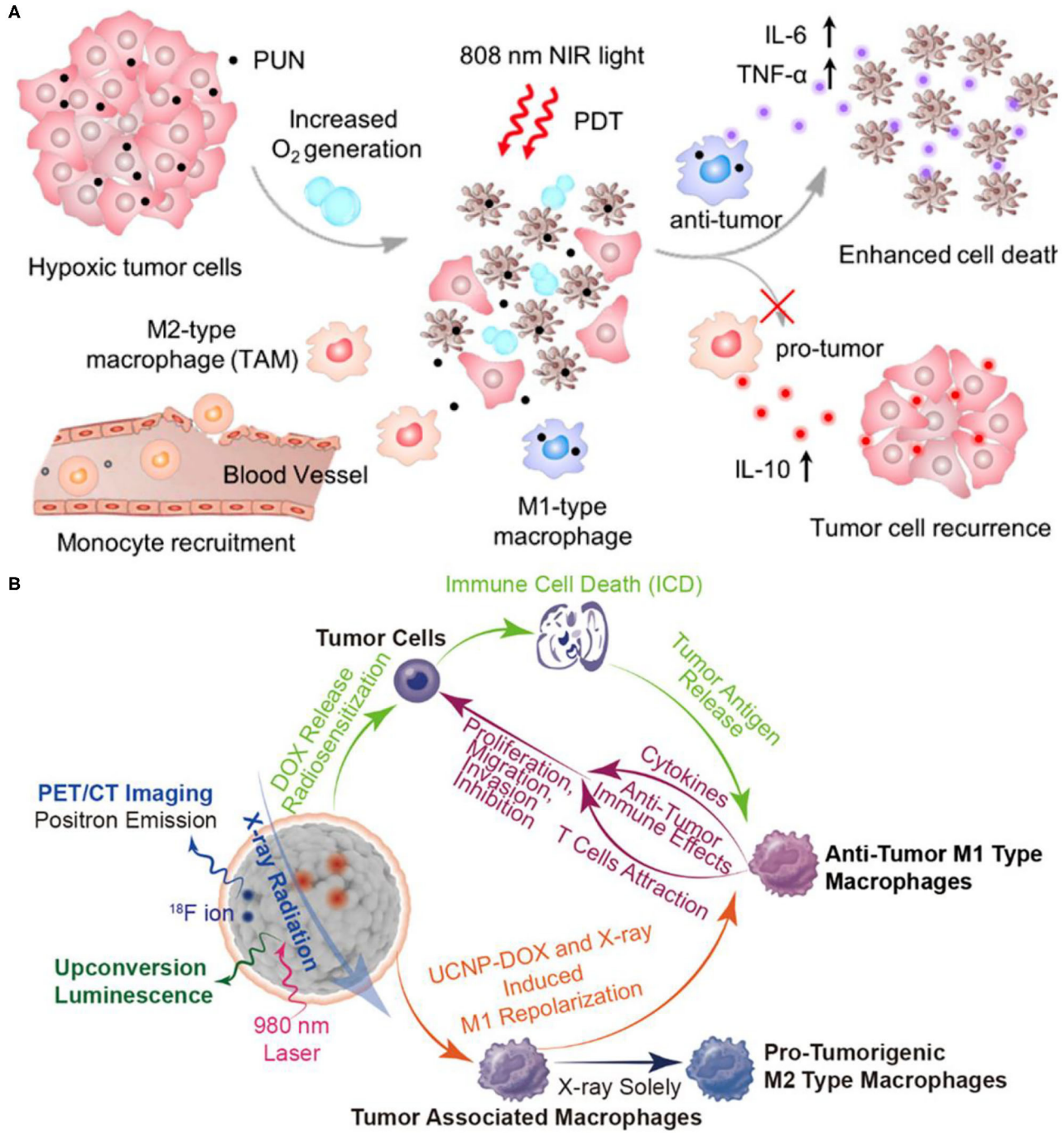

FIGURE 12 | (A) Scheme of improved therapy by attenuating hypoxia status and reprogramming tumor-associated macrophages (TAMs) from M2 to M1 phenotype to inhibit the recurrence of tumor cells toward immunotherapy during the post-PDT period. Copyright 2018, American Chemical Society (Ai et al., 2018). **(B)** Mesoporous Bi-Containing radiosensitizer loading with DOX to repolarize tumor-associated macrophages and elicit immunogenic tumor cell death to inhibit tumor progression. Copyright 2020, American Chemical Society (Qin et al., 2020).

inhibition effect. This work promotes the transformation of radiotherapy from local tumor treatment to systemic treatment, and lays the foundation for the ultimate inhibition of tumor metastasis.

CONCLUTION AND OUTLOOK

Taken together, we summarized the application of UCNPs-based tumor photoimmunotherapy. It has been demonstrated that

UNCPs-based PDT can induce ICD, promote dendritic cells maturation, and activate tumor specific immune response. Especially, the combination of UNCPs with various immunity strategies can overcome the limitations of single therapy, which can not only eliminate the primary tumor, but also inhibit the growth of metastatic or recurrent distal tumor.

UCNPs combined with immunotherapy has improved the therapeutic effect of tumor, but it still has challenges and room for growth as detailed below.

First, optimizing energy utilization rate of UCNPs can not only reduce the toxicity from dosage, but also improve the therapeutic effect of nanoparticles. UCNPs are usually combined with PS to produce ROS (He et al., 2017; Shi et al., 2020). However, most PSs can only absorb single emission light by UCNPs with low energy utilization rate. When two PSs excited by different wavelengths were modified to UCNPs, not only the energy utilization rate would be improved, but also more ROS could be produced to enhance the therapeutic effect of tumor. On the other hand, it is also considerable to improve the quantum efficiency of UCNPs by improving the symmetry of crystal field, laser annealing, and doping concentration and surface interface to gain higher energy utilization rate (Tan et al., 2011; Chung et al., 2012).

Second, the most immune checkpoint inhibitors were administered intravenously at a later stage, which act on immune cells universally rather than specific tumor antigens with the risks of inducing side effects (Shao et al., 2020). Linking UCNPs with immune checkpoint inhibitors together in a nanoplatform to release immune checkpoint inhibitors to tumor site through the enhanced permeability and retention (EPR) effect would be a promising strategy to improve the therapeutic efficacy of immunotherapy and reduce immune-related side effects (Li et al., 2019a).

Third, at present, there is no systematic biosafety evaluation on the dispersion, excretion, toxicity, stability, surface loading, and dosage of UCNPs *in vivo* and *in vitro*. In particular, there are few reports on the distribution sites of UCNPs in cells. The potential distribution sites of UCNPs include plasma membrane, lysosome, and cytoplasm, but few in nucleus, endoplasmic reticulum, or mitochondria. On the other hand, the endocytosis of UCNP is complex, involving many factors, such as electrical properties, ligands, culture conditions, and so on (Jin et al., 2011; Zhou et al., 2012). Targeting technology can change the biodistribution sites *in vivo*, especially the cumulative proportion in tumors (Xiong et al., 2009; Yao et al., 2020). The distribution site and UCNPs need further investigation.

Forth, for the distribution of UCNPs *in vivo* after intravenous injection, except for some ultra-small nanoparticles, regardless of the size and surface ligands of UCNPs, the final deposition sites are mainly liver and spleen. The distribution of these organs is related to the injection dose ratio and the size, shape, surface ligands, and time after injection of UCNPs. Recognition and clearance of nanomaterials by cells in the liver, spleen, and reticuloendothelial system may reduce the drug concentration in tumor sites, and shorter blood circulation is also a challenge to be overcome. At present, ligands such as PEG have been widely used to prolong blood circulation (Moghimi et al., 2001). On the other hand, arterial injection, as a method that has been studied for a long time in clinical medicine, provides an opportunity to improve the treatment efficiency of UCNPs by improving UCNPs uptake of tumor.

Fifth, size of nanoparticles has a great influence on its excretion efficiency and toxicity (Cheng et al., 2011). In general, smaller sizes can reduce the *in vivo* elimination time of UCNPs through renal excretion. However, the ultra-small size (such as <5 nm) UCNPs have poor UCL signal due to lattice defects. However, large UCNPs cannot be eliminated by kidney, and the elimination way is mainly through biliary tract, but this way needs more time and has hepatotoxicity. Considering the complexity of UCNPs scavenging process, in addition to the development of UCNPs with both luminous efficiency and scavenging efficiency, more studies on the excretion time of UCNPs may be needed.

Finally, the researches of tumor therapeutic nanoplatforms have sprung up in an endless stream. Most of the current tumor researches are based on mouse model, which still have some differences with human tumor. Some nanodrugs have obvious effect in mouse model, but not in human body. In addition, immunotherapy has shown excellent inhibitory effect on metastatic and recurrent tumors, however, further study is needed about controlling the dosage of immunostimulants. Excessive immune reaction can cause severe damage to the immune system of the patient and even the normal tissues.

The occurrence of tumor is not overnight. And the factors involved are complex and diverse. Similarly, the treatment of cancer cannot be achieved overnight, we need to step out of the dilemma and achieve greater breakthrough. The limitation of single therapy cannot meet our demand for cancer treatment, and the combination therapy is a general trend in the further. How to build a simple and functional treatment nanoplatform needs more enthusiasm and effort of researchers.

AUTHOR CONTRIBUTIONS

All authors listed have made a substantial, direct and intellectual contribution to the work, and approved it for publication.

FUNDING

This project was funded by the National Natural Science Foundation of China (51872263), Taishan Scholars Project of Shandong Province (ts20190911), and the Open Funds of the State Key Laboratory of Rare Earth Resource Utilization (RERU2020005).

REFERENCES

Adamus, T., and Kortylewski, M. (2018). The revival of CpG oligonucleotide-based cancer immunotherapies. *Wspolczesna Onkol.* 2018, 56–60. doi: 10.5114/wo.2018.73887

Ai, X., Hu, M., Wang, Z., Lyu, L., Zhang, W., Li, J., et al. (2018). Enhanced cellular ablation by attenuating hypoxia status and reprogramming tumor-associated macrophages via NIR light-responsive upconversion nanocrystals. *Bioconjugate Chem.* 29, 928–938. doi: 10.1021/acs.bioconjchem.8b00068

Amir, Y., Ben-Ishay, E., Levner, D., Ittah, S., Abu-Horowitz, A., and Bachelet, I. (2014). Universal computing by DNA origami robots in a living animal. *Nat. Nanotechnol.* 9, 353–357. doi: 10.1038/nnano.2014.58

Anassi, E., and Ndefo, U. A. (2011). Sipuleucel-T (Provenge) injection the first immunotherapy agent (Vaccine) for hormone-refractory prostate cancer. *P T.* 36, 197–202.

Ankenbruck, N., Courtney, T., Naro, Y., and Deiters, A. (2018). Optochemical control of biological processes in cells and animals. *Angew. Chem. Int. Ed.* 57, 2768–2798. doi: 10.1002/anie.201700171

Antaris, A. L., Chen, H., Diao, S., Ma, Z., Zhang, Z., Zhu, S., et al. (2017). A high quantum yield molecule-protein complex fluorophore for near-infrared II imaging. *Nat. Commun.* 8:15269. doi: 10.1038/ncomms15269

Banchereau, J., Briere, F., Caux, C., Davoust, J., Lebecque, S., Liu, Y., et al. (2000). Immunobiology of dendritic cells. *Annu. Rev. Immunol.* 18, 767–811. doi: 10.1146/annurev.immunol.18.1.767

Bao, Y., Zhang, Z., Cao, B., Liu, Y., Shang, J., Yang, Y., et al. (2019). Energy transfer from Er to Nd ions by the thermal effect and promotion of the photocatalysis of the $NaYF_4$:Yb,Er,Nd/$W_{18}O_{49}$ heterostructure. *Nanoscale* 11, 7433–7439. doi: 10.1039/C9NR00409B

Barker, H. E., Paget, J. T. E., Khan, A. A., and Harrington, K. J. (2015). The tumour microenvironment after radiotherapy: mechanisms of resistance and recurrence. *Nat. Rev. Cancer* 15, 409–425. doi: 10.1038/nrc3958

Beatty, G. L., and Gladney, W. L. (2015). Immune escape mechanisms as a guide for cancer immunotherapy. *Clin. Cancer Res.* 21, 687–692. doi: 10.1158/1078-0432.CCR-14-1860

Berd, D. (2004). M-Vax: an autologous, hapten-modified for human cancer. *Expert Rev. Vaccines* 3, 521–527. doi: 10.1586/14760584.3.5.521

Beug, S. T., Tang, V. A., LaCasse, E. C., Cheung, H. H., Beauregard, C. E., Brun, J., et al. (2014). Smac mimetics and innate immune stimuli synergize to promote tumor death. *Nat. Biotechnol.* 32, 182–190. doi: 10.1038/nbt.2806

Bigall, N. C., Parak, W. J., and Dorfs, D. (2012). Fluorescent, magnetic and plasmonic - hybrid multifunctional colloidal nano objects. *Nano Today* 7, 282–296. doi: 10.1016/j.nantod.2012.06.007

Bouchie, A. (2013). First microRNA mimic enters clinic. *Nat. Biotechnol.* 31, 577–577. doi: 10.1038/nbt0713-577

Brodin, J. D., Sprangers, A. J., McMillan, J. R., and Mirkin, C. A. (2015). DNA-mediated cellular delivery of functional enzymes. *J. Am. Chem. Soc.* 137, 14838–14841. doi: 10.1021/jacs.5b09711

Cameron, F., Whiteside, G., and Perry, C. (2011). Ipilimumab. *Drugs* 71, 1093–1104. doi: 10.2165/11594010-000000000-00000

Castano, A. P., Mroz, P., and Hamblin, M. R. (2006). Photodynamic therapy and anti-tumour immunity. *Nat. Rev. Cancer* 6, 535–545. doi: 10.1038/nrc1894

Chang, M., Hou, Z., Wang, M., Wang, M., Dang, P., Liu, J., et al. (2020). Cu_2 MoS_4/Au heterostructures with enhanced catalase-like activity and photoconversion efficiency for primary/metastatic tumors eradication by phototherapy-induced immunotherapy. *Small* 16:1907146. doi: 10.1002/smll.201907146

Chang, M., Wang, M., Wang, M., Shu, M., Ding, B., Li, C., et al. (2019). A multifunctional cascade bioreactor based on hollow-structured Cu_2MoS_4 for synergetic cancer chemo-dynamic therapy/starvation therapy/phototherapy/immunotherapy with remarkably enhanced efficacy. *Adv. Mater.* 31:1905271. doi: 10.1002/adma.201905271

Chatterjee, S., Lesniak, W. G., and Nimmagadda, S. (2017). Noninvasive imaging of immune checkpoint ligand PD-L1 in tumors and metastases for guiding immunotherapy. *Mol. Imaging* 16:153601211771845. doi: 10.1177/1536012117718459

Chen, T. T., Tian, X., Liu, C. L., Ge, J., Chu, X., and Li, Y. (2015). Fluorescence activation imaging of cytochrome c released from mitochondria using aptameric nanosensor. *J. Am. Chem. Soc.* 137, 982–989. doi: 10.1021/ja511988w

Chen, W., Glackin, C. A., Horwitz, M. A., and Zink, J. I. (2019). Nanomachines and other caps on mesoporous silica nanoparticles for drug delivery. *Acc. Chem. Res.* 52, 1531–1542. doi: 10.1021/acs.accounts.9b00116

Cheng, L., Wang, C., Feng, L., Yang, K., and Liu, Z. (2014). Functional nanomaterials for phototherapies of cancer. *Chem. Rev.* 114, 10869–10939. doi: 10.1021/cr400532z

Cheng, L., Yang, K., Shao, M., Lu, X., and Liu, Z. (2011). *In vivo* pharmacokinetics, long-term biodistribution and toxicology study of functionalized upconversion nanoparticles in mice. *Nanomedicine* 6, 1327–1340. doi: 10.2217/nnm.11.56

Cheng, X., Sun, R., Yin, L., Chai, Z., Shi, H., and Gao, M. (2017). Light-triggered assembly of gold nanoparticles for photothermal therapy and photoacoustic imaging of tumors *in vivo*. *Adv. Mater.* 29:1604894. doi: 10.1002/adma.201604894

Chu, H., Zhao, J., Mi, Y., Di, Z., and Li, L. (2019). NIR-light-mediated spatially selective triggering of anti-tumor immunity via upconversion nanoparticle-based immunodevices. *Nat. Commun.* 10:2839. doi: 10.1038/s41467-019-10847-0

Chung, J. H., Ryu, J. H., Eun, J. W., Lee, J. H., Lee, S. Y., Heo, T. H., et al. (2012). High enhancement of green upconversion luminescence of Li+/Er3+/Yb3+ tri-doped $CaMoO_4$. *Mater. Chem. Phys.* 134, 695–699. doi: 10.1016/j.matchemphys.2012.03.052

Dariavach, P., Mattéi, M.-G., Golstein, P., and Lefranc, M.-P. (1988). Human Ig superfamily CTLA-4 gene: chromosomal localization and identity of protein sequence between murine and human CTLA-4 cytoplasmic domains. *Eur. J. Immunol.* 18, 1901–1905. doi: 10.1002/eji.1830181206

Deng, H., Zhou, Z., Yang, W., Lin, L., sen, Wang, S., Niu, G., et al. (2020). Endoplasmic reticulum targeting to amplify immunogenic cell death for cancer immunotherapy. *Nano Lett.* 20, 1928–1933. doi: 10.1021/acs.nanolett.9b05210

Desgranges, E., Marzi, S., Moreau, K., Romby, P., and Caldelari, I. (2019). Noncoding RNA. *Microbiol. Spectrum* 7, 1–15. doi: 10.1128/microbiolspec.GPP3-0038-2018

Di, Z., Liu, B., Zhao, J., Gu, Z., Zhao, Y., and Li, L. (2020). An orthogonally regulatable DNA nanodevice for spatiotemporally controlled biorecognition and tumor treatment. *Sci. Adv.* 6:eaba9381. doi: 10.1126/sciadv.aba9381

Diao, S., Blackburn, J. L., Hong, G., Antaris, A. L., Chang, J., Wu, J. Z., et al. (2015a). Fluorescence imaging *in vivo* at wavelengths beyond 1500 nm. *Angew. Chem. Int. Ed.* 54, 14758–14762. doi: 10.1002/anie.201507473

Diao, S., Hong, G., Antaris, A. L., Blackburn, J. L., Cheng, K., Cheng, Z., et al. (2015b). Biological imaging without autofluorescence in the second near-infrared region. *Nano Res.* 8, 3027–3034. doi: 10.1007/s12274-015-0808-9

Ding, B., Shao, S., Yu, C., Teng, B., Wang, M., Cheng, Z., et al. (2018). Large-pore mesoporous-silica-coated upconversion nanoparticles as multifunctional immunoadjuvants with ultrahigh photosensitizer and antigen loading efficiency for improved cancer photodynamic immunotherapy. *Adv. Mater.* 30:1802479. doi: 10.1002/adma.201802479

Ding, B., Yu, C., Li, C., Deng, X., Ding, J., Cheng, Z., et al. (2017). Cis-Platinum pro-drug-attached $CuFeS_2$ nanoplates for *in vivo* photothermal/photoacoustic imaging and chemotherapy/photothermal therapy of cancer. *Nanoscale* 9, 16937–16949. doi: 10.1039/C7NR04166G

Dong, H., Sun, L. D., and Yan, C. H. (2015). Energy transfer in lanthanide upconversion studies for extended optical applications. *Chem. Soc. Rev.* 44, 1608–1634. doi: 10.1039/C4CS00188E

Dranoff, G. (2004). Cytokines in cancer pathogenesis and cancer therapy. *Nat. Rev. Cancer* 4, 11–22. doi: 10.1038/nrc1252

Duan, X., Chan, C., and Lin, W. (2019). Nanoparticle-mediated immunogenic cell death enables and potentiates cancer immunotherapy. *Angew. Chem. Int. Ed.* 58, 670–680. doi: 10.1002/anie.201804882

Feng, Y., Wu, Y., Zuo, J., Tu, L., Que, I., Chang, Y., et al. (2019). Assembly of upconversion nanophotosensitizer *in vivo* to achieve scatheless real-time imaging and selective photodynamic therapy. *Biomaterials* 201, 33–41. doi: 10.1016/j.biomaterials.2019.02.015

Flanagan, K., Moroziewicz, D., Kwak, H., Hörig, H., and Kaufman, H. L. (2004). The lymphoid chemokine CCL21 costimulates naïve T cell expansion and Th1 polarization of non-regulatory CD4+ T cells. *Cell. Immunol.* 231, 75–84. doi: 10.1016/j.cellimm.2004.12.006

Francisco, L. M., Sage, P. T., and Sharpe, A. H. (2010). The PD-1 pathway in tolerance and autoimmunity. *Immunol. Rev.* 236, 219–242. doi: 10.1111/j.1600-065X.2010.00923.x

Gai, S., Li, C., Yang, P., and Lin, J. (2014). Recent progress in rare earth micro/nanocrystals: soft chemical synthesis, luminescent properties, and biomedical applications. *Chem. Rev.* 114, 2343–2389. doi: 10.1021/cr4001594

Gai, S., Yang, G., Yang, P., He, F., Lin, J., Jin, D., et al. (2018). Recent advances in functional nanomaterials for light–triggered cancer therapy. *Nano Today* 19, 146–187. doi: 10.1016/j.nantod.2018.02.010

Gao, F., Sun, M., Xu, L., Liu, L., Kuang, H., and Xu, C. (2017). Biocompatible cup-shaped nanocrystal with ultrahigh photothermal efficiency as tumor therapeutic agent. *Adv. Funct. Mater.* 27:1700605. doi: 10.1002/adfm.201700605

Garg, A. D., and Agostinis, P. (2014). ER stress, autophagy and immunogenic cell death in photodynamic therapy-induced anti-cancer immune responses. *Photochem. Photobiol. Sci.* 13, 474–487. doi: 10.1039/C3PP50333J

Garg, A. D., Dudek, A. M., and Agostinis, P. (2013). Cancer immunogenicity, danger signals, and DAMPs: what, when, and how? *BioFactors* 39, 355–367. doi: 10.1002/biof.1125

Georgoudaki, A. M., Prokopec, K. E., Boura, V. F., Hellqvist, E., Sohn, S., Östling, J., et al. (2016). Reprogramming tumor-associated macrophages by antibody targeting inhibits cancer progression and metastasis. *Cell Rep.* 15, 2000–2011. doi: 10.1016/j.celrep.2016.04.084

Gordon Steel, G., and Peckham, M. J. (1979). Exploitable mechanisms in combined radiotherapy-chemotherapy: the concept of additivity. *Int. J. Radiat. Oncol. Biol. Phys.* 5, 85–91. doi: 10.1016/0360-3016(79)90044-0

Gordon, S., and Martinez, F. O. (2010). Alternative activation of macrophages: mechanism and functions. *Immunity* 32, 593–604. doi: 10.1016/j.immuni.2010.05.007

Gu, Y., Guo, Z., Yuan, W., Kong, M., Liu, Y., Liu, Y., et al. (2019). High-sensitivity imaging of time-domain near-infrared light transducer. *Nat. Photonics* 13, 525–531. doi: 10.1038/s41566-019-0437-z

Guryev, E. L., Volodina, N. O., Shilyagina, N. Y., Gudkov, S. V., Balalaeva, I. V., Volovetskiy, A. B., et al. (2018). Radioactive (90Y) upconversion nanoparticles conjugated with recombinant targeted toxin for synergistic nanotheranostics of cancer. *Proc. Natl. Acad. Sci. U.S.A.* 115, 9690–9695. doi: 10.1073/pnas.1809258115

He, L., Brasino, M., Mao, C., Cho, S., Park, W., Goodwin, A. P., et al. (2017). DNA-assembled core-satellite upconverting-metal-organic framework nanoparticle superstructures for efficient photodynamic therapy. *Small* 13:1700504. doi: 10.1002/smll.201700504

Henderson, B. W., and Dougherty, T. J. (1992). How does photodynamic therapy work? *Photochem. Photobiol.* 55, 145–157. doi: 10.1111/j.1751-1097.1992.tb04222.x

Hokland, P., Hokland, M., and Cotter, F. (2018). The Nobel Prize for Medicine awarded for cancer therapy by inhibition of negative immune regulation. *Br. J. Haematol.* 183, 698–700. doi: 10.1111/bjh.15694

Homey, B., Müller, A., and Zlotnik, A. (2002). Chemokines: agents for the immunotherapy of cancer? *Nat. Rev. Immunol.* 2, 175–184. doi: 10.1038/nri748

Hong, G., Diao, S., Chang, J., Antaris, A. L., Chen, C., Zhang, B., et al. (2014). Through-skull fluorescence imaging of the brain in a new near-infrared window. *Nat. Photonics* 8, 723–730. doi: 10.1038/nphoton.2014.166

Hou, Z., Deng, K., Li, C., Deng, X., Lian, H., Cheng, Z., et al. (2016). 808 nm Light-triggered and hyaluronic acid-targeted dual-photosensitizers nanoplatform by fully utilizing Nd^{3+}-sensitized upconversion emission with enhanced anti-tumor efficacy. *Biomaterials* 101, 32–46. doi: 10.1016/j.biomaterials.2016.05.024

Hou, Z., Deng, K., Wang, M., Liu, Y., Chang, M., Huang, S., et al. (2019). Hydrogenated titanium oxide decorated upconversion nanoparticles: facile laser modified synthesis and 808 nm near-infrared light triggered phototherapy. *Chem. Mater.* 31, 774–784. doi: 10.1021/acs.chemmater.8b03762

Hu, F., Xu, S., and Liu, B. (2018a). Photosensitizers with aggregation-induced emission: materials and biomedical applications. *Adv. Mater.* 30:1801350. doi: 10.1002/adma.201801350

Hu, Q., Li, H., Wang, L., Gu, H., and Fan, C. (2019a). DNA nanotechnology-enabled drug delivery systems. *Chem. Rev.* 119, 6459–6506. doi: 10.1021/acs.chemrev.7b00663

Hu, Z., Ding, J., Ma, Z., Sun, R., Seoane, J. A., Scott Shaffer, J., et al. (2019b). Quantitative evidence for early metastatic seeding in colorectal cancer. *Nat. Genet.* 51, 1113–1122. doi: 10.1038/s41588-019-0423-x

Hu, Z., Ott, P. A., and Wu, C. J. (2018b). Towards personalized, tumour-specific, therapeutic vaccines for cancer. *Nat Rev Immunol* 18, 168–182. doi: 10.1038/nri.2017.131

Ikeda, H. (2016). T-cell adoptive immunotherapy using tumorinfiltrating T cells and genetically engineered TCR-T cells. *Int. Immunol.* 28, 349–353. doi: 10.1093/intimm/dxw022

Jin, F., Qi, J., Zhu, M., Liu, D., You, Y., Shu, G., et al. (2020). NIR-triggered sequentially responsive nanocarriers amplified cascade synergistic effect of chemo-photodynamic therapy with inspired antitumor immunity. *ACS Appl. Mater. Interfaces* 12, 32372–32387. doi: 10.1021/acsami.0c07503

Jin, J., Gu, Y.-J., Man, C. W.-Y., Cheng, J., Xu, Z., Zhang, Y., et al. (2011). Polymer-coated $NaYF_4$:Yb3+,Er3+ upconversion nanoparticles for charge-dependent cellular imaging. *ACS Nano* 5, 7838–7847. doi: 10.1021/nn201896m

Juarranz, Á., Jaén, P., Sanz-Rodríguez, F., Cuevas, J., and González, S. (2008). Photodynamic therapy of cancer. Basic principles and applications. *Clin. Transl. Oncol.* 10, 148–154. doi: 10.1007/s12094-008-0172-2

June, C. H., O'Connor, R. S., Kawalekar, O. U., Ghassemi, S., and Milone, M. C. (2018). CAR T cell immunotherapy for human cancer. *Science* 359, 1361–1365. doi: 10.1126/science.aar6711

Kalos, M., and June, C. H. (2013). Adoptive T cell transfer for cancer immunotherapy in the era of synthetic biology. *Immunity* 39, 49–60. doi: 10.1016/j.immuni.2013.07.002

Kapsenberg, M. L. (2003). Dendritic-cell control of pathogen-driven T-cell polarization. *Nat. Rev. Immunol.* 3, 984–993. doi: 10.1038/nri1246

Kawasaki, T., and Kawai, T. (2014). Toll-like receptor signaling pathways. *Front. Immunol.* 5:461. doi: 10.3389/fimmu.2014.00461

Kinjyo, I., Qin, J., Tan, S.-Y., Wellard, C. J., Mrass, P., Ritchie, W., et al. (2015). Real-time tracking of cell cycle progression during CD8+ effector and memory T-cell differentiation. *Nat. Commun.* 6:6301. doi: 10.1038/ncomms7301

Kobayashi, H., and Choyke, P. L. (2019). Near-infrared photoimmunotherapy of cancer. *Acc. Chem. Res.* 52, 2332–2339. doi: 10.1021/acs.accounts.9b00273

Kowalik, L., and Chen, J. K. (2017). Illuminating developmental biology through photochemistry. *Nat. Chem. Biol.* 13, 587–598. doi: 10.1038/nchembio.2369

Kuai, R., Yuan, W., Son, S., Nam, J., Xu, Y., Fan, Y., et al. (2018). Elimination of established tumors with nanodisc-based combination chemoimmunotherapy. *Sci. Adv.* 4:eaao1736. doi: 10.1126/sciadv.aao1736

Lan, G., Ni, K., and Lin, W. (2019). Nanoscale metal–organic frameworks for phototherapy of cancer. *Coord. Chem. Rev.* 379, 65–81. doi: 10.1016/j.ccr.2017.09.007

Lechner, M. G., Russell, S. M., Bass, R. S., and Epstein, A. L. (2011). Chemokines, costimulatory molecules and fusion proteins for the immunotherapy of solid tumors. *Immunotherapy* 3, 1317–1340. doi: 10.2217/imt.11.115

Lee, J. E., Lee, N., Kim, T., Kim, J., and Hyeon, T. (2011). Multifunctional mesoporous silica nanocomposite nanoparticles for theranostic applications. *Acc. Chem. Res.* 44, 893–902. doi: 10.1021/ar2000259

Lee, K. Y., Seow, E., Zhang, Y., and Lim, Y. C. (2013). Targeting CCL21-folic acid-upconversion nanoparticles conjugates to folate receptor-α expressing tumor cells in an endothelial-tumor cell bilayer model. *Biomaterials* 34, 4860–4871. doi: 10.1016/j.biomaterials.2013.03.029

Lei, P., An, R., Yao, S., Wang, Q., Dong, L., Xu, X., et al. (2017). Ultrafast synthesis of novel hexagonal phase $NaBiF_4$ upconversion nanoparticles at room temperature. *Adv. Mater.* 29:1700505. doi: 10.1002/adma.201700505

Li, L., Tong, R., Chu, H., Wang, W., Langer, R., and Kohane, D. S. (2014). Aptamer photoregulation *in vivo*. *Proc. Natl. Acad. Sci. U.S.A.* 111, 17099–17103. doi: 10.1073/pnas.1420105111

Li, Q., Zhang, D., Zhang, J., Jiang, Y., Song, A., Li, Z., et al. (2019a). A three-in-one immunotherapy nanoweapon via cascade-amplifying cancer-immunity cycle against tumor metastasis, relapse, and postsurgical regrowth. *Nano Lett.* 19, 6647–6657. doi: 10.1021/acs.nanolett.9b02923

Li, Y., Liu, J., Qin, X., Deng, Y., Zhang, J., and Sun, Y. (2019b). Ultrafast synthesis of fluorine-18 doped bismuth based upconversion nanophosphors for tri-modal CT/PET/UCL imaging *in vivo*. *Chem. Commun.* 55, 7259–7262. doi: 10.1039/C9CC02677K

Lin, B., Liu, J., Wang, Y., Yang, F., Huang, L., and Lv, R. (2020). Enhanced upconversion luminescence-guided synergistic antitumor therapy based on photodynamic therapy and immune checkpoint blockade. *Chem. Mater.* 32, 4627–4640. doi: 10.1021/acs.chemmater.0c01031

Liu, B., Li, C., Yang, P., Hou, Z., and Lin, J. (2017). 808-nm-light-excited lanthanide-doped nanoparticles: rational design, luminescence control and theranostic applications. *Adv. Mater.* 29:1605434. doi: 10.1002/adma.201605434

Liu, J., Deng, Y., Qin, X., Li, B., Zhang, J., Xu, Y., et al. (2019). Ultrafast synthesizing bismuth mesoporous nanolitchi radiosensitizer loading high dose DOX for CT-guided enhanced chemoradiotherapy. *ACS Appl. Mater. Interfaces* 11, 42932–42942. doi: 10.1021/acsami.9b13647

Liu, J., Liu, Y., Bu, W., Bu, J., Sun, Y., Du, J., et al. (2014). Ultrasensitive nanosensors based on upconversion nanoparticles for selective hypoxia imaging *in vivo* upon near-infrared excitation. *J. Am. Chem. Soc.* 136, 9701–9709. doi: 10.1021/ja5042989

Lu, K., He, C., and Lin, W. (2014). Nanoscale metal-organic framework for highly effective photodynamic therapy of resistant head and neck cancer. *J. Am. Chem. Soc.* 136, 16712–16715. doi: 10.1021/ja508679h

Lu, K., He, C., and Lin, W. (2015). A chlorin-based nanoscale metal-organic framework for photodynamic therapy of colon cancers. *J. Am. Chem. Soc.* 137, 7600–7603. doi: 10.1021/jacs.5b04069

Ma, Y., Zhang, Y., Li, X., Zhao, Y., Li, M., Jiang, W., et al. (2019). Near-infrared II phototherapy induces deep tissue immunogenic cell death and potentiates cancer immunotherapy. *ACS Nano* 13, 11967–11980. doi: 10.1021/acsnano.9b06040

Mai, H. X., Zhang, Y. W., Si, R., Yan, Z. G., Sun, L. D., You, L. P., et al. (2006). High-quality sodium rare-earth fluoride nanocrystals: controlled synthesis and optical properties. *J. Am. Chem. Soc.* 128, 6426–6436. doi: 10.1021/ja060212h

Mall, S., Yusufi, N., Wagner, R., Klar, R., Bianchi, H., Steiger, K., et al. (2016). Immuno-PET imaging of engineered human T cells in tumors. *Cancer Res.* 76, 4113–4123. doi: 10.1158/0008-5472.CAN-15-2784

Mao, D., Hu, F., Yi, Z., Kenry, K., Xu, S., Yan, S., et al. (2020). AIEgen-coupled upconversion nanoparticles eradicate solid tumors through dual-mode ROS activation. *Sci. Adv.* 6:eabb2712. doi: 10.1126/sciadv.abb2712

Mashino, K., Sadanaga, N., Yamaguchi, H., Tanaka, F., Ohta, M., Shibuta, K., et al. (2002). Expression of chemokine receptor CCR7 is associated with lymph node metastasis of gastric carcinoma. *Cancer Res.* 62, 2937–2941.

Maude, S. L., Frey, N., Shaw, P. A., Aplenc, R., Barrett, D. M., Bunin, N. J., et al. (2014). Chimeric antigen receptor T cells for sustained remissions in leukemia. *N. Engl. J. Med.* 371, 1507–1517. doi: 10.1056/NEJMoa1407222

Mazumder, A., and Rosenberg, S. A. (1984). Successful immunotherapy of natural killer-resistant established pulmonary melanoma metastases by the intravenous adoptive transfer of syngeneic lymphocytes activated *in vitro* by interleukin 2. *J. Exp. Med.* 159, 495–507. doi: 10.1084/jem.159.2.495

Moghimi, S. M., Hunter, A. C., and Murray, J. C. (2001). Long-circulating and target-specific nanoparticles: theory to practice. *Pharmacol. Rev.* 53, 283–318.

Morgan, R. A., Yang, J. C., Kitano, M., Dudley, M. E., Laurencot, C. M., and Rosenberg, S. A. (2010). Case report of a serious adverse event following the administration of t cells transduced with a chimeric antigen receptor recognizing ERBB2. *Mol. Ther.* 18, 843–851. doi: 10.1038/mt.2010.24

Mosser, D. M. (2003). The many faces of macrophage activation. *J. Leukocyte Biol.* 73, 209–212. doi: 10.1189/jlb.0602325

Pardoll, D. M. (2012). The blockade of immune checkpoints in cancer immunotherapy. *Nat. Rev. Cancer* 12, 252–264. doi: 10.1038/nrc3239

Park, J., Jiang, Q., Feng, D., Mao, L., and Zhou, H. C. (2016). Size-controlled synthesis of porphyrinic metal-organic framework and functionalization for targeted photodynamic therapy. *J. Am. Chem. Soc.* 138, 3518–3525. doi: 10.1021/jacs.6b00007

Qian, J., and Tang, B. Z. (2017). AIE luminogens for bioimaging and theranostics: from organelles to animals. *Chem* 3, 56–91. doi: 10.1016/j.chempr.2017.05.010

Qin, X., Liu, J., Xu, Y., Li, B., Cheng, J., Wu, X., et al. (2020). Mesoporous Bi-containing radiosensitizer loading with DOX to repolarize tumor-associated macrophages and elicit immunogenic tumor cell death to inhibit tumor progression. *ACS Appl. Mater. Interfaces* 12, 31225–31234. doi: 10.1021/acsami.0c08074

Quail, D. F., and Joyce, J. A. (2013). Microenvironmental regulation of tumor progression and metastasis. *Nat. Med.* 19, 1423–1437. doi: 10.1038/nm.3394

Rabie, H., Zhang, Y., Pasquale, N., Lagos, M. J., Batson, P. E., and Lee, K. (2019). NIR biosensing of neurotransmitters in stem cell-derived neural interface using advanced core–shell upconversion nanoparticles. *Adv. Mater.* 31:1806991. doi: 10.1002/adma.201806991

Randolph, G. J., Angeli, V., and Swartz, M. A. (2005). Dendritic-cell trafficking to lymph nodes through lymphatic vessels. *Nat. Rev. Immunol.* 5, 617–628. doi: 10.1038/nri1670

Reyes-Reyes, E. M., Teng, Y., and Bates, P. J. (2010). A new paradigm for aptamer therapeutic AS1411 Action: uptake by macropinocytosis and its stimulation by a nucleolin-dependent mechanism. *Cancer Res.* 70, 8617–8629. doi: 10.1158/0008-5472.CAN-10-0920

Robbins, P. F., Morgan, R. A., Feldman, S. A., Yang, J. C., Sherry, R. M., Dudley, M. E., et al. (2011). Tumor regression in patients with metastatic synovial cell sarcoma and melanoma using genetically engineered lymphocytes reactive with NY-ESO-1. *J. Clin. Oncol.* 29, 917–924. doi: 10.1200/JCO.2010.32.2537

Rodell, C. B., Arlauckas, S. P., Cuccarese, M. F., Garris, C. S., Li, R., Ahmed, M. S., et al. (2018). TLR7/8-agonist-loaded nanoparticles promote the polarization of tumour-associated macrophages to enhance cancer immunotherapy. *Nat. Biomed. Eng.* 2, 578–588. doi: 10.1038/s41551-018-0236-8

Salaun, B., Coste, I., Rissoan, M.-C., Lebecque, S. J., and Renno, T. (2006). TLR3 can directly trigger apoptosis in human cancer cells. *J. Immunol.* 176, 4894–4901. doi: 10.4049/jimmunol.176.8.4894

Sang, W., Zhang, Z., Dai, Y., and Chen, X. (2019). Recent advances in nanomaterial-based synergistic combination cancer immunotherapy. *Chem. Soc. Rev.* 48, 3771–3810. doi: 10.1039/C8CS00896E

Seiwert, T. Y., Salama, J. K., and Vokes, E. E. (2007). The concurrent chemoradiation paradigm - general principles. *Nat. Clin. Pract. Oncol.* 4, 86–100. doi: 10.1038/ncponc0714

Shao, K., Singha, S., Clemente-Casares, X., Tsai, S., Yang, Y., and Santamaria, P. (2015). Nanoparticle-based immunotherapy for cancer. *ACS Nano* 9, 16–30. doi: 10.1021/nn5062029

Shao, Y., Liu, B., Di, Z., Zhang, G., Sun, L.-D., Li, L., et al. (2020). Engineering of upconverted metal–organic frameworks for near-infrared light-triggered combinational photodynamic/chemo-/immunotherapy against hypoxic tumors. *J. Am. Chem. Soc.* 142, 3939–3946. doi: 10.1021/jacs.9b12788

Sharma, P., and Allison, J. P. (2015). The future of immune checkpoint therapy. *Science* 348, 56–61. doi: 10.1126/science.aaa8172

Sharma, V., Verma, D., and Okram, G. S. (2020). Influence of surfactant, particle size and dispersion medium on surface plasmon resonance of silver nanoparticles. *J. Phys. Condens. Matter.* 32:145302. doi: 10.1088/1361-648X/ab601a

Sharman, W. M., Allen, C. M., and van Lier, J. E. (1999). Photodynamic therapeutics: basic principles and clinical applications. *Drug Discov.Today* 4, 507–517. doi: 10.1016/S1359-6446(99)01412-9

Shekarian, T., Valsesia-Wittmann, S., Caux, C., and Marabelle, A. (2015). Paradigm shift in oncology: targeting the immune system rather than cancer cells. *Mutagenesis* 30, 205–211. doi: 10.1093/mutage/geu073

Shi, Z., Zhang, K., Zada, S., Zhang, C., Meng, X., Yang, Z., et al. (2020). Upconversion nanoparticle-induced multimode photodynamic therapy based on a metal–organic framework/titanium dioxide nanocomposite. *ACS Appl. Mater. Interfaces* 12, 12600–12608. doi: 10.1021/acsami.0c01467

Siegel, R. L., Miller, K. D., and Jemal, A. (2019). *Cancer statistics*, 2019. *CA Cancer J. Clin.* 69, 7–34. doi: 10.3322/caac.21551

Steinman, R. M. (2012). Decisions about dendritic cells: past, present, and future. *Annu. Rev. Immunol.* 30, 1–22. doi: 10.1146/annurev-immunol-100311-102839

Sullivan, L. A., and Brekken, R. A. (2010). The VEGF family in cancer and antibody-based strategies for their inhibition. *mAbs* 2, 165–175. doi: 10.4161/mabs.2.2.11360

Sun, L., Wei, Z., Chen, H., Liu, J., Guo, J., Cao, M., et al. (2014). Folic acid-functionalized up-conversion nanoparticles: toxicity studies *in vivo* and *in vitro* and targeted imaging applications. *Nanoscale* 6, 8878–8883. doi: 10.1039/C4NR02312A

Takeuchi, H., Fujimoto, A., Tanaka, M., Yamano, T., Hsueh, E., and Hoon, D. S. B. (2004). CCL21 chemokine regulates chemokine receptor CCR7 bearing malignant melanoma cells. *Clin. Cancer Res.* 10, 2351–2358. doi: 10.1158/1078-0432.CCR-03-0195

Tan, M. C., Al-Baroudi, L., and Riman, R. E. (2011). Surfactant effects on efficiency enhancement of infrared-to-visible upconversion emissions of

$NaYF_4$:Yb-Er. *ACS Appl. Mater. Interfaces* 3, 3910–3915. doi: 10.1021/am200768u

Tang, M., Zhu, X., Zhang, Y., Zhang, Z., Zhang, Z., Mei, Q., et al. (2019). Near-infrared excited orthogonal emissive upconversion nanoparticles for imaging-guided on-demand therapy. *ACS Nano* 13, 10405–10418. doi: 10.1021/acsnano.9b04200

Teixeiro, E., Daniels, M. A., Hamilton, S. E., Schrum, A. G., Bragado, R., Jameson, S. C., et al. (2009). Different T cell receptor signals determine CD8+ memory versus effector development. *Science* 323, 502–505. doi: 10.1126/science.1163612

Tran, T.-H., Rastogi, R., Shelke, J., and Amiji, M. M. (2015). Modulation of macrophage functional polarity towards anti-inflammatory phenotype with plasmid DNA delivery in CD44 targeting hyaluronic acid nanoparticles. *Sci. Rep*. 5:16632. doi: 10.1038/srep16632

Tsai, C. S., Chen, F. H., Wang, C. C., Huang, H. L., Jung, S. M., Wu, C. J., et al. (2007). Macrophages from irradiated tumors express higher levels of iNOS, Arginase-I and COX-2, and promote tumor growth. *Int. J. Radiat. Oncol. Biol. Phys.* 68, 499–507. doi: 10.1016/j.ijrobp.2007.01.041

Vermaelen, K. (2019). Vaccine strategies to improve anti-cancer cellular immune responses. *Front. Immunol.* 10:8. doi: 10.3389/fimmu.2019.00008

Wang, D., Liu, B., Quan, Z., Li, C., Hou, Z., Xing, B., et al. (2017). New advances on the marrying of UCNPs and photothermal agents for imaging-guided diagnosis and the therapy of tumors. *J. Mater. Chem. B* 5, 2209–2230. doi: 10.1039/C6TB03117J

Wang, F., Wen, S., He, H., Wang, B., Zhou, Z., Shimoni, O., et al. (2018a). Microscopic inspection and tracking of single upconversion nanoparticles in living cells. *Light: Sci. Appl.* 7, 18006–18007. doi: 10.1038/lsa.2018.7

Wang, H., Wang, K., He, L., Liu, Y., Dong, H., and Li, Y. (2020a). Engineering antigen as photosensitiser nanocarrier to facilitate ROS triggered immune cascade for photodynamic immunotherapy. *Biomaterials* 244:119964. doi: 10.1016/j.biomaterials.2020.119964

Wang, H. W., Putt, M. E., Emanuele, M. J., Shin, D. B., Glatstein, E., Yodh, A. G., et al. (2004). Treatment-induced changes in tumor oxygenation predict photodynamic therapy outcome. *Cancer Res.* 64, 7553–7561. doi: 10.1158/0008-5472.CAN-03-3632

Wang, M., Chang, M., Chen, Q., Wang, D., Li, C., Hou, Z., et al. (2020b). Au_2Pt-PEG-Ce_6 nanoformulation with dual nanozyme activities for synergistic chemodynamic therapy / phototherapy. *Biomaterials* 252:120093. doi: 10.1016/j.biomaterials.2020.120093

Wang, M., Song, J., Zhou, F., Hoover, A. R., Murray, C., Zhou, B., et al. (2019a). NIR-Triggered phototherapy and immunotherapy via an antigen-capturing nanoplatform for metastatic cancer treatment. *Adv. Sci.* 6:1802157. doi: 10.1002/advs.201802157

Wang, M., Wang, D., Chen, Q., Li, C., Li, Z., and Lin, J. (2019b). Recent advances in glucose-oxidase-based nanocomposites for tumor therapy. *Small* 15:1903895. doi: 10.1002/smll.201903895

Wang, S., Huang, P., Nie, L., Xing, R., Liu, D., Wang, Z., et al. (2013). Single continuous wave laser induced photodynamic/plasmonic photothermal therapy using photosensitizer-functionalized gold nanostars. *Adv. Mater.* 25, 3055–3061. doi: 10.1002/adma.201204623

Wang, T., Wang, D., Yu, H., Feng, B., Zhou, F., Zhang, H., et al. (2018b). A cancer vaccine-mediated postoperative immunotherapy for recurrent and metastatic tumors. *Nat. Commun.* 9:1532. doi: 10.1038/s41467-018-03915-4

Wang, X., Li, X., Ito, A., Watanabe, Y., Sogo, Y., Tsuji, N. M., et al. (2016a). Stimulation of *in vivo* antitumor immunity with hollow mesoporous silica nanospheres. *Angew. Chem. Int. Ed.* 55, 1899–1903. doi: 10.1002/anie.201506179

Wang, X., Li, X., Yoshiyuki, K., Watanabe, Y., Sogo, Y., Ohno, T., et al. (2016b). Comprehensive mechanism analysis of mesoporous-silica-nanoparticle-induced cancer immunotherapy. *Adv. Healthcare Mater.* 5, 1169–1176. doi: 10.1002/adhm.201501013

Wimalachandra, D. C., Li, Y., Liu, J., Shikha, S., Zhang, J., Lim, Y. C., et al. (2019). Microfluidic-based immunomodulation of immune cells using upconversion nanoparticles in simulated blood vessel-tumor system. *ACS Appl. Mater. Interfaces* 11, 37513–37523. doi: 10.1021/acsami.9b15178

Wing, K., Onishi, Y., Prieto-Martin, P., Yamaguchi, T., Miyara, M., Fehervari, Z., et al. (2008). CTLA-4 control over $Foxp^{3+}$ regulatory T cell function. *Science* 322, 271–275. doi: 10.1126/science.1160062

Workenhe, S. T., Simmons, G., Pol, J. G., Lichty, B. D., Halford, W. P., and Mossman, K. L. (2014). Immunogenic HSV-mediated oncolysis shapes the antitumor immune response and contributes to therapeutic efficacy. *Mol. Ther.* 22, 123–131. doi: 10.1038/mt.2013.238

Xiang, J., Xu, L., Gong, H., Zhu, W., Wang, C., Xu, J., et al. (2015). Antigen-loaded upconversion nanoparticles for dendritic cell stimulation, tracking, and vaccination in dendritic cell-based immunotherapy. *ACS Nano* 9, 6401–6411. doi: 10.1021/acsnano.5b02014

Xiong, L.-Q., Chen, Z.-G., Yu, M.-X., Li, F.-Y., Liu, C., and Huang, C.-H. (2009). Synthesis, characterization, and *in vivo* targeted imaging of amine-functionalized rare-earth up-converting nanophosphors. *Biomaterials* 30, 5592–5600. doi: 10.1016/j.biomaterials.2009.06.015

Xu, J., Han, W., Yang, P., Jia, T., Dong, S., Bi, H., et al. (2018a). Tumor microenvironment-responsive mesoporous MnO_2 -coated upconversion nanoplatform for self-enhanced tumor theranostics. *Adv. Funct. Mater.* 28:1803804. doi: 10.1002/adfm.201803804

Xu, J., Xu, L., Wang, C., Yang, R., Zhuang, Q., Han, X., et al. (2017a). Near-infrared-triggered photodynamic therapy with multitasking upconversion nanoparticles in combination with checkpoint blockade for immunotherapy of colorectal cancer. *ACS Nano* 11, 4463–4474. doi: 10.1021/acsnano.7b00715

Xu, J., Yang, P., Sun, M., Bi, H., Liu, B., Yang, D., et al. (2017b). Highly emissive dye-sensitized upconversion nanostructure for dual-photosensitizer photodynamic therapy and bioimaging. *ACS Nano* 11, 4133–4144. doi: 10.1021/acsnano.7b00944

Xu, X., Lu, H., and Lee, R. (2020). Near infrared light triggered photo/immuno-therapy toward cancers. *Front Bioeng Biotechnol.* 8:488. doi: 10.3389/fbioe.2020.00488

Xu, X. L., Lu, K. J., Zhu, M. L., Du, Y. L., Zhu, Y. F., Zhang, N. N., et al. (2018b). Sialic acid-functionalized pH-triggered micelles for enhanced tumor tissue accumulation and active cellular internalization of orthotopic hepatocarcinoma. *ACS Appl. Mater. Interfaces* 10, 31903–31914. doi: 10.1021/acsami.8b09498

Yan, S., Zeng, X., Tang, Y., Liu, B., Wang, Y., and Liu, X. (2019). Activating antitumor immunity and antimetastatic effect through polydopamine-encapsulated core–shell upconversion nanoparticles. *Adv. Mater.* 31:1905825. doi: 10.1002/adma.201905825

Yang, D., Ma, P., Hou, Z., Cheng, Z., Li, C., and Lin, J. (2015). Current advances in lanthanide ion (Ln3+)-based upconversion nanomaterials for drug delivery. *Chem. Soc. Rev.* 44, 1416–1448. doi: 10.1039/C4CS00155A

Yang, F., Jin, H., Wang, J., Sun, Q., Yan, C., Wei, F., et al. (2016). "Adoptive Cellular Therapy (ACT) for Cancer Treatment," in *Progress in Cancer Immunotherapy*, ed S. Zhang (Dordrecht: Springer Netherlands), 169–239. doi: 10.1007/978-94-017-7555-7_4

Yang, T., Ke, H., Wang, Q., Tang, Y., Deng, Y., Yang, H., et al. (2017). Bifunctional tellurium nanodots for photo-induced synergistic cancer therapy. *ACS Nano* 11, 10012–10024. doi: 10.1021/acsnano.7b04230

Yao, X., Li, M., Li, B., Xue, C., Cai, K., Zhao, Y., et al. (2020). Tumor-targeted upconverting nanoplatform constructed by host-guest interaction for near-infrared-light-actuated synergistic photodynamic-/chemotherapy. *Chem. Eng. J.* 390:124516. doi: 10.1016/j.cej.2020.124516

Zhang, L., Chen, Y., Li, Z., Li, L., Saint-Cricq, P., Li, C., et al. (2016). Tailored synthesis of octopus-type janus nanoparticles for synergistic actively-targeted and chemo-photothermal therapy. *Angew. Chem. Int. Ed.* 55, 2118–2121. doi: 10.1002/anie.201510409

Zhang, M., Yue, J., Cui, R., Ma, Z., Wan, H., Wang, F., et al. (2018). Bright quantum dots emitting at ∼1,600 nm in the NIR-IIb window for deep tissue fluorescence imaging. *Proc. Natl. Acad. Sci. U.S.A.* 115, 6590–6595. doi: 10.1073/pnas.1806153115

Zheng, W., Huang, P., Tu, D., Ma, E., Zhu, H., and Chen, X. (2015). Lanthanide-doped upconversion nano-bioprobes: electronic structures, optical properties, and biodetection. *Chem. Soc. Rev.* 44, 1379–1415. doi: 10.1039/C4CS00178H

Zhong, Y., Ma, Z., Wang, F., Wang, X., Yang, Y., Liu, Y., et al. (2019). *In vivo* molecular imaging for immunotherapy using ultra-bright near-infrared-IIb rare-earth nanoparticles. *Nat. Biotechnol.* 37, 1322–1331. doi: 10.1038/s41587-019-0262-4

Zhong, Y., Ma, Z., Zhu, S., Yue, J., Zhang, M., Antaris, A. L., et al. (2017). Boosting the down-shifting luminescence of rare-earth nanocrystals

for biological imaging beyond 1500 nm. *Nat. Commun.* 8:737. doi: 10.1038/s41467-017-00917-6

Zhong, Y., Tian, G., Gu, Z., Yang, Y., Gu, L., Zhao, Y., et al. (2014). Elimination of photon quenching by a transition layer to fabricate a quenching-shield sandwich structure for 800 nm excited upconversion luminescence of Nd^{3+}-sensitized nanoparticles. *Adv. Mater.* 26, 2831–2837. doi: 10.1002/adma.201304903

Zhou, J., Zhu, X., Chen, M., Sun, Y., and Li, F. (2012). Water-stable $NaLuF_4$-based upconversion nanophosphors with long-term validity for multimodal lymphatic imaging. *Biomaterials* 33, 6201–6210. doi: 10.1016/j.biomaterials.2012.05.036

Zhou, Z., Song, J., Nie, L., and Chen, X. (2016). Reactive oxygen species generating systems meeting challenges of photodynamic cancer therapy. *Chem. Soc. Rev.* 45, 6597–6626. doi: 10.1039/C6CS00271D

Zou, W., Visser, C., Maduro, J. A., Pshenichnikov, M. S., and Hummelen, J. C. (2012). Broadband dye-sensitized upconversion of near-infrared light. *Nat. Photonics* 6, 560–564. doi: 10.1038/nphoton.2012.158

Conflict of Interest: The authors declare that the research was conducted in the absence of any commercial or financial relationships that could be construed as a potential conflict of interest.

frontiers in Chemistry

MINI REVIEW
published: 09 November 2020
doi: 10.3389/fchem.2020.593398

Optical Manipulation of Lanthanide-Doped Nanoparticles: How to Overcome Their Limitations

Elisa Ortiz-Rivero[1], *Lucía Labrador-Páez*[2], *Paloma Rodríguez-Sevilla*[3] and *Patricia Haro-González*[1,4]*

[1] Fluorescence Imaging Group, Departamento de Física de Materiales, Universidad Autónoma de Madrid, Madrid, Spain, [2] Department of Applied Physics, Royal Institute of Technology (KTH), Stockholm, Sweden, [3] Scottish Universities Physics Alliance (SUPA), School of Physics and Astronomy, University of St Andrews, St Andrews, United Kingdom, [4] Instituto Nicolás Cabrera, Universidad Autónoma de Madrid, Madrid, Spain

Since Ashkin's pioneering work, optical tweezers have become an essential tool to immobilize and manipulate microscale and nanoscale objects. The use of optical tweezers is key for a variety of applications, including single-molecule spectroscopy, colloidal dynamics, tailored particle assembly, protein isolation, high-resolution surface studies, controlled investigation of biological processes, and surface-enhanced spectroscopy. In recent years, optical trapping of individual sub-100-nm objects has got the attention of the scientific community. In particular, the three-dimensional manipulation of single lanthanide-doped luminescent nanoparticles is of great interest due to the sensitivity of their luminescent properties to environmental conditions. Nevertheless, it is really challenging to trap and manipulate single lanthanide-doped nanoparticles due to the weak optical forces achieved with conventional optical trapping strategies. This limitation is caused, firstly, by the diffraction limit in the focusing of the trapping light and, secondly, by the Brownian motion of the trapped object. In this work, we summarize recent experimental approaches to increase the optical forces in the manipulation of lanthanide-doped nanoparticles, focusing our attention on their surface modification and providing a critical review of the state of the art and future prospects.

Keywords: nanoparticle, lanthanide, rare-earth, optical trapping, optical force

OPEN ACCESS

Edited by:
Lining Sun,
Shanghai University, China

Reviewed by:
Jochen Fick,
UPR2940 Institut Neel (NEEL), France
Venkataramanan Mahalingam,
Indian Institute of Science Education and Research Kolkata, India
Adolfo Speghini,
University of Verona, Italy

***Correspondence:**
Patricia Haro-González
patricia.haro@uam.es

Specialty section:
This article was submitted to Nanoscience, a section of the journal Frontiers in Chemistry

Received: *10 August 2020*
Accepted: *29 September 2020*
Published: *09 November 2020*

Citation:
Ortiz-Rivero E, Labrador-Páez L, Rodríguez-Sevilla P and Haro-González P (2020) Optical Manipulation of Lanthanide-Doped Nanoparticles: How to Overcome Their Limitations. Front. Chem. 8:593398. doi: 10.3389/fchem.2020.593398

INTRODUCTION

Optical trapping (OT) of nanoparticles (NPs) by the forces exerted by a tightly focused laser beam has allowed innumerable advances in the study of single molecules and cells and the characterization of photonic nanomaterials. OT stands out for its ability to isolate and manipulate NPs for their study in a contactless and non-invasive way, and it has enabled the development of different techniques, such as photonic force microscopy, the optical manipulation for assembly or actuation in nanostructures, and diverse types of local contactless sensing (Maragò et al., 2013; Rodríguez-Sevilla et al., 2017a; Bradac, 2018; Bunea and Glückstad, 2019). For the application of optical tweezers in biological science, Arthur Ashkin, the inventor of the technique, was awarded with the Nobel Prize in Physics in 2018.

The most commonly optically trapped inorganic particles are silica and polystyrene beads. They are usually tracked to infer properties of the environment or employed as handlers for non-direct

manipulation of, for example, biological molecules. However, their detection can become challenging if their size is reduced below the resolution limit of the optical setup. In contrast, OT of luminescent particles has the advantage of enabling their detection by their luminescence even if they are smaller than the resolution limit of the imaging system. Moreover, they have a great potential for sensing as most of them show environment-sensitive luminescence. Several types of luminescent particles have been already optically trapped: quantum dots (Jauffred et al., 2008; Jensen et al., 2016), nanodiamonds (Geiselmann et al., 2013; Neukirch et al., 2013, 2015), semiconductor nanowires (Reece et al., 2009; Wang et al., 2011a), niobate nanowires (Nakayama et al., 2007; Dutto et al., 2011), and lanthanide-doped nanoparticles (NPs:Ln) (Haro-Gonzalez et al., 2013; Rodríguez-Sevilla et al., 2015, 2016a; Kang et al., 2019). NPs:Ln stand out due to their photostability, long luminescence decay time, narrow and multiple emission bands, and tailorable luminescence characteristics. Within the NPs:Ln library, upconverting nanoparticles (UCNPs) are the most frequently optically trapped particles because they show low biotoxicity and present biocompatible excitation routes. They can absorb light of low energy and emit photons of higher energy through a non-linear process, e.g., emitting visible light after the successive absorption of two or more infrared photons (Labrador-Páez et al., 2018; Zheng et al., 2019). Thus, the combination of infrared biocompatible laser wavelengths with visible luminescence facilitates the detection and tracking of the trapped particle, making them great candidates for bio-applications as contactless local probes.

Multiple applications of NPs:Ln have been explored. Their temperature-sensitive luminescence can be used for local non-invasive temperature sensing of cells (Rodríguez-Sevilla et al., 2016; Drobczynski et al., 2017). Moreover, their polarized emission allows the measurement of the viscosity of the cytoplasm and the detection of single cells (Rodríguez-Sevilla et al., 2016b; Ortiz-Rivero et al., 2019). Other applications include the measurement of the size of bacteria and the labeling of RNA and cancer biomarkers for their quantification in bioassays (Li et al., 2017, 2018; Xin et al., 2017).

For all the aforementioned outstanding characteristics and the multitude of applications as remote contactless biosensors, the use of NPs:Ln for OT has been growing in the last decade. For these reasons, we have chosen to focus our attention on the OT of NPs:Ln and the challenges that the community is currently facing. In the next sections, we will firstly introduce the fundamentals of OT and its limitations for single NP:Ln manipulation. Then, we will discuss how these can be overcome, and we will envision future fields of application of OT of NPs:Ln.

OPTICAL TRAPPING: FUNDAMENTALS

Optical manipulation is based on the optical forces that a tightly focused laser beam can exert on a particle thanks to the interaction between the electromagnetic field of the light and matter. The magnitude of these optical forces depends on the properties of the light (power, polarization, and beam shape), but predominantly on the characteristics of the particle (size, shape, and polarizability) (Ashkin et al., 1986; Rohrbach and Stelzer, 2001; Bendix et al., 2014).

From a simplified point of view, the optical force exerted on a particle could be visualized as the combination of the gradient and scattering forces. The gradient force acts as a restoring force that attracts the particle toward the maximum intensity of the laser beam, while the scattering force points in the same direction as the beam propagates and destabilizes the trap, pushing the particle away from the stable position. These forces should be balanced for achieving stable trapping conditions.

In the case of particles much smaller than the wavelength of the trapping light (Rayleigh regime), the scattering force can be neglected and the dynamics of the trapped particle can be described, taking into account only the action of the gradient force (Spesyvtseva and Dholakia, 2016). This is only completely true for nanoparticles with diameters smaller than some tens of nanometers. Bigger nanoparticles are still pushed by the optical scattering force, although its effect is usually neglected for simplification, as NP stable trapping can only be achieved when the gradient force overcomes the scattering force. The gradient force acting on the NP can be expressed as

$$\mathbf{F_{grad}} = \frac{1}{2}\alpha_{\mathbf{NP}}\nabla\langle \mathbf{E_{TRAP}}^2\rangle, \tag{1}$$

where E_{TRAP} is the electric field of the trapping light and $\alpha_{\mathbf{NP}}$ is the polarizability of the particle

$$\alpha_{\mathbf{NP}} = 4\pi\varepsilon_0 \mathbf{V_{NP}}\frac{\varepsilon_{\mathbf{NP}} - \varepsilon_{\mathbf{m}}}{\varepsilon_{\mathbf{NP}} + 2\varepsilon_{\mathbf{m}}}, \tag{2}$$

which depends on the volume of the particle (V_{NP}), and the electric permittivity of vacuum (ε_0), the surrounding medium (ε_m), and the nanoparticle (ε_{NP}). Thus, in this situation, the optical force decreases as the volume of the particle does. This is the main limitation in OT of NPs.

For biological applications, NPs are manipulated in liquid media. Thus, the trapped particle is subjected to the temperature-dependent Brownian fluctuations which destabilize it and make it oscillate around the equilibrium position. If the optical force is not large enough to compensate this motion (i.e., if the optical potential does not exceed at least 10 times the thermal energy k_BT, where k_B is the Boltzmann constant and T, the temperature), the particle will escape the optical trap, making its manipulation impossible.

For this reason, optical forces should be enhanced enabling the manipulation of NPs in liquid media. From expression (1), the magnitude of the optical force depends on the power of the trapping beam (i.e., $F_{grad} \propto E_{TRAP}{}^2$). However, increasing the trapping power in favor of higher optical forces would present side effects related to the absorption of the trapping radiation by either the particle or the medium. This could lead to a deterioration of the sample, but more importantly, it can cause an increase in temperature that would enhance the Brownian fluctuations (Peterman et al., 2003; Rodríguez-Sevilla et al., 2017b). Therefore, this solution is usually ruled out.

Other properties of the beam can also be tailored for the enhancement of the optical force. Expression (1) shows that the force depends on the gradient of the intensity of the beam (i.e., $F_{grad} \propto \nabla\langle {E_{TRAP}}^2 \rangle$). For this reason, far-field optical manipulation of small particles makes use of high numerical aperture objective lenses to focus the laser beam to a small spot comparable to the particle size (Bartlett and Henderson, 2002; Rohrbach, 2005). However, the diffraction limit ($\sim \frac{\lambda}{2NA}$) restricts the smallest spot that can be generated for a given trapping wavelength (λ) and numerical aperture (NA). For this reason, novel trapping strategies have been developed for OT of entities much smaller than the trapping wavelength (see section Optical Force Increase Based on the Reduction of the Optical Trap Volume).

The properties of the particle can also be tailored to enhance the optical force. The polarizability of the particle depends on the material of which it is made but also on the molecules that surround it (see section Optical Force Increase Based on Surface Modifications). In addition, it depends on the nanoparticle morphology. Anisotropic nanoparticles may show a certain degree of polarization. Their effective induced polarization is non-isotropic, which produced an optical torque to align the electric field with the particle polarization. Thus, the stable orientation inside the optical trap is strongly dependent on the incident electric field and the NP geometrical axis.

The trapped particle can add new functionalities to the optical manipulation tool, since it not only is useful to control its position and motion but also can be used as a force transducer. For this purpose, the optical trap should be calibrated. This can be done by different techniques that are based on the analysis of the motion of the trapped particle (Sarshar et al., 2014). These dynamics can be detected imaging the particle (video-tracking) or from the intensity fluctuation produced in the laser beam when it is scattered by the particle (Bui et al., 2018). The luminescence of NPs:Ln is advantageous since particles much smaller than the diffraction limit can be detected. However, the emission should be intense enough for a good signal-to-noise ratio. This is hard to achieve for very small particles due to their weak emission and the short acquisition times (high frame rates) required to effectively detect the particle dynamics. Although techniques have been developed for the use of limited frame rate (Wong and Halvorsen, 2006), NPs:Ln facilitate the use of this method thanks to their outstanding resistance to photobleaching that permit, for example, to track the particle for long periods of time. Single NP:Ln luminescence has been reported by different groups that managed to achieve the emission spectra of individual trapped nanoparticles based on drop-casting a diluted suspension (Schietinger et al., 2010; Gargas et al., 2014). However, for most bio-applications, the interest falls on assessing single NP emission in a colloidal suspension (Haro-Gonzalez et al., 2013; Rodríguez-Sevilla et al., 2015). The luminescence of single NP:Ln in solution has been spectroscopically characterized, which enabled the comparisons of the performance between different particles, and to study inter-particle interactions (Roder et al., 2015; Zhou et al., 2020).

OPTICAL TRAPPING OF LANTHANIDE-DOPED NANOPARTICLES

As explained in section Optical Trapping: Fundamentals, it is challenging to manipulate NPs with conventional OT strategies as the optical forces decrease with the particle volume. In this section, we describe different strategies used to increase the magnitude of the optical forces, which either modify the particle surface (section Optical Force Increase Based on Surface Modifications) or reduce the optical trap volume (section Optical Force Increase Based on the Reduction of the Optical Trap Volume). **Table 1** summarizes the most relevant NPs:Ln used to date, as well as the maximum optical forces achieved.

Optical Force Increase Based on Surface Modifications

OT of NPs:Ln is challenging because they are dielectric particles with low polarizability (α_{NP}) and the trapping force scale with α_{NP}. Expression (2) shows that α_{NP} depends on the dielectric constants of the NP and that of the environment, so that α_{NP} optimization can be achieved by modifying the NP material and/or the surrounding medium. A large number of methods for surface modification of NPs have been reported (Wang et al., 2011b; Hirsch, 2020), which enhance the NPs:Ln luminescence (i.e., easing the tracking) and their colloidal stability, while providing the possibility of subsequent bioconjugation. However, despite its interest, the optimization of the optical forces acting on single NP:Ln through its surface modification is a route that has not been thoroughly explored. Some synthesis/surface modification strategies are included in **Table 1**.

Colloidal NPs present a superficial charge which interacts with the solvent's ions. These changes distribute around the particle forming an electric double layer characterized by the zeta potential, as depicted in **Figures 1A,B**, which influences α_{NP}. The NPs may have a surface coating to improve their colloidal properties and zeta potential. For the optimization of α_{NP}, Rodríguez-Rodríguez et al. (2015) studied the influence of the surface coating of 8-nm SrF_2:Er,Yb NPs:Ln on the trapping efficiency. They increased α_{NP} by replacing the cationic species on the NP surface by more mobile ones in solution. This modification led to an almost 50-fold enhancement in the trapping efficiency, showing that the contribution of the surface coating to the net polarizability dominates over that of the NP:Ln core material. This study was continued by Rodríguez-Sevilla et al. (2018), determining the optical forces acting on $NaYF_4$:Er,Yb NPs:Ln of different sizes (ranging from 5 to 100 nm). They experimentally demonstrated that the optical forces (parameterized by the trapping factor Q) acting on a NP:Ln depend on the electrostatic properties (zeta potential) of the interface between the NP and the surrounding medium more strongly than on their volume (see expression 2 and **Figure 1C**). Alternatively, selecting the right medium (the solvent molecules) can be essential to optimizing the zeta potential value. Likewise, the temperature of the medium, which affects its permittivity (Catenaccio et al., 2003) and conductivity (Cao et al., 2019) and indirectly α_{NP}, can lead to the enhancement

TABLE 1 | Classification of the most relevant techniques used on NPs:Ln to enhance their optical force.

References	Nanoparticle	Size (nm)	Synthesis method	Max. trap efficiency (pN μm^{-1} W^{-1})	Strategy used
Synthesis/surface modification					
Anbharasi et al. (2020)	$LiYF_4$:Yb,Er	238	Hydrothermal	0.0055	Calcination
Rodríguez-Rodríguez et al. (2015) and Rodríguez-Sevilla et al. (2015)	SrF_2:Yb,Egr	8	Hydrothermal	0.33	Surface charge tailoring
Kang et al. (2019)	$NaYF_4$:Yb, Er	370	Thermal decomposition	1	Hydrophobic encapsulation and ligand exchange
Rodríguez-Sevilla et al. (2018)	$NaYF_4$:Yb,Er	8–200	Thermal decomposition	25	Core–shell
Reduction of the optical trap volume					
Mor et al. (2014)	$NaYF_4$:Yb,Er	230	Flame-fusion and hydrothermal		PFM
Schietinger et al. (2010)	$NaYF_4$:Yb,Er	30	Microwave-assisted		AFM tip
Xin et al. (2017)	KLu_2F_7:Yb,Er	120	Hydrothermal	14.1	Fiber tip
Leménager et al. (2018)	$NaYF_4$:Gd,Yb,Er	600–2,000	Solvothermal	4	Dual fiber tweezers
Kumar et al. (2020)	$NaYF_4$:Eu	l:220 0, d:120	Solvothermal	6	Dual fiber tweezers
Li Y. et al. (2017)	$NaYF_4$:Yb,Tm @ SiO_2-NH_2	28	Hydrothermal	448 (trapped *E-coli* covered with NPs)	Fiber tip + bio-microlens

They are divided depending on the strategy used: synthesis/surface modification of the nanoparticle or reduction of the optical trap volume. Where "l" and "d" refers to lenght and diameter, respectively. PFM, photonic force microscopy.

of the optical forces, though the Brownian motion increase may be detrimental.

Optical Force Increase Based on the Reduction of the Optical Trap Volume

An alternative strategy to improve the optical forces acting on single NP:Ln consists of the reduction of the optical trap size to increase the electric field gradient [see expression (1)]. When the dimensions of a bulk material are reduced, new properties appear such as the ability to confine light into a region much smaller than the wavelength (Koya et al., 2020). With that purpose, plasmonic effects and optical resonances have been employed to enhance the trapping forces and luminescence of NPs:Ln.

Optical nanotweezers are metallic or dielectric nanostructures that can generate strong electromagnetic field gradients as they can confine the light to a subwavelength region using lower laser powers than conventional OT (Shoji and Tsuboi, 2014; Huang and Yang, 2015). Their development was mainly motivated by the aim to suppress the scattering forces for NP trapping (Min et al., 2013).

Nanotweezers have been proven to allow the manipulation and detection of single NP and small molecules, controlling their motion in the nanoscale. Different plasmonic and dielectric nanostructures have been developed for OT of luminescent NPs (e.g., polystyrene fluorescent beads or quantum dots Yoo et al., 2018; Xu and Crozier, 2019; Kotsifaki et al., 2020). Furthermore, the luminescence of the trapped particle can be excited by an additional beam or through an upconversion process using the trapping beam. Although the manipulation of sub-30-nm dielectric nanoparticles by plasmonic optical tweezers has been demonstrated, the manipulation of NPs:Ln by this technique is yet to be achieved (to our knowledge), which would bring the outstanding capabilities of these particles to the nanoscale.

In a different strategy, several studies have developed innovative optical tweezers based on optical fibers, which was firstly demonstrated by Fuh et al. (1987) and Constable et al. (1993). As an alternative to bulky high-numerical aperture objective lenses, optical fibers can create a sub-diffraction spot at their tip if it is judiciously modified, i.e., providing it with a lenticular shape (Li et al., 2015; Li Y.-C. et al., 2016; Li Y. et al., 2017). This has the advantage of compactness and high manipulation flexibility due to their reduced size. Moreover, it also results in different trapping and luminescence recording configurations. The focusing capabilities of the optical fiber can be optimized by modifying the shape of its tip and, for example, overcome the diffraction limit (Berthelot et al., 2014; Asadollahbaik et al., 2020; Zhao et al., 2020). Direct trapping of NPs:Ln has been achieved with a single fiber-coupled laser, reducing drastically the size of the experimental setup. H. Xin et al. used a tapered fiber tip capable of tightly focusing the output light resulting in a high-intensity gradient. As shown in **Figure 1D**, they employed this strategy to measure the length of single bacterium by co-trapping in a row a KLu_2F_7:Yb,Er NP:Ln of 120 nm (with a trap stiffness of 14.1 pN/m W), a single *E. coli* bacterium, and then a second NP:Ln (12.8 pN/mW). In comparison with other Yb, Er co-doped NPs:Ln included in **Table 1**, their trapping stiffness was several orders of magnitude larger, demonstrating the efficiency of this approach.

Another approach to optimize OT of NPs is based on dual fiber tweezers. Counter-propagating traps based on two opposite

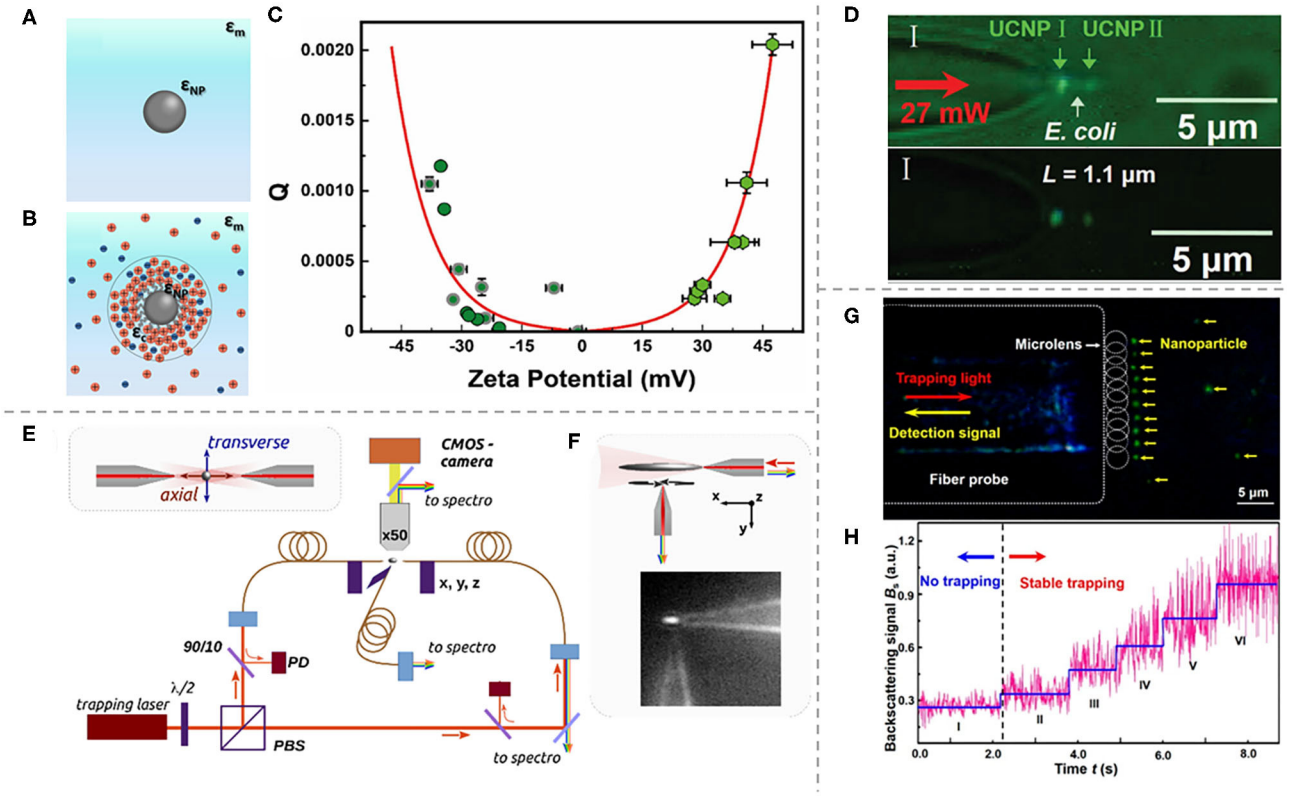

FIGURE 1 | Optical trapping of a NP:Ln in a solvent by different systems based on the reduction of the optical trap volume. **(A)** A ligand-free lanthanide-doped dielectric NP (permittivity ε_{NP}) in a medium (permittivity ε_m). **(B)** A dielectric NP:Ln coated with ligands (coating permittivity ε_c). The electric double layer is indicated by the circles. **(C)** Optical trapping strength, represented by the Q-factor, as a function of the zeta potential for different types of NP:Ln. Adapted with permission from Rodríguez-Sevilla et al. (2018). Copyright 2018 American Chemical Society. **(D)** Bright-field (top) and dark-field (bottom) images of two NPs:Ln (I and II) and an *E. coli* bacterium trapped in a row by optical fiber tweezers. Adapted with permission from Xin et al. (2017). Copyright 2017 John Wiley and Sons. **(E)** Schematic of a dual optical fiber tweezer system. **(F)** Schematic and microscopy image of a single fiber tip trap including the auxiliary fiber tip used for particle emission recording of a single NP:Ln. OSA Open Access License for OSA-Formatted Journal Article PDFs (Leménager et al., 2018). **(G)** Tip of an optical fiber with an array of coupled spherical microlenses that are able to trap nanoparticles. The fiber probe also records the detection signal. The sequential growth, in backscattering signal, as different nanoparticles are trapped by the microlenses is shown in **(H)**. Adapted with permission from Li Y. et al. (2016). Copyright 2016 American Chemical Society.

fibers have been proven to be able to stably trap NPs:Ln for the study of their luminescence. Although the optical forces exerted on the NPs have not been reported, their magnitude is expected to be higher than for conventional OT. For example, Leménager et al. (2018) recorded the anisotropic emission of trapped $NaYF_4$:Er,Yb,Gd nanorods in three orthogonal directions using distinct methods: through the microscope objective, by coupling it into one of the trapping fiber tip, and by coupling it into a third fiber (see **Figures 1E,F**). In a similar way, Kumar et al. (2020) studied nanorods of $NaYF_4$:Eu, measuring their 3D orientation by europium ion polarization-dependent luminescence.

The dual-beam configuration can be further improved by its combination with the modification of the fiber tip, adding a micro-lens. The main advantage of using microscopic lenses over typically macroscopic ones is their considerably smaller focusing spot size and mobility inside the sample. This has been reported to enhance the optical forces for nanosized polystyrene particles so it could also be used for NP:Ln. For instance, Asadollahbaik et al. positioned 3D-printed diffractive Fresnel lenses at the tip of the fibers in a counter-propagating arrangement. This novel miniaturized optical setup can produce a variety of NA with a large working distance and a reduced trapping spot, increasing the trap stiffness by a factor of 35–50 (1762.87 pN/µm W). On the other hand, a microlens can also be realized by a colloidal particle such as a dielectric microcylinder or microsphere.

When it is optically trapped, the particle focuses the light and a nanosized photonic jet is generated at its shadow-side surface. Photonic nanojets can propagate over a distance corresponding to several optical wavelengths without significant divergence, and their waist size is below the diffraction limit, depending on the microlens diameter, diffraction index, and laser wavelength (Chen et al., 2004; Neves, 2015). In addition, the light backscattering and the nanoparticle luminescence can be enhanced and recorded, making fiber-coupled microspheres suitable for NPs:Ln optical manipulation. Li et al. reported different types of cells as natural bio-microlens. Then, NPs:Ln were coupled to pathogenic bacteria, which then were subsequently trapped individually or in

chains. The maximum trapping efficiency they obtained was 448 pN μm^{-1} W^{-1} for an NP:Ln-covered *E. coli* bacterium. More complex systems present a parallel photonic nanojet array, produced by assembling and binding microlenses on a single optical fiber tip, as depicted in **Figures 1G,H** (Li Y. et al., 2016; Schäffner et al., 2020).

FUTURE PERSPECTIVES AND CONCLUSIONS

Lanthanide-doped nanoparticles present unique, environment-sensitive, selective, and bio-compatible spectroscopic characteristics that stand out among other dielectric luminescent nanoparticles. Hence, they are ideal for optical trapping, a non-invasive and versatile tool used to manipulate small objects. Their main drawback is their reduced size of nanoparticles, which is below the diffraction limit of the optics system and reduces the achievable optical forces. In this review, we have analyzed the strategies that have been developed or would be of potential use to overcome this limitation, i.e., the modification of the lanthanide-doped nanoparticle's characteristics and the optimization of the optical tweezer setup. Some of these techniques can also enhance the luminescence of the lanthanide-doped nanoparticle, which is of great interest for numerous applications. Despite the potential of the reviewed techniques, their implementation is an underdeveloped field. We think these already proven strategies could open the door to widen the application of lanthanide-doped nanoparticles, which present better capabilities and multifunctionalities than other commonly used nanoparticles.

AUTHOR CONTRIBUTIONS

All authors listed have made a substantial, direct and intellectual contribution to the work, and approved it for publication.

FUNDING

This work was supported by the Ministerio de Ciencia e Innovación de España (PID2019-105195RA-I00) and by Universidad Autónoma de Madrid, Comunidad Autónoma de Madrid (SI1/PJI/2019-00052). LL-P acknowledges Carl Tryggers Foundation (CTS 18: 229).

REFERENCES

Anbharasi, L., Bhanu Rekha, E. A., Rahul, V. R., Roy, B., Gunaseelan, M., Yamini, S., et al. (2020). Tunable emission and optical trapping of upconverting LiYF4:Yb,Er nanocrystal. *Opt. Laser Technol.* 126:106109. doi: 10.1016/j.optlastec.2020.106109

Asadollahbaik, A., Thiele, S., Weber, K., Kumar, A., Drozella, J., Sterl, F., et al. (2020). Highly efficient dual-fiber optical trapping with 3D printed diffractive fresnel lenses. *ACS Photonics* 7, 88–97. doi: 10.1021/acsphotonics.9b01024

Ashkin, A., Dziedzic, J. M., Bjorkholm, J. E., and Chu, S. (1986). Observation of a single-beam gradient force optical trap for dielectric particles. *Opt. Lett.* 11, 288–290. doi: 10.1364/OL.11.000288

Bartlett, P., and Henderson, S. (2002). Three-dimensional force calibration of a single-beam optical gradient trap. *J. Phys. Condensed Matter.* 14, 7757–7768. doi: 10.1088/0953-8984/14/33/314

Bendix, P. M., Jauffred, L., Norregaard, K., and Oddershede, L. B. (2014). Optical trapping of nanoparticles and quantum dots. *IEEE J. Selected Topics Quant. Electron.* 20, 15–26. doi: 10.1109/JSTQE.2013.2287094

Berthelot, J., Aćimović, S. S., Juan, M. L., Kreuzer, M. P., Renger, J., and Quidant, R. (2014). Three-dimensional manipulation with scanning near-field optical nanotweezers. *Nat. Nanotechnol.* 9, 295–299. doi: 10.1038/nnano.2014.24

Bradac, C. (2018). Nanoscale optical trapping: a review. *Adv. Opt. Mater.* 6:1800005. doi: 10.1002/adom.201800005

Bui, A. A. M., Kashchuk, A. V., Balanant, M. A., Nieminen, T. A., Rubinsztein-Dunlop, H., and Stilgoe, A. B. (2018). Calibration of force detection for arbitrarily shaped particles in optical tweezers. *Sci. Rep.* 8:10798. doi: 10.1038/s41598-018-28876-y

Bunea, A. I., and Glückstad, J. (2019). Strategies for optical trapping in biological samples: aiming at microrobotic surgeons. *Laser Photon. Rev.* 13:1800227. doi: 10.1002/lpor.201800227

Cao, W., Chern, M., Dennis, A. M., and Brown, K. A. (2019). Measuring nanoparticle polarizability using fluorescence microscopy. *Nano Lett.* 19, 5762–5768. doi: 10.1021/acs.nanolett.9b02402

Catenaccio, A., Daruich, Y., and Magallanes, C. (2003). Temperature dependence of the permittivity of water. *Chem. Phys. Lett.* 367, 669–671. doi: 10.1016/S0009-2614(02)01735-9

Chen, Z., Taflove, A., and Backman, V. (2004). Photonic nanojet enhancement of backscattering of light by nanoparticles: a potential novel visible-light ultramicroscopy technique. *Opt. Express* 12, 1214–1220. doi: 10.1364/OPEX.12.001214

Constable, A., Kim, J., Mervis, J., Zarinetchi, F., and Prentiss, M. (1993). Demonstration of a fiber-optical light-force trap. *Opt. Lett.* 18, 1867–1869. doi: 10.1364/OL.18.001867

Drobczynski, S., Prorok, K., Tamarov, K., Dus-Szachniewicz, K., Lehto, V.-P., and Bednarkiewicz, A. (2017). Toward controlled photothermal treatment of single cell: optically induced heating and remote temperature monitoring *in vitro* through double wavelength optical tweezers. *ACS Photonics* 4, 1993–2002. doi: 10.1021/acsphotonics.7b00375

Dutto, F., Raillon, C., Schenk, K., and Radenovic, A. (2011). Nonlinear optical response in single alkaline niobate nanowires. *Nano Lett.* 11, 2517–2521. doi: 10.1021/nl201085b

Fuh, M.-R. S., Burgess, L. W., Hirschfeld, T., Christian, G. D., and Wang, F. (1987). Single fibre optic fluorescence pH probe. *Analyst* 112, 1159–1163. doi: 10.1039/an9871201159

Gargas, D. J., Chan, E. M., Ostrowski, A. D., Aloni, S., Altoe, M. V. P., Barnard, E. S., et al. (2014). Engineering bright sub-10-nm upconverting nanocrystals for single-molecule imaging. *Nat. Nanotechnol.* 9, 300–305. doi: 10.1038/nnano.2014.29

Geiselmann, M., Juan, M. L., Renger, J., Say, J. M., Brown, L. J., De Abajo, F. J. G., et al. (2013). Three-dimensional optical manipulation of a single electron spin. *Nat. Nanotechnol.* 8:175. doi: 10.1038/nnano.2012.259

Haro-Gonzalez, P., del Rosal, B., Maestro, L. M., Martin Rodriguez, E., Naccache, R., Capobianco, J. A., et al. (2013). Optical trapping of NaYF4:Er3+,Yb3+ upconverting fluorescent nanoparticles. *Nanoscale* 5:12192. doi: 10.1039/c3nr03644h

Hirsch, T. (2020). "Surface modification of near infrared-emitting nanoparticles for biomedical applications," in *Near Infrared-Emitting Nanoparticles for Biomedical Applications,* eds A. Benayas, E. Hemmer, G. Hong, and D. Jaque (Cham: Springer International Publishing), 49–61. doi: 10.1007/978-3-030-32036-2_3

Huang, J.-S., and Yang, Y.-T. (2015). Origin and future of plasmonic optical tweezers. *Nanomaterials* 5, 1048–1065. doi: 10.3390/nano5021048

Jauffred, L., Richardson, A. C., and Oddershede, L. B. (2008). Three-dimensional optical control of individual quantum dots. *Nano Lett.* 8, 3376–3380. doi: 10.1021/nl801962f

Jensen, R. A., Huang, I.-C., Chen, O., Choy, J. T., Bischof, T. S., Loncar, M., et al. (2016). Optical trapping and two-photon excitation of colloidal quantum dots using bowtie apertures. *ACS Photonics* 3, 423–427. doi: 10.1021/acsphotonics.5b00575

Kang, Y.-F., Zheng, B., Song, C.-Y., Li, C.-Y., Chen, Z.-L., Wu, Q.-S., et al. (2019). Evaluation of luminescence properties of single hydrophilic upconversion nanoparticles by optical trapping. *J. Phys. Chem. C* 123, 10107–10113. doi: 10.1021/acs.jpcc.9b00430

Kotsifaki, D. G., Truong, V. G., and Chormaic, S. N. (2020). Fano-resonant, asymmetric, metamaterial-assisted tweezers for single nanoparticle trapping. *Nano Lett.* 20, 3388–3395. doi: 10.1021/acs.nanolett.0c00300

Koya, A. N., Cunha, J., Guo, T.-L., Toma, A., Garoli, D., Wang, T., et al. (2020). Novel plasmonic nanocavities for optical trapping-assisted biosensing applications. *Adv. Opti. Mater.* 8:1901481. doi: 10.1002/adom.201901481

Kumar, A., Kim, J., Lahlil, K., Julie, G., Nic Chormaic, S., Kim, J., et al. (2020). Optical trapping and orientation-resolved spectroscopy of europium-doped nanorods. *J. Phys. Photonics* 2:025007. doi: 10.1088/2515-7647/ab83e3

Labrador-Páez, L., Ximendes, E. C., Rodríguez-Sevilla, P., Ortgies, D. H., Rocha, U., Jacinto, C., et al. (2018). Core–shell rare-earth-doped nanostructures in biomedicine. *Nanoscale* 10, 12935–12956. doi: 10.1039/C8NR02307G

Leménager, G., Thiriet, M., Pourcin, F., Lahlil, K., Valdivia-Valero, F., Colas des Francs, G., et al. (2018). Size-dependent trapping behavior and optical emission study of NaYF4 nanorods in optical fiber tip tweezers. *Opt. Express* 26, 32156–32167. doi: 10.1364/OE.26.032156

Li, C.-Y., Cao, D., Qi, C.-B., Kang, Y.-F., Song, C.-Y., Xu, D.-D., et al. (2018). Combining holographic optical tweezers with upconversion luminescence encoding: imaging-based stable suspension array for sensitive responding of dual cancer biomarkers. *Anal. Chem.* 90, 2639–2647. doi: 10.1021/acs.analchem.7b04299

Li, C.-Y., Cao, D., Song, C.-Y., Xu, C.-M., Ma, X.-Y., Zhang, Z.-L., et al. (2017). Integrating optical tweezers with up-converting luminescence: a non-amplification analytical platform for quantitative detection of microRNA-21 sequences. *Chem. Commun.* 53, 4092–4095. doi: 10.1039/C7CC01133D

Li, Y., Liu, X., Yang, X., Lei, H., Zhang, Y., and Li, B. (2017). Enhancing upconversion fluorescence with a natural bio-microlens. *ACS Nano* 11:10672. doi: 10.1021/acsnano.7b04420

Li, Y., Xin, H., Cheng, C., Zhang, Y., and Li, B. (2015). Optical separation and controllable delivery of cells from particle and cell *mixture. Nanophotonics* 4:353. doi: 10.1515/nanoph-2015-0008

Li, Y., Xin, H., Liu, X., Zhang, Y., Lei, H., and Li, B. (2016). Trapping and detection of nanoparticles and cells using a parallel photonic nanojet array. *ACS Nano* 10, 5800–5808. doi: 10.1021/acsnano.5b08081

Li, Y.-C., Xin, H.-B., Lei, H.-X., Liu, L.-L., Li, Y.-Z., Zhang, Y., et al. (2016). Manipulation and detection of single nanoparticles and biomolecules by a photonic nanojet. *Light Sci. Appl.* 5, e16176–e16176. doi: 10.1038/lsa.2016.176

Maragò, O. M., Jones, P. H., Gucciardi, P. G., Volpe, G., and Ferrari, A. C. (2013). Optical trapping and manipulation of nanostructures. *Nat. Nanotechnol.* 8, 807–817. doi: 10.1038/nnano.2013.208

Min, C., Shen, Z., Shen, J., Zhang, Y., Fang, H., Yuan, G., et al. (2013). Focused plasmonic trapping of metallic particles. *Nat. Commun.* 4:2891. doi: 10.1038/ncomms3891

Mor, F. M., Sienkiewicz, A., Forr,ó, L., and Jeney, S. (2014). Upconversion particle as a local luminescent brownian probe: a photonic force microscopy study. *ACS Photonics* 1, 1251–1257. doi: 10.1021/ph500189w

Nakayama, Y., Pauzauskie, P. J., Radenovic, A., Onorato, R. M., Saykally, R. J., Liphardt, J., et al. (2007). Tunable nanowire nonlinear optical probe. *Nature* 447, 1098–1101. doi: 10.1038/nature05921

Neukirch, L. P., Gieseler, J., Quidant, R., Novotny, L., and Nick Vamivakas, A. (2013). Observation of nitrogen vacancy photoluminescence from an optically levitated nanodiamond. *Opt. Lett.* 38, 2976–2979. doi: 10.1364/OL.38.002976

Neukirch, L. P., Von Haartman, E., Rosenholm, J. M., and Vamivakas, A. N. (2015). Multi-dimensional single-spin nano-optomechanics with a levitated nanodiamond. *Nat. Photonics* 9, 653–657. doi: 10.1038/nphoton.2015.162

Neves, A. A. R. (2015). Photonic nanojets in optical tweezers. *J. Quant. Spectrosc. Radiat. Transf.* 162, 122–132. doi: 10.1016/j.jqsrt.2015.03.019

Ortiz-Rivero, E., Prorok, K., Skowickł, M., Lu, D., Bednarkiewicz, A., Jaque, D., et al. (2019). Single-cell biodetection by upconverting microspinners. *Small* 15:1904154. doi: 10.1002/smll.201904154

Peterman, E. J. G., Gittes, F., and Schmidt, C. F. (2003). Laser-induced heating in optical traps. *Biophys. J.* 84, 1308–1316. doi: 10.1016/S0006-3495(03)74946-7

Reece, P. J., Paiman, S., Abdul-Nabi, O., Gao, Q., Gal, M., Tan, H. H., et al. (2009). Combined optical trapping and microphotoluminescence of single InP nanowires. *Appl. Phys. Lett.* 95:101109. doi: 10.1063/1.3225148

Roder, P. B., Smith, B. E., Zhou, X., Crane, M. J., and Pauzauskie, P. J. (2015). Laser refrigeration of hydrothermal nanocrystals in physiological media. *Proc. Natl. Acad. Sci. U.S.A.* 112, 15024–15029. doi: 10.1073/pnas.1510418112

Rodríguez-Rodríguez, H., Rodríguez Sevilla, P., Martín Rodríguez, E., Ortgies, D. H., Pedroni, M., Speghini, A., et al. (2015). Enhancing optical forces on fluorescent up-converting nanoparticles by surface charge tailoring. *Small* 11, 1555–1561. doi: 10.1002/smll.201402587

Rodríguez-Sevilla, P., Zhang, Y., Haro-González, P., Sanz-Rodríguez, F., Jaque, F., García Sole, J., et al. (2017b). *Avoiding Induced Heating in Optical Trap.* San Diego, CA: SPIE Nanoscience + Engineering.

Rodríguez-Sevilla, P., Labrador-Páez, L., Jaque, D., and Haro-González, P. (2017a). Optical trapping for biosensing: materials and applications. *J. Mater. Chem. B* 5, 9085–9101. doi: 10.1039/C7TB01921A

Rodríguez-Sevilla, P., Labrador-Páez, L., Wawrzyńczyk, D., Nyk, M., Samoć, M., Kar, A. K., et al. (2016a). Determining the 3D orientation of optically trapped upconverting nanorods by in situ single-particle polarized spectroscopy. *Nanoscale* 8, 300–308. doi: 10.1039/C5NR06419H

Rodríguez-Sevilla, P., Prorok, K., Bednarkiewicz, A., Marqués, M. I., García-Martín, A., García Solé, J., et al. (2018). Optical forces at the nanoscale: size and electrostatic effects. *Nano Lett.* 18, 602–609. doi: 10.1021/acs.nanolett.7b04804

Rodríguez-Sevilla, P., Rodríguez-Rodríguez, H., Pedroni, M., Speghini, A., Bettinelli, M., Sol,é, J. G., et al. (2015). Assessing single upconverting nanoparticle luminescence by optical tweezers. *Nano Lett.* 15, 5068–5074. doi: 10.1021/acs.nanolett.5b01184

Rodríguez-Sevilla, P., Zhang, Y., de Sousa, N., MarquÃ©s, M. I., Sanz-Rodríguez, F., Jaque, D., et al. (2016b). Optical torques on upconverting particles for intracellular microrheometry. *Nano Lett.* 16, 8005–8014. doi: 10.1021/acs.nanolett.6b04583

Rodríguez-Sevilla, P., Zhang, Y., Haro-González, P., Sanz-Rodríguez, F., Jaque, F., Solé, J. G., et al. (2016). Thermal scanning at the cellular level by an optically trapped upconverting fluorescent particle. *Adv. Mater.* 28, 2421–2426. doi: 10.1002/adma.201505020

Rohrbach, A. (2005). Stiffness of optical traps: quantitative agreement between experiment and electromagnetic theory. *Phys. Rev. Lett.* 95:168102. doi: 10.1103/PhysRevLett.95.168102

Rohrbach, A., and Stelzer, E. H. K. (2001). Optical trapping of dielectric particles in arbitrary fields. *J. Opt. Soc. Am. A* 18, 839–853. doi: 10.1364/JOSAA.18.000839

Sarshar, M., Wong, W., and Anvari, B. (2014). Comparative study of methods to calibrate the stiffness of a single-beam gradient-force optical tweezers over various laser trapping powers. *J. Biomed. Opt.* 19:115001. doi: 10.1117/1.JBO.19.11.115001

Schäffner, D., Preuschoff, T., Ristok, S., Brozio, L., Schlosser, M., Giessen, H., et al. (2020). Arrays of individually controllable optical tweezers based on 3D-printed microlens arrays. *Opt. Express* 28, 8640–8645. doi: 10.1364/OE.386243

Schietinger, S., Aichele, T., Wang, H.-Q., Nann, T., and Benson, O. (2010). Plasmon-enhanced upconversion in single NaYF4:Yb3+/Er3+ codoped nanocrystals. *Nano Lett.* 10, 134–138. doi: 10.1021/nl903046r

Shoji, T., and Tsuboi, Y. (2014). Plasmonic optical tweezers toward molecular manipulation: tailoring plasmonic nanostructure, light source, and resonant trapping. *J. Phys. Chem. Lett.* 5, 2957–2967. doi: 10.1021/jz501231h

Spesyvtseva, S. E. S., and Dholakia, K. (2016). Trapping in a material world. *ACS Photonics* 3, 719–736. doi: 10.1021/acsphotonics.6b00023

Wang, F., Reece, P. J., Paiman, S., Gao, Q., Tan, H. H., and Jagadish, C. (2011a). Nonlinear optical processes in optically trapped InP nanowires. *Nano Lett.* 11, 4149–4153. doi: 10.1021/nl2020262

Wang, M., Abbineni, G., Clevenger, A., Mao, C., and Xu, S. (2011b). Upconversion nanoparticles: synthesis, surface modification and biological applications. *Nanomedicine* 7, 710–729. doi: 10.1016/j.nano.2011.02.013

Wong, W. P., and Halvorsen, K. (2006). The effect of integration time on fluctuation measurements: calibrating an optical trap in the presence of motion blur. *Opt. Express* 14, 12517–12531. doi: 10.1364/OE.14.012517

Xin, H., Li, Y., Xu, D., Zhang, Y., Chen, C.-H., and Li, B. (2017). Single upconversion nanoparticle–bacterium cotrapping for single-bacterium labeling and analysis. *Small* 13, 1603418. doi: 10.1002/smll.201603418

Xu, Z., and Crozier, K. B. (2019). All-dielectric nanotweezers for trapping and observation of a single quantum dot. *Opt. Express* 27, 4034–4045. doi: 10.1364/OE.27.004034

Yoo, D., Gurunatha, K. L., Choi, H.-K., Mohr, D. A., Ertsgaard, C. T., Gordon, R., et al. (2018). Low-power optical trapping of nanoparticles and proteins with resonant coaxial nanoaperture using 10 nm gap. *Nano Lett.* 18, 3637–3642. doi: 10.1021/acs.nanolett.8b00732

Zhao, X., Zhao, N., Shi, Y., Xin, H., and Li, B. (2020). Optical fiber tweezers: a versatile tool for optical trapping and manipulation. *Micromachines* 11:114. doi: 10.3390/mi11020114

Zheng, K., Loh, K. Y., Wang, Y., Chen, Q., Fan, J., Jung, T., et al. (2019). Recent advances in upconversion nanocrystals: expanding the kaleidoscopic toolbox for emerging applications. *Nano Today* 29:100797. doi: 10.1016/j.nantod.2019.100797

Zhou, J., Chizhik, A. I., Chu, S., and Jin, D. (2020). Single-particle spectroscopy for functional nanomaterials. *Nature* 579, 41–50. doi: 10.1038/s41586-020-2048-8

Conflict of Interest: The authors declare that the research was conducted in the absence of any commercial or financial relationships that could be construed as a potential conflict of interest.

frontiers in Chemistry

REVIEW
published: 08 December 2020
doi: 10.3389/fchem.2020.610481

Metal Ions Doping for Boosting Luminescence of Lanthanide-Doped Nanocrystals

*Shihao Pei, Xiaoqian Ge and Lining Sun**

Research Center of Nano Science and Technology, College of Sciences, Shanghai University, Shanghai, China

With the developing need for luminous materials with better performance, lanthanide-doped nanocrystals have been widely studied for their unique luminescence properties such as their narrow bandwidth emission, excellent chemical stability, and photostability, adjustable emission color, high signal-to-background ratio, deeper tissue penetration with less photo-damage, and low toxicity, etc., which triggered enthusiasm for research on the broad applications of lanthanide-doped nanocrystals in bioimaging, anti-counterfeiting, biosensing, and cancer diagnosis and treatment. Considerable progress has been made in the past few decades, but low upconversion luminescence efficiency has been a hindrance in achieving further progress. It is necessary to summarize the recently relevant literature and find solutions to improve the efficiency. The latest experimental and theoretical studies related to the deliberate design of rare earth luminescent nanocrystals have, however, shown the development of metal ion-doped approaches to enhance the luminescent intensity. Host lattice manipulation can enhance the luminescence through increasing the asymmetry, which improves the probability of electric dipole transition; and the energy transfer modulation offers a reduced cross-relaxation pathway to improve the efficiency of the energy transfer. Based on the mechanisms of host lattice manipulation and energy transfer modulation, a wide range of enhancements at all wavelengths or even within a particular wavelength have been accomplished with an enhancement of up to a hundred times. In this mini review, we present the strategy of metal ion-doped lanthanide nanocrystals to cope with the issue of enhancing luminescence, overview the advantages and tricky challenges in boosting the luminescence, and provide a potential trend of future study in this field.

Keywords: metal ion doping, host lattice manipulation, energy transfer modulation, lanthanide doped nanocrystals, enhanced luminescence

OPEN ACCESS

Edited by:
Xiaomin Li,
Fudan University, China

Reviewed by:
Xiaoji Xie,
Nanjing Tech University, China
Yong Fan,
Fudan University, China

****Correspondence:***
Lining Sun
lnsun@shu.edu.cn

Specialty section:
This article was submitted to Nanoscience, a section of the journal Frontiers in Chemistry

Received: *26 September 2020*
Accepted: *09 November 2020*
Published: *08 December 2020*

Citation:
Pei S, Ge X and Sun L (2020) Metal Ions Doping for Boosting Luminescence of Lanthanide-Doped Nanocrystals. Front. Chem. 8:610481. doi: 10.3389/fchem.2020.610481

INTRODUCTION

Fluorescence imaging has attracted increasing attention for observing a vast number of biological structures due to high sensitivity, superior subcellular resolution, and ultrafast real-time imaging (Weissleder and Pittet, 2008). The frequent fluorescent probes that are exploited in imaging include fluorescent proteins (Ben et al., 2006), metal complexes (Zhao et al., 2010, 2011), organic fluorescent dyes (Terai and Nagano, 2008; Beija et al., 2009; Yuan et al., 2013), and semiconductor quantum dots (Zhou J. et al., 2015; Xu et al., 2016; Hildebrandt et al., 2017). However, most of them are excited

by ultraviolet or visible light, which leads to significant background noise and low penetration depth (Fan and Zhang, 2019). Moreover, high-energy ultraviolet or visible light may cause cell apoptosis or tissue damage.

Alternatively, lanthanide-doped nanocrystals (LDNCs) are excited by near infrared (NIR) light, such as 980 or 808 nm, offering lower scattering coefficients and autofluorescence, and a higher penetration depth (Kobayashi et al., 2009; Yuan et al., 2013). Besides the NIR light excitation, the LDNCs also have several spectroscopic benefits: (1) a sharp emission band with a full-width at half-maximum (FWHM) <10 nm and a long decay lifetime (μs to ms) (Bünzli, 2010; Fan et al., 2018); (2) hundreds of nanometers of anti-Stokes or Stokes shift (upconversion or downshifting the luminescence process) (Su et al., 2017); and (3) excellent photo and chemical stability (no photoblinking or photobleaching) (Su et al., 2017). Although LDNCs possess such excellent spectroscopic characteristics, the major drawback of LDNCs is their low quantum yield (QY) due to the low extinction coefficient of lanthanide ions in the NIR region and energy lost during multi non-radiative electronic transitions (Wang et al., 2011). In recent years, researchers have been devoted to solving this drawback, such as constructing core-shell structures (Chen et al., 2015; Zhuo et al., 2017) and anchoring NIR dyes on the surface of nanocrystals (Wu X. et al., 2016; Hazra et al., 2018). Among countless methods for improving the QY (Zhang et al., 2010; Yin et al., 2016), metal ion doping is the simplest since it is carried out in fewer modulation steps (Niu et al., 2012; Ding et al., 2015), and it only weakly changes the shape of the LDNCs. Moreover, metal ion doping can integrate with other methods to simultaneously improve the QY of LDNCs.

Here, we aim to provide a summary regarding the recent progress in metal ion doping for improving the QY of LDNCs. In this mini review, we first discuss the two mechanisms of metal ion doping: host lattice manipulation and energy transfer modulation. More cases outlining how to carry out metal ion doping are also included. Finally, we discuss the challenges and future applications of LDNCs with metal ion doping. We also hope that this mini review can serve as a guide for researchers who are involved in metal ion doping for LDNCs study.

MECHANISMS OF LUMINESCENCE ENHANCEMENT BY DOPING METAL IONS

Host Lattice Manipulation

The optical characteristic of lanthanide NPs is derived from its intrinsic trivalent lanthanide ions (Ln^{3+}), which are considered the most stable state of lanthanides. Ln^{3+} ions have the configuration of $[Xe]4f^n$, $n = 0$–14, and the electronic transitions in the 4f orbital are diverse, resulting in the emissions from these electronic transitions being distributed within wide wavelengths (Hatanaka and Yabushita, 2014). There are several decisive factors for the energy levels of free Ln^{3+} ions in their 4f orbitals, like the Coulombic interaction and the spin-orbit coupling between f electrons (Han et al., 2014), which are rather sensitive to minor changes of the host lattice.

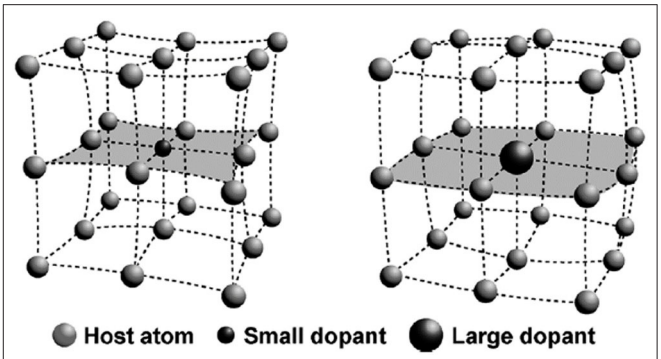

FIGURE 1 | The contraction (left) and expansion (right) of the host lattice after adopting a small or large dopant. This figure was adopted from Han et al. (2014).

As for metal ion doping, the lanthanide ions sites in the host lattice are replaced, and the host lattice may be distorted and its interplanar spacing will change due to the radius difference between the metal ions and lanthanide ions. When using a high metal ion concentration, the lattice gap will be filled with metal ions (Dou and Zhang, 2011). Thus, the asymmetric host lattice affects the environment of inner lanthanide ions, leading to the increase of lanthanide luminescence. For example, the probability of the electric dipole transition can be dramatically increased by the asymmetric crystal field.

By disrupting the symmetric environment of the central ions, the mixing of the opposite-parity configurations can break the Laporte selection rule (Harris and Bertolucci, 1978), which was applied to a centrosymmetric system where the electric dipole transitions are barely allowed. Therefore, reasonably, with the introduction of the asymmetric crystal field, the probability of the electric dipole transition can be dramatically increased. Then the luminescence intensity of the nanocrystal can be enhanced by increasing the asymmetry around the lanthanides.

For doping metal ions with different radii, the host lattice may undergo different changes. The host lattice will shrink after doping metal ions with a small radius, whereas metal ions with a large radius lead to the expansion of the host lattice (**Figure 1**). The changing of the host lattice dramatically alters the splitting of the crystal field and the coordination environment, resulting in the increase of the probability of the electric dipole transition, and then enhancing the luminescence intensity (Han et al., 2014).

Energy Transfer Modulation

All fluorescence light usually follows the well-known Stokes' law which illustrates that the energy level of the excitation photons is higher than the emitted photons, whereas the doping of lanthanides or transition metal ions can violate this principle under a properly powered excitation, generating anti-Stokes emission.

The anti-Stokes process is a multi-ions process. In principle, the premise of energy transfer is that the absorption and emission are not in the same center, and it can take place without

charge transport. Moreover, energy transfer can be divided into radiative, non-radiative, resonant, and phonon-assisted energy transfer (Hatanaka and Yabushita, 2014). The energy transfer process contains two steps, whose natural efficiencies are $\leq$1. Therefore, finding a way to reduce the unwanted cross-relaxation type of energy transfer and converting this energy into a certain wavelength of emission improves the luminescent intensity by energy transfer modulation. Higher doping of activator ions could be a potential candidate that can lead to the enhancement of luminescence, whereas the quenching effect has been a hindrance in achieving this goal. Therefore, owing to the macroscopic diffusion process, the overall efficiency enhancement brought about by energy transfer can only be obtained through spatial averaging (Auzel, 2004).

The metal ion doping in the LDNCs can modulate the energy transfer between the doped metal ions and other lanthanide ions in the host lattice (Han et al., 2014). This modulation depends on controlling the re-distribution of all ions in the host lattice (Auzel, 2004). Specifically, the distance between activators and sensitizers in the host lattice is changed by doping metal ions, neither too long nor too short, which is crucial for boosting the luminescence intensity. For example, the increase of doping ions can facilitate the harmful cross-relaxation between dopants due to their proximity (Qin et al., 2019). For another method of manipulating the ion distribution reported by Qin et al. (2014), they indicate that, in a particular host lattice, the lanthanide ions tend to segregate in the form of chains or clusters upon host cation substitution. As a result, the five-photon upconversion (Wang et al., 2014) and single band emission (Wu M. et al., 2016) can be achieved.

Moreover, the re-distribution of activators decreases the probability of cross-relaxation, and a photon energy depletion pathway arises from activators or between an activator and a defect in the host lattice. Thus, the lower cross-relaxation probability allows us to use a higher activator concentration so that the luminescence intensity enhances, which is also called breaking the concentration quenching effect (Auzel, 2004). Most importantly, the d-d electronic transition of metal ions may be involved in the energy transfer between activators and sensitizers in the host lattice, and it is an effective energy transfer pathway (Han et al., 2014). So, if the energy transfer pathway produced by the doped transition metal ions works out, the upconversion luminescence of the LDNCs should be enhanced.

Unlike the normal f-f transition, the emission intensity of the hypersensitive transition will change dramatically even if its surrounding environment has a tiny change. By changing the environment around the rare-earth ions, a hypersensitive transition can be produced. The doping of different kinds of metal ions should be an easy way to alter the environment around the rare-earth ions. It is well-known that the upconversion luminescence intensity of lanthanide ions is mainly dependent on electronic transition probabilities (Hatanaka and Yabushita, 2014). Owing to their unique properties, increasing the probability of hypersensitive transition will be beneficial in increasing the luminescence intensity of LDNCs.

CASES OF METAL ION-DOPED LANTHANIDE NANOCRYSTALS AND THEIR BIOAPPLICATIONS

Li^+ Ion Doping

The radius of metal ions has a significant impact on the luminescent intensity of LDNCs through changing the symmetry of its host lattice around the lanthanide ions (**Figures 2A–D**). This impact was verified by doping ions, including Li^+, Ca^{2+} (Zhao et al., 2020), and Bi^{3+} ions (Jiang et al., 2012; Niu et al., 2012) into the host lattice. For example, the Li^+ ion owns the smallest alkali ionic radius, around 0.73–1.06 Å, enabling a high doped concentration in the host lattice (Dou and Zhang, 2011). Chen et al. reported that 5% of Li^+-doped Y_2O_3:Yb,Er nanocrystals (NCs) (Chen et al., 2008) show 25 times and 8 times more luminescent intensity enhancements for the green and red emissions, respectively, in comparison with Y_2O_3:Yb,Er NCs without Li^+ doping. The similar luminescence enhancement was also found in Li^+-doped ZrO_2 (Liu et al., 2011), and $NaGd(MoO_4)_2$ (Chen et al., 2020) host lattices. However, the symmetry of the host lattice may undergo different changes when using different synthesized temperatures. For example, at 1,073 K, the Er^{3+}-Li^+ co-doped TiO_2 NCs showed an accelerated phase transition from anatase to rutile when increasing the Li^+ concentration, resulting in the decrease of luminescence intensity. At 1,273 K, the phase structure of Er^{3+}-Li^+ co-doped TiO_2 NCs was unchanged no matter what the Li^+ concentration was, yet the crystal field symmetry decreased, resulting in significantly enhanced emission intensities (Cao et al., 2010).

Besides, it was reported that the doping of Li^+ can achieve the enhancement of luminescent intensity at a particular wavelength range. Yin et al. (2012) reported that GdF_3:Er,Yb co-doped with Li^+, with a color-tuned emission from yellow to red, showed a slightly decreased green emission whereas the red emission had a dramatic increase of up to 8-fold. And the red light displayed a deep penetration depth, which was used for the *in vivo* imaging (**Figure 2E**). This phenomenon can be attributed to the energy back transfer process initiated by the doping of Li^+ ions.

As for host lattice materials, a fluoride-based host lattice is an excellent candidate for co-doped Li^+ ions. In 2017, Hu et al. (2017) reported 18 times and 7 times luminescence enhancement of 478 and 804 nm emissions of $NaLuF_4$:Yb,Tm with a 7% Li^+-doped concentration, respectively. Zhao C. et al. (2013) developed 8 times luminescence enhancement of the upconversion emission of 452 nm in $NaYF_4$:Yb,Tm NCs with a Li^+ concentration of 7%. Furthermore, Ding et al. (2015) studied different kinds of lanthanide ions co-doped with Li^+ in an $NaGdF_4$ host lattice crystal, which all afford large enhancement in lanthanide luminescence intensity. Dou and Zhang (2011) have concluded the possible substitution sites of Li^+-doped and K^+-doped ions in an $NaYF_4$ host lattice, respectively, in which the substitution and the interstitial occupation both exist, only related to the concentration of the doping ion. As shown in **Figures 2F,G**, with an increase in Li^+ concentration from 40 to 60%, the morphology of nanocrystals changed from nanorods to nanospheres, and

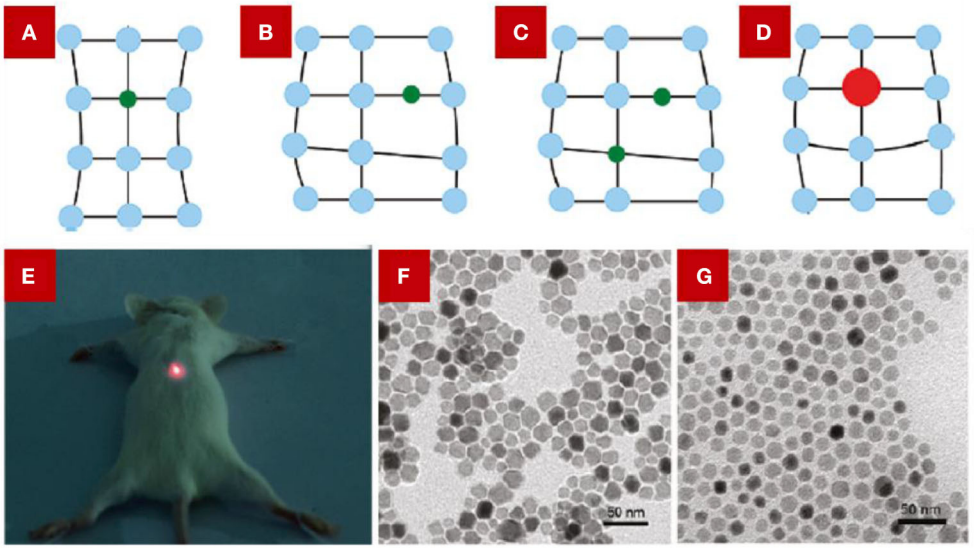

FIGURE 2 | The scheme shows the possible ways of doping alkali ions in the host lattice of $NaYF_4$. **(A)** Substitution by a small atom. **(B)** Interstitial occupation by a small atom. **(C)** Combination of substitution and interstitial occupation. **(D)** Substitution by a large atom. From Dou and Zhang (2011). **(E)** The digital image of an anesthetized mouse under the irradiation of a 980 nm laser. The mouse was injected the GdF_3:Er,Yb co-doped with Li^+ dispersion in the back muscle. **(E)** was adopted from Yin et al. (2012). And **(F,G)** are TEM images of $Na_{(1-x)}Li_xYF_4$:Er,Yb NCs. **(F)** x = 40 mol%, **(G)** x = 60 mol%. **(F,G)** were adopted from Dou and Zhang (2011).

the phase changed from a hexagonal to a cubic phase as well.

What also needs to be considered is the doping efficiency. Wang et al. studied the doping efficiency of Li^+ in the KSc_2F_7 host lattice, they indicated that Li^+ doping efficiency is highly related to its initial concentration (Wang et al., 2017). In general, the actual amount of Li^+ doped into the host lattice is much lower than its initial concentration.

Fe^{3+} ion Doping

Similar to Li^+, Fe^{3+} doping can also alter the symmetry of the host lattice in LDNCs. In an $NaGdF_4$ host lattice, the Fe^{3+} doping can meet the goal of boosting the luminescent intensity through altering the asymmetry around the lanthanide ions, and this enhancement is a general improvement for all emission ranges around the luminescence center (Ramasamy et al., 2013). Interestingly, the synthesis method of LDNCs influences the crystal structure, and thus affects the symmetry of the host lattice after doping Fe^{3+}. For example, the hexagonal $NaYF_4$ became tetragonal after increasing the Fe^{3+} concentration when using a hydrothermal method (Tang et al., 2015). However, the crystal structure of the $NaGdF_4$ host lattice is inert to the thermal decomposition even using a high Fe^{3+} concentration (**Figures 3A,B**) (Ramasamy et al., 2013). In addition, the doping of Fe^{3+} can tailor the crystal field environment of Er^{3+}, which helps the hypersensitive transition, leading to the enhancement of upconversion luminescence (Ramasamy et al., 2013).

Besides, the Yb^{3+}-Fe^{3+} dimer was formed in the host lattice, which can be applied to modulate the energy transfer between activators and sensitizers, in particular modulating the energy transfer for the red emission (Tang et al., 2015; Du et al., 2019). For the Fe^{3+}-doped $NaYF_4$:Yb,Er NCs (**Figure 3C**), the existence of a Yb^{3+}-Fe^{3+} dimer can be deduced from the much lower n value (n represents the number of phonons process) of green/red emissions of the hydrothermal method-synthesized LDNCs compared with the traditional two-phonon process. The energy level of $|^2F_{7/2}, {}^4T_{1g}>$ of the Yb^{3+}-Fe^{3+} dimer receives the photon energy from the energy level of $^2H_{11/2}$ of Er^{3+}, and the received photon energy can partially return to the energy level of $^4F_{7/2}$ and $^4S_{3/2}$ of Er^{3+}. After the photon energy in $^4F_{7/2}$ and $^4S_{3/2}$ relaxes to the $^4F_{9/2}$ level, the probability of the electronic transition between $^4F_{9/2}$ and $^4I_{15/2}$ of Er^{3+} increases, which contributes to increase the intensity of the red emission of Er^{3+}. Meanwhile, the green/red emission of Fe^{3+}-doped NCs synthesized by the thermal decomposition method has been confirmed as a two-phonon process (Ramasamy et al., 2013), which has less correlation with the Fe^{3+} concentration. However, the Fe^{3+}-doped NCs synthesized by the hydrothermal method show the potential relationship between the concentration of Fe^{3+} and the phonon process, suggesting that the formation of the Yb^{3+}-Fe^{3+} dimer might be related to the synthesis method of the LDNCs. Furthermore, the Fe^{3+}-doped NCs were used in the upconversion luminescence (UCL) imaging of HeLa cells (**Figures 3D–F**), which demonstrates a potential application in bioimaging.

Mn^{2+} ion Doping

It was discovered that the Mn^{2+} ion can also modulate the energy transfer between activators and sensitizers in the host lattice of LDNCs (Wang J. et al., 2011). With the example of Mn^{2+}-doped

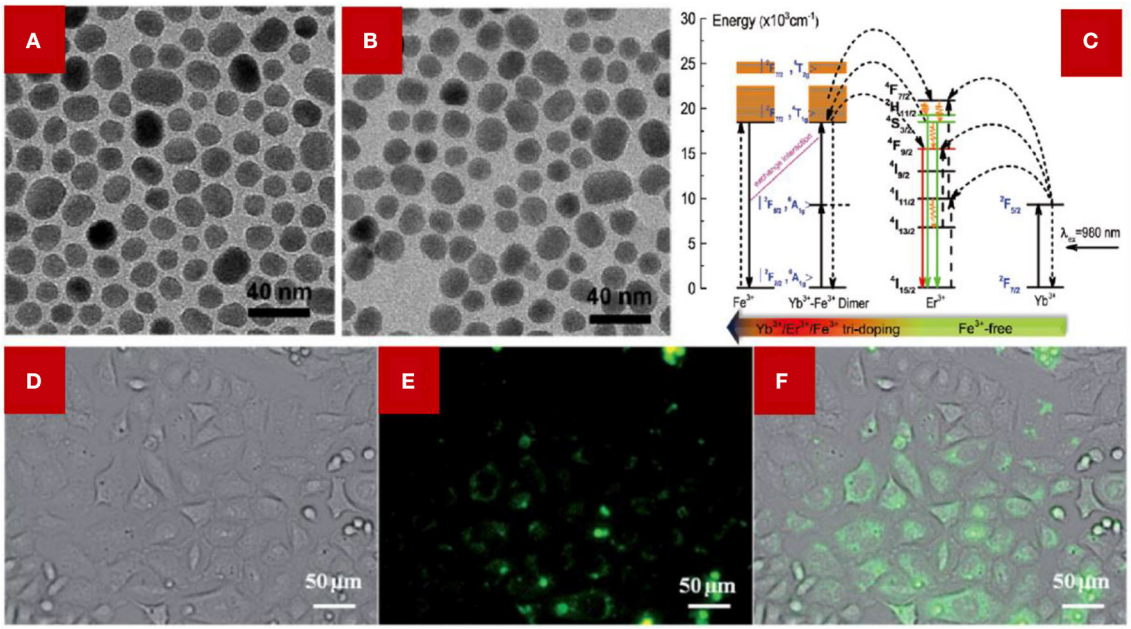

FIGURE 3 | TEM images of $NaGdF_4$:Yb,Er,Fe NCs, **(A)** 0 mol % Fe^{3+} doping; **(B)** 30 mol% Fe^{3+}. Adopted from Ramasamy et al. (2013) **(C)** Illustration of the proposed energy transfer mechanism of Fe^{3+} co-doped $NaYF_4$:Yb,Er NCs and $NaYF_4$:Yb,Er NCs without Fe^{3+} doped. The color arrow in the below indicates the Fe^{3+} content varied from 0 to 5–40 mol%. **(C)** was adopted from Tang et al. (2015); **(D–F)** $NaGdF_4$:Yb,Er,Fe NCs were used for cellular luminescence imaging. **(D)** The bright field image of HeLa cells incubated with $NaGdF_4$:Yb,Er,Fe NCs. **(E)** The confocal fluorescence image. The HeLa cells were irradiated with a 980 nm laser. **(F)** The merging of **(D,E)**. **(D,E)** were adopted from Ramasamy et al. (2013).

$NaYF_4$:Yb/Er NCs (**Figures 4A,B**), the single red emission can be ascribed to the energy transfer from the $^2H_{9/2}$ and $^4S_{3/2}$ energy level of Er^{3+} to the $^4T_1$ energy level of Mn^{2+}, and then the received photon energy in $^4T_1$ transfers back to the $^4F_{9/2}$ energy level of Er^{3+}, which contributes to the red emission of the $NaYF_4$:Yb/Er NCs ($^4F_{9/2} \rightarrow {}^4I_{15/2}$) (Tian et al., 2012). The single red emission phenomenon was also confirmed in the Mn^{2+}-doped $NaYF_4$ (Zeng et al., 2014), $NaGdF_4$ (Li et al., 2015), and $NaLuF_4$ (Zeng et al., 2014) host lattices.

Owing to the sensitivity of Mn^{2+} to the ligand field (Zhou et al., 2018), the energy level state of $^4T_1$ is different in different host lattices, such as $NaGdF_4$ or $LiYF_4$. The higher energy level of $^4T_1$ of Mn^{2+} in an $LiYF_4$ host lattice matches the green luminescence energy level of $^4S_{3/2}$ of Er^{3+}, and the lower energy level of $^4T_1$ of Mn^{2+} matches better with the red emission energy level of $^4F_{9/2}$ of Er^{3+} in the $NaGdF_4$ host lattice, and thus explains that the ratio of green and red emission intensity is not a fixed value (Zhou et al., 2018). Thus, the sensitivity of Mn^{2+} endorses the potential application of Mn^{2+} in modulating the energy transfer of different lanthanide ions. Moreover, Mn^{2+} doping can induce the phase transition of the $NaYF_4$ host lattice, from hexagonal to cubic, when using the hydrothermal method. In spite of the fact that the cubic $NaYF_4$ lattice was confirmed to have a lower luminescence efficiency than the hexagonal one, the asymmetry of the $NaYF_4$ changed because the Y^{3+} sites were replaced by Mn^{2+} ions with a smaller radius, then the luminescence intensity increased. Fig. 4a shows the cubic phase of $NaYF_4$:Yb,Er doped with 30 mol% Mn^{2+} ions. The red emission has a higher signal-to-noise ratio and lower autofluorescence than the green emission. Therefore, lanthanide NCs with a single red emission are beneficial for *in vivo* small-animal imaging (**Figures 4C–E**).

RARE EARTH IONS DOPING

Besides activators and sensitizers, doping other rare earth ions into a host lattice is also an efficient way to boost the luminescence intensity. For example, Sc^{3+} has been widely studied because it has the smallest radius among all the rare earth ions, meaning it can be easily doped into a host lattice. With a similar host lattice manipulation mechanism, the symmetry of an $NaYF_4$ host lattice was broken when doping Sc^{3+} into $NaYF_4$:Er,Yb NCs; thus, the overall emission intensity of $NaYF_4$:Er,Yb NCs showed a 2-fold enhancement when doped with 10% mol Sc^{3+} (Huang et al., 2010).

And other lanthanide ions, for example, activator ions with a high doping concentration such as Er^{3+}, Tm^{3+}, and Ho^{3+}, have been used to accept photon energy from sensitizer ions. However, the high concentration activator ions lead to the concentration quenching effect that is generated from cross-relaxation between activator ions. Zhao J. et al. (2013) built a combined system with micro-structured optical fiber (**Figure 5A**), which confines the high-power laser into a micrometer-sized circle. They demonstrated that a 70-fold enhanced luminescence intensity was obtained with high concentration doping of 8% mol Tm^{3+}. This method solved the quenching effect using a high-power

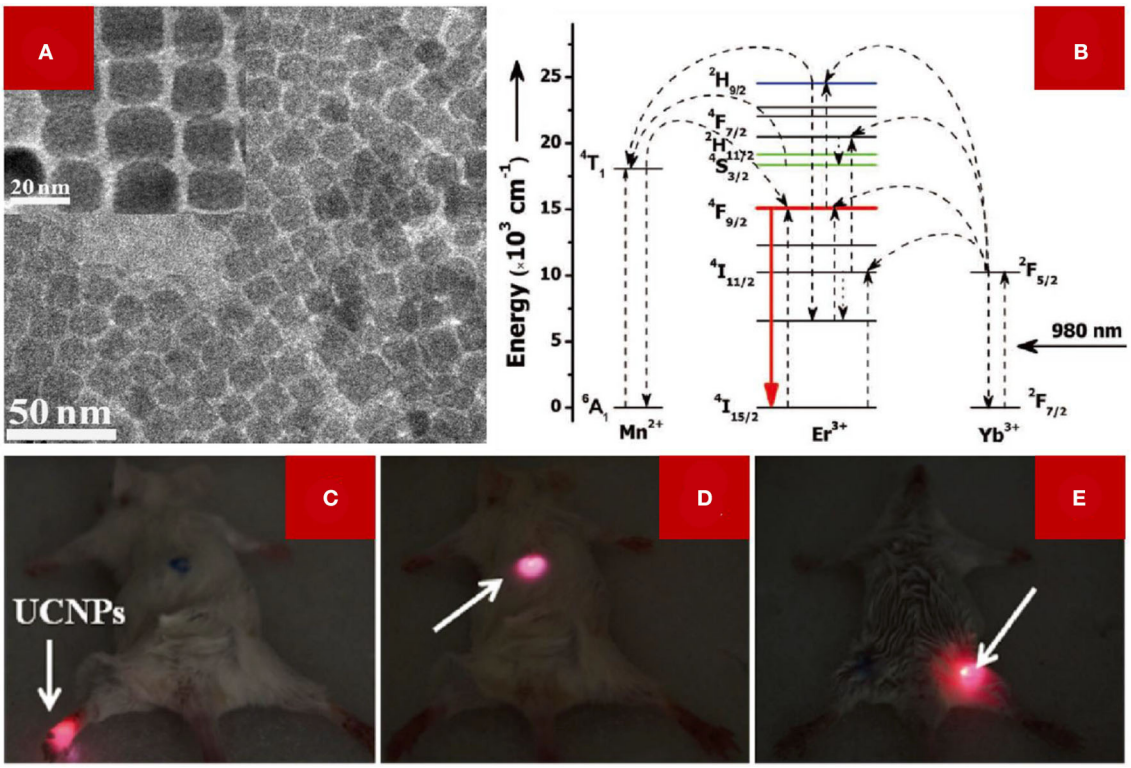

FIGURE 4 | (A) The TEM image (inset: HRTEM image) of $NaYF_4$:Er,Yb NCs doped with 30 mol% Mn^{2+} ions. **(B)** Schematic illustration of the mechanism of single red emission of Mn^{2+}-doped $NaYF_4$: Yb/Er NCs. **(C–E)** Small animal imaging of Kunming mouse with irradiation of a 980 nm laser. The arrow indicates the injected site of the LDNCs dispersion. **(A–E)** were adopted from Tian et al. (2012).

pump up to 2.5 10^6 W/cm^2. The quenching effect is mainly caused by the cross-relaxation of the $^1G_4$ to $^3H_4$ and $^3H_6$ to $^3H_5$ transitions, which usually occur under low-power irradiation (**Figure 5B**). For the high-power laser, the $^3H_4$ energy level is more likely to be promoted to a higher level, which leads to the absence of cross-relaxation and the enhanced upconversion emission intensity as well. Other similar results were illustrated, like the high doping level of Yb^{3+}, to enhance the luminescence of a sub 10 nm matrix, and the authors claimed that the enhanced upconversion emission intensity was endorsed by the energy transfer from Yb^{3+} to Tm^{3+} (Zhai et al., 2014).

In addition, the overlap between the energy levels of different rare earth ions was studied. Cheng et al. (2018) demonstrated an energy level overlap of Er^{3+} and Ho^{3+}, which lead to enhanced upconversion luminescence. **Figures 5C,D** show the TEM images of different concentrations of Ho^{3+}-doped $NaYF_4$:Yb,Er. Because of the similar ion sizes of Er^{3+} and Ho^{3+}, the host lattice manipulation should be excluded. Under excitation at 1,532 nm (the energy can only be absorbed by Er^{3+}), part of the energy is accumulated at the $^2H_{11/2}$ and $^4F_{9/2}$ energy levels of the over-doped Er^{3+} ion, then the energy could be transferred to the $^5F_4/^5S_2$ and $^5F_5$ energy levels of the co-doped Ho^{3+} ions. Then the emissions at 544/550 and 648 nm, which are produced by Ho^{3+}, overlapped with the emissions of Er^{3+} at 525/545 and 660 nm (**Figures 5F,G**). Therefore, the enhanced upconversion emissions of Er^{3+} and Ho^{3+} co-doped nanocrystals can be ascribed to the dual contribution from both Ho^{3+} and Er^{3+} ions.

As for the downshifting luminescence of lanthanide ions, the gadolinium-based host lattice has been widely studied due to its optically active Gd^{3+} sublattices (Wang F. et al., 2007). The energy transfer between Ce^{3+} and Ln^{3+} (Ln = Tb, Eu, Sm, or Dy) can be quickly achieved by a Gd^{3+} sublattice over a long distance. One of the benefits that the Gd^{3+} sublattice affords is that migrating energy can be trapped at a rather low doping concentration. Also, Gd^{3+} can act as an intermediary state to solve electron transfer quenching like the energy transfer from Ce^{3+} to Eu^{3+} (Wang F. et al., 2007). Ce^{3+} can also promote the energy transfer between activators and sensitizers. In 2019, Li et al. (2019) reported an enhanced downshifting emission located at ∼1,525 nm by doping Ce^{3+} into $NaLuF_4$:Gd/Yb/Er nanorods. The ∼1,525 nm second near-infrared (NIR-II) emission was produced from the electronic transition between the excited state $^4I_{13/2}$ to $^4I_{15/2}$ of Er^{3+}. However, the energy gap between the ground state $^2F_{5/2}$ and the excited state $^2F_{7/2}$ of Ce^{3+} matches well with the energy difference between the electronic transition of $^4I_{11/2} \rightarrow {}^4I_{13/2}$ of Er^{3+}. The excited state $^4I_{11/2}$ of Er^{3+} could suffer an efficient non-radiative phonon-assisted cross-relaxation process, resulting in the significantly accumulated excited state $^4I_{13/2}$ of Er^{3+}. Therefore, the electronic transition of $^4I_{13/2}$

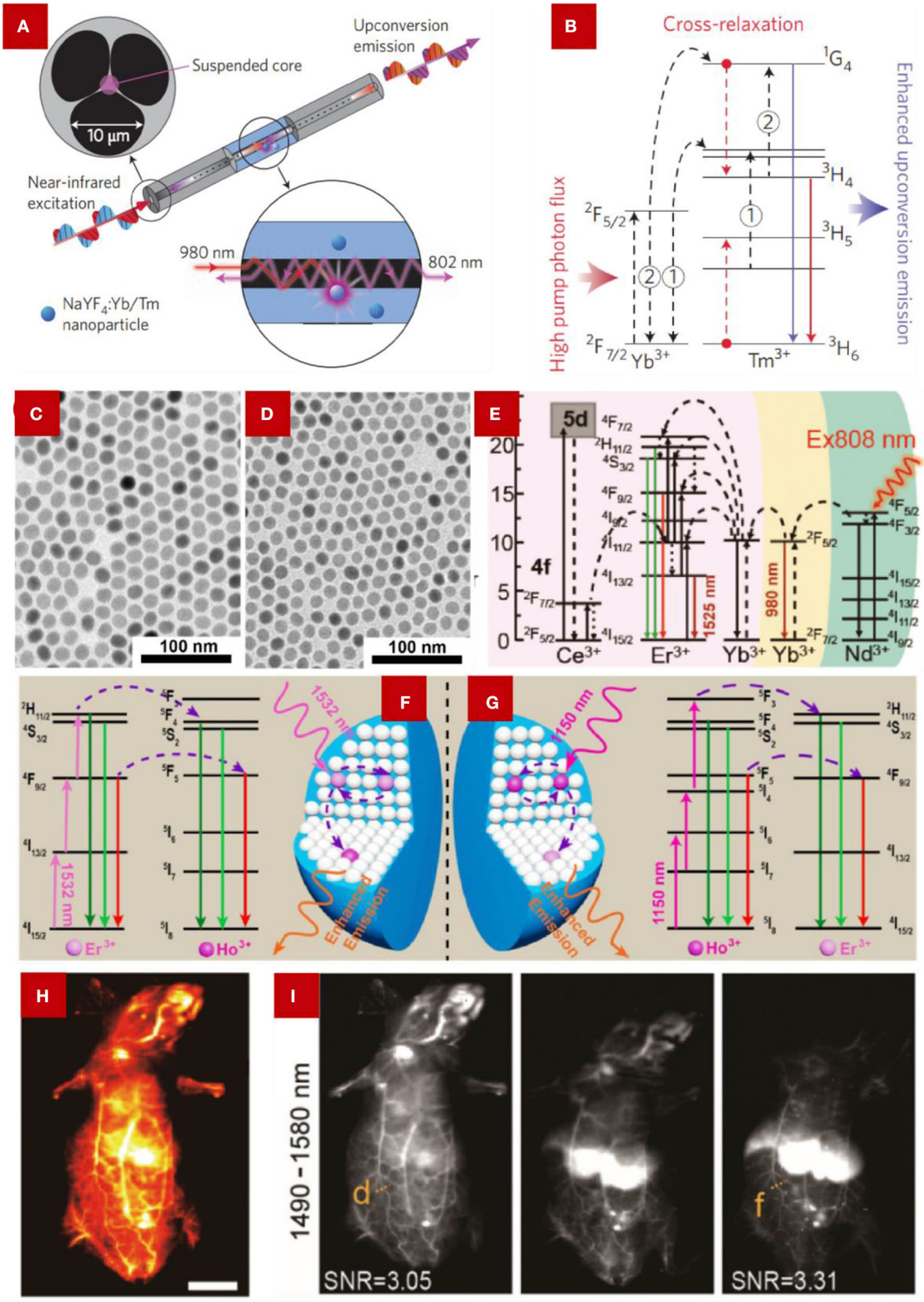

FIGURE 5 | (A) Schematic illustration of the integrated system with the micro-structured optical fiber with $NaYF_4$:Yb/Tm nanoparticles and **(B)** the simplified mechanism of the energy transfer between Yb^{3+} and Tm^{3+} under 980 nm excitation, 1 and 2 represent two subsequent energy-transfer processes from Yb^{3+} to

(Continued)

FIGURE 5 | Tm^{3+} ions. From Zhang and Liu (2013). TEM images of **(C)** $NaYF_4$:Er/Ho (10/0.2 mol%) NCs, **(D)** $NaYF_4$:Er/Ho (10/1 mol%) NCs. **(C,D)** were adopted from Cheng et al. (2018). **(E)** Schematic illustration of energy transfer in Ce^{3+}-doped $NaYbF_4$:Ce,Er NCs for boosting the ~1,525 nm emission. **(C)** were adopted from Cao et al. (2020). **(F,G)** Illustration of the scheme of the energy transfer process of Er^{3+} and Ho^{3+} under the irradiation of 1,532 and 1,150 nm, respectively. From Cheng et al. (2018). **(H)** Blood vessels imaging using $NaYbF_4$:Er,Ce@$NaYF_4$:Yb@$NaYF_4$:Nd NCs. **(I)** NIR region luminescence collected from different time points (10 min, 4 h, 10 h). The emission light was collected between the 1,490–1,580 nm regions, with the excitation of an 808 nm laser. **(H,I)** were adopted from Cao et al. (2020).

TABLE 1 | The summary of doping different metal ions into suitable host lattices and their possible mechanism for enhanced luminescence.

Metal ions	Host lattice	Crystal phase	Synthesized methods	Possible mechanism
Li^+	ZrO_2 (Liu et al., 2011)	Monoclinic phase Tetragonal phase	Sol-gel process	Host lattice manipulation
	$BaTiO_3$ (Sun et al., 2011)	Cubic phase	Sol-gel process	
	Y_2O_3 (Chen et al., 2008)	Cubic phase	–	
	$NaYF_4$ (Dou and Zhang, 2011; Zhao C. et al., 2013)	Hexagonal phase	High temperature thermal-decomposition method	
	$NaGdF_4$ (Ding et al., 2015)	Hexagonal phase	Co-precipitation method	
	$NaLuF_4$ (Hu et al., 2017)	Hexagonal phase	Solvothermal method	
	TiO_2 (Cao et al., 2010)	Anatase phase Rutile phase	Sol-gel process	
	GdF_3 (Yin et al., 2012)	Orthorhombic phase	Hydrothermal procedure	
Fe^{3+}	$NaBiF_4$ (Du et al., 2019)	Hexagonal phase	Chemical precipitation method	Host lattice manipulation, energy transfer modulation
	$NaGdF_4$ (Ramasamy et al., 2013)	Hexagonal phase	High temperature thermal-decomposition method	
	$NaYF_4$ (Tang et al., 2015)	Hexagonal phase Cubic phase	Hydrothermal method	
Mn^{2+}	$NaYF_4$ (Tian et al., 2012; Zeng et al., 2014)	Hexagonal phase Cubic phase	Solvothermal method	Host lattice manipulation, energy transfer modulation
	$NaLuF_4$ (Zeng et al., 2014)	Hexagonal phase Cubic phase	Hydrothermal method	
	$NaGdF_4$ (Li et al., 2015)	Cubic phase	Thermal decomposition	
	$NaYbF_4$ (Zeng et al., 2014)	Hexagonal phase Cubic phase	Hydrothermal method	
	$NaMnF_3$ (Zhang et al., 2012)	Cubic phase	High temperature thermal-decomposition method	
	$KMnF_3$ (Ning et al., 2020)	Cubic phase	High temperature thermal-decomposition method	
	$LiYF_4$ (Zhou et al., 2018)	Tetragonal phase	Thermal decomposition	
Zn^{2+}	$NaYbF_4$ (Zhong et al., 2019)	Cubic phase	High temperature thermal-decomposition method	Host lattice manipulation
Ca^{2+}	$NaYF_4$ (Zhao et al., 2020)	Cubic phase Hexagonal phase	Co-precipitation method	Host lattice manipulation
Bi^{3+}	$NaYF_4$ (Niu et al., 2012)	Cubic phase Hexagonal phase	Facial microwave reflux method	Host lattice manipulation
Ce^{3+}	$NaYF_4$ (Li et al., 2019)	Hexagonal phase	Hydrothermal process	Energy transfer modulation
	$NaYbF_4$ (Zhong et al., 2017; Li et al., 2019; Cao et al., 2020)	Cubic phase	Thermolysis method	
	$NaLnF_4$ (Li et al., 2019)	Hexagonal phase	Hydrothermal process	
	$NaGdF_4$ (Wang F. et al., 2007; Li et al., 2019)	Hexagonal phase	Hydrothermal process	
Eu^{3+}	$NaErF_4$ (Shang et al., 2018)	Hexagonal phase	High-temperature co-precipitation method	Energy transfer modulation
	$NaGd(MoO_4)_2$ (Chen et al., 2020)	Tetragonal phase	Solid-state reaction method	
Tb^{3+}	$NaYbF_4$ (Zhou B. et al., 2015)	Hexagonal phase	Co-precipitation method	Energy transfer modulation
Ho^{3+}	$NaYF_4$ (Cheng et al., 2018)	Hexagonal phase	High-temperature co-precipitation method	Energy transfer modulation
	$LiYF_4$ (Cheng et al., 2018)	Hexagonal phase	High-temperature co-precipitation method	
Sc^{3+}	$NaYF_4$ (Huang et al., 2010)	Hexagonal phase	Hydrothermal method	Energy transfer modulation
Tm^{3+}	$NaErF_4$ (Chen et al., 2017; Shang et al., 2018; Zhang et al., 2019)	Hexagonal phase	High-temperature co-precipitation method	Energy transfer modulation

$\rightarrow$ $^4I_{15/2}$ of Er^{3+} is also promoted, which helps enhance the ∼1,525 nm emission intensity (**Figure 5E**). Cao et al. (2020) reported a similar result when they synthesized a core-shell structure of NCs, $NaYbF_4$:Er,Ce@$NaYF_4$:Yb@$NaYF_4$:Nd. Under 808 nm excitation, the $NaYbF_4$:Er,Ce@$NaYF_4$:Yb@$NaYF_4$:Nd NCs showed a 10 times luminescence enhancement at 1525 nm than the NCs without doping Ce^{3+}. As the light in the NIR-II window affords a superior signal to noise ratio and lower autofluorescence than the light in the first NIR window, the NIR-II emission gets increasing attention in deep tissue imaging. In **Figures 5H,I**, the blood vessels can be clearly observed by using the $NaYbF_4$:Er,Ce@$NaYF_4$:Yb@$NaYF_4$:Nd NCs, and the resolution can remain up to 0.25 mm even 10 h after the injection. Therefore, these excellent properties provide a potential application for LDNCs in the bioimaging fields.

SUMMERY AND PERSPECTIVES

Through summarizing the recent studies on how to improve the luminescence of LDNCs, breakthroughs have been made in some aspects. In this review, we summarize the recently reported methods on how to boost the upconversion and even downshift luminescence by doping metal ions, and introduce the related two mechanisms of doping in detail (**Table 1**).

Through the manipulation of the host lattice, the metal ions play a significant role in increasing the asymmetry around the lanthanides, therefore, leading to the increase of dipole transition. And for the energy transfer modulation, metal ions improve the overall energy transfer efficiency and decrease the quenching effect by providing an effective pathway in the process of energy transfer.

On the basis of improving emission intensity, some problems, still have not been explained clearly. For example, when introducing metal ions into the main lattice, especially for the mechanism of energy transfer regulation, the influence of the host lattice manipulation should not be ignored, which may disrupt the accuracy of the results. To resolve this effect, it can only be reduced by introducing metal ions with a small difference in the ion radius between the doping and occupied ions. And for ions like Fe^{3+}, the enhancement of luminescence is the result of the combination of the two mechanisms. At the same time, how the metal ion is doped into the host lattice has not been fully explained. Site occupation or lattice filling might both exist in the same host lattice, and the method of metal ion doping has a relatively close relationship with the concentration and radius of the doping ions.

With further exploration of the research, the importance of the NIR-II light also shows itself. For deeper penetration, higher signal-to-noise ratio, and smaller scattering effect, the NIR-II light arouses increasing attention. Therefore, a rapidly growing number of recent studies have focused on improving near infrared luminescence, such as the emission of Er^{3+} at ∼1,530 nm. The application of Er^{3+} in biological imaging is worth exploring. In addition, the enhancement of a certain emission band which was caused by non-radiative transition between two or more different rare earth ions is also the main focus of future research. It is necessary to develop more non-radiative transitions between different rare earth ions with good energy level matching to enhance the desired emission intensity. For now, most studies on the enhanced luminescence have been applied in the biological field, such as bioimaging and biosensing. There are some other applications that have been explored for the broader use of enhanced luminescence, such as anti-counterfeiting (Ding et al., 2020) and finger print latency (Wang et al., 2020), which endorse the importance of enhancing luminescence. Nonetheless, we believe that the rare earth ion-doped upconversion nanomaterials will have a wider range of applications and bright prospects in basic studies and technology fields.

AUTHOR CONTRIBUTIONS

SP collected and read papers, and wrote the draft manuscript. XG and LS outlined the main text content, discussed, and revised the manuscript. All authors contributed to the article and approved the submitted version.

FUNDING

We are grateful for the financial support from the National Natural Science Foundation of China (Grant No. 51872183) and Shuguang scholar of the Shanghai Municipal Education Commission (19SG38).

REFERENCES

Auzel, F. O. (2004). Upconversion and anti-stokes processes with f and d ions in solids. *Chem. Rev.* 104, 139–173. doi: 10.1021/cr020357g

Beija, M., Afonso, C. A. M., and Martinho, J. M. G. (2009). Synthesis and applications of Rhodamine derivatives as fluorescent probes. *Chem. Soc. Rev.* 38, 2410–33. doi: 10.1039/b901612k

Ben, N. G., Adams, S. R., Mark Ellisman, H., and Roger Tsien, Y. (2006). The fluorescent toolbox for assessing protein location and function. *Science* 312, 217–224. doi: 10.1126/science.1124618

Bünzli, J.-C. G. (2010). Lanthanide luminescence for biomedical analyses and imaging. *Chem. Rev.* 110, 2729–2755. doi: 10.1021/cr900362e

Cao, B. S., Feng, Z. Q., He, Y. Y., Li, H., and Dong, B. (2010). Opposite effect of Li^+ codoping on the upconversion emissions of Er^{3+}-doped TiO_2 powders. *J. Sol. Gel Sci. Technol.* 54, 101–104. doi: 10.1007/s10971-010-2163-3

Cao, C., Wu, N., Yuan, W., Gu, Y., Ke, J., Feng, W., et al. (2020). Ln(3+)-doped nanoparticles with enhanced NIR-II luminescence for lighting up blood vessels in mice. *Nanoscale* 12, 8248–8254. doi: 10.1039/D0NR01098G

Chen, G., Liu, H., Liang, H., Somesfalean, G., and Zhang, Z. (2008). Upconversion emission enhancement in $Yb^{3+}Er^{3+}$-codoped Y_2O_3 nanocrystals by tridoping with Li^+ ions. *J. Phys. Chem. C* 112, 12030–12036. doi: 10.1021/jp804064g

Chen, H., Ai, S., Dong, C., Wang, H., Ning, Z., Liu, M., et al. (2020). Eu^{3+}-induced multicolor luminescence properties and enhanced thermal stability in the novel phosphors of $Li_{0.1}Na_{0.9}Gd_{0.5}Tb_{0.5-x}Eux(MoO_4)_2$. *J. Lumin.* 222:117116. doi: 10.1016/j.jlumin.2020.117116

Chen, Q., Xie, X., Huang, B., Liang, L., Han, S., Yi, Z., et al. (2017). Confining excitation energy in Er(3+) -sensitized upconversion nanocrystals through

Tm(3+) -mediated transient energy trapping. *Angew. Chem. Int. Ed.* 56, 7605–7609. doi: 10.1002/anie.201703012

Chen, X., Peng, D., Ju, Q., and Wang, F. (2015). Photon upconversion in core-shell nanoparticles. *Chem. Soc. Rev.* 44, 1318–1330. doi: 10.1039/C4CS00151F

Cheng, X., Ge, H., Wei, Y., Zhang, K., Su, W., Zhou, J., et al. (2018). Design for brighter photon upconversion emissions via energy level overlap of lanthanide ions. *ACS Nano* 12, 10992–10999. doi: 10.1021/acsnano.8b04988

Ding, M., Dong, B., Lu, Y., Yang, X., Yuan, Y., Bai, W., et al. (2020). Energy manipulation in lanthanide-doped core-shell nanoparticles for tunable dual-mode luminescence toward advanced anti-counterfeiting. *Adv. Mater.* 2020:2002121. doi: 10.1002/adma.202002121

Ding, M., Ni, Y., Song, Y., Liu, X., Cui, T., Chen, D., et al. (2015). Li + ions doping core–shell nanostructures: an approach to significantly enhance upconversion luminescence of lanthanide-doped nanocrystals. *J. Alloy. Compd.* 623, 42–48. doi: 10.1016/j.jallcom.2014.10.089

Dou, Q., and Zhang, Y. (2011). Tuning of the structure and emission spectra of upconversion nanocrystals by alkali ion doping. *Langmuir* 27, 13236–13241. doi: 10.1021/la201910t

Du, P., Zhang, Q., Wang, X., Luo, L., and Li, W. (2019). Upconversion luminescence, temperature sensing and internal heating behaviors of $Er^{3+}/Yb^{3+}/Fe^{3+}$-tridoped $NaBiF_4$ nanoparticles. *J. Alloy. Compd.* 805, 171–179. doi: 10.1016/j.jallcom.2019.07.054

Fan, Y., Wang, P., Lu, Y., Wang, R., Zhou, L., Zheng, X., et al. (2018). Lifetime-engineered NIR-II nanoparticles unlock multiplexed in vivo imaging. *Nat. Nanotechnol.* 13, 941–946. doi: 10.1038/s41565-018-0221-0

Fan, Y., and Zhang, F. (2019). A new generation of NIR-II probes: lanthanide-based nanocrystals for bioimaging and biosensing. *Adv. Opt. Mater.* 7:1801417. doi: 10.1002/adom.201801417

Han, S., Deng, R., Xie, X., and Liu, X. (2014). Enhancing luminescence in lanthanide-doped upconversion nanoparticles. *Angew. Chem. Int. Ed.* 53, 11702–11715. doi: 10.1002/anie.201403408

Harris, D. C., and Bertolucci, M. D. (1978). *Symmetry and Spectroscopy*. New York, NY: Oxford University Press.

Hatanaka, M., and Yabushita, S. (2014). Mechanisms of f–f hypersensitive transition intensities of lanthanide trihalide molecules: a spin–orbit configuration interaction study. *Theor. Chem. Acc.* 133:1517. doi: 10.1007/s00214-014-1517-2

Hazra, C., Ullah, S., Serge Correales, Y. E., Caetano, L. G., and Ribeiro, S. J. L. (2018). Enhanced NIR-I emission from water-dispersible NIR-II dye-sensitized core/active shell upconverting nanoparticles. *J. Mate. Chem. C* 6, 4777–4785. doi: 10.1039/C8TC00335A

Hildebrandt, N., Spillmann, C. M., Algar, W. R., Pons, T., Stewart, M. H., Oh, E., et al. (2017). Energy transfer with semiconductor quantum dot bioconjugates: a versatile platform for biosensing, energy harvesting, and other developing applications. *Chem. Rev.* 117, 536–711. doi: 10.1021/acs.chemrev.6b00030

Hu, M., Ma, D., Cheng, Y., Liu, C., Zhang, Z., Cai, Y., et al. (2017). Synergistically enhanced upconversion luminescence in Li(+)-doped core-shell-structured ultrasmall nanoprobes for dual-mode deep tissue fluorescence/CT imaging. *J. Mater. Chem. B* 5, 2662–2670. doi: 10.1039/C6TB02976K

Huang, Q., Yu, J., Ma, E., and Lin, K. (2010). Synthesis and characterization of highly efficient near-infrared upconversion $Sc^{3+}/Er^{3+}/Yb^{3+}$ tridoped $NaYF_4$. *J. Phys. Chem. C* 4719–4724. doi: 10.1021/jp908645h

Jiang, L., Xiao, S., Yang, X., Ding, J., and Dong, K. (2012). Enhancement of up-conversion luminescence in Zn_2SiO_4:Yb^{3+}, Er^{3+} by co-doping with Li^+ or Bi^{3+}. *Appl. Phys. B* 107, 477–481. doi: 10.1007/s00340-012-4986-9

Kobayashi, H., Kosaka, N., Ogawa, M., Morgan, N. Y., Smith, P. D., Murray, C. B., et al. (2009). *In vivo* multiple color lymphatic imaging using upconverting nanocrystals. *J. Mater. Chem.* 19:6481. doi: 10.1039/b910512c

Li, X., Liu, X., Chevrier, D. M., Qin, X., Xie, X., Song, S., et al. (2015). Energy migration upconversion in manganese(II)-doped nanoparticles. *Angew. Chem. Int. Ed.* 54, 13312–13317. doi: 10.1002/anie.201507176

Li, Y., Zeng, S., and Hao, J. (2019). Non-invasive optical guided tumor metastasis/vessel imaging by using lanthanide nanoprobe with enhanced down-shifting emission beyond 1500 nm. *ACS Nano* 13, 248–259. doi: 10.1021/acsnano.8b05431

Liu, L., Wang, Y., Zhang, X., Yang, K., Bai, Y., Huang, C., et al. (2011). Efficient two-color luminescence of $Er^{3+}/Yb^{3+}/Li^+$:ZrO_2 nanocrystals. *Opt. Mater.* 33, 1234–1238. doi: 10.1016/j.optmat.2011.02.019

Ning, H., Jing, L., Hou, Y., Kalytchuk, S., Li, Y., Huang, X., et al. (2020). Manganese-mediated growth of ZnS shell on $KMnF_3$:Yb,Er cores toward enhanced up/downconversion luminescence. *ACS Appl. Mater. Inter.* 12, 11934–11944. doi: 10.1021/acsami.9b21832

Niu, N., He, F., Gai, S., Li, C., Zhang, X., Huang, S., et al. (2012). Rapid microwave reflux process for the synthesis of pure hexagonal $NaYF_4$:Yb^{3+},Ln^{3+},Bi^{3+} (Ln^{3+} = Er^{3+}, Tm^{3+}, Ho^{3+}) and its enhanced UC luminescence. *J. Mater. Chem.* 22:21613. doi: 10.1039/c2jm34653b

Qin, W.-P., Liu, Z.-Y., Sin, C.-N., Wu, C.-F., Qin, G.-S., Chen, Z., et al. (2014). Multi-ion cooperative processes in Yb^{3+} clusters. *Light Sci. Appl.* 3:e193. doi: 10.1038/lsa.2014.74

Qin, X., Xu, J., Wu, Y., and Liu, X. (2019). Energy-transfer editing in lanthanide-activated upconversion nanocrystals: a toolbox for emerging applications. *ACS Cent. Sci.* 5, 29–42. doi: 10.1021/acscentsci.8b00827

Ramasamy, P., Chandra, P., Rhee, S. W., and Kim, J. (2013). Enhanced upconversion luminescence in $NaGdF_4$:Yb,Er nanocrystals by Fe^{3+} doping and their application in bioimaging. *Nanoscale* 5, 8711–8717. doi: 10.1039/c3nr01608k

Shang, Y., Hao, S., Lv, W., Chen, T., Tian, L., Lei, Z., et al. (2018). Confining excitation energy of Er^{3+}-sensitized upconversion nanoparticles through introducing various energy trapping centers. *J. Mater. Chem. C* 6, 3869–3875. doi: 10.1039/C7TC05742C

Su, Q., Feng, W., Yang, D., and Li, F. (2017). Resonance energy transfer in upconversion nanoplatforms for selective biodetection. *Acc. Chem. Res.* 50, 32–40. doi: 10.1021/acs.accounts.6b00382

Sun, Q., Chen, X., Liu, Z., Wang, F., Jiang, Z., and Wang, C. (2011). Enhancement of the upconversion luminescence intensity in Er^{3+} doped $BaTiO_3$ nanocrystals by codoping with Li^+ ions. *J. Alloy. Compd.* 509, 5336–5340. doi: 10.1016/j.jallcom.2010.12.212

Tang, J., Chen, L., Li, J., Wang, Z., Zhang, J., Zhang, L., et al. (2015). Selectively enhanced red upconversion luminescence and phase/size manipulation via Fe(3+) doping in $NaYF_4$:Yb,Er nanocrystals. *Nanoscale* 7, 14752–14759. doi: 10.1039/C5NR04125B

Terai, T., and Nagano, T. (2008). Fluorescent probes for bioimaging applications. *Curr. Opin. Chem. Biol.* 12, 515–521. doi: 10.1016/j.cbpa.2008.08.007

Tian, G., Gu, Z., Zhou, L., Yin, W., Liu, X., Yan, L., et al. (2012). Mn^{2+} dopant-controlled synthesis of $NaYF_4$:Yb/Er upconversion nanoparticles for *in vivo* imaging and drug delivery. *Adv. Mater.* 24, 1226–1231. doi: 10.1002/adma.201104741

Wang, F., Deng, R., Wang, J., Wang, Q., Han, Y., Zhu, H., et al. (2011). Tuning upconversion through energy migration in core-shell nanoparticles. *Nat. Mater.* 10, 968–973. doi: 10.1038/nmat3149

Wang, F., Fan, X., Wang, M., and Zhang, Y. (2007). Multicolour PEI/$NaGdF_4$:Ce^{3+},Ln^{3+}nanocrystals by single-wavelength excitation. *Nanotechnology* 18:025701. doi: 10.1088/0957-4484/18/2/025701

Wang, J., Deng, R., MacDonald, M. A., Chen, B., Yuan, J., Wang, F., et al. (2014). Enhancing multiphoton upconversion through energy clustering at sublattice level. *Nat. Mater.* 13, 157–162. doi: 10.1038/nmat3804

Wang, J., Wang, F., Wang, C., Liu, Z., and Liu, X. (2011). Single-band upconversion emission in lanthanide-doped $KMnF_3$ nanocrystals. *Angew. Chem. Int. Ed.* 50, 10369–10372. doi: 10.1002/anie.201104192

Wang, X., Yan, L., Liu, S., Zhang, P., Huang, R., and Zhou, B. (2020). Enhancing energy migration upconversion through a migratory interlayer in the core-shell-shell nanostructure towards latent fingerprinting. *Nanoscale* 12, 18807–18814. doi: 10.1039/D0NR03817B

Wang, Y., Wei, T., Cheng, X., Ma, H., Pan, Y., Xie, J., et al. (2017). Insights into Li^+-induced morphology evolution and upconversion luminescence enhancement of KSc_2F_7:Yb/Er nanocrystals. *J. Mater. Chem. C* 5, 3503–3508. doi: 10.1039/C7TC00649G

Weissleder, R., and Pittet, M. J. (2008). Imaging in the era of molecular oncology. *Nature* 452, 580–589. doi: 10.1038/nature06917

Wu, M., Song, E. H., Chen, Z. T., Ding, S., Ye, S., Zhou, J. J., et al. (2016). Single-band red upconversion luminescence of Yb^{3+}-Er^{3+}via nonequivalent substitution in perovskite $KMgF_3$ nanocrystals. *J. Mater. Chem. C* 4, 1675–1684. doi: 10.1039/C5TC03600C

Wu, X., Zhang, Y., Takle, K., Bilsel, O., Li, Z., Lee, H., et al. (2016). Dye-sensitized core/active shell upconversion nanoparticles for optogenetics and bioimaging applications. *ACS Nano* 10, 1060–1066. doi: 10.1021/acsnano.5b06383

Xu, G., Zeng, S., Zhang, B., Swihart, M. T., Yong, K. T., and Prasad, P. N. (2016). New generation cadmium-free quantum dots for biophotonics and nanomedicine. *Chem. Rev.* 116, 12234–12327. doi: 10.1021/acs.chemrev.6b00290

Yin, W., Zhao, L., Zhou, L., Gu, Z., Liu, X., Tian, G., et al. (2012). Enhanced red emission from GdF_3:Yb^{3+},Er^{3+} upconversion nanocrystals by Li^+ doping and their application for bioimaging. *Chemistry* 18, 9239–9245. doi: 10.1002/chem.201201053

Yin, Z., Li, H., Xu, W., Cui, S., Zhou, D., Chen, X., et al. (2016). Local field modulation induced three-order upconversion enhancement: combining surface plasmon effect and photonic crystal effect. *Adv. Mater.* 28, 2518–2525. doi: 10.1002/adma.201502943

Yuan, L., Lin, W., Zheng, K., He, L., and Huang, W. (2013). Far-red to near infrared analyte-responsive fluorescent probes based on organic fluorophore platforms for fluorescence imaging. *Chem. Soc. Rev.* 42, 622–661. doi: 10.1039/C2CS35313J

Zeng, S., Yi, Z., Lu, W., Qian, C., Wang, H., Rao, L., et al. (2014). Simultaneous realization of phase/size manipulation, upconversion luminescence enhancement, and blood vessel imaging in multifunctional nanoprobes through transition metal Mn^{2+} doping. *Adv. Funct. Mater.* 24, 4051–4059. doi: 10.1002/adfm.201304270

Zhai, X., Liu, S., Zhang, Y., Qin, G., and Qin, W. (2014). Controlled synthesis of ultrasmall hexagonal $NaTm_{0.02}Lu_{0.98-x}Yb_xF_4$ nanocrystals with enhanced upconversion luminescence. *J. Mater. Chem. C* 2:2037. doi: 10.1039/c3tc31760a

Zhang, H., Fan, Y., Pei, P., Sun, C., Lu, L., and Zhang, F. (2019). Tm(3+) -sensitized NIR-II fluorescent nanocrystals for *in vivo* information storage and decoding. *Angew. Chem. Int. Ed.* 58, 10153–10157. doi: 10.1002/anie.201903536

Zhang, H., Li, Y., Ivanov, I. A., Qu, Y., Huang, Y., and Duan, X. (2010). Plasmonic modulation of the upconversion fluorescence in $NaYF_4$:Yb/Tm hexaplate nanocrystals using gold nanoparticles or nanoshells. *Angew. Chem. Int. Ed.* 49, 2865–2868. doi: 10.1002/anie.200905805

Zhang, Y., Lin, J. D., Vijayaragavan, V., Bhakoo, K. K., and Tan, T. T. (2012). Tuning sub-10 nm single-phase $NaMnF_3$ nanocrystals as ultrasensitive hosts for pure intense fluorescence and excellent T_1 magnetic resonance imaging. *Chem. Commun.* 48, 10322–10324. doi: 10.1039/c2cc34858f

Zhang, Y., and Liu, X. (2013). Nanocrystals: shining a light on upconversion. *Nat. Nanotechnol.* 8, 702–703. doi: 10.1038/nnano.2013.199

Zhao, C., Kong, X., Liu, X., Tu, L., Wu, F., Zhang, Y., et al. (2013). Li^+ ion doping: an approach for improving the crystallinity and upconversion emissions of $NaYF_4$:Yb^{3+}, Tm^{3+} nanoparticles. *Nanoscale* 5, 8084–8089. doi: 10.1039/c3nr01916k

Zhao, J., Hu, Y., Lin, S. W., Resch-Genger, U., Zhang, R., Wen, J., et al. (2020). Enhanced luminescence intensity of near-infrared-sensitized upconversion nanoparticles via Ca^{2+} doping for a nitric oxide release platform. *J. Mater. Chem. B.* 2020, 6481–6489. doi: 10.1039/D0TB00088D

Zhao, J., Jin, D., Schartner, E. P., Lu, Y., Liu, Y., Zvyagin, A. V., et al. (2013). Single-nanocrystal sensitivity achieved by enhanced upconversion luminescence. *Nat. Nanotechnol.* 8, 729–734. doi: 10.1038/nnano.2013.171

Zhao, Q., Huang, C., and Li, F. (2011). Phosphorescent heavy-metal complexes for bioimaging. *Chem. Soc. Rev.* 40:2508. doi: 10.1039/c0cs00114g

Zhao, Q., Li, F., and Huang, C. (2010). Phosphorescent chemosensors based on heavy-metal complexes. *Chem. Soc. Rev.* 39, 3007–3030. doi: 10.1039/b915340c

Zhong, Y., Ma, Z., Wang, F., Wang, X., Yang, Y., Liu, Y., et al. (2019). *In vivo* molecular imaging for immunotherapy using ultra-bright near-infrared-IIb rare-earth nanoparticles. *Nat. Biotechnol.* 37, 1322–1331. doi: 10.1038/s41587-019-0262-4

Zhong, Y., Ma, Z., Zhu, S., Yue, J., Zhang, M., Antaris, A., et al. (2017). Boosting the down-shifting luminescence of rare-earth nanocrystals for biological imaging beyond 1500 nm. *Nat. Commun.* 8:737. doi: 10.1038/s41467-017-00917-6

Zhou, B., Xu, B., He, H., Gu, Z., Tang, B., Ma, Y., et al. (2018). Enhanced green upconversion luminescence in tetrahedral $LiYF_4$:Yb/Er nanoparticles by manganese(ii)-doping: the key role of the host lattice. *Nanoscale* 10, 2834–2840. doi: 10.1039/C7NR07709B

Zhou, B., Yang, W., Han, S., Sun, Q., and Liu, X. (2015). Photon upconversion through Tb(3+) -mediated interfacial energy transfer. *Adv. Mater.* 27, 6208–6212. doi: 10.1002/adma.201503482

Zhou, J., Yang, Y., and Zhang, C. Y. (2015). Toward biocompatible semiconductor quantum dots: from biosynthesis and bioconjugation to biomedical application. *Chem. Rev.* 115, 11669–11717. doi: 10.1021/acs.chemrev.5b00049

Zhuo, Z., Liu, Y., Liu, D., Huang, P., Jiang, F., Chen, X., et al. (2017). Manipulating energy transfer in lanthanide-doped single nanoparticles for highly enhanced upconverting luminescence. *Chem. Sci.* 8, 5050–5056. doi: 10.1039/C7SC01393K

Conflict of Interest: The authors declare that the research was conducted in the absence of any commercial or financial relationships that could be construed as a potential conflict of interest.

frontiers in Chemistry

MINI REVIEW
published: 14 December 2020
doi: 10.3389/fchem.2020.608578

Synthesis and Biomedical Applications of Lanthanides-Doped Persistent Luminescence Phosphors With NIR Emissions

Xinyuan Qin[1], *Jie Wang*[1] *and Quan Yuan*[1,2]*

[1] *Key Laboratory of Biomedical Polymers of Ministry of Education, College of Chemistry and Molecular Sciences, Wuhan University, Wuhan, China,* [2] *State Key Laboratory of Chemo/Biosensing and Chemometrics, College of Chemistry and Chemical Engineering, Institute of Chemical Biology and Nanomedicine (ICBN), Hunan University, Changsha, China*

Persistent luminescence phosphors (PLPs) are largely used in biomedical areas owing to their unique advantages in reducing the autofluorescence and light-scattering interference from tissues. Moreover, PLPs with long-lived luminescence in the near-infrared (NIR) region are able to be applied in deep-tissue bioimaging or therapy due to the reduced light absorption of tissues in NIR region. Because of their abundant election levels and energy transfer channels, lanthanides are widely doped in PLPs for the generation of NIR persistent emissions. In addition, the crystal defects introduced by lanthanides-doping can serves as charge traps in PLPs, which contributes to the enhancement of persistent luminescence intensity and the increase of persistent time. In this paper, the research progress in the synthesis and biomedical applications of lanthanides-doped PLPs with NIR emissions are systematically summarized, which can provide instructions for the design and applications of PLPs in the future.

Keywords: lanthanides, persistent luminescence, near-infrared, bioimaging, therapy

OPEN ACCESS

Edited by:
Lining Sun,
Shanghai University, China

Reviewed by:
Xian Chen,
Shenzhen University, China
Xiaoji Xie,
Nanjing Tech University, China

****Correspondence:***
Quan Yuan
yuanquan@whu.edu.cn

Specialty section:
This article was submitted to Nanoscience, a section of the journal Frontiers in Chemistry

Received: *21 September 2020*
Accepted: *06 November 2020*
Published: *14 December 2020*

Citation:
Qin X, Wang J and Yuan Q (2020) Synthesis and Biomedical Applications of Lanthanides-Doped Persistent Luminescence Phosphors With NIR Emissions. Front. Chem. 8:608578. doi: 10.3389/fchem.2020.608578

INTRODUCTION

Persistent luminescence phosphors (PLPs) are photoluminescent materials that will remain luminescence after the excitation light is extinguished (Yang et al., 2016; Feng et al., 2018). It is generally accepted that the crystal defects in PLPs can store photogenerated electrons and holes during excitation. After the excitation light is closed, the electrons and holes in the defects can escape from the defects under stimulation, and their recombination generates the persistent luminescence phenomenon (Wang et al., 2018). The delayed luminescence in PLPs enables researchers to completely avoid the interference of autofluorescence in biological samples, which greatly improves the signal-to-noise ratio (SNR) of bioimaging (Rosticher et al., 2016; Gong et al., 2017). In addition, PLPs with near-infrared (NIR) emissions provides the possibility for bioimaging in deep tumor tissues. In 2007, Chermont et al. first applied PLPs to bioimaging, and they realized long-term *in-vivo* imaging for more than 1 h by using the delayed luminescence of PLPs (Chermont et al., 2007). Nowadays, persistent luminescence materials are widely studied in biomedical fields, including biosensing, bioimaging, and tumor therapy.

Generally, PLPs consist of host materials and the doped ions (Hu et al., 2018). The host materials usually display broad emission peaks at 350–600 nm, so their applications in bioimaging and so on are limited. Doping is an effective way to generate narrow band emission at different

wavelengths in PLPs (Hai et al., 2020). Lanthanides have a lot of electron energy levels and long-lived excitation states, which can generate a variety of radiation absorption and emission (Zhao L. et al., 2019). Lanthanides-doping is often used to generate the desired visible or NIR emissions in PLPs. Moreover, the doped lanthanides can participate in the charge trapping and detrapping processes. These doped lanthanides may enhance the persistent luminescence intensity and prolong the persistent time (Zhang et al., 2019). In 1996, Matsuzawa et al. reported the milestone $SrAl_2O_4:Eu^{2+}$, Dy^{3+} PLPs with bright and durable persistent luminescence (Matsuzawa et al., 1996). In $SrAl_2O_4:Eu^{2+}$, Dy^{3+}, the Eu^{2+} is the emission center, and Dy^{3+} participates in the charge trapping/detrapping processes. Inspired by Matsuzawa's work, many different lanthanides-doped PLPs have been synthesized, whose applications in biomedical areas have also been investigated (Zhang et al., 2015).

Recently, there are several good reviews on PLPs (Singh, 2014; Liang et al., 2019; Lin et al., 2020). In these reviews, the luminescence mechanisms, the different kinds of PLPs, the controlled synthesis of persistent luminescence materials, and the design of persistent luminescence nanoprobes for biomedical applications have been systematically reviewed (Lin et al., 2019; Ma et al., 2019). Whereas, the design of lanthanides-doped PLPs with NIR emissions and their biomedical applications have not been overviewed. In this review, the development of lanthanides-doped PLPs in recent years is systematically introduced from two aspects: synthesis and biomedical application. This paper mainly reviews the controlled synthesis of lanthanides-doped PLPs with emissions in the NIR region, and the applications of PLPs in biosensing, bioimaging, drug delivery, and phototherapy, which may provide instructions for the future studies on lanthanides-doped PLPs.

SYNTHESIS OF LANTHANIDES-DOPED PLPs WITH NIR EMISSIONS

Fluorescence imaging in the NIR window (650–1,700 nm) has been widely used in the field of biotechnology, such as bioimaging and targeted disease therapy (Gong et al., 2019). Generally, NIR biological window can be divided into NIR-I (650–1,000 nm) region and NIR-II (1,000–1,700 nm) region according to the wavelength (Liu Y. et al., 2019). Some PLPs whose emission located in the NIR biological window will have deep tissue penetration depth in bioimaging (Zhao H. et al., 2019). Due to having various electron energy levels, lanthanides are highly efficient in producing emissions in the NIR region. This section will introduce the methods for the design and synthesis of lanthanides-doped PLPs with NIR emissions.

Lanthanides-Doped PLPs With Emissions in NIR-I Region

In the process of NIR luminescence, the doped ions can be used as the luminescence centers to generate corresponding emissions (Zhang et al., 2018). Lanthanides atoms have abundant electron energy levels, long-lived excited states, and more than 200,000 transition channels, which can produce various radiation absorption and emission. Therefore, lanthanides-doping is widely used in the design of NIR luminescence materials, including PLPs. Li et al. prepared lanthanides-doped $SrZrO_3:Yb^{3+}$ PLPs by high-temperature solid-state reaction (HTSSR) (Li Z. et al., 2018). This phosphor could produce stable luminescence at around 986 nm under UV excitation. Calculations showed that the luminescence at 986 nm was originated from the doped Yb^{3+}:$^2F_{2/5}$-$^2F_{2/7}$. The NIR persistent luminescence at 986 nm was also detected in $SrZrO_3:Yb^{3+}$, and the electrons stored in oxygen vacancies was proved to generate the persistent luminescence. Additionally, they showed the persistent luminescence intensity in $SrZrO_3:Yb^{3+}$ was related to the concentration of the doped Yb^{3+}. The NIR persistent luminescence intensity increased with raising the concentration of Yb^{3+}, whereas a high concentration of Yb^{3+} resulted in quench of the NIR luminescence. The optimal concentration of the doped Yb^{3+} in $SrZrO_3:Yb^{3+}$ was determined to be 2.5%. This work showed the good promise of lanthanides in the generation of NIR persistent luminescence by serving as the luminescence centers.

In addition to being luminescence centers, lanthanides can also serve as defects to regulate the energy storage and transfer process. Li et al. directly synthesized $ZnSn_2O_4$:Cr, Eu PLPs by a hydrothermal reaction (**Figure 1A**) (Li et al., 2017). In $ZnSn_2O_4$:Cr,Eu, Cr^{3+} acts as the NIR luminescence center with emission at 800 nm (**Figure 1B**), and Eu^{3+} acts as the trap center to capture photo-generated electrons and generate persistent luminescence after excitation ceases (**Figure 1C**). The $ZnSn_2O_4$:Cr,Eu PLPs can effectively avoid the light scattering interference and show deep-tissue penetration in bioimaging. Moreover, the authors realized the covalent modification of folic acids on the $ZnSn_2O_4$:Cr,Eu surface for target tumor imaging.

Generally, PLPs need to be charged by UV light, and this largely limits their biomedical applications. Considering the deep penetration of NIR light, the PLPs which are excited by NIR light have a better promise in biomedical areas. Qin et al. successfully synthesized a upconversion PLPs $Zn_{1.3}Ga_{1.4}Sn_{0.3}O_4:Yb^{3+},Er^{3+},Cr^{3+}$ by HTSSR (Qin et al., 2019). Due to the tailored energy transfer (ET) between doping ions, this phosphor shows the NIR emission of Cr^{3+}. In these PLPs, Yb^{3+} first absorbs NIR (980 nm) photons and transfers the energy to Er^{3+} by upconversion (UC) emission, and then Er^{3+} transfers the energy to Cr^{3+} by ET to realize NIR persistent luminescence emission of Cr^{3+} at 694 nm. Due to the special luminescence property, these PLPs will reduce photodamage to biological tissues as well as improving the penetrability of the excitation light, which provides the possibility for deep tumors imaging and therapy.

Lanthanides-Doped PLPs With Emissions in NIR-II Region

As previously introduced, a longer emission wavelength of PLPs can effectively improve the penetration depth of bioimaging (Zhang et al., 2018). Therefore, the PLPs in NIR-II have a better

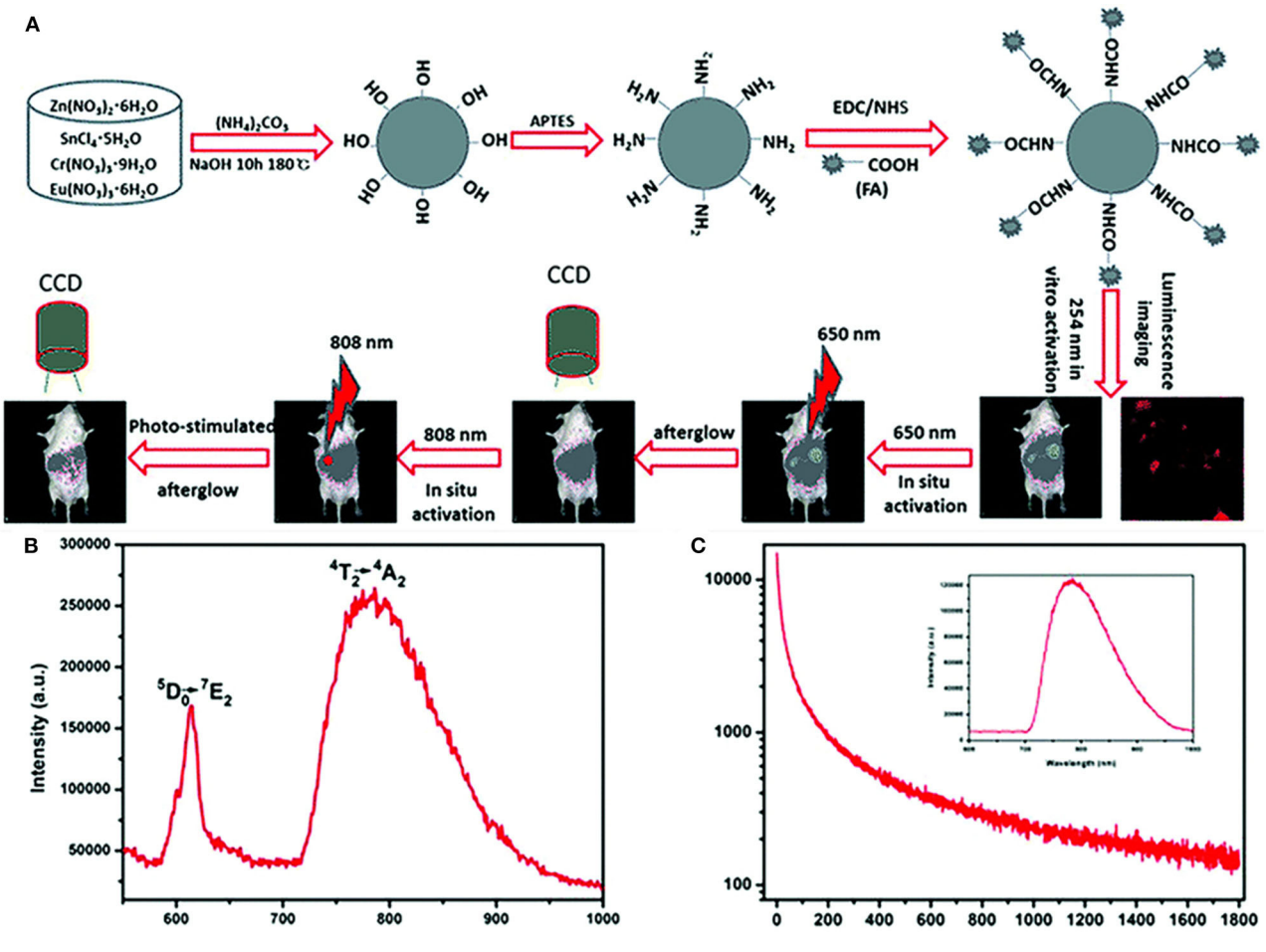

FIGURE 1 | (A) Schematic diagram of the synthesis and bioimaging applications of the $ZnSn_2O_4$:Cr,Eu PLPs, **(B)** emission spectrum of the PLPs of excitation at 254 nm, **(C)** decay curve of the PLPs of excitation at 254 nm and the inset is PersL spectrum. Reproduced from a literature Li et al. (2017) with permission from Royal Society of Chemistry.

application prospect in biomedical fields. Xu et al. synthesized the $Y_3Al_2Ga_3O_{12}$:Er^{3+},Cr^{3+} PLPs with emissions in NIR-II region by HTSSR (Xu et al., 2018b). Due to the ET from Cr^{3+} to Er^{3+}, these PLPs have the persistent luminescence of both Cr^{3+} (690 nm) and Er^{3+} (1,532 nm). The authors also proved that PLPs did have deep penetration depth in tissues, which improved SNR of bioimaging. In addition, by doping Ho^{3+} in $LaAlO_3$ and $LaGaO_3$ perovskite, Xu et al. also successfully developed two kinds of persistent luminescence perovskite particles with multi-wavelength emissions (NIR-I and NIR-II) (Xu et al., 2018a). This work indicated that the method of lanthanides doping can be used to adjust the emission wavelength of various types of PLPs. Therefore, this lanthanides co-doping method provides a reference for the synthesis of other PLPs with emissions in NIR-II.

Recently, Xu et al. synthesized a $Y_3Al_2Ga_3O_{12}$:Nd^{3+}, Ce^{3+},Cr^{3+} PLPs with multi-wavelength emissions at about 880, 1,064, and 1,335 nm by HTSSR (Xu et al., 2015). Calculations showed that the multi-wavelength luminescence was originated from the doped Nd^{3+}:$^4F_{3/2}$ to $^4I_{9/2}$, $^4I_{11/2}$, and $^4I_{13/2}$, respectively. Since its emissions match with the NIR-I and NIR-II region, PLPs with long persistent luminescence have promising applications in bioimaging and tumor therapy.

In addition to inorganic materials, organic lanthanides co-doped system also shows the persistent luminescence phenomenon. Li et al. synthesized an organic Er^{3+} complex $Er(F\text{-}TPIP)_3$ [tetrakis(pentafluorophenyl)imidodiphosphinate] successfully (Li H.-F. et al., 2020). This complex had the NIR emission at around 1,500 nm due to the $^4I_{13/2}$-$^4I_{15/2}$ transition of Er^{3+}. The lifetime of the $Er(F\text{-}TPIP)_3$ is 2.65 ms, which was the longest Er^{3+} lifetime in the hydrogenous organic environment. The authors realized the enhancement of Er^{3+} emission through the co-doping of a photosensitizer (phosphororganic molecule), whose enhancement effect was up to 1,600 times. This photosensitizer and lanthanides co-doped method is expected to realize the design and synthesis of organic lanthanides system with strong NIR persistent emissions.

BIOSENSING BASED ON LANTHANIDES-DOPED PLPs

PLPs are ideal materials for building fluorescent probes for biosensing due to their delayed luminescence properties (Kumar et al., 2017; Zhang X. et al., 2018). Li et al. synthesized the PLPs nanoprobe Ir(III)@SiNPs-Eu^{3+} with 653 nm emission for tetracycline (TC) detection (Li X. et al., 2020). Since TC will enhance the emission intensity of doped Er^{3+} and quench the original Ir(III)@SiNPs luminescence, this nanoprobe could realize the ratiometric analysis of the TC in complicated tissues. The authors demonstrated that the nanoprobe was sensitive to TC in the serum background, and the TC-nanoprobe complex could also detect Hg^{2+} sensitively through the ratiometric luminescence mode. In addition, the nanoprobe had low cytotoxicity. The developed nanoprobe has a great application potential in biological detection, including the detection of TC and Hg^{2+} in biological samples.

Recently, Dou et al. synthesized a $La_2O_2CO_3$:Eu^{3+},Ho^{3+} PLPs with emission at around 704 nm, whose size and persistent luminescence could be adjusted by changing the reaction conditions such as time and reaction power (Dou et al., 2019). They found that the PLPs had good stability in water, which can achieve long-term preservation in liquid environment for more than 1 week. In addition, they demonstrated the $La_2O_2CO_3$:Eu^{3+},Ho^{3+} nanoprobe could achieve highly sensitive detection of H_2O_2 in the serum environment because the H_2O_2 can quench the luminescence of this probe. Glucose, on the other hand, can produce H_2O_2 through enzymatic (glucose oxidase) reaction *in vivo*, so this probe can determine the serum glucose concentration. Different from traditional detecting methods based on enzymes, this PLP-based method isn't sensitive to the change of temperature and pH. Therefore, this probe will have a broader prospect in the clinical monitoring of patients with hyperglycemia or diabetes.

The application of PLPs has also been extended to the field of food safety. Liu et al. successfully synthesized a kind of persistent luminescence nanophosphors (PLNPs, $ZnGa_2O_4$:Ga,Er,Yb)@MIP (molecularly imprinted) with 700 nm emission, which can selectively adsorb the biological toxins such as ochratoxin and aflatoxin *in vivo* and *in vitro* (Liu J. et al., 2019). In this material, MIP has specific recognition ability for three biotoxins (sterigmatocystin, ochratoxin, and aflatoxin), and PLNPs act as fluorescent probes to eliminate background interference. In mice, the PLNPs@MIP in the tissues that contained biotoxins will have a brighter luminescence and a slower rate of being cleared out. In addition, the characteristic of persistent luminescence enabled PLNPs@MIP to realize the tracking of biological toxins, so as to explain the damage mechanism of biological toxins to human body. This work showed had a good application prospect in the detection of biological toxins in food.

BIOIMAGING BASED ON LANTHANIDES-DOPED PLPs

As mentioned in the first part, PLPs are ideal materials for bioimaging since they can effectively avoid spontaneous fluorescence of biological tissues (Abdukayum et al., 2013; Li et al., 2020). However, the PLPs synthesized by traditional high-temperature reactions lack appropriate modifiable group on the surface (Du et al., 2017). Moreover, the persistent luminescence of PLPs will diminish over time *in vivo*, and they cannot be effectively reactivated by UV light due to the limited penetration of UV. Shi et al. proposed a synthesis method for the preparation of amino functionalized $ZnGa_2O_4$:Cr,Eu PLPs with emission at 700 nm (**Figures 2A–C**) (Shi et al., 2016). The particle size and persistent luminescence of the PLPs can be controlled by changing the reaction conditions including time, pH, and so on. Due to the surface amino groups, the PLPs can be easily modified with biological molecules, such as folic acid for bioimaging. Lanthanides-doping in the PLPs significantly enhanced the persistent emission of Cr^{3+} at 700 nm. As a result, a high SNR (>4.0) was achieved in tumor imaging (**Figure 2D**). The authors also demonstrated that the PLPs can be re-excited *in vivo* to restore the signal intensity by NIR stimulation at 808 nm. This work paves the way for the development of PLPs with easy surface modification and *in-vivo* reactivation, showing a great application prospect in sustainable biological imaging.

Recently, Li et al. proposed a hydrothermal method for the synthesis of monodisperse $Zn_{1.25}Ga_{1.5}Ge_{0.25}O_4$:$Cr^{3+}$,$Yb^{3+}$,$Er^{3+}$ PLPs with a broad emission from 650 to 850 nm (Li and Yan, 2016). These triple-doped PLPs had high quantum yields (9.86%) and long persistent luminescence time (>20 days). They found that after modifying folic acid on the surface, the particle that was low in biotoxicity can achieve targeted imaging of the tumor. Moreover, the therapy effect of oral administration was better than intravenous administration. The oral administration imaging based on this lanthanides-doped PLPs can improve the imaging time window while avoiding the injection step. These PLPs were expected to achieve effective optical imaging of oral drugs.

Terminal cancer is often difficult to treat because of the metastasis of cancer cells, so it is necessary to develop an imaging method to track the cancer metastasis in order to achieve more accurate treatment (Sengar et al., 2019). Lanthanides-doped PLPs have good promise in tumor tracking and metastasis imaging due to their bright and rechargeable persistent luminescence. Zhao et al. synthesized alginate containing PLPs $Zn_{1.1}Ga_{1.8}G_{e0.1}O_4$:$Eu_{0.009}$,$Cr_{0.09}$ with the emission at around 698 nm, and they covalently modified the PLPs with 4-carboxyphenylboric acid to target breast cancer cells (Zhao et al., 2020). The PLP probe was not interfered by spontaneous fluorescence and could achieve long-term tumor imaging. They found that the composite PLPs could target breast cancer cells precisely in mice by endocytosis. In addition, with the increase of labeled cells, the SNR increased as well.

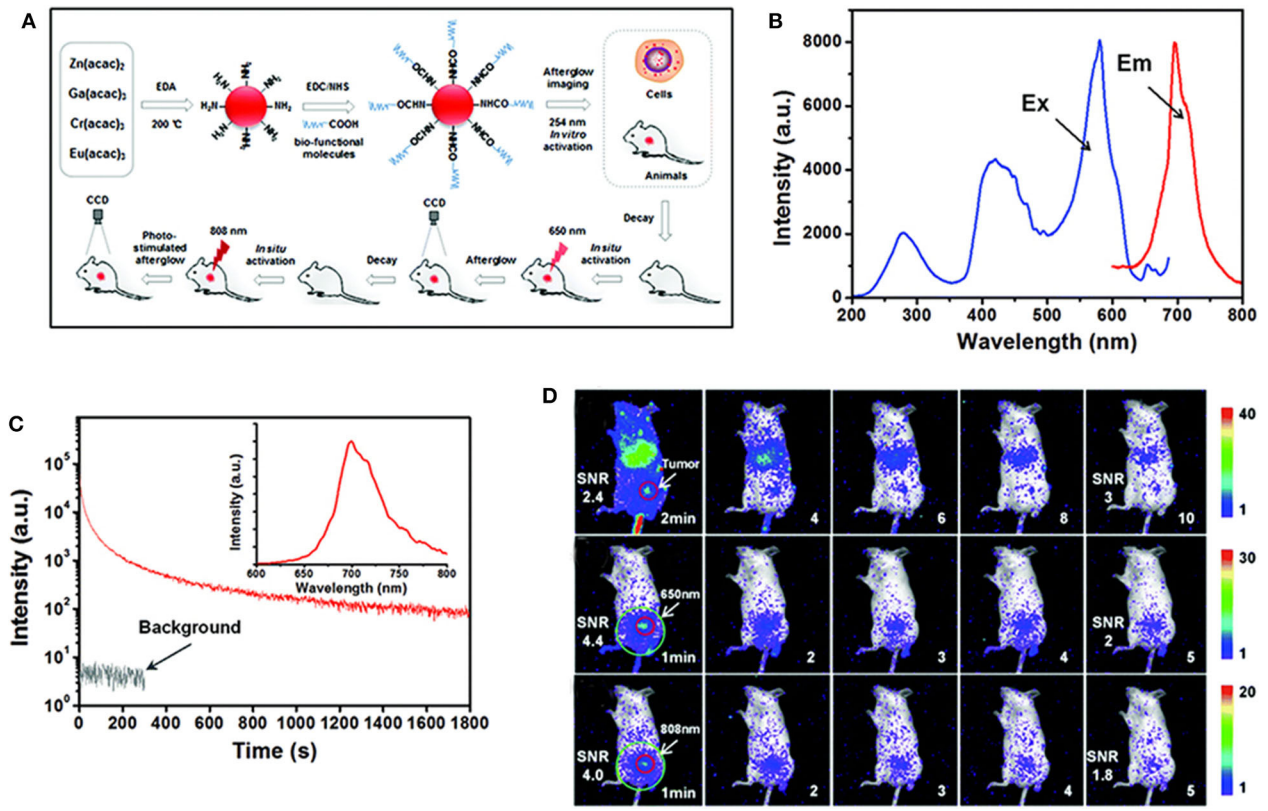

FIGURE 2 | (A) Schematic diagram of synthesis and bioimaging application of the PLPs, **(B)** emission and excitation spectra of the PLPs, **(C)** decay curve of the PLPs of excitation at 254 nm and the inset is PersL spectrum, **(D)** bioimaging in mice after injection of PLPs. Reproduced from a literature Shi et al. (2016) with permission from Royal Society of Chemistry.

When the number of labeled cells was 10, the SNR is up to 3.0 ± 0.1. They also showed that these PLPs can be covalently modified with other targeted agents to achieve long-term tracking of other cancer metastasis. This tailored composite PLPs can solve the problems of cancer metastasis monitoring and provide a common platform for the accurate detection of cancer.

In bioimaging, the penetration depth of excitation light directly affects the imaging sensitivity in deep tissues (Rosticher et al., 2015; Zhong et al., 2019). Although X-rays have high energy and deep penetration, they are harmful to the human body (Song et al., 2017). So researchers hope to develop PLP probes that can be directly excited by NIR light. Xue et al. synthesized a kind of UC PLP ($Zn_3Ga_2GeO_8$:Yb/Er/Cr). The PLPs have a NIR persistent luminescence emission at around 700 nm under NIR excitation and a duration of up to 15 h (Xue et al., 2017). Different from previous X-rays and UV excitation, NIR excitation shows less toxic effect on biological samples. The authors found can be recharged by stimulating light to recover the persistent luminescence *in vivo* for long-term bioimaging. This dual-mode NIR charging/emission imaging PLPs greatly improves the sensitivity and penetration depth of bioimaging, and the PLPs are expected to achieve long-term imaging of deep tissues.

DRUG DELIVERY BASED ON LANTHANIDES-DOPED PLPs

In addition to bioimaging, PLPs can also be used as drug carriers to construct a bioimaging-guided drug delivery system (Zhang D. et al., 2018). Previous studies have shown that folate-modified PLPs can precisely target tumor cells, so the researchers attempted to load the PLPs with anti-tumor drugs to treat tumors *in situ* (Jabalera et al., 2020). Shi et al. synthesized the PLP probe $Zn_{1.1}Ga_{1.8}Ge_{0.1}O_4$:$Cr^{3+}$,$Eu^{3+}$@$SiO_2$ with a 696 nm emission (Shi et al., 2015). The PLPs were covalently modified with folic acid and further loaded with anticancer drug doxorubicin to achieve targeted drug delivery. The PLP probe had strong NIR luminescence and long persistent time (>10 days). The authors showed that the probe was sensitive enough to tumor cells and could deliver drugs *in situ*. In addition, the PLPs can be readily recharged by excitation light, which can be applied in monitoring tumor cells for a long time for exploring the therapeutic mechanisms of antitumor drugs. This targeted drug delivery system has a good promise in tumor detection and cancer therapy.

Most PLP-based drug carriers have poor biocompatibility, so they are easy to be swallowed by macrophages in delivering drugs. In order to solve this problem, Liu et al. combined

$Zn_{1.25}Ga_{1.5}Ge_{0.25}O_4:Cr^{3+},Er^{3+},Yb^{3+}$ PLPs with membrane structure to prepare a new type of nanocarrier with biological characteristics (Liu et al., 2018). This nanocarrier has the NIR emission at around 700 nm, and displayed long persistent luminescence for over 20 days. In a proof of concept study, the erythrocyte membrane-coated nanocarriers effectively evaded the body's immune system and delivered drugs efficiently. The erythrocyte membrane-coated nanocarriers also retained the excellent luminescence performance of PLPs. Additionally, the authors found that the nanocarriers not only have good biocompatibility and bright persistent luminescence but also can achieve the release of drugs guided by bioimaging. This new drug carrier has a great prospect in targeted tumor therapy and other biological fields.

Addition to the poor biocompatibility, the drug-loading amount of PLPs is usually limited, which will affect the efficiency of drugs delivery and cancer therapy. Recently, Li et al. synthesized porous PLPs $GdAlO_3:Cr^{3+},Sm^{3+}$ for drug delivery (Li J. et al., 2018). These PLPs showed strong persistent luminescence at around 732 nm under UV excitation. They modified the surface of the PLPs with carboxymethyl chitosan to reduce their biotoxicity. The drug carriers based on this porous PLPs had high drug-loading efficiency. They also demonstrated in this composite that PLPs can achieve slow drug release when loaded with ibuprofen, an anti-inflammatory drug. These porous PLPs have a broad application prospect in drug delivery guided by bioimaging and can serve as a potential platform to explore the kinetics of drug release *in vivo*.

PHOTOTHERAPY BASED ON LANTHANIDES-DOPED PLPs

Phototherapy has great advantages in tumor therapy because it has little toxicity to normal cells and can effectively kill cancer cells (Yang et al., 2018; Hu et al., 2019). The traditional photodynamic therapy (PDT) platform is usually composed of a fluorescent probe and photosensitizers. Due to its delayed luminescence, PLPs do not require long-term excitation light irradiation. Therefore, PLP-based fluorescent probes can effectively reduce the light damage to biological tissues and have a good application prospect in PDT. Most porphyrin-based photosensitizers are excited by UV light, but the long irradiation of UV is damage to biological tissues. To reduce the time of UV irradiation, Wang et al. synthesized $Zn_{1.25}Ga_{1.5}Ge_{0.25}O_4:Cr^{3+},Yb^{3+},Er^{3+}$ PLPs for PDT (Wang et al., 2017). These PLPs had strong persistent luminescence at about 690 nm. They found that the persistent luminescence of these PLNPs can effectively activated the photosensitizers aluminum phthalocyanine to generate $^1O_2$. They coated PLNPs with mesoporous silica to reduce its biotoxicity and conjugated photosensitizer to this the PLNPs to build the platform for PDT (The PLNPs were coated with mesoporous silica to reduce their biotoxicity and were further modified with the photosensitizer to construct the PDT platform). The authors demonstrated that the PDT platform can effectively eliminate cancer cells under short periods of UV irradiation. Therefore, the PLPs show good promise in UV-based PDT as the second excitation source to a photosensitizer and can provide possibilities for low-dose UV-excited PDT.

PLPs are often applied in phototherapy as fluorescent probes, but some PLPs do not have good water solubility, which affects their application in phototherapy. Homayoni et al. prepared $Sr_2MgSi_2O_7:Eu^{2+},Dy^{3+}$ PLPs with good water solubility by the sol-gel method, and used APTES to modify their surface (Homayoni et al., 2016). These PLPs had emission at around 660 nm under the X-ray excitation due to the $^4F_{9/2}$-$^6H_{13/2}$ transitions of Dy^{3+}. The PLPs were covalently modified with folic acid and were further modified with protoporphyrin, a photosensitizer, to achieve targeted PDT. The protoporphyrin was excited by the emission of PLPs in this PDT system, which enhanced the luminescence of protoporphyrin by 10 times. By integrating *in-situ* biological imaging and photodynamic therapy, this PDT system was able to produce $^1O_2$ continuously upon the primary X-ray excitation to achieve efficient tumor therapy. This work showed the good promise of these PLPs in tumor phototherapy and radiotherapy.

Besides PDT, photothermal therapy (PTT) is also an effective phototherapy method, and the traditional PTT platform is usually composed of fluorescent probe and photothermal agent (Zheng et al., 2016; Zhao et al., 2017; Zhen et al., 2018). Different from the previous method of carrying photothermal agent, Wu et al. synthesized a $Zn_3Ga_2SnO_8:Cr^{3+},Nd^{3+},Gd^{3+}$ PLPs with photothermal effect (Wu et al., 2016). These PLPs had strong persistent luminescence at about 700 nm because of the ^2E–$^4A_2$ transition of Cr^{3+}. This use of PLPs that don't need the prolonged exposure of high-energy excitation light could effectively reduce light damage in PTT. The doped Nd^{3+} can absorb the energy of excitation light at 808 nm and convert it into heat energy for ablating the tumor cells. Due to the combination of persistent luminescence and photothermal effect, this PLP-based integrated platform is expected to realize efficient PTT guided by bioimaging, which can effectively reduce the side effects of PTT. This work provides a reference for the designing of non-composite PTT platform.

CONCLUSION

Lanthanides ions are often doped as luminescence centers or defects to regulate the persistent luminescence of PLPs. With proper lanthanides doping, the researchers have synthesized many kinds of PLPs with NIR persistent luminescence. These PLPs can effectively avoid spontaneous luminescence in tissues, and NIR luminescence allows PLPs to have deeper penetration. Therefore, the lanthanides-doped PLPs are ideal materials for biosensing, bioimaging, and cancer therapy. Various synthetic methods and modification strategies were proposed to improve the water solubility and biocompatibility of the PLPs. The PLP-based composite platforms have a broader prospect in biomedicine applications. In this paper, the synthesis and biomedical applications, including biosensing, bioimaging, drug delivery, and phototherapy of lanthanides-doped PLPs with NIR

emission, are reviewed, aiming to provide instructions for the further studies on lanthanides-doped PLPs.

Although PLPs with NIR emission have great promise in biomedicine, great challenges are still confronted by PLPs before their practical applications. Currently, PLPs with NIR emission are generally synthesized with "top-down" methods, such as wet grinding, particularly for PLPs with emission in the NI-II region. Such PLPs usually show irregular size/shape, poor dispersibility, and surface modification. The "bottom-up" methods need to be developed for the controlled synthesis of PLPs with NIR emission. On the other hand, the PLPs with NIR emission are usually activated by UV light. The UV light has shallow tissue penetration and usually causes serious photo damage to tissues. Developing PLPs that can be directly charged by NIR light is highly desired for deep-tissue imaging and therapy. Last but not the least, research about the biosafety of the PLPs with NIR emission is rather limited. Many efforts have to be made to systematically investigate the biosafety of PLPs. With further research, these challenges are expected to be addressed, and the lanthanides-doped PLPs with NIR emission will be readily implemented into the clinical workflow for disease diagnosis and therapy.

AUTHOR CONTRIBUTIONS

QY supervised the project and mainly wrote the paper. XQ and JW co-wrote the paper. All authors discussed the reviewed results and commented on the manuscript.

FUNDING

This research was supported by National Natural Science Foundation of China (21925401, 21675120, and 21904100) and the National Key R&D Program of China (2017YFA0208000).

REFERENCES

Abdukayum, A., Chen, J.-T., Zhao, Q., and Yan, X.-P. (2013). Functional near infrared-emitting Cr^{3+}/Pr^{3+} co-doped zinc gallogermanate persistent luminescent nanoparticles with superlong afterglow for *in vivo* targeted bioimaging. *J. Am. Chem. Soc.* 135, 14125–14133. doi: 10.1021/ja404243v

Chermont, l. M. d. Q., Chaneac, C., Seguin, J., Pelle, F., Maitrejean, S., Jolivet, J. P., et al. (2007). Nanoprobes with near-infrared persistent luminescence for *in vivo* imaging. *Proc. Natl. Acad. Sci. U.S.A.* 104, 9266–9271. doi: 10.1073/pnas.0702427104

Dou, X., Li, Y., Vaneckova, T., Kang, R., Hu, Y., Wen, H., et al. (2019). Versatile persistent luminescent oxycarbonates: morphology evolution from nanorods through bamboo-like nanorods to nanoparticles. *J. Lumin.* 215:116635. doi: 10.1016/j.jlumin.2019.116635

Du, J., Clercq, O. Q. D., Korthout, K., and Poelman, D. (2017). $LaAlO_3:Mn^{4+}$ as near-infrared emitting persistent luminescence phosphor for medical imaging: a charge compensation study. *Materials* 10:1422. doi: 10.3390/ma10121422

Feng, F., Chen, X., Li, G., Liang, S., Hong, Z., and Wang, H. F. (2018). Afterglow resonance energy transfer inhibition for fibroblast activation protein-alpha assay. *ACS Sensors* 3, 1846–1854. doi: 10.1021/acssensors.8b00680

Gong, Z., Liu, Y., Yang, J., Yan, D., Zhu, H., Liu, C., et al. (2017). A Pr^{3+} doping strategy for simultaneously optimizing the size and near infrared persistent luminescence of $ZGGO:Cr^{3+}$ nanoparticles for potential bio-imaging. *Phys. Chem. Chem. Phys.* 19, 24513–24521. doi: 10.1039/C7CP02909H

Gong, Z., Yang, J., Zhu, H., Yan, D., Liu, C., Xu, C., et al. (2019). The synergistically improved afterglow and magnetic resonance imaging induced by Gd^{3+} doping in $ZGGO:Cr^{3+}$ nanoparticles. *Mater. Res. Bull.* 113, 122–132. doi: 10.1016/j.materresbull.2019.01.031

Hai, O., Yang, E., Wei, B., Ren, Q., Wu, X., and Zhu, J. (2020). The trap control in the long afterglow luminescent material $(Ca,Sr)_2MgSi_2O_7:Eu^{2+},Dy^{3+}$. *J. Solid State Chem.* 283:121174. doi: 10.1016/j.jssc.2020.121174

Homayoni, H., Ma, L., Zhang, J., Sahi, S. K., Rashidi, L. H., Bui, B., et al. (2016). Synthesis and conjugation of $Sr_2MgSi_2O_7:Eu^{2+}$, Dy^{3+} water soluble afterglow nanoparticles for photodynamic activation. *Photodiagn. Photodyn.* 16, 90–99. doi: 10.1016/j.pdpdt.2016.08.012

Hu, X., Yang, H., Guo, T., Shu, D., Shan, W., Li, G., et al. (2018). Preparation and properties of Eu and Dy co-doped strontium aluminate long afterglow nanomaterials. *Ceram. Int.* 44, 7535–7544. doi: 10.1016/j.ceramint.2018.01.157

Hu, Y., Yang, Y., Li, X., Wang, X., Li, Y., Li, T., et al. (2019). Super long green persistent luminescence from X-ray excited β-$NaYF_4$: Tb^{3+}. *Preprints* 02:0241. doi: 10.20944/preprints201902.0241.v1

Jabalera, Y., Oltolina, F., Prat, M., Jimenez-Lopez, C., Fernández-Sánchez, J. F., Choquesillo-Lazarte, D., et al. (2020). Eu-doped citrate-coated carbonated apatite luminescent nanoprobes for drug delivery. *Nanomaterials* 10:199. doi: 10.3390/nano10020199

Kumar, D., Umrao, S., Mishra, H., Srivastava, R. R., Srivastava, M., Srivastava, A., et al. (2017). $Eu:Y_2O_3$ highly dispersed fluorescent PVA film as turn off luminescent probe for enzyme free detection of H_2O_2. *Sens. Actuators B Chem.* 247, 170–178. doi: 10.1016/j.snb.2017.02.128

Li, H.-F., Liu, X.-Q., Lyu, C., Gorbaciova, J., Wen, L.-L., Shan, G.-G., et al. (2020). Enhanced 1.54-μm photo- and electroluminescence based on a perfluorinated Er(III) complex utilizing an iridium(III) complex as a sensitizer. *Light Sci. Appl.* 9:32. doi: 10.1038/s41377-020-0266-3

Li, J., Shi, J., Wang, C., Li, P., Yu, Z., and Zhang, H. (2017). Five-nanometer $ZnSn_2O_4$: Cr, Eu ultra-small nanoparticles as new near infrared-emitting persistent luminescent nanoprobes for cellular and deep tissue imaging at 800 nm. *Nanoscale* 9, 8631–8638. doi: 10.1039/C7NR02468A

Li, J., Wang, C., Shi, J., Li, P., Yu, Z., and Zhang, H. (2018). Porous $GdAlO_3:Cr^{3+}$, Sm^{3+} drug carrier for real-time long afterglow and magnetic resonance dual-mode imaging. *J. Lumin.* 199, 363–371. doi: 10.1016/j.jlumin.2018.03.071

Li, X., Fan, K., Yang, R., Du, X., Qu, B., Miao, X., et al. (2020). A long lifetime ratiometrically luminescent tetracycline nanoprobe based on Ir(III) complex-doped and Eu^{3+}-functionalized silicon nanoparticles. *J. Hazard. Mater.* 386:121929. doi: 10.1016/j.jhazmat.2019.121929

Li, Y.-J., and Yan, X.-P. (2016). Synthesis of functionalized triple-doped zinc gallogermanate nanoparticles with superlong near-infrared persistent luminescence for long-term orally administrated bioimaging. *Nanoscale* 8, 14965–14970. doi: 10.1039/C6NR04950H

Li, Z., Wu, J., Wang, Q., Liang, T., Ge, J., Wang, P., et al. (2020). A universal strategy to construct lanthanide-doped nanoparticles-based activable NIR-II luminescence probe for bioimaging. *iScience* 23:100962. doi: 10.1016/j.isci.2020.100962

Li, Z., Zhang, S., Xu, Q., Duan, H., Lv, Y., Lin, X., et al. (2018). Long persistent phosphor $SrZrO_3:Yb^{3+}$ with dual emission in NUV and NIR region: a combined experimental and first-principles methods. *J. Alloys Compd.* 766, 663–671. doi: 10.1016/j.jallcom.2018.06.376

Liang, L., Chen, N., Jia, Y., Ma, Q., Wang, J., Yuan, Q., et al. (2019). Recent progress in engineering near-infrared persistent luminescence nanoprobes for time-resolved biosensing/bioimaging. *Nano Res.* 12, 1279–1292. doi: 10.1007/s12274-019-2343-6

Lin, Q., Li, Z., Ji, C., and Yuan, Q. (2020). Electronic structure engineering and biomedical applications of low energy-excited persistent luminescence nanoparticles. *Nanoscale Adv.* 2, 1380–1394. doi: 10.1039/C9NA00817A

Lin, Q., Li, Z., and Yuan, Q. (2019). Recent advances in autofluorescence-free biosensing and bioimaging based on persistent luminescence nanoparticles. *Chin. Chem. Lett.* 30, 1547–1556. doi: 10.1016/j.cclet.2019.06.016

Liu, J., Wang, Z., Li, C., Lv, S., Zhao, N., and Wang, S. (2019). Construction of molecularly imprinted nanoplatforms with persistent luminescence for *in vitro*

specific adsorption and *in vivo* targeted regulation of food-borne biotoxins. *New J. Chem.* 43, 15097–15104. doi: 10.1039/C9NJ03231B

Liu, J.-M., Zhang, D.-D., Fang, G.-Z., and Wang, S. (2018). Erythrocyte membrane bioinspired near-infrared persistent luminescence nanocarriers for *in vivo* long-circulating bioimaging and drug delivery. *Biomaterials* 165, 39–47. doi: 10.1016/j.biomaterials.2018.02.042

Liu, Y., Liu, J., Chen, D., Wang, X., Liu, Z., Liu, H., et al. (2019). Quinoxaline-based semiconducting polymer dots for *in vivo* NIR-II fluorescence imaging. *Macromolecules* 52, 5735–5740. doi: 10.1021/acs.macromol.9b01142

Ma, Q., Wang, J., Li, Z., Lv, X., Liang, L., and Yuan, Q. (2019). Recent progress in time-resolved biosensing and bioimaging based on lanthanide-doped nanoparticles. *Small* 15:1804969. doi: 10.1002/smll.201804969

Matsuzawa, T., Aoki, Y., Takeuchi, N., and Murayama, Y. (1996). A new long phosphorescent phosphor with high brightness, $SrAI_2O_4:Eu^{2+},Dy^{3+}$. *J. Electrochem. Soc.* 143:2670. doi: 10.1149/1.1837067

Qin, J., Xiang, J., Suo, H., Chen, Y., Zhang, Z., Zhao, X., et al. (2019). NIR persistent luminescence phosphor $Zn_{1.3}Ga_{1.4}Sn_{0.3}O_4:Yb^{3+},Er^{3+},Cr^{3+}$ with 980 nm laser excitation. *J. Mater. Chem. C* 7, 11903–11910. doi: 10.1039/C9TC03882E

Rosticher, C., Viana, B., Fortin, M. A., Lagueux, J., Faucher, L., and Chanéac, C. (2016). Gadolinium oxysulfide nanoprobes with both persistent luminescent and magnetic properties for multimodal imaging. *RSC Adv.* 6, 55472–55478. doi: 10.1039/C6RA05030A

Rosticher, C., Viana, B., Laurent, G., Le Griel, P., and Chanéac, C. (2015). Insight into $CaMgSi_2O_6:Eu^{2+},Mn^{2+},Dy^{3+}$ nanoprobes: influence of chemical composition and crystallinity on persistent red luminescence. *Eur. J. Inorg. Chem.* 2015, 3681–3687. doi: 10.1002/ejic.201500257

Sengar, P., García-Tapia, K., Can-Uc, B., Juárez-Moreno, K., Contreras-López, O. E., and Hirata, G. A. (2019). Simultaneous paramagnetic and persistence-luminescence in GAGG:Ce,Pr nanoparticles synthesized by sol-gel for biomedical applications. *J. Appl. Phys.* 126:083107. doi: 10.1063/1.5098788

Shi, J., Sun, X., Li, J., Man, H., Shen, J., Yu, Y., et al. (2015). Multifunctional near infrared-emitting long-persistence luminescent nanoprobes for drug delivery and targeted tumor imaging. *Biomaterials* 37, 260–270. doi: 10.1016/j.biomaterials.2014.10.033

Shi, J., Sun, X., Zhu, J., Li, J., and Zhang, H. (2016). One-step synthesis of amino-functionalized ultrasmall near infrared-emitting persistent luminescence nanoparticles for *in vitro* and *in vivo* bioimaging. *Nanoscale* 8, 9798–9804. doi: 10.1039/C6NR00590J

Singh, S. K. (2014). Red and near infrared persistent luminescence nanoprobes for bioimaging and targeting applications. *RSC Adv.* 4, 58674–58698. doi: 10.1039/C4RA08847F

Song, L., Lin, X., Song, X., Chen, S., Chen, X., Li, J., et al. (2017). Repeatable deep-tissue activation of persistent luminescence nanoparticles by soft X-ray for high sensitivity long-term *in vivo* bioimaging. *Nanoscale* 9, 2718–2722 doi: 10.1039/C6NR09553D

Wang, J., Li, J., Yu, J., Zhang, H., and Zhang, B. (2018). Large hollow cavity luminous nanoparticles with near-infrared persistent luminescence and tunable sizes for tumor afterglow imaging and chemo-/photodynamic therapies. *ACS Nano* 12, 4246–4258. doi: 10.1021/acsnano.7b07606

Wang, J., Li, Y., Mao, R., Wang, Y., Yan, X., and Liu, J. (2017). Persistent luminescent nanoparticles as energy mediators for enhanced photodynamic therapy with fractionated irradiation. *J. Mater. Chem. B* 5, 5793–5805. doi: 10.1039/C7TB00950J

Wu, Y., Li, Y., Qin, X., and Qiu, J. (2016). A multifunctional biomaterial with NIR long persistent phosphorescence, photothermal response and magnetism. *Chem. Asian J.* 11, 2537–2541. doi: 10.1002/asia.201600569

Xu, J., Murata, D., So, B., Asami, K., Ueda, J., Heo, J., et al. (2018a). 1.2 lm persistent luminescence of Ho^{3+} in $LaAlO_3$ and $LaGaO_3$ perovskites. *J. Mater. Chem. C* 6:11374. doi: 10.1039/C8TC04393K

Xu, J., Murata, D., Ueda, J., Viana, B., and Tanabe, S. (2018b). Toward rechargeable persistent luminescence for the first and third biological windows via persistent energy transfer and electron trap redistribution. *Inorg. Chem.* 57, 5194–5203. doi: 10.1021/acs.inorgchem.8b00218

Xu, J., Tanabe, S., Sontakke, A. D., and Ueda, J. (2015). Near-infrared multi-wavelengths long persistent luminescence of Nd^{3+} ion through persistent energy transfer in Ce^{3+}, Cr^{3+} co-doped $Y_3Al_2Ga_3O_{12}$ for the first and second bio-imaging windows. *Appl. Phys. Lett.* 107:081903. doi: 10.1063/1.4929495

Xue, Z., Li, X., Li, Y., Jiang, M., Ren, G., Liu, H., et al. (2017). A 980 nm laser-activated upconverted persistent probe for NIR-to-NIR rechargeable *in vivo* bioimaging. *Nanoscale* 9, 7276–7283. doi: 10.1039/C6NR09716B

Yang, Y., Wang, K. Z., and Yan, D. (2016). Ultralong persistent room temperature phosphorescence of metal coordination polymers exhibiting reversible pH-responsive emission. *ACS Appl. Mater. Interfaces* 8, 15489–15496. doi: 10.1021/acsami.6b03956

Yang, Y.-M., Li, Z.-Y., Zhang, J.-Y., Lu, Y., Guo, S.-Q., Zhao, Q., et al. (2018). X-ray-activated long persistent phosphors featuring strong UVC afterglow emissions. *Light Sci. Appl.* 7:88. doi: 10.1038/s41377-018-0089-7

Zhang, D., Liu, J., Song, N., Liu, Y., Dang, M., Fang, G., et al. (2018). Fabrication of mesoporous $La_3Ga_5GeO_{14}$: Cr^{3+}, Zn^{2+} persistent luminescence nanocarriers with super-long afterglow for bioimaging-guided *in vivo* drug delivery to gut. *J. Mater. Chem. B* 6, 1479–1488. doi: 10.1039/C7TB02759A

Zhang, J., Chen, W., and Chen, G. (2019). Luminescence of long-persistent $Ca_2MgSi_2O_{7-1.5x}N_x:Eu^{2+},Dy^{3+}$ phosphors for LEDs applications. *J. Mater. Sci. Mater. Electron.* 30, 4056–4063. doi: 10.1007/s10854-019-00692-8

Zhang, L., Lei, J., Liu, J., Ma, F., and Ju, H. (2015). Persistent luminescence nanoprobe for biosensing and lifetime imaging of cell apoptosis via time-resolved fluorescence resonance energy transfer. *Biomaterials* 67, 323–334. doi: 10.1016/j.biomaterials.2015.07.037

Zhang, X., Xu, N.-Y., Ruan, Q., Lu, D.-Q., Yang, Y.-H., and Hu, R. (2018). A label-free and sensitive photoluminescence sensing platform based on long persistent luminescence nanoparticles for the determination of antibiotics and 2,4,6-trinitrophenol. *RSC Adv.* 8, 5714–5720. doi: 10.1039/C7RA12222E

Zhang, Y., Huang, R., Lin, Z., Li, H., Hou, D., Song, J., et al. (2018). Positive effect of codoping Yb^{3+} on the super-long persistent luminescence of Cr^{3+}-doped zinc aluminum germanate. *Ceram. Int.* 44, 17377–17382. doi: 10.1016/j.ceramint.2018.06.202

Zhao, H., Liu, C., Gu, Z., Dong, L., Li, F., Yao, C., et al. (2020). Persistent luminescent nanoparticles containing hydrogel for targeted, sustained and autofluorescence-free tumor metastasis imaging. *Nano Lett.* 20, 252–260. doi: 10.1021/acs.nanolett.9b03755

Zhao, H., Shu, G., Zhu, J., Fu, Y., Gu, Z., and Yang, D. (2019). Persistent luminescent metal-organic frameworks with long-lasting near infrared emission for tumor site activated imaging and drug delivery. *Biomaterials* 217:119332. doi: 10.1016/j.biomaterials.2019.119332

Zhao, L., Mao, J., Jiang, B., Wei, X., Yin, M., and Chen, Y. (2019). A new yellow long persistent luminescence phosphor $Ca_2Al_2SiO_7:Eu^{2+},Tm^{3+}$ found by co-doping Ln^{3+} (Ln = Ce, Pr, Nd, Sm, Gd, Tb, Dy, Ho, Er, Tm, Yb, Lu) with Eu^{2+} in $Ca_2Al_2SiO_7$ host. *J. Lumin.* 206, 6–10. doi: 10.1016/j.jlumin.2018.10.038

Zhao, P., Ji, W., Zhou, S., Qiu, L., Li, L., Qian, Z., et al. (2017). Upconverting and persistent luminescent nanocarriers for accurately imaging-guided photothermal therapy. *Mater. Sci. Eng. C* 79, 191–198. doi: 10.1016/j.msec.2017.05.046

Zhen, X., Xie, C., and Pu, K. (2018). Temperature-correlated afterglow of a semiconducting polymer nanococktail for imaging-guided photothermal therapy. *Angew. Chem. Int. Ed. Engl.* 57, 3938–3942. doi: 10.1002/anie.201712550

Zheng, B., Chen, H.-B., Zhao, P.-Q., Pan, H.-Z., Wu, X.-L., Gong, X.-Q., et al. (2016). Persistent luminescent nanocarrier as an accurate tracker *in vivo* for near infrared-remote selectively triggered photothermal therapy. *ACS Appl. Mater. Interfaces* 8, 21603–21611. doi: 10.1021/acsami.6b07642

Zhong, X., Wang, X., Zhan, G., Tang, Y., Yao, Y., Dong, Z., et al. (2019). $NaCeF_4$:Gd,Tb scintillator as an X-ray responsive photosensitizer for multimodal imaging-guided synchronous radio/radiodynamic therapy. *Nano Lett.* 19, 8234–8244. doi: 10.1021/acs.nanolett.9b03682

Conflict of Interest: The authors declare that the research was conducted in the absence of any commercial or financial relationships that could be construed as a potential conflict of interest.

frontiers in Chemistry

ORIGINAL RESEARCH
published: 21 December 2020
doi: 10.3389/fchem.2020.613334

Assessing the Covalent Attachment and Energy Transfer Capabilities of Upconverting Phosphors With Cofactor Containing Bioactive Enzymes

Letitia Burgess[1,2], *Hannah Wilson*[1,2,3], *Alex R. Jones*[1,2,3†], *Sam Hay*[1,2*] and *Louise S. Natrajan*[1,3*]

[1] Department of Chemistry, School of Natural Sciences, The University of Manchester, Manchester, United Kingdom, [2] Manchester Institute of Biotechnology, The University of Manchester, Manchester, United Kingdom, [3] Photon Science Institute, The University of Manchester, Manchester, United Kingdom

Upconverting phosphors (UCPs) convert multiple low energy photons into higher energy emission via the process of photon upconversion and offer an attractive alternative to organic fluorophores for use as luminescent probes. Examples of biosensors utilizing the apparent energy transfer of UCPs and nanophosphors (UCNPs) with biomolecules have started to appear in the literature but very few exploit the covalent anchoring of the biomolecule to the surface of the UCP to improve the sensitivity of the systems. Here, we demonstrate a robust and versatile method for the covalent attachment of biomolecules to the surface of a variety of UCPs and UCNPs in which the UCPs were capped with functionalized silica in order to provide a surface to covalently conjugate biomolecules with surface-accessible cysteines. Variants of BM3Heme, cytochrome C, glucose oxidase, and glutathione reductase were then attached via maleimide-thiol coupling. BM3Heme, glucose oxidase, and glutathione reductase were shown to retain their activity when coupled to the UCPs potentially opening up opportunities for biosensing applications.

Keywords: lanthanides, upconversion, luminescence, protein conjugation, energy transfer, enzyme kinetics

OPEN ACCESS

Edited by:
Ho Seong Jang, Korea Institute of Science and Technology, South Korea

Reviewed by:
Jean-Claude Georges Bunzli, École Polytechnique Fédérale de Lausanne, Switzerland
Venkataramanan Mahalingam, Indian Institute of Science Education and Research Kolkata, India

****Correspondence:***
Sam Hay
sam.hay@manchester.ac.uk
Louise S. Natrajan
louise.natrajan@manchester.ac.uk

†Present address:
Alex R. Jones, Biometrology, Chemical and Biological Sciences, National Physical Laboratory, Middlesex, United Kingdom

Specialty section:
This article was submitted to Inorganic Chemistry, a section of the journal Frontiers in Chemistry

Received: *02 October 2020*
Accepted: *30 November 2020*
Published: *21 December 2020*

Citation:
Burgess L, Wilson H, Jones AR, Hay S and Natrajan LS (2020) Assessing the Covalent Attachment and Energy Transfer Capabilities of Upconverting Phosphors With Cofactor Containing Bioactive Enzymes. Front. Chem. 8:613334. doi: 10.3389/fchem.2020.613334

INTRODUCTION

Lanthanide-doped upconverting phosphors (UCPs) have attracted considerable attention in recent years as an important and versatile class of luminescent nanoparticles (Zhou et al., 2015b). Upconversion (UC) is an anti-Stokes process involving the sequential absorption of multiple low-energy photons and subsequent emission of one higher-energy photon, facilitated by the ladder-like arrangement of long-lived energy levels found in lanthanide ions (Haase and Schäfer, 2011). This means that, in contrast to conventional fluorophores, upconverting materials can achieve visible emission with excitation in the near-Infra-Red (nIR) region of the electromagnetic spectrum.

While the upconversion phenomenon has recently been observed in discrete molecular complexes (Aboshyan-Sorgho et al., 2011; Blackburn et al., 2012; Suffren et al., 2013; Nonat et al., 2016; Charbonnière, 2018; Golesorkhi et al., 2019, 2020; Woodward et al., 2019; Nonat and Charbonnière, 2020), UC is most efficiently achieved by doping lanthanide ions into a low-phonon crystalline matrix (e.g., $NaYF_4$, Gd_2O_2S), where non-radiative decay can be minimized (Haase and Schäfer, 2011). The past two decades have seen the successful translation of these materials from the bulk solid to nanocrystals with controlled size, morphology and surface-properties, enabling an increasingly diverse range of applications (Zhou et al., 2015a). In particular, the ability to modify the surface of UCPs in a stable aqueous dispersion lends itself well to biological applications including bio-imaging, sensing, and photodynamic therapy (Wang et al., 2005; Chatterjee et al., 2008; Idris et al., 2012).

In biological media, excitation in the nIR enables deeper penetration through tissue and an improved signal-to-noise via the avoidance of background auto-fluorescence (Haase and Schäfer, 2011). In addition to these merits, UCPs also offer negligible photobleaching, no photoblinking and low cyto-toxicity (Haase and Schäfer, 2011; Gnach et al., 2015). Furthermore, excitation at a single wavelength can produce simultaneous emission from a number of different doped lanthanide ions, with characteristic emission bands easily resolved by wavelength or by lifetime (typically μs-ms) (Wang and Liu, 2008; Eliseeva and Bünzli, 2010).

Many UCP biosensing systems developed in the literature to date utilize luminescence resonance energy transfer (LRET). This is a distance-dependent energy transfer process that only occurs when a donor and acceptor moiety are within the Förster radius (<10 nm) of each other (Lakowicz, 2006). For example, UCP donor emission can be quenched by an LRET acceptor that is brought into range by the presence of the target analyte, as with labeled antibodies in a sandwich immunoassay (Wang et al., 2009). Alternatively, UCP donor emission can be restored by separation from an LRET acceptor by analyte-induced cleavage of a connection between the two (Wang et al., 2012).

Rather than modulating the separation distance of donor and acceptor, we have recently reported the development of systems that exploit a change in the spectral overlap of a biomolecule acceptor with the UCP. This approach has often been applied to the detection of metal ions, whereby the absorption maximum of a moiety on the UCP surface is modulated by complexation of a metal ion (Liu et al., 2011; Peng et al., 2015). Interestingly, there are a number of active biomolecules with chromophoric co-factors that could be monitored in a similar way (Burgess et al., 2020).

Our initial work showed that UCPs could be used to monitor enzyme turnover for pentaerythritol tetranitrate reductase (PETNR), a flavin-dependent enzyme with spectrally distinct redox states, and we later expanded the scope to the detection of a number of PETNR substrate analytes (Harvey et al., 2014; Oakland et al., 2017). In these earlier studies where the enzyme was added to the UCP containing solution, we were unable to conclusively assign the mechanism of apparent energy transfer (AET) between the UCP donor and PETNR-flavin mononucleotide (FMN) acceptor. However, in order to maximize the energy transfer efficiency in such systems, it is advantageous for the biomolecule acceptor to be attached to the UCP surface, thereby placing the donor and acceptor within (or close to) the Förster radius. Our more recent work has therefore reported the covalent attachment of PETNR to UCPs, showing that catalytic activity is retained upon attachment, and that it is still possible to ratiometrically monitor the enzyme redox state and reversibly detect substrates (Natrajan et al., 2020).

In considering the covalent attachment of active biomolecules to UCPs, it is important to acknowledge the dependence of activity on a highly specific structure, such as the shape of an enzyme active site, or the position of an active cofactor (Sapsford et al., 2013). Bioconjugation must therefore ensure minimal structural disruption and take into account the resulting orientation of the bound enzyme or biomolecule on the UCP surface.

Methods that have been used to attach active enzymes have appeared in the literature, such as using a DNA linker to attach horseradish peroxidase (Lu et al., 2015). Parallels can also be drawn with the attachment of non-catalytic proteins, such as the use of carbodiimide chemistry to attach a folate binding protein (Arppe et al., 2015), and a number of different antibodies (Sedlmeier and Gorris, 2015). However, although commonly utilized bioconjugation strategies should be feasible with UCPs, studies in this area are lacking and there remains no reliable bio-toolbox for the attachment of active enzymes to UCPs, particularly when looking to optimize separation distances for efficient LRET.

Here we expand on our reports of covalently bound active PETNR by screening a number of conjugation methods to contribute to the aforementioned bio-toolbox. Starting with organic dye models, we establish the importance of using several characterization methods in analyzing the success of a reaction. We then use a green fluorescent protein (GFP) to screen bioconjugation methods, before selecting one robust and versatile method for the attachment of a variety of active biomolecules. Finally, we prove that the activity of these proteins is retained upon conjugation, thus presenting an opportunity for the development of highly sensitive UCP-biomolecule sensors.

MATERIALS AND METHODS

Materials

Hexagonal phase Gd2O2S:Yb,Tm (PTIR475) and Gd2O2S:Yb,Er (PTIR545) upconverting phosphors were donated by Phosphor Technology Ltd. See **Supplementary Figure 30** for powder X-ray diffraction spectra. Enhanced GFP was prepared as described previously (Natrajan et al., 2020). The heme domain of cytochrome P450 BM3/CYP102A1 and *N*-palmitoylglycine (NPG) were prepared as described previously (Brenner et al., 2007) and donated by the Munro group (The University of Manchester). Glucose oxidase and glutathione reductase were purchased from Sigma-Aldrich. Sulfo-SMCC was purchased from Thermo-Fischer Scientific. 6-maleimidohexanoic acid (MHA) was purchased from Alfa Aesar. SAMSA fluorescein (SF) was purchased from Life Technologies Limited. Fluorescein

maleimide was purchased from Vector Laboratories Limited. Carboxyethylsilanetriol di-sodium salt was purchased from Fluorochem Limited. All other solvents, reagents and biomolecules were purchased from Sigma-Aldrich. All reagents and solvents were used as received. Deionised (DI) water was obtained from a Millipore Synergy water purification system.

Characterization Methods

Emission spectra were recorded in 1 cm^3 quartz cuvettes using an Edinburgh Instrument FP920 phosphorescence lifetime spectrometer (with single 300 mm focal length excitation and emission monochromators in Czerny Turner configuration) equipped with a 45 mW continuous wave (CW) 980 nm diode laser (Edinburgh Instruments) and a red sensitive photomultiplier in peltier (air cooled) housing (Hamamatsu R928P). No detector correction files were used when collecting the emission spectra in order to observe the 475 nm blue emission band and the nIR emission band at 800 nm of the upconverting phosphors on the same intensity scale and to observe the quenching of the 475 nm emission band during the experiments (i.e., without having to expand the blue region of the spectra manually).

TEM images were obtained on a 200 kV Phillips Microscope on carbon coated copper grids and were analyzed using the Gatan3 Digital Micrograph Software Package. The TEM grids were purchased from Agar Scientific Limited and were prepared by the drop cast method using a dilute sample of the UCPs and air-dried.

Fourier transform Infrared (FTIR) spectra were obtained using solid samples on a Bruker alpha FT-IR spectrometer and the data was analyzed using the OMNIC software.

Raman Spectra were recorded on a Horiba Xplora plus confocal Raman spectrometer on glass microscope slides, data were analyzed using the LabSpec software.

The dynamic light scattering (DLS) size and zeta potential analysis was performed on a 1 mg/mL aqueous solution of the UCPs. Both measurements were recorded in disposable folded capillary cells (DST1070) using a 633 nm laser as the excitation source on a Malvern Zetasizer nano ZS instrument. The data were analyzed using the Zetasizer programme and the results quoted are the average of three measurements.

UV visible spectra were recorded on a 1 mg/mL aqueous solution of UCPs on a Cary 60 Spectrophotometer (Aglient) using a 1 cm^3 quartz cuvette, the data were analyzed using the Cary WinUV software.

Enzyme kinetic studies were carried out in a Belle glovebox under an $N_{2(g)}$ atmosphere, using a Cary 60 bio UV-Vis spectrometer and the Cary kinetics program.

Reflectance spectra were recorded using a Perkin Elmer Lambda 1050 UV/Vis/nIR spectrometer with a tungsten lamp and a 150 mm InGaAs integrating sphere. Data were analyzed using the Perkin Elmer UV WinLab programme.

The microanalytical department at The University of Manchester carried out thermogravimetric analysis (TGA) from 35 to 600°C on dry UCP samples in air using a Mettler Toledo TGA/DSC1 Star System.

Synthetic Procedures

General Procedure for the Synthesis of Silica Capped Industry Upconverting Phosphors

Silica capped **(silica475 and silica545);** (3-aminopropyl)triethoxysilane capped **(APTES475 and APTES545);** (3-mercaptopropyl)trimethoxysilane capped **(MPTMS475 and MPTMS545).**

Industry procured gadolinium oxysulfide of hexagonal (β-) phase Gd_2O_2S (**Supplementary Figure 30**) upconverting phosphors (PTIR-UCPs) (15 mg) were dispersed in a mixture of cyclohexane (40 mL) and Igepal CO-520 (1.5 mL, 3.39 mmol) before 25% ammonium hydroxide (0.5 mL) was added. After stirring for 60 min TEOS (60 μL, 0.00039 mmol) was added. After a further 60 min, APTES (60 μL, 0.00029 mmol) or MPTMS (60 μL, 0.00031 mmol) was optionally added to give further functionalisation as appropriate. The reaction mixture was then stirred for 48 h in a sealed flask at room temperature. Acetone (15 mL) was added to cause the nanoparticles to precipitate. The precipitate was collected by centrifugation (60 min, 4,000 rpm). The pellet was washed with acetone (2 × 25 mL) and then with ethanol:water (2:1, 30 mL) and collected by centrifugation (60 min, 4,000 rpm).

Triethoxysilane-PEG-maleimide capped **(MPS475)**

As prepared above, silica475 (20 mg) were dispersed in deionized water:ethanol (22 mL, 1:10 v/v) before 25% ammonium hydroxide (1 mL) was added. Triethoxysilane-PEG-maleimide (20 mg, 0.004 mmol) was then dissolved in deionized water:ethanol (1.5 mL, 2:1 v/v). The two solutions were combined and the reaction mixture was stirred overnight in a sealed flask at room temperature. The UCPs were collected by centrifugation and washed with ethanol (2 × 20 mL) then water (1 × 20 mL).

General Procedure for the Solvo(hydro)Thermal Synthesis of Functionalized $NaYF_4$:Yb,Tm Upconverting Nanoparticles

According to modifications of our previous works (Oakland et al., 2017), an aqueous solution of NaOH was combined with solutions of organic ligands in either ethanol or water. Oleic acid was then added (if required), followed by 10 min of stirring to form a homogenous solution. Two further additions were each followed by 10 min of stirring: (a) an aqueous solution of lanthanide salts; (b) an aqueous solution of NaF (dropwise). The resulting mixture was transferred to a Teflon lined reaction vessel and heated at 120°C for 30 min, before increasing the temperature to 200°C for 5 h. After cooling, the solution was centrifuged to obtain the product, and washed with ethanol three times.

Exact reagent quantities are given below:

6-aminohexanoic acid, 6-maleimidohexanoic acid and oleic acid capped (AHAMHAOAYbTm): 5 mL aqueous solution of NaOH (1 g, 24.4 mmol) and AHA (5 g, 38 mmol); 8.5 mL ethanol solution of MHA (2 g, 9.5 mmol); 17 mL of OA; 1.2 mL aqueous solution of $LnCl_3.6H_2O$ (0.5 M, 20 % Yb, 0.2 % Tm, 79.8 % Y); 4 mL aqueous solution of NaF (168 mg, 4 mmol).

6-maleimidohexanoic acid capped (MHAYbTm): 4 mL aqueous solution of NaOH (1 g, 24.4 mmol); 25 mL ethanol

solution of MHA (11.4 g, 54 mmol); 1.2 mL aqueous solution of $LnCl_3.6H_20$ (0.5 M, 20 % Yb, 0.2 % Tm, 79.8 % Y); 4 mL aqueous solution of NaF (168 mg, 4 mmol).

Dimercaptosuccinic acid capped (DMSAYbTm): 2 mL aqueous solution of NaOH (0.2 g, 5 mmol); 5 mL ethanol solution of DMSA (0.7697 g, 4.22 mmol); 0.24 mL aqueous solution of $LnCl_3.6H_20$ (0.5 M, 20 % Yb, 0.2 % Tm, 79.8 % Y); 1 mL aqueous solution of NaF (33.58 mg, 0.8 mmol).

Cysteine capped (cysteineYbTm): 3 mL aqueous solution of NaOH (0.940 g, 7.76 mmol); 18.5 mL ethanol solution of cysteine (4.9273 g, 40.5 mmol); 1.2 mL aqueous solution of $LnCl_3.6H_20$ (0.5 M, 20 % Yb, 0.2 % Tm, 79.8 % Y); 4 mL aqueous solution of NaF (168 mg, 4 mmol).

Polyethylenimine capped (PEIYbTm): $Y(NO_3)_3.6H_2O$ (0.0715 g, 0.1868 mmol), $Yb(NO_3)_3.6H_2O$ (0.0281 g, 0.0625 mmol) and $Tm(NO_3)_3.6H_2O$ (0.0033 g, 0.0075 mmol) were dissolved in deionised water (9 mL) before PEI (340 mg, 0.0034 mmol) was added and the reaction mixture stirred for 5 min. Then an aqueous solution (9 mL) of NaF (126 mg, 3 mmol) was added with vigorous stirring. Ethanol (9 mL) was added and the reaction mixture stirred for 10 min before a second addition of ethanol (9 mL) was added and the contents were transferred to a Teflon lined reaction vessel and heated at 120°C for 30 min before increasing the temperature to 200°C for 17 h. The solution was centrifuged after cooling. Washed with ethanol (3 × 10 mL).

General Procedures for the Covalent Attachment of GFP to the Surface of Functionalized UCPs

An aqueous solution of functionalized UCPs (1 mL) was diluted with PBS buffer (1 mL, 100 mM, pH 7.4), before the addition of GFP. Mixtures were left under gentle agitation at 4°C for 24 h. Products were collected by centrifugation (10 min, 10,000 rpm) and washed three times with PBS. The mass of UCPs in the initial 1 mL dispersion is given in brackets below for all conjugations.

The following were all reacted with 0.004 μmol of GFP (300 μL of 13 μM stock solution): **AHAMHAOAYbTm_GFP** (12.1 mg); **MHAYbTm_GFP** (18.6 mg); **DMSAYbTm_GFP** (8.3 mg); **CysteineYbTm_GFP** (17.7 mg).

The following were both reacted with 0.01 μmol of GFP (500 μL of 33 μM stock solution): **MPS475_GFP** (1.8 mg); **MPTMS475_GFP** (10.6 mg).

The following were reacted with 0.02 μmol of GFP (400 μL of 40 μM stock solution), which had previously been combined at room temperature for 30 min with 100 μL of sulfo-SMCC cross-linking reagent (1 mg, 2.3 μmol): **APTES475_GFP** (52.1 mg); **PEIYbTm** (39.3 mg).

General Procedures for the Covalent Attachment of Other Biomolecules to the Surface of Functionalized UCPs

Sulfo-SMCC (2 mg, 4.6 μmol) was dissolved in deionized water (200 μL) then diluted with PBS buffer (1 mL, pH 7.4, 100 mM). After addition of the biomolecule (see quantities below), the mixture was left at room temperature for 30 min. An aqueous solution (1 mL) of APTES475 or APTES545 (10 mg) was added, and the mixture left under gentle agitation at 4°C for 24 h. Products were collected by centrifugation (10 min, 10,000 rpm) and washed three times with PBS.

Quantities of biomolecule added were as follows:

0.04 μmol **BM3Heme** (500 μL of 75 μM solution); 0.4 μmol **CytC** (5 mg); 0.014 μmol **glucose oxidase** (2.3 mg); 0.006 μmol **glutathione reductase** (500 μL of 1.5 mg/mL suspension).

RESULTS AND DISCUSSION

Preliminary Screening With Organic Dyes

Given the large, variable size and complexity of biomolecules, covalent attachment methods were first investigated using a range of structurally more simple organic dyes that absorb visible light (structures shown in **Supplementary Figure 1**). Five dyes were selected based on their spectral overlap with UC emission (**Supplementary Figure 2**) and on the presence of functional groups ideal for different conjugation methods. We have previously demonstrated the ability of these organic dyes to act as apparent energy transfer (AET) acceptors in non-covalent systems with UCPs (Burgess et al., 2020).

Reactions are summarized in **Table 1**, with further experimental details provided in the **Supplementary Information**. All reactions used Gd_2SO_4 upconverting phosphors, referred to by the wavelength of their key upconversion emission band as PTIR475 and PTIR545 for Tm^{3+} and Er^{3+} doped crystals, respectively. Functional groups were introduced via silica capping as indicated in **Table 1**.

The four conjugation methods were all found to be successful and, most importantly, this screening process enabled us to identify the most appropriate characterization methods for determining this success. Full characterization was conducted using UV-vis solution spectroscopy, reflectance spectroscopy, fluorescence spectroscopy, IR spectroscopy, Raman spectroscopy, thermogravimetric analysis (TGA), dynamic light scattering (DLS), transmission electron microscopy (TEM), and visual inspection. A comprehensive summary of all data can be found in **Supplementary Figures 4–12**, with highlights illustrated in **Figures 1**, **2**.

Visual inspection gave the first indication of successful attachment; the white UCP precursors became highly colored after the reaction workup (as seen for SF475 in **Figure 1A**, and other dyes in **Supplementary Figure 4**). Note that pellets were washed repeatedly until the supernatant was shown to contain no free dye by UV-vis absorption spectroscopy (**Supplementary Figure 3**), so the color is most likely to originate from organic dye covalently attached to the UCP surface.

Solution UV-vis spectra of the re-dispersed SF475 and SF545 products, as an example, clearly show absorption maxima corresponding to the dye molecule (**Figure 1B**). However, the absorption maximum is slightly shifted to lower energy compared to the starting material SF dye, which can be rationalized in terms of the coupling reaction used. Given the thiol ether was first deprotected then coupled with sulfo-SMCC (sulfosuccinimidyl 4-(*N*-maleimidomethyl)cyclohexane-1-carboxylate) in a thiol-malemide coupling, slight changes in the electronic structure of the aromatic system and solvatochromism in solution would account for the observed

TABLE 1 | Summary of initial methods screened for the attachment of organic dyes to the surface of functionalized PTIR475 or PTIR545 upconverting phosphors.

Dye	Further dye functionalisation	Functionalized silane capping on PTIR475 or PTIR545	Coupling Method
Fluorescein isothiocyanate (FITC)	n/a	3-aminopropyl triethoxysilane (APTES)	Isothiocyanate + amine
Rhodamine B isothiocyanate (RBITC)			
Methyl red (MR)	Carbodiimide activation of carboxylic acid		Carbodiimide coupling
SAMSA fluorescein (SF)	Basic deprotection of thiol (acetyl group)		Thiol + maleimide (with a sulfo-SMCC crosslinker)
Fluorescein maleimide (FM)	n/a	3-mercaptopropyl trimethoxysilane (MPTMS)	Thiol + maleimide

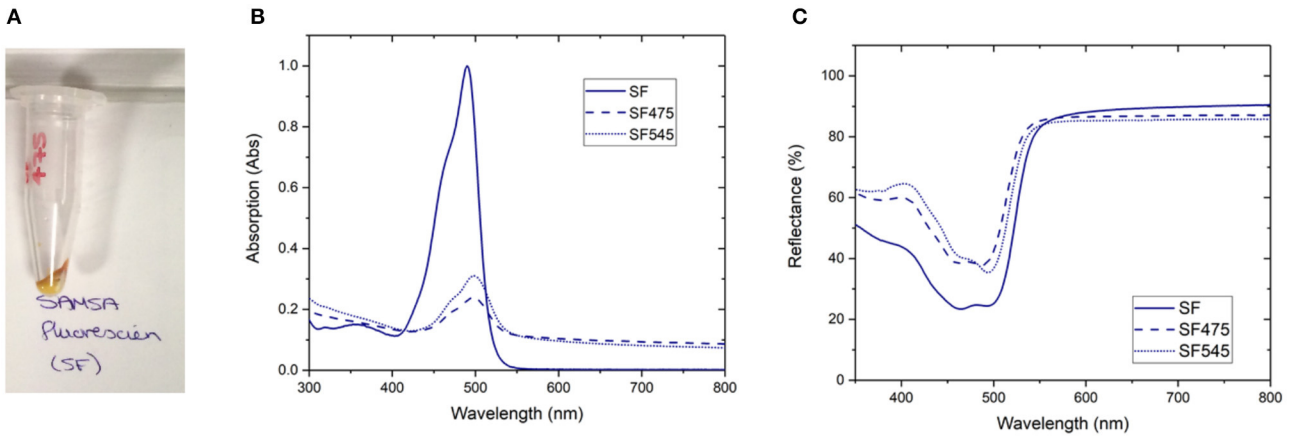

FIGURE 1 | A selection of characterization data for the attachment of SAMSA fluorescein (SF) to PTIR475 or PTIR545 **(A)** photograph of the SF475 product, **(B)** solution UV-vis spectra for SF, SF475, and SF545, **(C)** reflectance spectra for SF, SF475, and SF545.

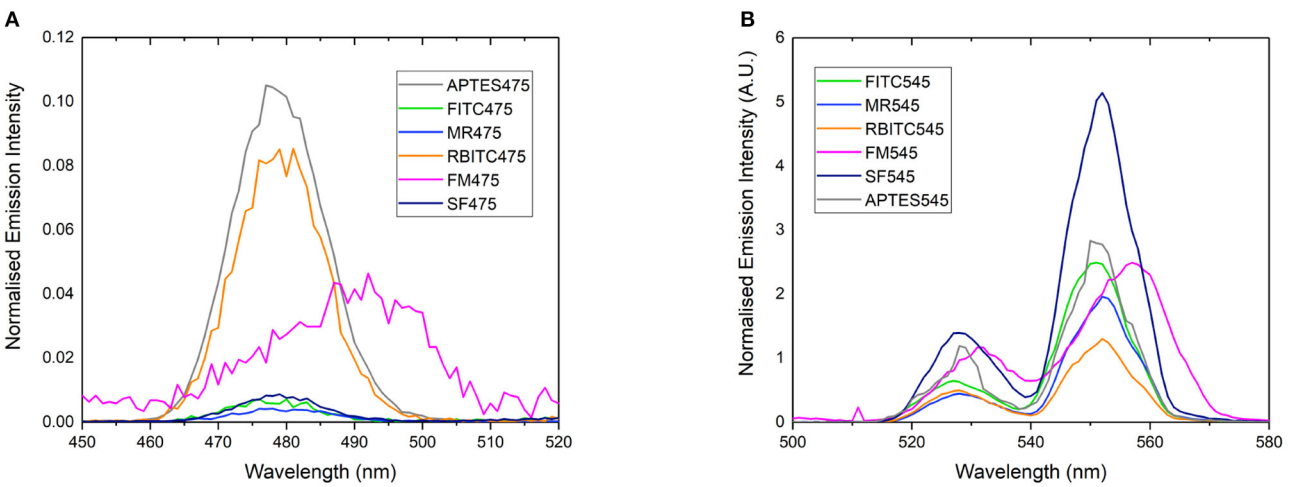

FIGURE 2 | Normalized emission spectrum of **(A)** APTES475, FITC475, RBITC475, MR475, SF475, and FM475 showing only the 475 nm band and **(B)** APTES545, FITC545, RBITC545, MR545, SF545, and FM545 showing only the 545 nm band. All solutions were 1 mg/mL in 100 mM PBS pH 7.4. Excitation at 980 nm. All spectra are reported uncorrected for the detector response. Spectra are normalized relative to the unquenched emission bands at 800 or 660 nm (not shown here, see **Supplementary Figure 7** for expanded spectra).

red shift. In addition, the UV-vis solution spectra also featured scattering attributed to the UCPs (∼1–2 μM in size). In most other reactions, this obscured the identification of any dye absorption bands (**Supplementary Figure 5**). Scattering effects in solution can be avoided by conducting reflectance spectroscopy, where samples are drop cast and dried onto glass slides. The resulting spectra are inversely proportional to absorbance, and characteristic reflectance bands were observed for both SF475 and SF545 (**Figure 1C**) and all other dye reactions (**Supplementary Figure 6**). We concluded that reflectance offered superior characterization to solution UV-vis spectroscopy for these UCP dispersions.

Further characterization should be possible using IR spectroscopy by identifying key absorption bands in the reaction products. However, although correct functional group vibrations were present in the UCP-dye conjugate spectra, the overall poorer resolution prevented full spectral assignments, particularly in the fingerprint region (**Supplementary Figure 8**). Raman spectroscopy also yielded little useful information regarding conjugation, primarily due to the free dye spectra being reasonably featureless and pronounced lattice vibrations from the UCPs (**Supplementary Figure 9**).

Rather than identifying the dye itself, we also looked to characterize the resulting energy transfer from the UCP to the surface-bound dyes. It is clear from emission spectra (**Figure 2**) that the UC band is quenched in almost all dye-UCP conjugates when compared to the precursor APTES475 or APTES545 UCPs. Of note, the spectra of FM475 and FM545 (**Figure 2**) are bathochromically shifted by ca. 12 nm with respect to the parent MPTMS475 and MPTMS545 UCPs (See **Supplementary Figure 29**) and those functionalized with all the other dye molecules in this study. The exact reason behind this is not immediately obvious, but one possible reason is that in the FM conjugated systems, additional crystal field effects imposed by the different surface functionalisation with FM is more pronounced (Eliseeva and Bünzli, 2010; Hatanaka and Satoshi, 2014). Additionally, the upconverted emission spectrum of SF545 shows an apparent increase in intensity compared to the APTES545 precursor. Given that the corresponding spectra in the SF475 system show the expected decrease in emission intensity, this observation suggests that the normalization (to the UCNP 660 emission band) is giving an artificially inflated signal due to a small degree of spectral overlap of the FM dye with both 550 and 660 nm emission bands in the UCP (Burgess et al., 2020) (**Supplementary Figure 2**).

The success of the dye-attachment to the UCPs was additionally examined by DLS, TEM and/or TGA. However, negligible differences between the starting materials and products were observed in the DLS and TEM data, whilst the presence of several different organic moieties hindered accurate assignment of weight losses by TGA. Because the addition of a layer of organic dye will only impart a small effect on the hydrodynamic ratios in solution (DLS) and not significantly add to the scattering observable by TEM, these observations are not surprising. Conducting these measurements are nevertheless important to show that there has been no change to the bulk morphology and dispersion of the UCPs following conjugation reactions (**Supplementary Figures 10–12**). In different systems, the attachment of larger or more charged molecules, it may be possible to identify the presence of an additional capping layer via DLS or TEM. It may also be possible in some cases to quantify the amount of dye attached using TGA.

From this preliminary work, we demonstrated that the success of covalent attachment to UCPs requires analysis using the combination of several spectroscopic techniques. Here, reflectance UV-vis absorption spectroscopy, emission spectroscopy alongside visual inspection were found to be most useful. We note, in the case of IR spectroscopy, however, that the data may not always be as conclusive as expected, highlighting the importance of a comprehensive approach to characterization.

From here we moved on to screening coupling methods with a range of suitable proteins.

Screening With GFP

Although proteins do not naturally contain either isothiocyanate or maleimide groups for bioconjugation reactions using these functional groups, the natural amino acids present include thiol, amine and carboxylic acid groups, which are available moieties for a variety of bioconjugation reactions. However, the prevalence of carboxylic acid and amine groups makes it unfeasible to target a single residue, leading to issues with non-specific orientation of the conjugated protein on the UCP surface. More specific conjugation can be achieved by targeting the thiol side-chain of cysteine residues. While these are often engaged in disulfide bridging within the tertiary structure of a biomolecule, certain surface cysteine residues are readily accessible for functionalization and the proteins herein, were chosen so as to take advantage of this fact. In cases, where the protein has no available surface cysteine group, protein engineering can be utilized to introduce an accessible surface cysteine residue at a specific location that can be optimized for bioconjugation with retention of catalytic activity.

Therefore, we next screened the potential of a variety of UCPs in coupling to proteins with surface cysteine residues (**Scheme 1**). Enhanced GFP was chosen for the conjugation screening because it is a stable and well-characterized protein whose absorption profile overlaps with the 475 nm band of thulium doped UCPs (Burgess et al., 2020). In total, eight different UCPs and UCNPs were screened, as summarized in **Scheme 1**. Three UCPs possess surface thiol groups (DMSAYbTm, MPTMS475, and cysteineYbTm), three have surface maleimide groups (AHAMHAOAYbTm, MPS475, and MHAYbTm), and two have surface amine groups (PEIYbTm and APTES475). The surface amines were further functionalized with a sulfo-SMCC linker to convert the amine into a maleimide group. All reactions are classified as either thiol-thiol couplings, or thiol-maleimide couplings.

For all GFP conjugation reactions, the phosphor/nanophosphor was suspended in PBS (100 mM, pH 7.4) and left to react at 4°C under gentle agitation for 48 h. The reaction must be carried out at a pH between pH 6.5–pH 7.5 for it to be selective for the surface cysteine group (thiol containing side chain) over the lysine residues (amine containing side chain) in GFP. In this pH range, the thiol group

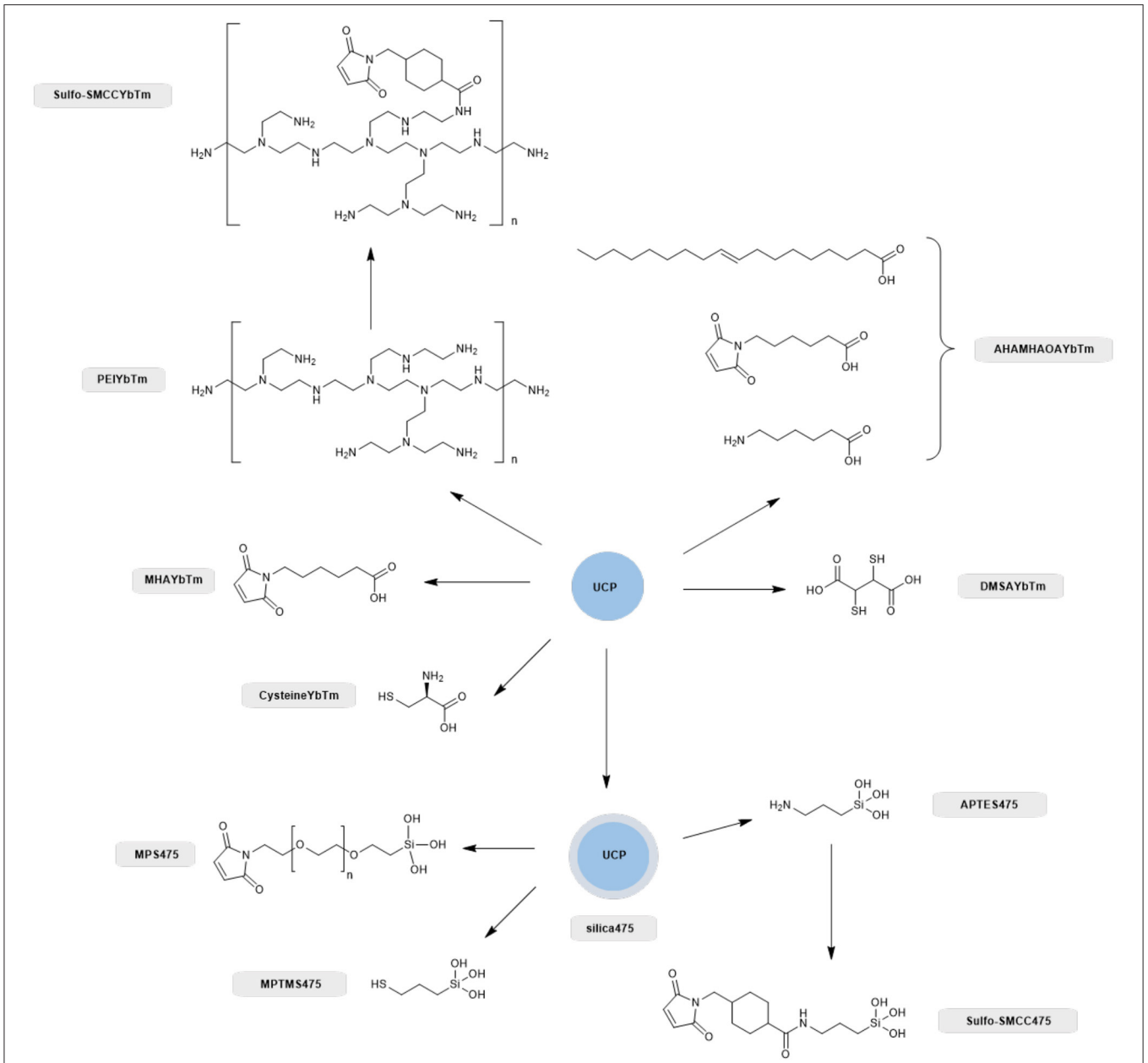

SCHEME 1 | Overview of the different ligand systems investigated for the covalent attachment of GFP with compound names shown alongside. All systems that relied on a silica capping layer for the attachment of the thiol or maleimide functional group were derived from the PTIR UCPs (silica475), whereas synthesized nanoparticles directly capped with carboxylate containing thiol, amine and maleimide linkers negated the use of a silica capping layer and these were nanoparticles based on solvo(hydro)thermal syntheses as described previously (Oakland et al., 2017).

of the cysteine is nucleophilic and will react with the maleimide group whereas the amine groups are protonated and unreactive. Outside of this pH range, the amines may be nucleophilic enough to compete with the thiol groups.

The product was then collected by centrifugation and washed with PBS until the supernatants were shown to be clear (free of unbound GFP) by solution UV-visible spectroscopy (**Supplementary Figure 13**). The color of the resulting pellet gave the first indication of whether the reaction has been a success, as shown in **Figure 3**. A green pellet is consistent with GFP being bound to the UCPs; therefore MHAYbTm, APTES475, PEIYbTm, AHAMHAOAYbTm, and DMSAYbTm are the most likely to have been covalently attached to GFP successfully. The pellets for cysteineYbTm, MPTMS475, and MPS475 remained white after work up, indicating attachment of either a very small amount of GFP, or none at all.

Based on these observations, maleimide capped phosphors are likely to be superior for bioconjugation. This is also seen

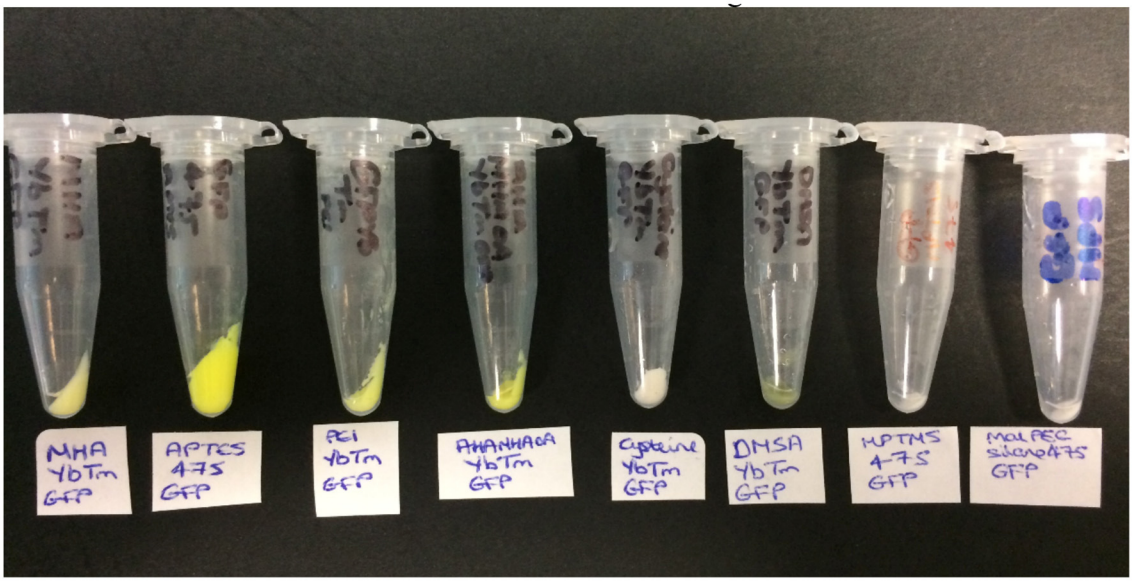

FIGURE 3 | The products obtained from the covalent attachment of GFP reactions (from left to right): MHAYbTm_GFP, APTES475_GFP, PEIYbTm_GFP, AHAMHAOAYbTm_GFP, CysteineYbTm_GFP, DMSAYbTm_GFP, MPTMS475_GFP, and MPS475_GFP.

in wider protein chemistry; commercial routes for labeling of biomolecules focuses on this maleimide-thiol chemistry and not thiol-thiol chemistry. This is due to the reversible formation of the thiol-thiol bond rendering this method less robust than desired.

The UCP-GFP conjugates were fully characterized using methods as with UCP-dye studies; a comprehensive summary is provided in the **Supplementary Figures 13–21**.

As observed with the UCP-dye conjugates, the quality of the data obtained for the UCP-GFP conjugates varied depending on the system in question, so that no single technique could be used to verify the success of the bioconjugation reaction. This point is highlighted in **Table 2**. Certain data show changes likely originating from successful GFP attachment (✓✓); some data show changes but cannot reliably be attributed to GFP (✓); some data show no changes at all (χ). Notably, the spectral data do not always align with the color changes observed by eye, which renders robust analysis of the relative success of UCP-GFP conjugation reactions challenging.

Nevertheless, we believe that the characterization data for the reaction with APTES475 (highlighted row in **Table 2**) provides compelling evidence for a successful bioconjugation reaction. Our previous work with the covalent attachment of PETNR (Natrajan et al., 2020) utilized this same coupling method, and our results here are an encouraging indication of its suitability in comparison to other screened systems. From here, we moved on to studying the attachment of other active biomolecules (truncated heme domain of cytochrome P450 BM3/CYP102A1 (BM3Heme), cytochrome *c* (cytC), glucose oxidase (GO) and glutathione reductase (GR).

Covalent Attachment of Active Proteins

Four proteins possessing surface exposed cysteine residues and suitable co-factors for energy transfer studies were selected for covalent attachment to the surface of the UCPs. These are the truncated heme domain of cytochrome P450 BM3/CYP102A1 (BM3Heme), cytochrome *c* (cytC), glucose oxidase (GO) and glutathione reductase (GR). **Figure 4** shows the overlap for the absorption spectra of each of these biomolecules with the emission from the UCPs: BM3Heme and cytC with the Er(III)-centered emission at 545 nm, and GO and GR with the Tm(III)-centered emission at 475 nm.

BM3Heme and cytC are heme proteins whose function depends upon the iron-porphyrin complex within the active site (Paoli et al., 2002). P450s enzymes such as BM3 are a family of enzymes that catalyse the oxygenation of a number of substrates (Girvan et al., 2007) and are responsible for the metabolism of drugs within the body (Ogu and Maxa, 2000). cytC is a small (12 kDa) redox active protein that is important for life (Hüttemann et al., 2011). It is the final electron carrier in the electron transport chain of the mitochondria during respiration (Hüttemann et al., 2011). It is also an important component in apoptosis (cell death). The electron transport capabilities of cytC lies in its heme cofactor, which is bound to the enzyme by two thioether bonds to cysteine residues from the protein (Bertini et al., 2006; Hüttemann et al., 2011).

GO and GR are flavoenzymes from a group of enzymes that catalyse the oxidation of a variety of different substrates (Walsh and Wencewicz, 2013). They contain either FMN or FAD (flavin adenine dinucleotide) redox active cofactor. GO is a FAD containing enzyme that catalyses the oxidation of β-D-glucose to

TABLE 2 | An overview of the results obtained from the analytical analysis of all the UCP-GFP conjugates.

UCP used *(avg. diameter of product by TEM)*	Color	Emission	Solution UV-Vis	Reflectance	IR	Raman	DLS	TEM	TGA
AHAMHAOAYbTm *(170 nm)*	✓✓	χ	✓✓	✓✓	✓	✓	✓	✓	✓
APTES475 *(0.8 μm)*	✓✓	✓✓	✓✓	✓✓	✓	✓	✓	✓✓	–
PEIYbTm *(80 nm)*	✓✓	χ	χ	✓✓	✓	✓	✓	✓	✓
DMSAYbTm *(640 nm)*	✓✓	✓	✓✓	χ	✓	✓	✓	✓	✓
MHAYbTm *(360 nm)*	✓✓	✓	χ	✓✓	✓	✓	✓	✓	χ
CysteineYbTm *(1.5 μm)*	χ	✓	χ	χ	χ	✓	✓	✓	✓
MPS475 *(1.2 μm)*	χ	χ	χ	χ	✓	χ	✓	✓	–
MPTMS475 *(1.0 μm)*	χ	✓	χ	χ	✓	χ	✓	✓	–

A double tick indicates that there has been a change in the observable behavior of the system after the GFP attachment reaction and that it is likely to be due to GFP attachment, a single tick indicates that there has been a change in the observable behavior of the system after the GFP attachment reaction but that it cannot be conclusively determined to be due to GFP attachment, a cross indicates that there has been no change in the observable behavior of the system after the GFP attachment reaction and a dash means that this measurement could not collected for this system.

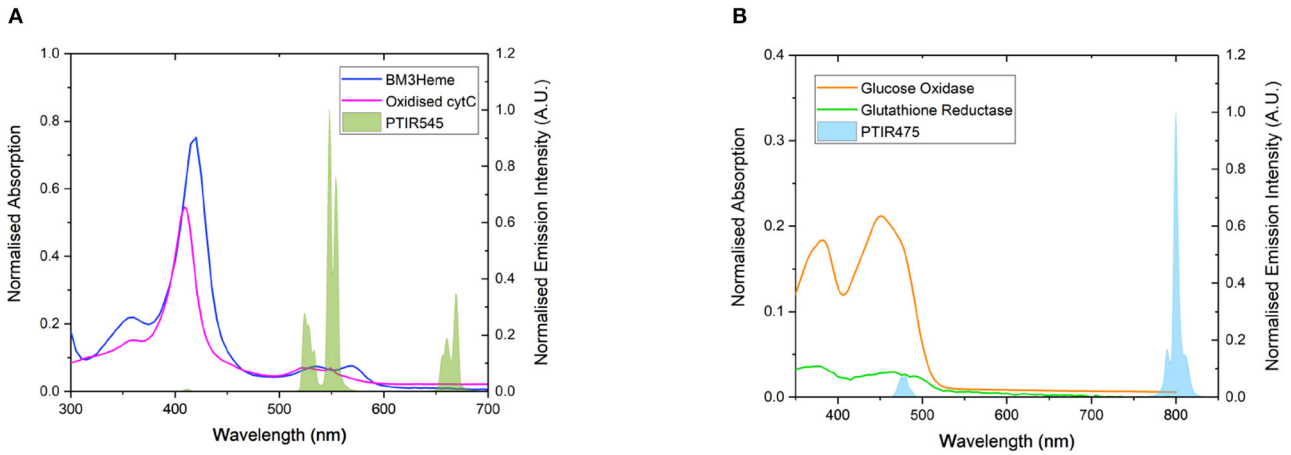

FIGURE 4 | (A) The overlap of the absorption bands of BM3Heme (8 μM) in 100 mM PBS pH 7.4 and oxidized cytC (10 μM) in 100 mM TRIS pH 7 with the emission bands of PTIR545 (1 mg/mL) in 100 mM PBS pH 7.4. Excitation at 980 nm. **(B)** The overlap of the absorption bands of GO (10 μM) and GR with the emission bands of PTIR475 (1 mg/mL). Excitation at 980 nm. All spectra were recorded in 0.1 M sodium acetate buffer pH 5.1.

β-D-glucono-1,5-lactone and H_2O_2 (Gibson et al., 1964). GO is most commonly used as an electrochemical blood glucose sensor for monitoring/diagnosing diseases such as diabetes (Heller and Feldman, 2008; Harper and Anderson, 2010; Bruen et al., 2017). GR is an NADPH dependent enzyme containing a FAD cofactor (Mavis and Stellwagen, 1968; Mittl and Schulz, 1994) that catalyses the reduction of oxidized glutathione disulphide (GSSG) to reduced glutathione (GSH) (Nimse and Pal, 2015). Reduced glutathione is used as an antioxidant in human tissues and can act as a biomarker for diseases such as Parkinson's, Alzheimer's, diabetes and HIV (Timur et al., 2008; Liu et al., 2017).

Based on the results from our screening studies with GFP, these 4 proteins/enzymes were all attached to UCPs using the method illustrated in **Scheme 2**. PTIR475 and PTIR545 UCPs were first capped with silica using a reverse microemulsion synthesis, with IGEPAL® CO-520 used to stabilize the procedure during the polymerization of tetraethyl orthosilicate (TEOS) (Muhr et al., 2014). The silica layer is important as it protects that UCP surface against solution quenching processes, it adds biocompatibility and provides the ability to easily functionalize further. In addition to TEOS (3-aminopropyl)triethoxysilane (APTES), was added to the reaction mixture to produce an accessible surface layer of primary amines within the silica shell.

The resulting APTES-coated UCPs can be coupled to the proteins with surface cysteines using a sulfo-SMCC cross-linker. This linker contains both an NHS ester and a maleimide and was first allowed to couple (via maleimide-cysteine conjugation) to the protein before the addition of APTES545 or APTES475 (via NHS-ester-amine conjugation). The reaction mixture was gently agitated under mild conditions to allow the coupling to progress and after each stage of this multi-step procedure the UCPs were centrifuged and washed several times to remove unreacted reagents.

As with dye-UCP and GFP-UCP conjugation reactions, visible color changes were an initial indication of reaction

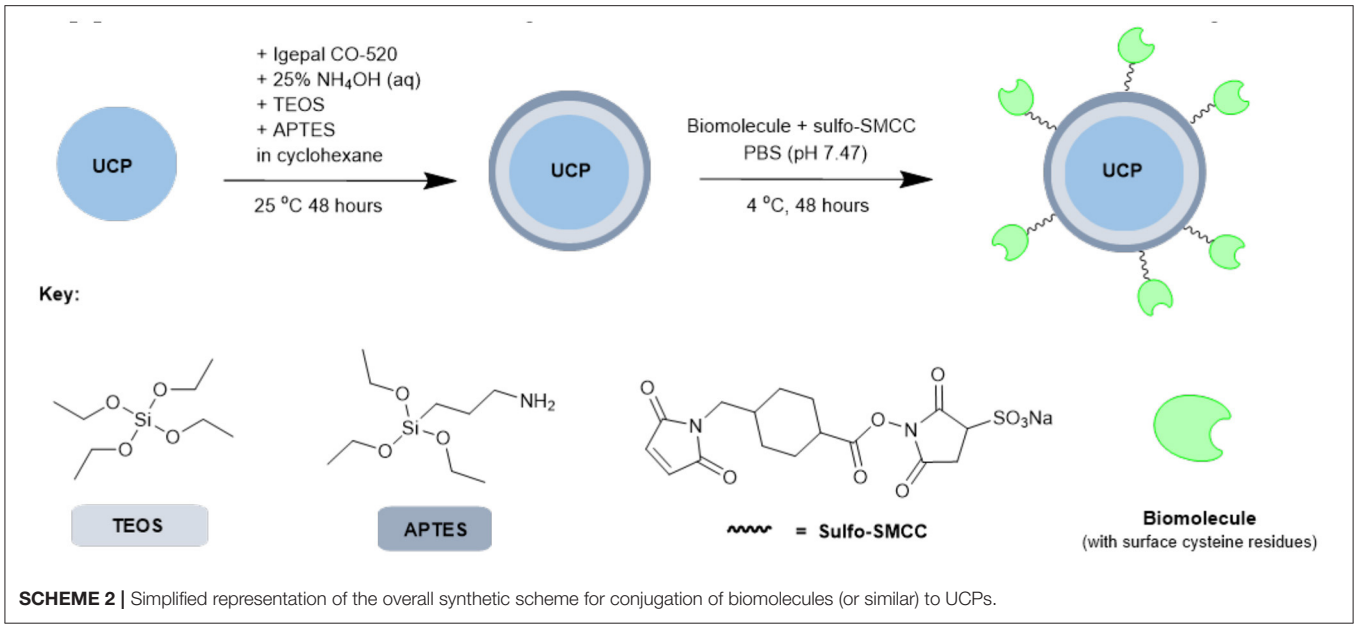

SCHEME 2 | Simplified representation of the overall synthetic scheme for conjugation of biomolecules (or similar) to UCPs.

success (**Figure 5**). Again, the pellets were washed until no free biomolecule (protein or cofactor) could be observed in the supernatants by UV-vis absorption spectroscopy (**Supplementary Figure 22**). Note that the presence of biomolecule absorption in the first of these washes indicates that they were added in suitable excess in all cases. The reactions with BM3Heme and cytC produced pellets with a strong red color, and with GO, a yellow pellet was obtained. The reaction with GR did not result in an observable color change by eye, but it should be noted that the quantity of enzyme in this reaction was far smaller due to availability of the stock suspension. Therefore, it is quite possible that the concentration of GR conjugated is simply too low to be seen with the naked eye.

As with the initial organic dye studies, UV-vis spectra (**Figure 6**) were dominated by scattering from the UCP dispersion. BM3Heme545 (**Figure 6A**) did, however, show a distinct peak at 418 nm corresponding to the absorption maximum of BM3Heme (Munro et al., 2007). Furthermore, cytC545 exhibited small peaks at 280 and 410 nm, which do align with the absorption peaks of cytC, albeit with different relative magnitudes. Reflectance measurements were also conducted (**Supplementary Figure 27**), and also show features centered at 280 nm from BM3Heme545, cytC545, and GR475, which is likely to originate from the aromatic residues in these proteins.

The IR spectra for all bioconjugates show the characteristic profiles of proteins, with the amide (NH, CO), carboxylic acid and CH fundamental stretching modes apparent, consistent with the presence of BM3Heme, cytC, GO, and GR on the surface of the UCPs (**Figure 7**). The GR475 spectrum exhibits weaker intensity than the other protein-UCP conjugates. This suggests, as indicated by visual inspection, that there is a low concentration of protein present in this system.

If the protein has successfully been attached to the surface of the UCPs, it is expected that a decrease in the emission intensity of the UCP emission bands will be observed due to AET from the UCP to the protein cofactor (heme or flavin). Therefore, a comparison of the emission profiles of the UCP-biomolecule to the precursor UCPs can be used to determine if the intact protein is present on the surface of the UCPs. The expected decrease in emission intensity was observed for cytC545, GO475, and GR475 (**Figures 8B–D**). The same was not found for BM3Heme545 (**Figure 8A**), which instead shows an increased emission; the reason for which remains unclear, but may indicate that this protein is acting as an extra hydrophobic layer preventing extra quenching of the UCPs with the surrounding water molecules and/or that surface coverage of the UCP has changed during manipulation. However, the data generally support a successful attachment of proteins/enzymes.

The analysis of the UV-vis, IR, fluorescence and color change of the UCPs, strongly suggests that the method described can be used to attach a range of proteins and enzymes that possess a surface/solvent-exposed cysteine residue. We have demonstrated the versatility of this method, having attached four different proteins; BM3Heme, cytC, GO, and GR (in addition to GFP). However, in order for future applications of UCP-protein systems as biosensors, it is necessary to prove that activity is retained upon conjugation.

Cytochrome P450 catalyses the oxidation of a variety of substrates within the body such as *N*-palmitoylglycine (NPG) (Zhang et al., 2020). Within the enzyme, the BM3Heme domain is responsible for substrate binding but requires the partner redox domain in order to be catalytically competent. Substrate binding causes a change in the relative intensities of the absorption bands (**Figure 9A**). This 10 nm shift in the absorption band of BM3Heme upon binding to NPG is also observed in the UV-vis spectrum of BM3Heme545 (**Figure 9B**) suggesting that the BM3Heme bound to the surface of the UCP has maintained its ability to bind to substrate in a way that is similar to the protein

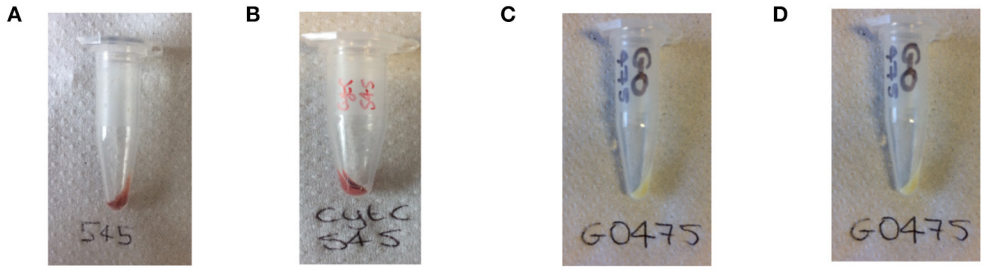

FIGURE 5 | Photograph of the: **(A)** BM3Heme545 product obtained from the covalent attachment of BM3Heme to APTES545, **(B)** cytC545 product obtained from the covalent attachment of cytC to APTES545, **(C)** GO475 product obtained from the covalent attachment of GO to APTES475, **(D)** GR475 product obtained from the covalent attachment of GR to APTES475.

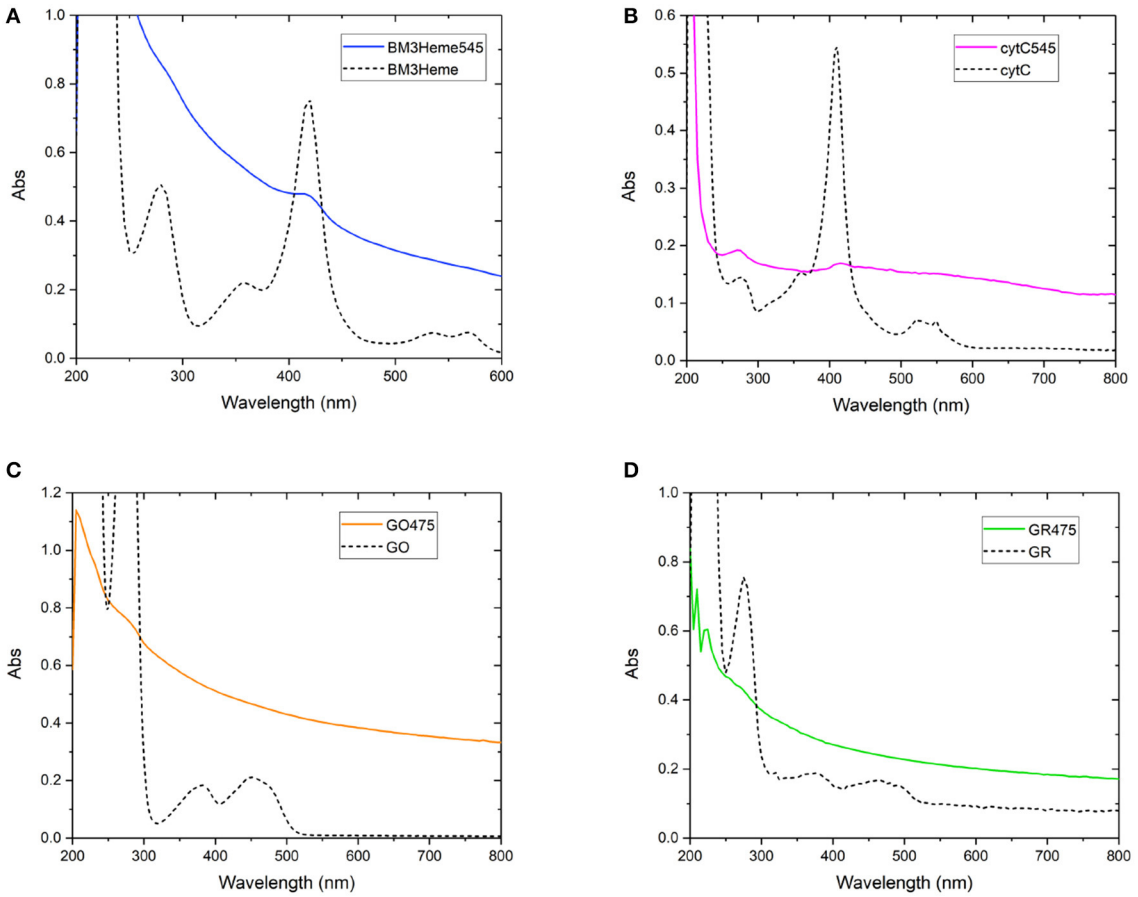

FIGURE 6 | Solution UV-vis spectra of biomolecule-UCP conjugates (solid lines), overlaid with the UV-vis spectrum of each relevant biomolecule (dashed lines): **(A)** BM3Heme545 and BM3Heme (10 mM PBS, pH 7.4), **(B)** cytC545 and cytC (100 mM PBS pH 7.4), **(C)** GO475 and GO (100 mM PBS, pH 7.4), and **(D)** GR475 and GR (10 mM PBS pH 7.4).

free in solution. Like BM3Heme, the UV-vis spectrum of cytC differs depending on whether the enzyme is in its oxidized or reduced form (**Supplementary Figure 24**). However, as we were unable to obtain a reliable UV-vis spectrum of cytC545 we were unable to repeat this experiment to see if cytC had maintained its activity when bound to the UCP surface.

GO is an FAD containing enzyme that catalyses the oxidation of β -D-glucose to β -D-glucono-1,5-lactone and H_2O_2 (Gibson

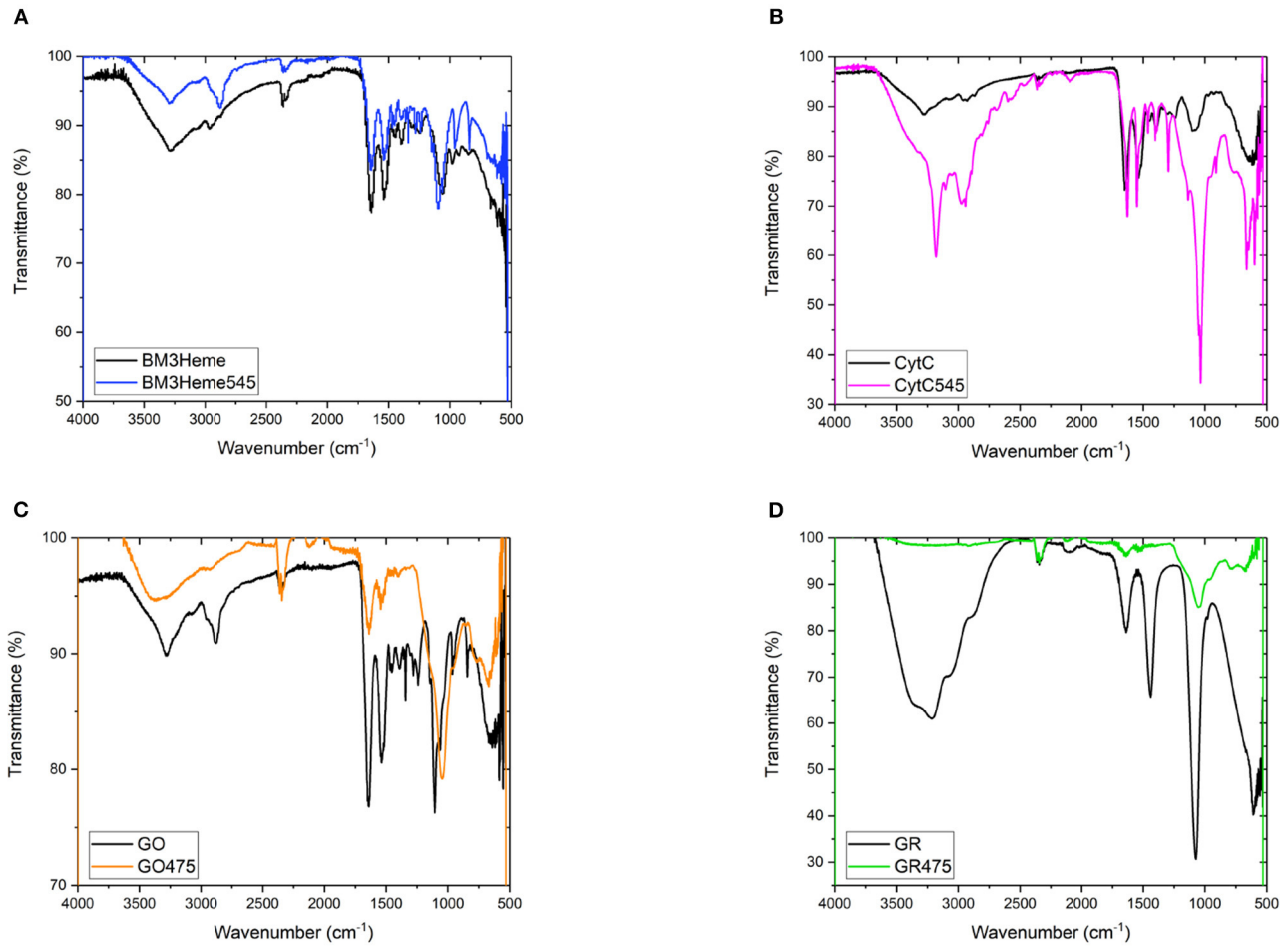

FIGURE 7 | (A) The FTIR spectra of BM3Heme and BM3Heme545, **(B)** the FTIR spectra of CytC and cytC545, **(C)** the FTIR spectra of GO and GO475, and **(D)** the FTIR spectra of GR and GO475.

et al., 1964). During the reaction, the cofactor FAD accepts an electron from the glucose substrate resulting in reduced GO. Then oxygen or an artificial oxidant acts as an electron acceptor, accepting the electron from reduced GO, resulting in oxidized GO. This oxygen then reduces to produce the H_2O_2 by-product (Leskovac et al., 2005). In order to determine if GO has retained its catalytic ability when covalently bound to the UCP surface, the steady state turnover and kinetics were measured. **Figure 10** below shows a Michaelis-Menten plot for the D-glucose concentration dependence of the activity of free GO and for GO475. Both GO and GO475 show typical Michaelis-Menten (saturation) behavior when using D-glucose as the limiting substrate and an excess of benzoquinone as the electron acceptor. These data were fitted to the Michaelis-Menten equation:

$$V_{obs} = \frac{V_{\max}[S]}{K_M + [S]};\ V_{\max} = k_{cat}[E]_0$$

giving a k_{cat} value of 1,139 ± 29 s^{-1} and a K_M value of 49.5 ± 4.8 mM for GO, which is close to the literature value of K_M = 33–110 mM (Gibson et al., 1964). A K_M of 14.5 ± 1.4 mM and V_{max} of 19.5 ± 0.5 μM s^{-1} were found for 1 mg/mL GO475. The difference in K_m values suggest changes to the kinetics of glucose binding and/or dissociation perhaps through some modest alteration or occlusion of the enzyme active site. Nevertheless, the K_M values for the GO475 system is of the same order of magnitude as the free GO, suggesting that there is an appreciable quantity of GO bound to the UCP that has retained its catalytic function after covalent attachment.

GR is an NADPH dependent, FAD containing enzyme that catalyses the reduction of oxidized glutathione disulfide (GSSG) to reduced glutathione (Nimse and Pal, 2015). The first step is the reduction of the FAD by NADPH before binding of the substrate GSSG in the active site. The enzyme then catalyses the reduction of the disulfide bond in GSSG to produce two glutathione molecules and the re-oxidized GR enzyme (Nimse and Pal, 2015). Again, to assess whether GR has retained its catalytic ability when covalently bound to the UCP surface, the enzyme kinetics of GR and GR475 were measured (**Figure 11**). Both GR and GR475 show typical Michaelis-Menten type behavior with the oxidizing

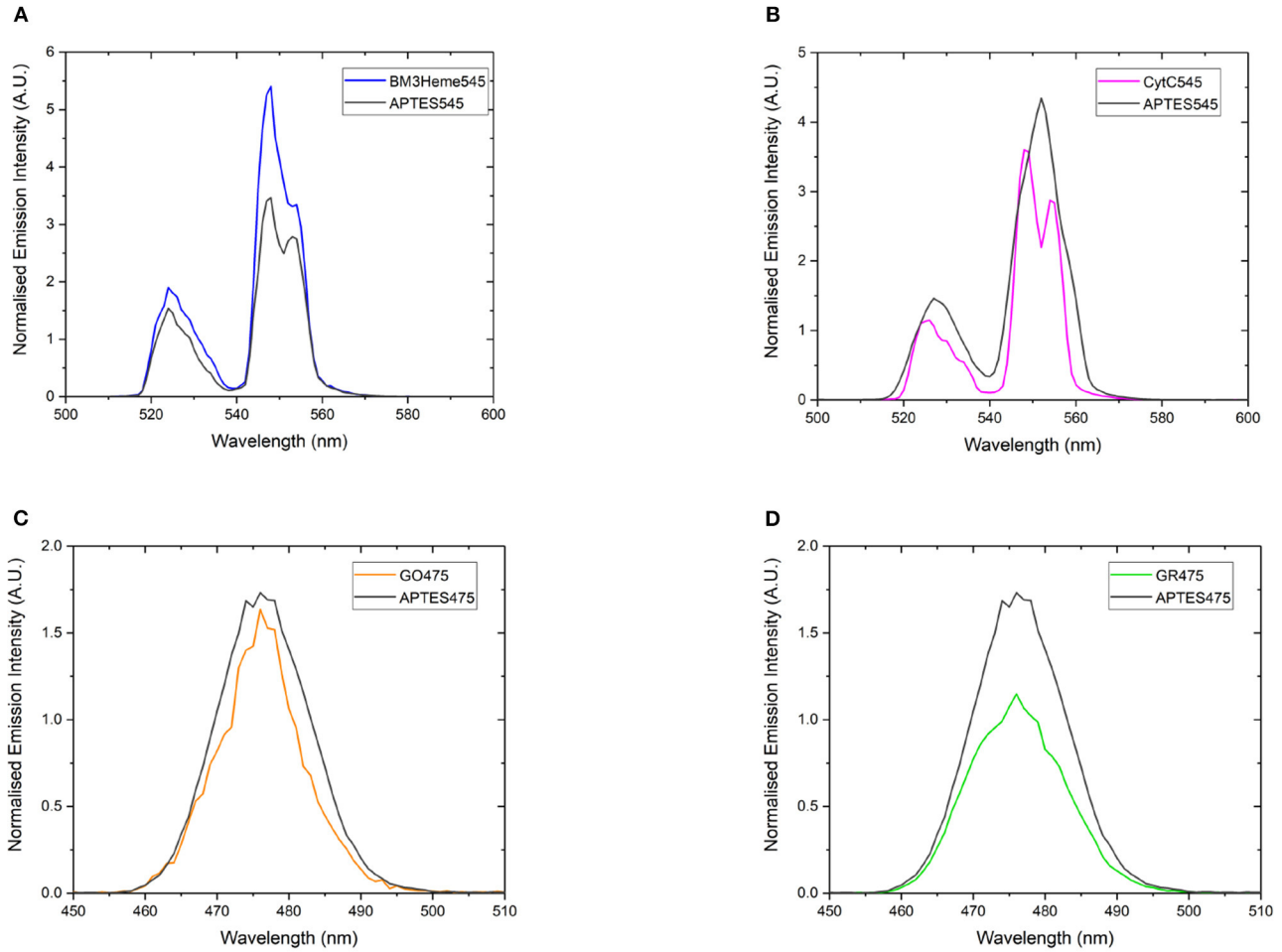

FIGURE 8 | The normalized emission spectra of: **(A)** APTES545 and BM3Heme545 showing only the 545 nm band, **(B)** APTES545 and cytC545 showing only the 545 nm band, **(C)** APTES475 and GO475 showing only the 475 nm band, **(D)** APTES475 and GR475 showing only the 475 nm band. All samples were 1 mg/mL in in PBS buffer (100 mM, pH 7.4). All spectra have been recorded following excitation at 980 nm and are reported without correcting for the detector response. **(A,B)** Have been normalized to the 660 nm band, and **(C,D)** have been normalized to the 800 nm band (not shown here, see **Supplementary Figure 25** for expanded spectra).

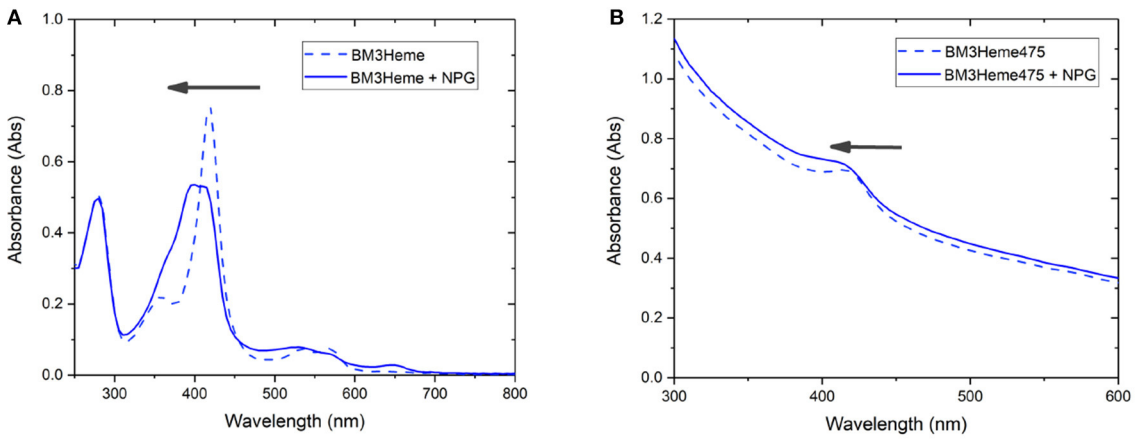

FIGURE 9 | The UV-vis spectrum of: **(A)** BM3Heme (10 μM in 100 mM PBS, pH 7.4) before and after the addition of NPG (10 μM) **(B)** BM3Heme545 (1 mg/mL in 100 mM PBS pH 7.4) before and after the addition of 20 μM NPG (20 μM).

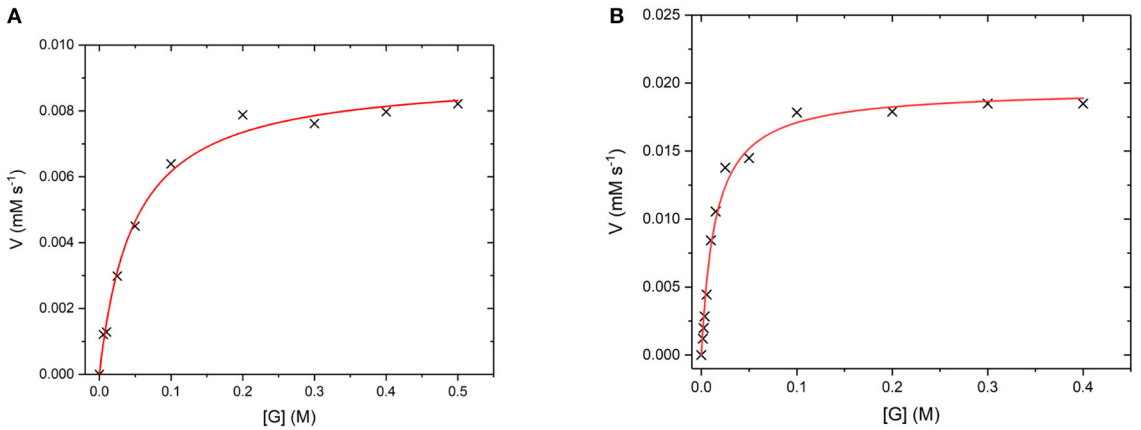

FIGURE 10 | (A) Michaelis-Menten curves for the reaction of **(A)** GO (8 nM) and **(B)** GO475 (1 mg/mL) with D-glucose (G) as the substrate and 2.3 mM benzoquinone as the electron acceptor. Reactions were performed in degassed 0.1 M sodium acetate buffer at pH 5.1 by monitoring the formation of reduced benzoquinone (hydroquinone) at 290 nm using $\varepsilon = 2.31\ mM^{-1}\ cm^{-1}$. Red lines show fits to the Michaelis-Menten equation and fitted parameters are given in the main text.

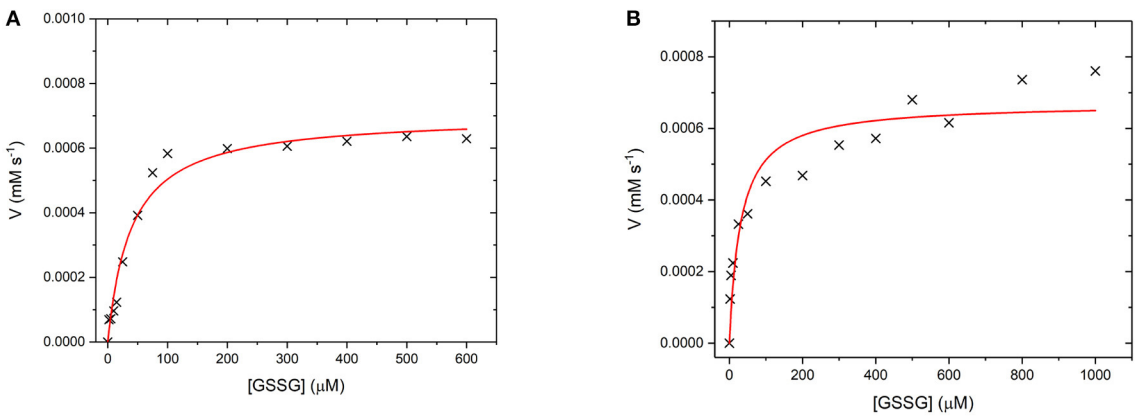

FIGURE 11 | (A) Michaelis-Menten curve for the enzyme turnover of **(A)** GR (10 nM) and **(B)** GR475 (1 mg/mL) with 93 μM NADPH and varying GSSG. Reactions were performed in degassed potassium phosphate buffer, pH 7 by monitoring the depleting of NADPH at 340 nm using $\varepsilon = 6.022\ mM^{-1}\ cm^{-1}$. Red lines show fits to the Michaelis-Menten equation and fitted parameters are given in the main text.

substrate GSSG when NADPH consumption is measured. A k_{cat} value of 70 ± 3 s^{-1} and K_M value of 39.4 ± 6.2 μM was obtained for GR, with the K_M similar to the literature value of 53.1 ± 3.4 μM (Can et al., 2010). 1 mg/ml GR475 gives a K_M value of 30.9 ± 9.6 μM, which is not significantly different to that measured for free GR and a V_{max} value of 0.67 ± 0.01 μM s^{-1}. These data suggest that binding of GR to the UCP is successful and the enzyme maintains its activity.

CONCLUSION

In summary, we have demonstrated that a variety of different conjugation methods can be used to covalently attach a wide variety of different molecules including organic dyes, enzymes and proteins to the surface of UCPs. Several thiol-thiol and thiol-maleimide coupling methods were screened for the attachment of enhanced GFP as a model protein with surface exposed cysteine residue to the surface of a range of UCPs (80 nm to 1.5 μM in diameter). One particularly successful method was identified and demonstrated to be a robust and versatile method for the covalent attachment of proteins containing an accessible surface cysteine group to the surface of upconverting phosphors. This method was used to attach the proteins and enzymes: BM3Heme and cytochrome C to YbEr doped UCPs (PTIR-545), and glucose oxidase and glutathione reductase to YbTm doped UCPs (PTIR-475). The significance of this conjugation method is that the proteins remain catalytically active when coupled to the UCP surface. This opens up the opportunity to develop UCP-biomolecule biosensors with increased sensitivity due to the close proximity (within AET distance) of the UCP donor and biomolecule acceptor, particularly with smaller UCNPs where Förster resonance energy transfer of the majority of emitting ions within the entirety of the nanoparticle can be exploited.

Studies toward this (to enhance the luminescence response) are in progress.

DATA AVAILABILITY STATEMENT

The original contributions presented in the study are included in the article/**Supplementary Materials** further inquiries can be directed to the corresponding author/s.

AUTHOR CONTRIBUTIONS

LB, AJ, SH, and LN conceived and designed the experiments. LB performed the experiments and resulting analysis, with input from HW. LB and HW wrote the manuscript with input from all authors. All authors contributed to the article and approved the submitted version.

ACKNOWLEDGMENTS

We thank the BBSRC for doctoral training partnership studentships (LB and HW) and a David Phillips fellowship (SH; BB/H021523/1) and the EPSRC for funding a Career Acceleration Fellowship (LN; EP/G004846/1). We also thank the Leverhulme Trust for a research Leadership award (LN; RL-2012-072) and the Royal Society for a small equipment grant. We are additionally grateful to the University of Manchester for funding a University Photon Science fellowship (AJ) and for general support.

SUPPLEMENTARY MATERIAL

The Supplementary Material for this article can be found online at: https://www.frontiersin.org/articles/10.3389/fchem.2020.613334/full#supplementary-material

REFERENCES

Aboshyan-Sorgho, L., Besnard, C., Pattison, P., Kittilstved, K. R., Aebischer, A., Bünzli, J. C. G., et al. (2011). Near-infrared→ visible light upconversion in a molecular trinuclear d-f-d complex. *Angew. Chem. Int. Ed.* 50, 4108–4112. doi: 10.1002/anie.201100095

Arppe, R., Mattsson, L., Korpi, K., Blom, S., Wang, Q., Riuttamäki, T., et al. (2015). Homogeneous assay for whole blood folate using photon upconversion. *Anal. Chem.* 87, 1782–1788. doi: 10.1021/ac503691m

Bertini, I., Cavallaro, G., and Rosato, A. (2006). Cytochrome c: occurrence and functions. *Chem. Rev.* 106, 90–115. doi: 10.1021/cr050241v

Blackburn, O. A., Tropiano, M., Sorensen, T. J., Thom, J., Beeby, A., Bushby, L. M., et al. (2012). Luminescence and upconversion from thulium(III) species in solution. *Phys. Chem. Chem. Phys.* 14, 13378–13384. doi: 10.1039/c2cp42228j

Bruen, D., Delaney, C., Florea, L., and Diamond, D. (2017). Glucose sensing for diabetes monitoring: recent developments. *Sensors* 17:1866. doi: 10.3390/s17081866

Burgess, L., Wilson, H., Jones, A. R., Hay, S., and Natrajan, L. (2020). Evaluating spectral overlap with the degree of quenching in UCP luminescence energy transfer systems. *Methods Appl. Fluoresc.* 8:045003. doi: 10.1088/2050-6120/aba87f

Can, B., Erkmen, G. K., Dalmizrak, O., Ogus, I. H., and Ozer, N. (2010). Purification and characterisation of rat kidney glutathione reductase. *Protein J.* 29, 250–256. doi: 10.1007/s10930-010-9246-4

Charbonnière, L. J. (2018). Bringing upconversion down to the molecular scale. *Dalt. Trans.* 47, 8566–8570. doi: 10.1039/c7dt04737a

Chatterjee, D. K., Rufaihah, A. J., and Zhang, Y. (2008). Upconversion fluorescence imaging of cells and small animals using lanthanide doped nanocrystals. *Biomaterials* 29, 937–943. doi: 10.1016/j.biomaterials.2007.10.051

Eliseeva, S. V., and Bünzli, J. C. G. (2010). Lanthanide luminescence for functional materials and bio-sciences. *Chem. Soc. Rev.* 39, 189–227. doi: 10.1039/b905604c

Gibson, Q. H., Swoboda, B. E. P., and Massey, V. (1964). Kinetics and mechanism of action of glucose oxidase. *J. Biol. Chem.* 239, 3927–3934.

Girvan, H. M., Seward, H. E., Toogood, H. S., Cheesman, M. R., Leys, D., and Munro, A. W. (2007). Structural and spectroscopic characterization of P450 BM3 mutants with unprecedented P450 heme iron ligand sets: new heme ligation states influence conformational equilibria in P450 BM3. *J. Biol. Chem.* 282, 564–572. doi: 10.1074/jbc.M607949200

Gnach, A., Lipinski, T., Bednarkiewicz, A., Rybka, J., and Capobianco, J. A. (2015). Upconverting nanoparticles: assessing the toxicity. *Chem. Soc. Rev.* 44, 1561–1584. doi: 10.1039/c4cs00177j

Golesorkhi, B., Fürstenberg, A., Nozary, H., and Piguet, C. (2019). Deciphering and quantifying linear light upconversion in molecular erbium complexes. *Chem. Sci.* 10, 6876–6885. doi: 10.1039/c9sc02068c

Golesorkhi, B., Nozary, H., Fürstenberg, A., and Piguet, C. (2020). Erbium complexes as pioneers for implementing linear light-upconversion in molecules. *Mater. Horizons* 7, 1279–1296. doi: 10.1039/c9mh01899a

Haase, M., and Schäfer, H. (2011). Upconverting nanoparticles. *Angew. Chem. Int. Ed.* 50, 5808–5829. doi: 10.1002/anie.201005159

Harper, A., and Anderson, M. R. (2010). Electrochemical glucose sensors—developments using electrostatic assembly and carbon nanotubes for biosensor construction. *Sensors* 10, 8248–8274. doi: 10.3390/s100908248

Harvey, P., Oakland, C., Driscoll, M. D., Hay, S., and Natrajan, L. S. (2014). Ratiometric detection of enzyme turnover and flavin reduction using rare-earth upconverting phosphors. *Dalt. Trans.* 43, 5265–5268. doi: 10.1039/c4dt00356j

Hatanaka, M., and Satoshi, Y., (2014), Mechanisms of f-f hypersensitive transition intensities of lanthanide trihalide molecules: a spin-orbit configuration interaction study *Theor. Chem.* Acc. 133, 1517. doi: 10.1007/s00214-014-1517-2

Heller, A., and Feldman, B. (2008). Electrochemical glucose sensors and their applications in diabetes management. *Chem. Rev.* 108, 2482–2505. doi: 10.1021/cr068069y

Hüttemann, M., Pecina, P., Rainbolt, M., Sanderson, T. H., Kagan, V. E., Samavati, L., et al. (2011). The multiple functions of cytochrome c and their regulation in life and death decisions of the mammalian cell: from respiration to apoptosis. *Mitochondrion* 11, 369–381. doi: 10.1016/j.mito.2011.01.010

Idris, N. M., Gnanasammandhan, M. K., Zhang, J., Ho, P. C., Mahendran, R., and Zhang, Y. (2012). *In vivo* photodynamic therapy using upconversion nanoparticles as remote-controlled nanotransducers. *Nat. Med.* 18, 1580–1585. doi: 10.1038/nm.2933

Lakowicz, J. R. (2006). *Principles of Fluorescence Spectroscopy*. Berlin: Springer.

Leskovac, V., Trivić, S., Wohlfahrt, G., Kandrač, J., and Peričin, D. (2005). Glucose oxidase from *Aspergillus niger*: the mechanism of action with molecular oxygen, quinones, and one-electron acceptors. *Int. J. Biochem. Cell Biol.* 37, 731–750. doi: 10.1016/j.biocel.2004.10.014

Liu, J., Meng, L., Fei, Z., Dyson, P. J., Jing, X., and Liu, X. (2017). MnO2 nanosheets as an artificial enzyme to mimic oxidase for rapid and sensitive detection of glutathione. *Biosens. Bioelectron.* 90, 69–74. doi: 10.1016/j.bios.2016.11.046

Liu, Q., Peng, J., Sun, L., and Li, F. (2011). High-efficiency upconversion luminescent sensing and bioimaging of Hg(II) by chromophoric ruthenium complex-assembled nanophosphors. *ACS Nano* 5, 8040–8048. doi: 10.1021/nn202620u

Lu, J., Chen, Y., Liu, D., Ren, W., Lu, Y., Shi, Y., et al. (2015). One-step protein conjugation to upconversion nanoparticles. *Anal. Chem.* 87, 10406–10413. doi: 10.1021/acs.analchem.5b02523

Mavis, R. D., and Stellwagen, E. (1968). Purification and subunit structure of glutathione reductase from bakers' yeast. *J. Biol. Chem.* 243, 809–814.

Mittl, P. R. E., and Schulz, G. E. (1994). Structure of glutathione reductase from *Escherichia coli* at 1.86 Å resolution: comparison with the enzyme from human erythrocytes. *Protein Sci.* 3, 799–809. doi: 10.1002/pro.5560030509

Muhr, V., Wilhelm, S., Hirsch, T., and Wolfbeis, O. S. (2014). Upconversion nanoparticles: from hydrophobic to hydrophilic surfaces. *Acc. Chem. Res*. 47, 3481–3493. doi: 10.1021/ar500253g

Munro, A. W., Girvan, H. M., and McLean, K. J. (2007). Variations on a (t)heme - novel mechanisms, redox partners and catalytic functions in the cytochrome P450 superfamily. *Nat. Prod. Rep*. 24, 585–609. doi: 10.1039/b604190f

Natrajan, L., Hay, S., Harvey, P., Burgess, L., Wilson, H., and Jones, A. R. (2020). Covalent attachment of active enzymes to upconversion phosphors allows ratiometric detection of substrates. *Chem. Eur. J. Chem*. 26, 14817–14822. doi: 10.1002/chem.202001974

Nimse, S. B., and Pal, D. (2015). Free radicals, natural antioxidants, and their reaction mechanisms. *RSC Adv*. 5, 27986–28006. doi: 10.1039/c4ra13315c

Nonat, A., Chan, C. F., Liu, T., Platas-Iglesias, C., Liu, Z., Wong, W. T., et al. (2016). Room temperature molecular up conversion in solution. *Nat. Commun*. 7:11978. doi: 10.1038/ncomms11978

Nonat, A. M., and Charbonnière, L. J. (2020). Upconversion of light with molecular and supramolecular lanthanide complexes. *Coord. Chem. Rev*. 409:213192. doi: 10.1016/j.ccr.2020.213192

Oakland, C., Andrews, M. B., Burgess, L., Jones, A., Hay, S., Harvey, P., et al. (2017). Expanding the scope of biomolecule monitoring with ratiometric signaling from rare-earth upconverting phosphors. *Eur. J. Inorg. Chem*. 44, 5176–5185. doi: 10.1002/ejic.201700717

Ogu, C. C., and Maxa, J. L. (2000). Drug interactions due to cytochrome P450. *Baylor Univ. Med. Cent. Proc*. 13, 421–423. doi: 10.1080/08998280.2000.11927719

Paoli, M., Marles-Wright, J., and Smith, A. (2002). Structure-function relationships in heme-proteins. *DNA Cell Biol*. 21, 271–280. doi: 10.1089/104454902753759690

Peng, J., Xu, W., Lean Teoh, C., Han, S., Kim, B., Samanta, A., et al. (2015). High-efficiency *in vitro* and *in viv*o detection of Zn 2+ by dye-assembled upconversion nanoparticles. *J. Am. Chem. Soc*. 137, 2336–2342. doi: 10.1021/ja5115248

Sapsford, K. E., Algar, W. R., Berti, L., Gemmill, K. B., Casey, B. J., Oh, E., et al. (2013). Functionalizing nanoparticles with biological molecules: developing chemistries that facilitate nanotechnology. *Chem. Rev*. 113, 1904–2074. doi: 10.1021/cr300143v

Sedlmeier, A., and Gorris, H. H. (2015). Surface modification and characterization of photon-upconverting nanoparticles for bioanalytical applications. *Chem. Soc. Rev*. 44, 1526–1560. doi: 10.1039/c4cs00186a

Suffren, Y., Zare, D., Eliseeva, S. V., Gueeé, L., Nozary, H., Petoud, S., et al. (2013). Near-infrared to visible light-upconversion in molecules: from dream to reality. *J. Phys. Chem. C* 117, 26957–26963. doi: 10.1021/jp4107519

Timur, S., Odaci, D., Dincer, A., Zihnioglu, F., and Telefoncu, A. (2008). Biosensing approach for glutathione detection using glutathione reductase and sulfhydryl oxidase bienzymatic system. *Talanta* 74, 1492–1497. doi: 10.1016/j.talanta.2007.09.026

Walsh, C. T., and Wencewicz, T. A. (2013). Flavoenzymes: versatile catalysts in biosynthetic pathways. *Nat. Prod. Rep*. 30, 175–200. doi: 10.1039/c2np20069d

Wang, F., and Liu, X. (2008). Upconversion multicolor fine-tuning: visible to near-infrared emission from lanthanide-doped NaYF4 nanoparticles. *J. Am. Chem. Soc*. 130, 5642–5643. doi: 10.1021/ja800868a

Wang, L., Yan, R., Huo, Z., Wang, L., Zeng, J., Bao, J., et al. (2005). Fluorescence resonant energy transfer biosensor based on upconversion-luminescent nanoparticles. *Angew. Chemie Int. Ed*. 44, 6054–6057. doi: 10.1002/anie.200501907

Wang, M., Hou, W., Mi, C. C., Wang, W. X., Xu, Z. R., Teng, H. H., et al. (2009). Immunoassay of goat antihuman immunoglobulin G antibody based on luminescence resonance energy transfer between near-infrared responsive NaYF4:Yb, Er upconversion fluorescent nanoparticles and gold nanoparticles. *Anal. Chem*. 81, 8783–8789. doi: 10.1021/ac901808q

Wang, Y., Shen, P., Li, C., Wang, Y., and Liu, Z. (2012). Upconversion fluorescence resonance energy transfer based biosensor for ultrasensitive detection of matrix metalloproteinase-2 in blood. *Anal. Chem*. 84, 1466–1473. doi: 10.1021/ac202627b

Woodward, A., Wilson, H., and Natrajan, L. S. (2019). "Multiphoton and upconverted excitation of lanthanide(iii) ions in coordination complexes," in *Organometallic Chemistry, Vol. 42*, eds N. J. Patmore and P. I. P. Elliott (Cambridge: The Royal Society of Chemistry), 172–189.

Zhang, X., Peng, Y., Zhao, J., Li, Q., Yu, X., Acevedo-Rocha, C. G., et al. (2020). Bacterial cytochrome P450-catalyzed regio- and stereoselective steroid hydroxylation enabled by directed evolution and rational design. *Bioresour. Bioprocess*. 7:2. doi: 10.1186/s40643-019-0290-4

Zhou, B., Shi, B., Jin, D., and Liu, X. (2015a). Controlling upconversion nanocrystals for emerging applications. *Nat. Nanotech*. 10, 924–936. doi: 10.1038/NNANO.2015.251

Zhou, J., Liu, Q., Feng, W., Sun, Y., and Li, F. (2015b). Upconversion luminescent materials: advances and applications. *Chem. Rev*. 115, 395–465. doi: 10.1021/cr400478f

Conflict of Interest: The authors declare that the research was conducted in the absence of any commercial or financial relationships that could be construed as a potential conflict of interest.

frontiers in Chemistry

ORIGINAL RESEARCH
published: 08 January 2021
doi: 10.3389/fchem.2020.619764

PAA Modified Upconversion Nanoparticles for Highly Selective and Sensitive Detection of Cu^{2+} Ions

Shaoshan Su, Zhurong Mo, Guizhen Tan, Hongli Wen, Xiang Chen* and Deshmukh A. Hakeem**

Key Laboratory of Clean Chemistry Technology of Guangdong Regular Higher Education Institutions, School of Chemical Engineering and Light Industry, Guangdong University of Technology, Guangzhou, China

Detection of the Cu^{2+} ions is crucial because of its environmental and biological implications. The fluorescent-based organic sensors are not suitable for Cu^{2+} detection due to their short penetration depth caused by the UV/visible excitation source. Therefore, we have demonstrated a highly sensitive and selective near-infrared (NIR) excitable poly(acrylic acid) (PAA) coated upconversion nanoparticles (UCNPs) based sensor for Cu^{2+} detection. We construct the PAA modified Na(Yb, Nd)F_4@Na(Yb, Gd)F_4:Tm@$NaGdF_4$ core-shell-shell structured UCNPs based sensor via a co-precipitation route. The upconversion emission intensity of the PAA-UCNPs decreases linearly with the increase in the Cu^{2+} concentration from 0.125 to 3.125 μM due to the copper carboxylate complex formation between Cu^{2+} and PAA-UCNPs. The calculated detection limit of the PAA-UCNPs based sensor is 0.1 μM. The PAA-UCNPs based sensor is very sensitive and selective toward detecting the Cu^{2+} ions, even when the Cu^{2+} co-exist with other metal ions. The EDTA addition has significantly reversed the upconversion emission quenching by forming the EDTA-Cu^{2+} complex based on their greater affinity toward the Cu^{2+}. Therefore, the PAA-UCNPs based sensor can be a promising candidate for Cu^{2+} detection because of their higher sensitivity and selectivity under 980 nm NIR excitation.

Keywords: energy transfer, copper ions, fluorescent probe, poly(acrylic acid) (PAA), upconversion nanoparticles (UCNPs)

OPEN ACCESS

Edited by:
Qianqian Su,
Shanghai University, China

Reviewed by:
Eva Hemmer,
University of Ottawa, Canada
Tianying Sun,
Sun Yat-sen University, China

****Correspondence:***
Hongli Wen
hongliwen@gdut.edu.cn
Xiang Chen
chenxiang@gdut.edu.cn
Deshmukh A. Hakeem
abdulhakeem.desh@gdut.edu.cn

Specialty section:
This article was submitted to Nanoscience, a section of the journal Frontiers in Chemistry

Received: *21 October 2020*
Accepted: *09 December 2020*
Published: *08 January 2021*

Citation:
Su S, Mo Z, Tan G, Wen H, Chen X and Hakeem DA (2021) PAA Modified Upconversion Nanoparticles for Highly Selective and Sensitive Detection of Cu^{2+} Ions. Front. Chem. 8:619764. doi: 10.3389/fchem.2020.619764

INTRODUCTION

To detect the trace elements, both essential (Cr, Co, Cu, Fe, Li, Mg, Mn, Ni, Se, and Zn) and non-essentials (P and S), developing highly selective and sensitive sensors is a crucial, useful and challenging task in the fields of medical, environment, and biology (Helal et al., 2011). These elements are essential for numerous biological processes in living organisms; however, their excessive accumulation in the human body may lead to detrimental effects. A trace of these elements plays a crucial role by acting as a cofactor of enzymes in biological activities, e.g., the Mn ions regulate the physiological processes, including electron transport, oxygen transportation, protein modification, and neurotransmitter synthesis (Chen P. et al., 2016). These elements can accumulate in the brain, which affects the nervous system and catalyzes cytotoxic reactions at high concentrations. These ions anomaly could result in neurological disorders, heart attack, breathing problems, pseudotumor cerebri, and cranial nerve palsy related to Fe ions deficiency (Chen P. et al., 2016).

Among these elements, the copper (Cu^{2+}), being the third most essential and abundant micronutrient, exists in very low concentration and participates in various organism's physiological processes (Becker et al., 2005; Sikdar et al., 2018). Mostly, Cu^{2+} resides in the brain, particularly in basal ganglia, hippocampus, cerebellum, and numerous synaptic membranes (Vishal Desai, 2008). Several enzymes require Cu^{2+} for their functioning, such as tyrosinase, peptidyl glycine amidating monooxygenase, copper/zinc superoxide dismutase, ceruloplasmin, hephaestin, dopamine-hydroxylase, and cytochrome c oxidase (Vishal Desai, 2008). The anomaly in Cu^{2+} concentration may lead to multiple disorders (Jiang and Meng, 2013). The deficiency of Cu^{2+} could cause anemia, coronary heart diseases, and bone abnormalities (Fu et al., 2019). Simultaneously, the excess Cu^{2+} can initiate oxidative stress, leading to neurodegenerative diseases such as Menkes syndrome, Indian childhood cirrhosis, and Wilson's, Alzheimer's, Parkinson's, and prion diseases (Vishal Desai, 2008; Chen P. et al., 2016; Sikdar et al., 2018). Excessive Cu^{2+} consumption could cause kidney/liver damage, amyotrophic lateral sclerosis, and vomiting (Sikdar et al., 2018). On the other hand, Cu^{2+} generated as industrial waste is responsible for the marine environment pollution, thereby contaminating marine organisms, ultimately affecting human health through poisoning if the polluted marine organisms are consumed (Fu et al., 2019). Therefore, it is necessary to develop a highly sensitive and selective fluorescent probe for Cu^{2+} detection and quantification in environmental and biological samples.

The presence of trace amount of Cu^{2+} can be quantitatively estimated via traditional analytical techniques such as atomic absorption spectrometry (AAS) (Tokay and Bagdat, 2015), atomic emission spectrometry (AES) (Atanassova and Russeva, 1998), inductively coupled plasma mass spectrometry (ICP-MS) (Becker et al., 2005), colorimetry (Liu et al., 2018), solid-phase extraction (SPE) (Liu et al., 2020), voltammetry (Liu et al., 2020), and fluorescence spectrometry (Zhang et al., 2014). Colorimetry is mostly applied in paper-based analytical devices (PADs) for low-cost, fast, and simple analysis (Cate et al., 2015; Ostad et al., 2017). However, the detection capability or sensitivity of the colorimetric technique is not good (Liu et al., 2018). In voltammetry, the generally used toxic mercury and mercury coated electrodes (Sonthalia et al., 2004) are interchanged with non-toxic platinum (Bu et al., 2015), and screen printed carbon (Chaiyo et al., 2016) electrodes, which produce high background current during the detection, thus become un-appropriate for accurate detection (Liu et al., 2020). The above techniques relied on expensive equipment, complex testing procedures, and poor sensitivity, limiting its bio-application (Xu et al., 2016).

Fluorescence spectroscopy uses fluorescent probes as a detection tool to develop highly sensitive, selective, low cost, and simple methods for detecting Cu^{2+}. Up to now, most of the reported fluorescent probes are organic such as rhodamine-based derivatives (Tang et al., 2011), BODIPY-based derivatives (Loudet and Burgess, 2007), coumarin-based derivatives (Sheng et al., 2008), and naphthalimide-based fluorogenic probe (Xu et al., 2005; Zhang et al., 2014; Fu et al., 2019). These organic fluorescent probes absorb high energy UV/blue light, which resulted in low detectability due to the background fluorescence interference and shallow penetration depth (Jiang and Meng, 2013; Ostad et al., 2017). The nominal concentration of the Cu^{2+} in blood and drinking water allowed by the U.S. Environmental Protection Agency (EPA) is around 100–150 μg/dL (15.7–23.6 μM) and 1.3 ppm (∼20 μM), respectively (Helal et al., 2011; Jiang and Meng, 2013; Sikdar et al., 2018). Similarly, the World Health Organization (WHO) has announced that the oral intake of Cu^{2+} could not exceed more than a few milligrams (2 or 3 mg/day) in adults (Fu et al., 2019). Recently, the fluorescence whitening agent was used in paper-based sensors to achieve 160-fold improved Cu^{2+} detection with 69 nM detection limit (Liu et al., 2018). At the same time, the separation of the metal ions and the complication entities through a reaction boundary on a paper-based sensor achieve a detection limit of 10 mM. The Cu^{2+} ions with a detection limit of 12.5 μM can be detected via a reaction between metal ions and color developing agents. Another sensor for the Cu^{2+} detection was developed based on fluorophore (dansyl moiety) and a multidentate ligand. The reaction between the probe with Cu^{2+} produces a stable Cu^{2+} complex that quenches the fluorophore's emission. This method detects the Cu^{2+} up to 2 ppb (Zhang et al., 2014).

Upconversion nanoparticles (UCNPs), which convert the near Infrared (NIR) light (generally 808 or 980 nm) into visible light, have been become a promising candidate for the bio detection application. Compared with the dyes and quantum dots, the UCNPs exhibit several benefits: sizeable anti-Stokes shift, low toxicity, high chemical/photostability, lower photodamage, and deeper light-penetration depth (Zhang S. et al., 2018), establishing themselves as a promising candidate for bio detections application. Lanthanide (Ln^{3+}) doped UCNPs exhibit several intra 4f−4f transitions producing strong tunable emissions of different colors with longer lifetimes by changing the size and morphology of the UCNPs. Also, the UCNPs can produce tunable multi-color emissions via controlling the dopants concentrations. Low energy NIR light excitation provides a high sensitivity detection system with negligible auto-fluorescence and light scattering. In this regards, different research groups have developed UCNPs based sensors for the detection of organic and inorganic entities such as toluene/phenol (Ma et al., 2014), organophosphorus (Wang et al., 2016), Zinc (Han et al., 2010), Mercury (Li et al., 2014; Wu et al., 2016), Cyanide (Liu et al., 2011), and other entity (Huang et al., 2017).

Most of the UCNPs are hydrophobic because they are generally prepared by the thermal decomposition of the precursors (metal trifluoroacetate) in organic solvents (oleic acid (OA)/oleylamine/1-octadecene). Besides, the bare UCNPs induces the quenching effect due to the surface defects and vibrational deactivation from solvents (Wang et al., 2009; Zhu et al., 2013). Therefore, hydrophilic UCNPs with minimum quenching effect is desirable for efficient bio-detection. The surface modification overcomes the above limitations through well-known core-shell strategy and coating reactive functional moieties layer on UCNPs, which are excellent methods to minimize the quenching effect thereby significantly improving the luminescence intensity of UCNPs via the reduction in

surface defects and non-radiative loss (Chen et al., 2012). Various groups have reported the core-shell UCNPs, such as $NaYF_4$:Yb,Er@$NaGdF_4$ and $NaYbF_4$:Er/Tm@$NaGdF_4$ (Su et al., 2012; Zhang et al., 2012; Jin et al., 2013). Recently, Chen et al. (Chen X. et al., 2016) investigated the hexagonal phase $NaYF_4$@$NaYbF_4$:Tm@$NaYF_4$ core-shell structure with Yb^{3+} ions enclosed in the inner shell layer. The emission increased up to five-photon upconversion of Tm^{3+} due to the confined energy migration in $NaYF_4$@$NaYbF_4$:Tm@$NaYF_4$ core-shell structure. Yb^{3+} sensitizer highly absorbs NIR light (∼980 nm) and Yb^{3+} concentration can reach up to ∼100% in hexagonal $NaYF_4$:Yb^{3+}/Tm^{3+}@$NaYF_4$ core/shell nanocrystals after overcoming concentration quenching of Yb^{3+} (Ma et al., 2017; Pliss et al., 2017). Homann et al. (2018) investigated the quantum yields of the $NaYF_4$:Yb/Er@$NaYF_4$ nanoparticles by changing the $NaYF_4$ shell thickness. The increase in the thickness of $NaYF_4$ shell from 15 to 45 nm, increases the quantum yield from 3.4 to 9%. A similar study was performed by Würth et al. (2018) on hexagonal $NaGdF_4$:0.2Yb/0.02Er UCNPs upon altering the $NaYF_4$ shell thickness. Recently, Zhou et al. (2020) developed a core-shell-shell triple-layered $NaYF_4$:Er@$NaYbF_4$@$NaYF_4$ structure. Compared to $NaYF_4$:Yb,Er@$NaYF_4$, the upconversion emission intensity of the α-$NaYF_4$:10%Er@$NaYbF_4$@$NaYF_4$, where the Er^{3+} and Yb^{3+} were doped separately in the core and intermediate layer, was significantly increased, ∼100 times.

In UCNPs based sensors, the UCNPs serve as the energy donors, while, the target chromophores act as energy acceptors (Huang et al., 2017). Until now, the UCNPs are employed as energy donors and the family of rhodamine B (RhB) as energy acceptor in the Förster resonance energy transfer (FRET) based Cu^{2+} detection. Jiang and Meng (2013) made a sensor by combining β-$NaYF_4$:Yb^{3+}/Er^{3+} (UCNPs) and 2-amino-3′,6′-bis(ethylamino)-2′,7′-dimethyl-3′,9a′-dihydrospiro[isoindoline-1,9′-xanthen]-3-one (a rhodamine derivative) based on energy transfer process between UCNPs and rhodamine derivative. The rhodamine derivative was excited by the UCNPs, and detected Cu^{2+} in the 2–14 μM range with good selectivity and high chemo stability. The core-shell technology also helps to improve the sensitivity of Cu^{2+} detection. Zhang Y. et al. (2018), reported Cu^{2+} detection using core-shell $NaYF_4$@$NaYF_4$:Er^{3+}/Yb^{3+}@$NaYF_4$ UCNPs and RhB hydrazide as donor and acceptor, respectively. $NaYF_4$@$NaYF_4$:Er^{3+}/Yb^{3+}@$NaYF_4$ has higher emission intensity than the bare $NaYF_4$:Er^{3+}/Yb^{3+} UCNPs, which has enhanced the selectivity and specificity of the Cu^{2+} detection. Li et al. (2012) used RhB hydrazide doped porous SiO_2 shell to protect UCNPs. The addition of Cu^{2+} ions in UCNPs dispersion showed the color change and improved emission of RhB hydrazide–Cu^{2+} complex under 980 nm excitation, also, the green emission of the UCNPs decreased. However, these sensors exhibit low emission when dispersed in water, using RhB-hydrazide dye, silica shell and most importantly, the sensors involved are not reusable.

In this study, we construct a new upconversion sensor for Cu^{2+} detection using water-dispersible poly(acrylic acid) (PAA) functionalized Na(Yb,Nd)F_4@Na(Yb,Gd)F_4:Tm@$NaGdF_4$ core-shell-shell structured UCNPs, where the UCNPs work as the energy donor and Cu^{2+} ions as the acceptor. The reversible process of Cu^{2+} detection comprising the fluorescence quenching and recovery upon adding Cu^{2+} ions and EDTA, respectively, is schematically illustrated in **Scheme 1**. Efficient Na(Yb,Nd)F_4@Na(Yb,Gd)F_4:Tm@$NaGdF_4$ UCNPs, composed of $NaYb_{0.5}Nd_{0.5}F_4$ core, $NaYb_{0.5}Gd_{0.49}Tm_{0.01}F_4$ first shell and $NaGdF_4$ second shell were prepared by using co-precipitation method. At first, the OA ligand, attached during the preparation, was removed, followed by functionalization with PAA to form PAA-UCNPs for realizing efficient Cu^{2+} detection (Process I and II). With Cu^{2+} (Process III), the carboxylate group of PAA-UCNPs can bind selectively to the Cu^{2+} ions owing to the electrostatic interaction between Cu^{2+} and carboxylate anion of PAA, forming copper carboxylate complex to quench the UCNPs fluorescence. Upon 980 nm NIR light excitation, in the presence of Cu^{2+}, the emission intensity of the UCNPs was quenched linearly as the Cu^{2+} concentration increased from 0.125 to 3.125 μM with the detection limit of 0.1 μM. The upconversion emission intensity of the UCNPs was recovered up to 90% after further addition of EDTA (Process IV). Besides, the current UCNPs based nano-platform showed high sensitivity and selectivity of Cu^{2+} ions over the range of other metal ions (Al^{3+}, Ba^{2+}, Ca^{2+}, Co^{2+}, K^+, Li^+, Mg^{2+}, Mn^{2+}, Na^+, Ni^{2+}, and Zn^{2+}).

EXPERIMENTAL SECTIONS

Material and Reagents

Following chemicals with appropriate purities were used as received without further purification. $Nd(CH_3CO_2)_3 \cdot xH_2O$, 99.9%; $Yb(CH_3CO_2)_3 \cdot 4H_2O$, 99.9%; $Gd(CH_3CO_2)_3 \cdot xH_2O$, 99.9%, $Tm(CH_3CO_2)_3 \cdot xH_2O$, 99.9%; NaOH, >98%; NH_4F, >98%; 1-octadecene, 90%; oleic acid, 90%; poly(acrylic acid) (PAA), MW ≈ 1800; HCl, >98%, were purchased from Sigma-Aldrich. $C_{10}H_{14}N_2O_8Na_2 \cdot 2H_2O$ (EDTA) (>98%) were purchased from Sangon Biotech, China. Ethanol (99.5%), cyclohexane (99.5%), diethylene glycol (DEG) (>99%) were purchased from Macklin, China. The solutions of metal cations were performed from their corresponding salts of analytic grade or molecular biology grade, such as LiCl, NaCl, KCl, $MgCl_2 \cdot 6H_2O$, $CaCl_2 \cdot 4H_2O$, $AlCl_3 \cdot 6H_2O$, $BaCl_2$, $ZnCl_2$, $MnCl_2 \cdot 4H_2O$, $CoCl_2 \cdot 6H_2O$, $NiCl_2 \cdot 6H_2O$, and $CuCl_2 \cdot 3H_2O$. The water used in this work is ultrapure water (18.2 MΩ cm) deionized by the Milli-Q system.

Sample Synthesis

Preparation of Core UCNPs

The core UCNPs were synthesized by using a modified co-precipitation method, as reported elsewhere (Wang et al., 2011; Wen et al., 2013). In a typical procedure to the synthesis of $NaYb_{0.5}Nd_{0.5}F_4$ core nanoparticles, 2-mL water solution of $Nd(CH_3CO_2)_3$ (0.2 M) and $Yb(CH_3CO_2)_3$ (0.2 M) was mixed with 4 mL of oleic acid and 6 mL of 1-octadecene solution in 50-mL flask. The mixture was heated at 120°C for 30 min, then heated at 170°C for 40 min to form the lanthanide-oleate complexes and then cooled down to room

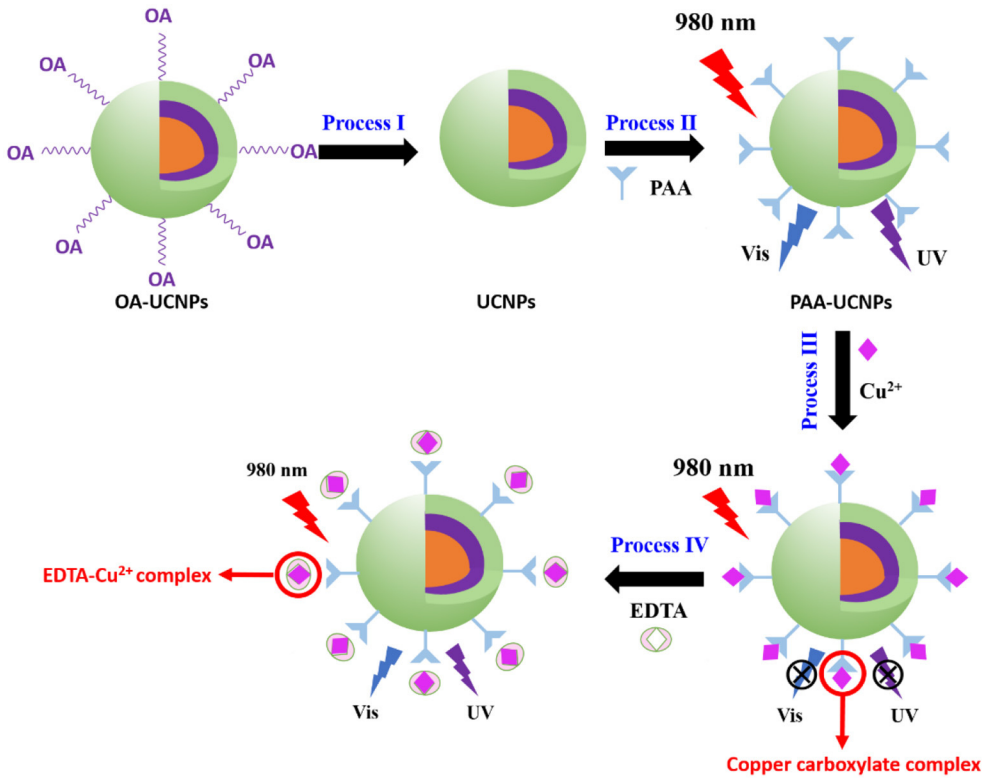

SCHEME 1 | Principle of Cu^{2+} detection based on energy transfer mechanism using core-shell-shell upconversion nanoparticles (UCNPs).

temperature. Thereafter, mixed methanol solution of NH_4F (1.5 mmol) and NaOH (1 mmol) was added to the above mixture and heated at 45°C for 30 min. After methanol evaporation at 110°C, the solution temperature was raised to 295°C and maintained for 1.5 h under argon. Post 295°C heating, the solution was cooled to room temperature and then the resulting nanoparticles were washed with ethanol and cyclohexane for several times and re-dispersed in 6.5 mL of cyclohexane.

Preparation of Core-Shell UCNPs

In a typical procedure to the shell growth of $NaYb_{0.5}Gd_{0.49}Tm_{0.01}F_4$ layer, the shell precursor were synthesized by adding 2 mL water solution of $Ln(CH_3CO_2)_3$ (0.2 M, Ln = Yb,Gd,Tm), 4 mL oleic acid and 6 mL 1-octadecene to a 50 mL flask, and heated at 120°C for 30 min, then heated at 170°C for 40 min to form the lanthanide-oleate complexes, and then cooled down to room temperature. The preformed core nanoparticles dispersed in 3 mL of cyclohexane with methanol solution of NH_4F (1.5 mmol) and NaOH (1 mmol) were added and heated to 45°C for 30 min. After methanol evaporation, the reactant was heated at 295°C for 1.5 h under argon atmosphere followed by cooling to room temperature. The resulting nanoparticles were washed several times with ethanol and cyclohexane, and re-dispersed in 4 mL of cyclohexane. The procedures were repeated for the preparation of core-shell-shell nanoparticles.

Preparation of Uncapped UCNPs (Kong et al., 2017)

The oleate capped UCNPs (denoted as OA-UCNPs) dispersed in 2 mL of cyclohexane were precipitated by ethanol and dispersed again in 2 mL of HCl solution (0.1 M). The mixture was then sonicated at 35°C for 1 h to remove the OA ligands. After the reaction, the uncapped UCNPs were collected via centrifugation for 0.5 h (at 15,000 rpm), followed by washing twice with deionized water and re-dispersed in deionized water (2 mL, 0.25 M).

Preparation of PAA Capped UCNPs (Kong et al., 2017)

Typically, 30 mg of poly acrylic acid (PAA) was added to the deionized water (9 mL) with NaOH (0.1 M in deionized water) to adjust the pH at 8 under robust stirring at room temperature, followed by the addition of uncapped UCNPs (1 mL) dropwise, and the mixture was stirred for another 2 h. This solution was then mixed with DEG (10 mL) and heated at 105°C for 1 h under stirring for water evaporation. The resultant solution was then heated at 160°C for 2 h in a 20 mL Teflon-lined autoclave. Next, the PAA capped UCNPs (denoted as PAA-UCNPs) were collected through centrifugation at 15,000 rpm for 0.5 h. PAA-UCNPs were washed several times with deionized water and ethanol, re-dispersed in deionized water (1 mL, 0.25 M), and stored at 4°C in fridge.

Characterization

To investigate the morphology/size of UCNPs, the samples were characterized by a HT7700 transmission electron microscope (TEM) with the working voltage of 100 KV (Hitachi, Japan). The crystal phase of UCNPs was identified by DY735 X-ray diffractometer (XRD) (Malvern Panalytical company, UK) with 2θ range from 10 to 80° at a scanning rate of 5° per minute, with Cu Kα irradiation (λ = 1.5406 Å). Fourier transform infrared (FT-IR) spectra of UCNPs using KBr pellet technique were recorded between 400 and 4,000 cm^{-1} at a resolution of 1 cm^{-1} using a Nicolet 6700 FT-IR Spectrometer (Thermo-Fisher Scientific, USA). Ultraviolet-visible (UV–Vis) spectra were measured on SHIMADZU UV2700 spectrophotometer. Upconversion luminescence spectra were recorded by FluoroMax-4 fluorescence spectrometer (HORIBA Jobin Yvon, USA) at the same condition, except using an external 980 nm CW laser at 3W or 808 nm laser at 2 W (Fiber coupled diode laser, BWT Beijing Ltd.). The photoluminescence intensity was obtained by integration the upconversion emission spectra in wavelengths range of 330–850 nm. Thermogravimetric analysis (TGA) was performed using Netzsch DTA-TG STA449F5 instrument under N_2 atmosphere at a heating rate of 10° per minute.

Sample Preparation for Metal Ion Sensing

The metal ion stock solutions with a concentration of 5×10^{-3} M were prepared in deionized water using the corresponding metal salts and diluted in deionized water at concentrations of 5×10^{-4} M and 5×10^{-6} M, respectively. The PAA-UCNPs dispersion with concentrations of 0.25 and 0.025 M were prepared in deionized water. The PAA dispersion with a concentration of 5×10^{-3} M was prepared in deionized water. The EDTA stock solution with a concentration of 5×10^{-3} M was prepared in deionized water.

In the UV-Vis experiment of **Figure 2A**, 2 mL PAA-UCNPs dispersion (0.025 M) was diluted to 4 mL in deionized water; 8 μL PAA-UCNPs dispersion (0.025 M) was mixed with 160 μL Cu^{2+} solution (5×10^{-4} M) and diluted to 4 mL in deionized water. In the UV-Vis experiment of **Figure 2B**, the PAA (5 mM), Cu^{2+} (5 μM) and PAA (40 μM) chelating with Cu^{2+} (40 μM) were prepared in deionized water by diluting corresponding bulk solutions. The mixture was filled in a quartz cell with an optical path of 1.0 cm to achieve an absorption spectrum. For the upconversion emission experiment with 980 nm laser excitation, 40 μL PAA-UCNPs dispersion (0.025 M) was added to a 4 mL bottle, then the Cu^{2+} solution (5×10^{-6} M) was added by means of a micro-pipette and diluted to 4 mL. The mixture was filled in a quartz cell with an optical path of 1.0 cm for testing. For the upconversion emission experiment with 808 nm laser excitation, 100 μL PAA-UCNPs dispersion (0.25 M) was added to a 3 mL bottle, then the Cu^{2+} solution (5×10^{-6} M) was added by means of a micro-pipette and diluted to 3 mL. The mixture was filled in a quartz cell with an optical path of 1.0 cm for testing. For upconversion emission spectra of the selective experiment with 980 nm laser excitation, 40 μL PAA-UCNPs dispersion (0.025 M) was added to a 4 mL bottle, then the metal ion solution (5×10^{-6} M or 5×10^{-4} M, respectively), was added by means of a micro-pipette and diluted to 4 mL. The mixture was filled in a quartz cell with an optical path of 1.0 cm for testing. For upconversion emission spectra of the reversibility experiment, EDTA was added dropwise to the solution of PAA-UCNPs whose fluorescence has been quenched by copper ions. After mixed well, filled it into a quartz cell with a 1.0 cm optical path for testing. After recovery experiment through addition of EDTA, the PAA-UCNPs were collected via centrifugation, followed by washing several times with deionized water and ethanol, re-dispersed in deionized water, and stored at 4°C in fridge for another Cu^{2+} sensing test.

Calculation of Limit of Detection

The limit of detection, LOD, of UCNPs chelating with Cu^{2+} was determined using the following equation (Peng et al., 2009; Guo et al., 2017):

$$\mathrm{LOD} = 3 \times \delta / S \tag{1}$$

$$\delta = \sqrt{\frac{\Sigma\,(x_i - x)^2}{N}} \tag{2}$$

where δ is the standard deviation of the blank solution, S is the slope of the calibration curve, x_i is the average value from the calculation, x is the measured data point, and N is the number of readings employed for obtaining average.

RESULTS AND DISCUSSION

Structural Characterizations and Morphology

The structure and morphology characteristics of the as-prepared $NaYb_{0.5}Nd_{0.5}F_4$@$NaYb_{0.5}Gd_{0.49}Tm_{0.01}F_4$@$NaGdF_4$ UCNPs were validated by XRD, FT-IR and TEM techniques. The XRD pattern of the as-prepared OA-UCNPs, as shown in **Figure 1A**, matches well with the standard JCPDS No. 16-0334, which corresponds to the pure hexagonal structure of $NaYF_4$. FT-IR technique validates the successful surface functionalization (i.e., the replacement of the OA with PAA) of the UCNPs. The FT-IR spectra of the OA-capped, un-capped, and PAA-capped UCNPs measured in the range of 500–4,000 cm^{-1} are presented in **Figure 1B**. The capping of the PAA molecules onto the surface of the UCNPs not only makes them water-dispersible but also provides multiple binding sites for detection of metal ions, specially Cu^{2+} ion. The FT-IR spectrum of the as-prepared OA-capped UCNPs exhibits five prominent peaks at 1,463, 1,558, 2,851, 2,921, and 3,443 cm^{-1}. The presence of the doublets at (1,463, 1,558 cm^{-1}) and (2,851 and 2,921 cm^{-1}) attributes to the [symmetric (ν_s) and asymmetric (ν_{as})] stretching vibrations of the carboxylic group (–COO) and methylene group (–CH_2), respectively, which indicates the presence of OA ligand on the surface of the UCNPs (Chen et al., 2008; Dai et al., 2016; Wang et al., 2019). Also, a broad singlet observed at 3,443 cm^{-1} originates from the stretching vibration of the hydroxyl (–OH) group (Sarkar et al., 2015). For bare UCNPs (without OA on the surface), these doublets are disappeared from the FT-IR spectrum (black line in **Figure 1B**) of the uncapped UCNPs,

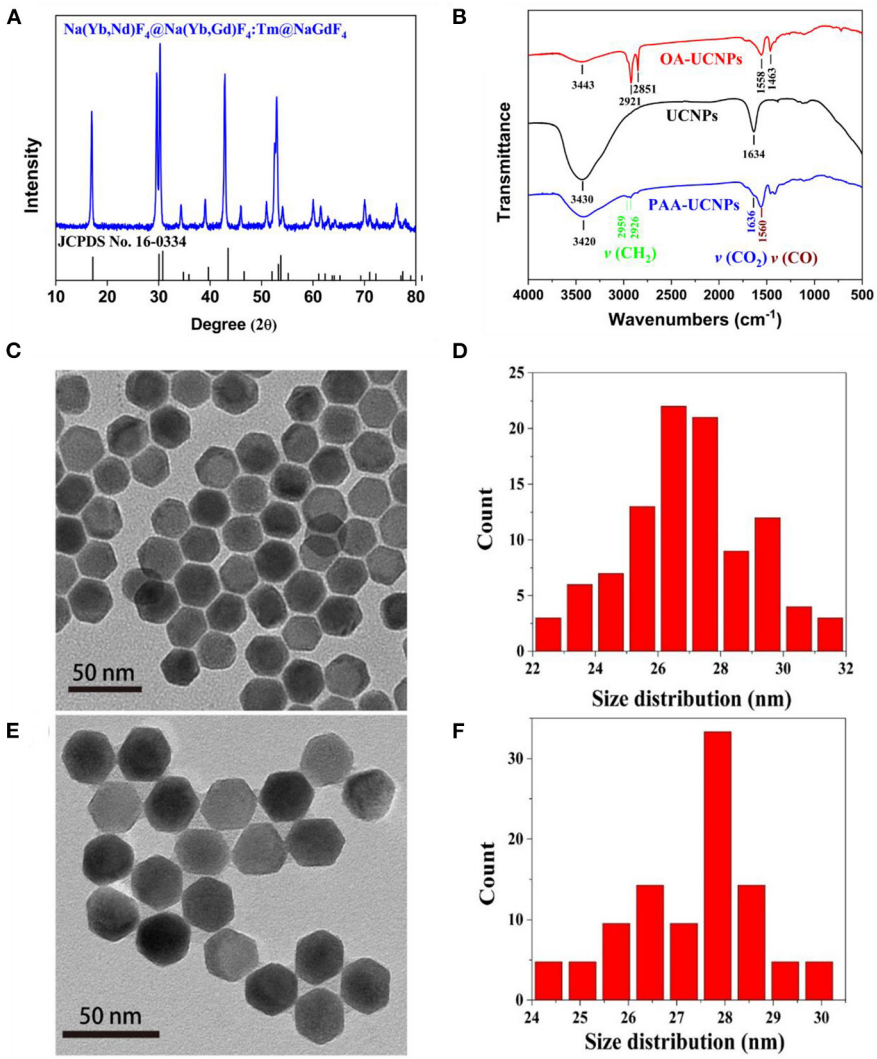

FIGURE 1 | (A) XRD pattern of OA-capped $NaYb_{0.5}Nd_{0.5}F_4$@$NaYb_{0.5}Gd_{0.49}Tm_{0.01}F_4$@$NaGdF_4$ UCNPs in comparison with standard JCPDS No. 16-0334, **(B)** FT-IR spectra of the OA-capped, un-capped, and PAA-capped $NaYb_{0.5}Nd_{0.5}F_4$@$NaYb_{0.5}Gd_{0.49}Tm_{0.01}F_4$@$NaGdF_4$ UCNPs, and **(C,E)** TEM images; and **(D,F)** size distribution of the as-prepared OA-capped and PAA-capped $NaYb_{0.5}Nd_{0.5}F_4$@ $NaYb_{0.5}Gd_{0.49}Tm_{0.01}F_4$@$NaGdF_4$ UCNPs, respectively.

indicating the successful removal of OA ligand from UCNPs surface after weak acidic treatment. Post OA removal, the UCNPs are further functionalized by the PAA and the FT-IR spectrum of the PAA-capped UCNPs is presented in **Figure 1B** (blue line), which clearly shows the characteristics doublet at 1,560 and 1,636 cm^{-1} assigned to asymmetric stretching vibrations of CO (ν_{CO}), and CO_2 (ν_{CO_2}) groups of PAA ligand, respectively (Liu et al., 2013; Feng et al., 2015; Kong et al., 2017). Another doublet at the higher wavenumber region, i.e., 2,926 and 2,959 cm^{-1} arises due to the symmetric and asymmetric stretching vibrations of CH_2 (ν_{CH_2}), respectively. The intensity of the doublet caused by the CH_2 (ν_{CH_2}) group decreases significantly in comparison to the OA capped UCNPs. Thus, we conclude that the capping of the PAA group onto the surface of the UCNPs is successful. This is consistent with the TGA results. The TGA plots of PAA-UCNPs and un-capped UCNPs are shown in **Supplementary Figure 1** (Supporting Information). The TGA curves clearly show that the decomposition temperature for PAA-UCNPs at ∼400 °C is higher than that of the pure PAA molecules at ∼200 °C (Sarkar et al., 2015), indicating the strong affinity of PAA molecules to the UCNPs. TEM images of both OA-UCNPs and PAA-UCNPs confirm the formation of hexagonal morphology (see **Figures 1C,E**). Irrespective of the capping agent used, the particle size (estimated 27 ± 2.2 nm) and the morphology of the UCNPs are hardly affected, as evident from **Figures 1C–F**. The replacement of the OA by PAA onto the surface of UCNPs significantly improves the water dispersibility without any particle aggregation in PAA-UCNPs (**Figure 1E**). **Supplementary Figure 2** (Supporting Information) shows the TEM images and size distribution of the as-prepared core of

$NaYb_{0.5}Nd_{0.5}F_4$ and core-shell structure with the composition of $NaYb_{0.5}Nd_{0.5}F_4@NaYb_{0.5}Gd_{0.49}Tm_{0.01}F_4$ nanoparticles, respectively. The core and core-shell particles exhibit the particle size of 18 ± 0.5 and 25 ± 2.1 nm, respectively. Thus, the thickness is ∼7 nm and ∼2 nm for the inner shell and outmost shell layer, respectively.

UV-Vis Absorption Spectra

The UV-Vis measurements were carried out to understand the sensing mechanism and the possibility of the interaction between the Cu^{2+} and PAA-UCNPs. The UV-Vis spectrum (**Figure 2A**) of the PAA-UCNPs does not show any absorption. In contrast, a noticeable absorption peak around 258 nm upon the addition of Cu^{2+} into PAA-UCNPs dispersion is due to the formation of the copper carboxylate complex based on PAA-UCNPs and Cu^{2+} interaction, in line with the reported literature (Schuetz and Caruso, 2003; Iatridi et al., 2008; Ma et al., 2008). This confirms the chelation between the Cu^{2+} and the carboxyl group of PAA on the surface of UCNPs. When mixing Cu^{2+} in PAA-UCNPs solution, the emission intensity of the UCNPs is expected to decline due to the formation of copper carboxylate complex. This could be explained either by FRET, inner-filter effect or an effect of the heavy metal ion. In order to rule out the FRET and inner-filter effect, the comparison between the UV-Vis spectra of the PAA, Cu^{2+}, PAA+Cu^{2+}, and upconversion emission spectrum of PAA-UCNPs has been presented in **Figure 2B**. Cu^{2+} ions exhibit a strong absorption band peaking at 234 nm. The interaction between the Cu^{2+} with PAA resulted in a strong, broadband at 260 nm along with a very weak broad band in the 600–800 nm region, which ascribe to $–COO^{-}$-Cu^{2+} charge transfer (Ma et al., 2008; Sarkar et al., 2015), and the complexation of PAA with Cu^{2+} (Iatridi et al., 2008), respectively, with the latter band overlapping with the 645, 695, 723, 801 nm emission of the UCNPs. However, the intensity of overlapped peaks is very weak, in addition, the prominent emission peaks of UCNPs (i.e., at 344, 360, and 450, and 474 nm), are not overlapped. Hence, the FRET and inner-filter effect can be ruled out as a preferred fluorescence quenching mechanism (Wang et al., 2017). In these circumstances, we believed that the effect of heavy metal ion is the main reason for the fluorescence

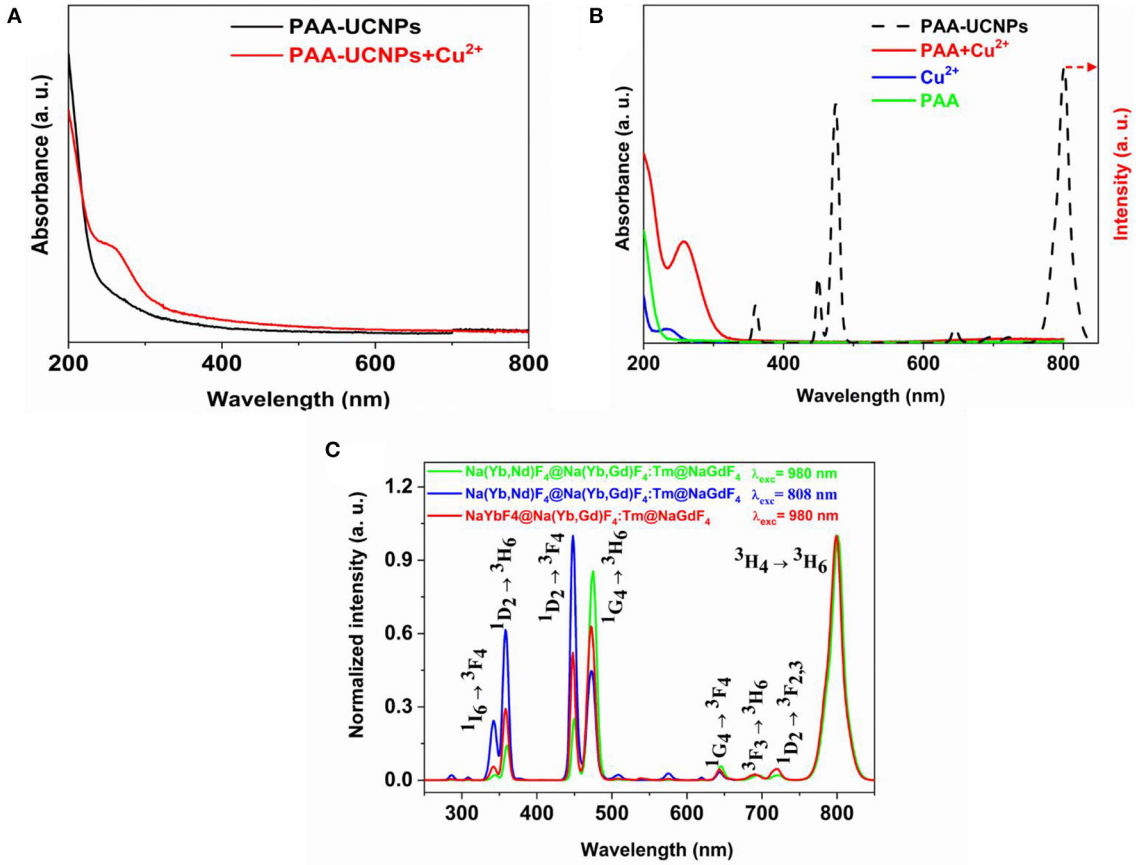

FIGURE 2 | (A) UV-vis spectra of PAA capped $NaYb_{0.5}Nd_{0.5}F_4@NaYb_{0.5}Gd_{0.49}Tm_{0.01}F_4@NaGdF_4$ UCNPs and PAA capped UCNPs chelating with Cu^{2+}; **(B)** UV-vis spectra of PAA, Cu^{2+}, and PAA chelating with Cu^{2+}, in comparison with upconversion emission spectra of PAA-capped $NaYb_{0.5}Nd_{0.5}F_4@NaYb_{0.5}Gd_{0.49}Tm_{0.01}F_4@NaGdF_4$ UCNPs under 980 nm excitation; and **(C)** Normalized upconversion emission spectra of PAA capped $NaYb_{0.5}Nd_{0.5}F_4@NaYb_{0.5}Gd_{0.49}Tm_{0.01}F_4@NaGdF_4$ UCNPs under 980 and 808 nm laser excitation, in comparison to PAA capped $NaYbF_4@NaYb_{0.5}Gd_{0.49}Tm_{0.01}F_4@NaGdF_4$ UCNPs under 980 nm laser excitation.

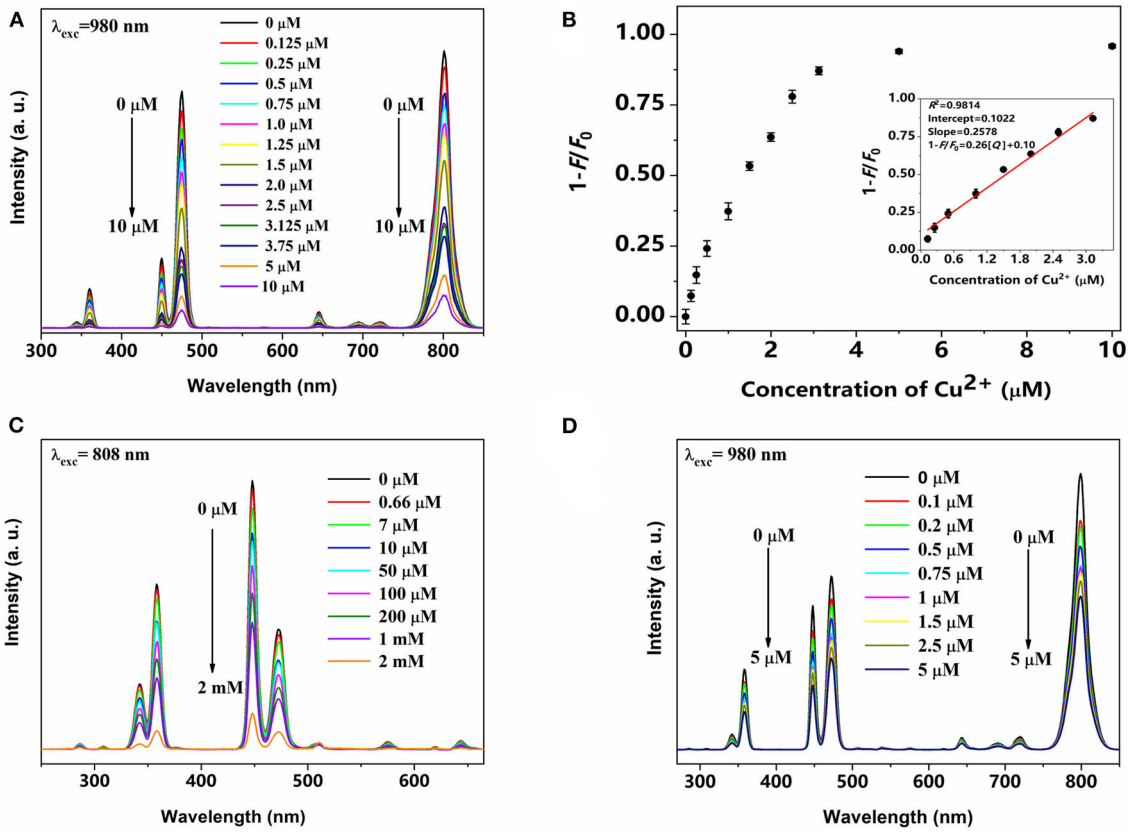

FIGURE 3 | Upconversion emission spectra of PAA-$NaYb_{0.5}Nd_{0.5}F_4$@$NaYb_{0.5}Gd_{0.49}Tm_{0.01}F_4$@$NaGdF_4$ UCNPs with various concentration of Cu^{2+} under **(A)** 980 nm and **(C)** 808 nm laser excitation, respectively; **(B)** The plot of emission quenching efficiency ($1\text{-}F/F_0$) vs. the Cu^{2+} concentration in (A); **(D)** Upconversion emission spectra of PAA-$NaYbF_4$@$NaYb_{0.5}Gd_{0.49}Tm_{0.01}F_4$@$NaGdF_4$ UCNPs with various concentration of Cu^{2+} under 980 nm laser excitation.

quenching of the UCNPs (Saleh et al., 2011; Liang et al., 2016).

Upconversion Emission Spectra

Figure 2C shows the upconversion emission spectra of the PAA-capped Na(Yb,Nd)F_4@Na(Yb,Gd)F_4:Tm@$NaGdF_4$ (excited at 980 and 808 nm, respectively), and $NaYbF_4$@ Na(Yb,Gd)F_4:Tm@$NaGdF_4$ UCNPs (excited at 980 nm) UCNPs. The emission spectra displayed several sharp characteristics peaks of Tm^{3+} at 344, 360, 450, 474, 645, 695, 723, and 801 nm, which can be attributed to the $^1I_6 \rightarrow {}^3F_4$, $^1D_2 \rightarrow {}^3H_6$, $^1D_2 \rightarrow {}^3F_4$, $^1G_4 \rightarrow {}^3H_6$, $^1G_4 \rightarrow {}^3F_4$, $^3F_3 \rightarrow {}^3H_6$ (Wang et al., 2010; Liu et al., 2017; Zhan et al., 2017), $^1D_2 \rightarrow {}^3F_{2,3}$ (Zhao et al., 2013; Zhan et al., 2017) and $^3H_4 \rightarrow {}^3H_6$ transitions of Tm^{3+}, respectively (Kenyon, 2002; Wang et al., 2010, 2011; Zhou et al., 2013). All the emission spectra shown in **Figure 2C** are identical, except for their emission intensity. The appearance of UV/blue upconversion emissions indicates that the core-shell structure has successfully suppressed the deleterious cross-relaxation processes (Wen et al., 2013). Among the Tm^{3+} transitions, $^3H_4 \rightarrow {}^3H_6$ (801 nm) transition shows significant higher emission intensity than the $^1G_4 \rightarrow {}^3H_6$ (474 nm). The higher emission intensity of the $^3H_4 \rightarrow {}^3H_6$ transition originates due to the depletion of $^3H_4$ level by surface quenching, which will supress the population of $^1G_4$ by subsequent excited state absorption or energy transfer (ET) (Wang et al., 2010). We have investigated the pump power-dependent upconversion luminescence with 980 nm excitation to figure out the actual number of photons involved in the upconversion process. **Supplementary Figure 3** displays the plot of log(Intensity) vs. log(Laser power) (Supporting Information). The slope of the plot for 344 nm emission was 4.15, showing that the upconversion is five photon process. Under the 808 nm excitation, in comparison to the 980 nm excited Na(Yb,Nd)F_4@Na(Yb,Gd)F_4:Tm@$NaGdF_4$, the emission intensity of the peaks below the 460 nm (UV and blue emissions) has increased with decrease in the 474 nm ($^1G_4 \rightarrow {}^3H_6$) emission peak, which agrees with the result as reported by Wen et al. (2013).

Detection of Cu^{2+}

The emission spectra of PAA-$NaYb_{0.5}Nd_{0.5}F_4$@$NaYb_{0.5}Gd_{0.49}Tm_{0.01}F_4$@$NaGdF_4$ UCNPs under 980 nm excitation with different Cu^{2+} were measured and presented in **Figure 3A**. With the increase in the Cu^{2+} ions concentration, the emission intensity of the PAA-UCNPs decreased monotonically. To comprehend the effect of the

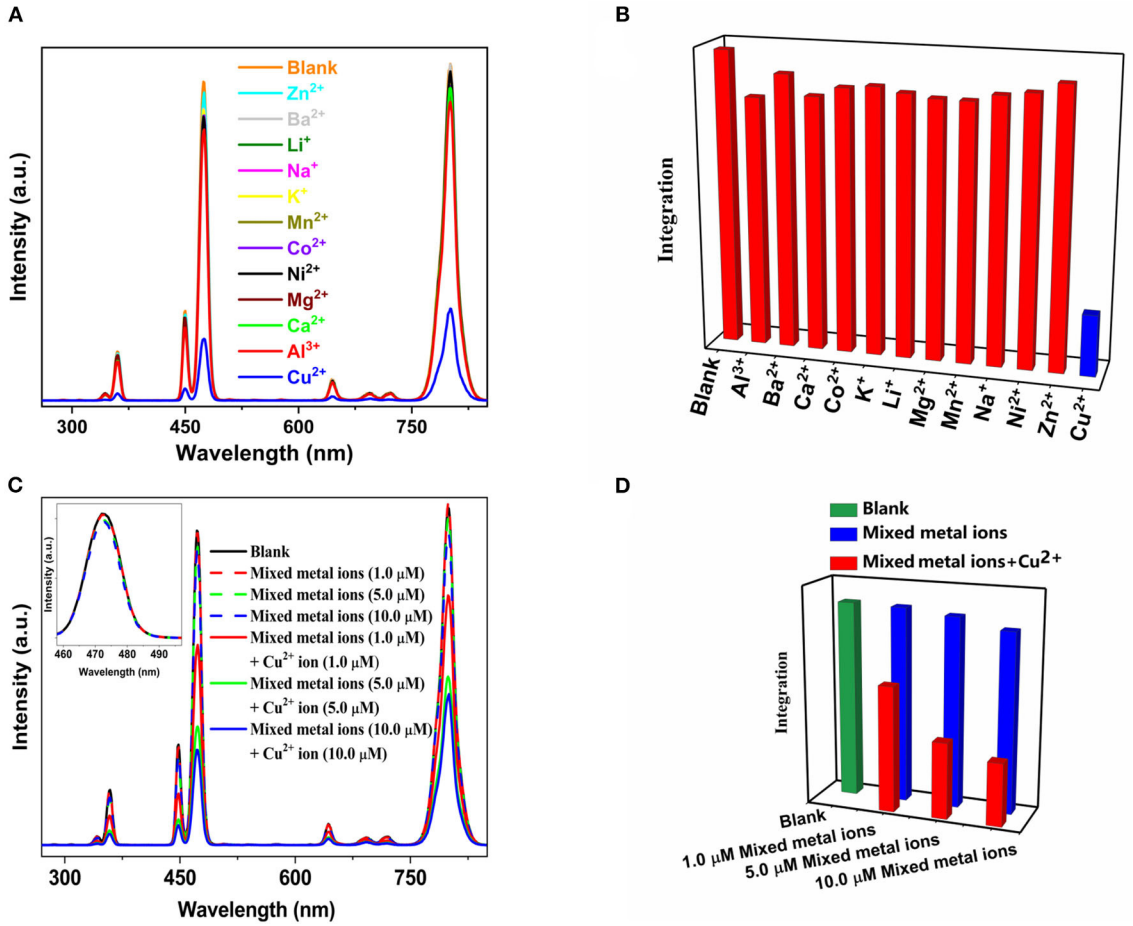

FIGURE 4 | (A) The effect of various equimolar metal ions i.e., Al^{3+}, Ba^{2+}, Ca^{2+}, Co^{2+}, K^{+}, Li^{+}, Mg^{2+}, Mn^{2+}, Na^{+}, Ni^{2+}, Zn^{2+}, and Cu^{2+} (2 μM) on the upconversion emission intensity of PAA-$NaYb_{0.5}Nd_{0.5}F_4$@$NaYb_{0.5}Gd_{0.49}Tm_{0.01}F_4$@$NaGdF_4$ UCNPs under 980 nm laser excitation; **(B)** graphical representation of **(A)**; **(C)** comparison of upconversion emission intensity of PAA-$NaYb_{0.5}Nd_{0.5}F_4$@$NaYb_{0.5}Gd_{0.49}Tm_{0.01}F_4$@$NaGdF_4$ UCNPs upon addition of mixed metals ions with and without Cu^{2+} ions under 980 nm laser excitation and **(D)** graphical representation of **(C)**.

Cu^{2+} on the luminescence quenching, a plot of emission quenching efficiency, $1\text{-}F/F_0$, where F_0 and F denote the emission intensity of UCNPs without and with Cu^{2+} ions vs. the concentration of Cu^{2+} ions, respectively, is displayed in **Figure 3B**. The Cu^{2+} concentration and $1\text{-}F/F_0$ of PAA-UCNPs presents a linear relationship with $R^2 = 0.9814$ within 0.125–3.125 μM range (**Figure 3B**), indicating the dynamic nature of the photoluminescence quenching (Sarkar et al., 2014). The fluorescence quenching efficiency reaches a plateau at higher concentration of Cu^{2+} after 4 μM, indicating the saturation of the chelating sites after Cu^{2+} binding (Wang et al., 2017). The LOD is calculated using the formula $3\delta/S$ where δ denotes standard deviation and S is the slope. The LOD of Cu^{2+} ions using current PAA-UCNPs based sensor is as low as 0.1 μM, which is superior to that of existing upconversion Cu^{2+} detection methods (Sarkar et al., 2014; Huang et al., 2017). Also, the LOD of the current PAA-UCNPs platform is comparable with the values reported in the literature (Wang et al., 2014). The meso-tetra(4-sulfonatophenyl)porphine dihydrochlorid (TSPP) on SiO_2-encapsulated $NaYF_4$:Yb,Er,Gd UCNPs based platform for the detection of Cu^{2+} ions with a LOD of 2.16 μM was reported by the Huang et al. (2017). These results indicate that the current PAA-UCNPs based platform exhibits superior sensitivity for Cu^{2+} detection. The PAA-$NaYb_{0.5}Nd_{0.5}F_4$@$NaYb_{0.5}Gd_{0.49}Tm_{0.01}F_4$@$NaGdF_4$ UCNPs based platform has also shown quite high sensitivity even at 808 nm laser excitation within 0.66–2,000 μM range, indicating that the Cu^{2+} ions can also be effectively detected by using 808 nm laser, as shown in **Figure 3C**. In addition, the Cu^{2+} can also be detected by using the PAA-UCNPs having 100% Yb^{3+} in the core ($NaYbF_4$@$NaYb_{0.5}Gd_{0.49}Tm_{0.01}F_4$@$NaGdF_4$ UCNPs) under 980 nm excitation within 0.1–5 μM range, as can be seen in **Figure 3D**. The obtained results i.e., different probes, LOD, and linear range monitored at specific excitation wavelength in this study are compared with that of the reported literature for the Cu^{2+} detection using different nanoplatforms (probes), see **Supplementary Table 1**. To the best of our knowledge, the exact mechanism underlying the cause of quenching is still very much

unclear because of highly complex nature of the upconversion luminescence. However, we can speculate about the quenching mechanism based on the observations reported in previous reports, i.e., dynamic and static quenching (Saleh et al., 2011). At low metal ion concentrations, the collisions between heavy metal ions and the UCNPs cause the dynamic quenching and form a complex between excited-state UCNPs and ground-state heavy metal ion during the excited-state lifetime of UCNPs. The excited state complex then loses its energy non-radiatively and falls to the ground state. On the other hand, the static quenching can also occurs at higher concentrations. In static quenching, the complex forms between the UCNPs and the heavy metal ions at ground state. Such a complex is very different from the excited-state complex and is temporally stable.

Selectivity

The selectivity of the PAA-$NaYb_{0.5}Nd_{0.5}F_4$@$NaYb_{0.5}Gd_{0.49}Tm_{0.01}F_4$@$NaGdF_4$ UCNPs under 980 nm excitation toward Cu^{2+} ions was further investigated by testing the PAA-UCNPs response toward a wide range of metal ions, particularly, equimolar Al^{3+}, Ba^{2+}, Ca^{2+}, Co^{2+}, K^{+}, Li^{+}, Mg^{2+}, Mn^{2+}, Na^{+}, Ni^{2+}, and Zn^{2+}. **Figure 4A** shows the response of the PAA-UCNPs toward these metal ions, shown by individual red column for each metal ion, in comparison to the PAA-UCNPs (blank) and Cu^{2+} ions response in **Figure 4B**. It is evident that the emission intensity of blank sample after the addition of various metal ions has not been significantly altered, except for the Cu^{2+}, indicating that the current PAA-UCNPs based sensing platform is most sensitive toward the Cu^{2+} ions. Furthermore, to confirm the competitive selectivity of the Cu^{2+} ion by PAA-UCNPs, the upconversion emission spectra of PAA-UCNPs in presence of mixed metal ions i.e., Al^{3+}, Ba^{2+}, Ca^{2+}, Co^{2+}, K^{+}, Li^{+}, Mg^{2+}, Mn^{2+}, Na^{+}, Ni^{2+}, and Zn^{2+} at different concentrations (1, 5, 10 μM) were measured and presented in **Figure 4C**. It can be seen that the mixture of the metal ions in absence of the Cu^{2+} do not show substantial difference in the emission intensity, however, as the Cu^{2+} ions were added to the solution containing other metal ions, the emission intensity was significantly decreased monotonically with increase in the Cu^{2+} concentration, see **Figure 4D**. The decrease in the upconversion emission intensity can be ascribed to the chelation of Cu^{2+} and PAA-UCNPs that leads to the efficient fluorescence quenching of PAA-UCNPs. These results demonstrate that the PAA-UCNPs based platform can serve as an upconversion detector for the detection of the Cu^{2+} with high sensitivity and selectivity. The preferred selectivity of the Cu^{2+} ions can be explained by considering the binding constants of the multi-valent ions to the PAA. Many researchers have measured the binding constants of the different multivalent metal ions and reported in the literature (Mandel and Leyte, 1964; Porasso et al., 1999; Giesecke et al., 2016). According to these reports, the selectivity of the metal ion not only depends on the pH of the solution but also on the ionic radii and their concentration. The reported trend for the different multivalence metal ions based on their binding constants is as follows, $Li^{+} < Na^{+} < K^{+} \approx Ba^{2+} < Ca^{2+} \approx Mg^{2+} < Al^{3+} < Co^{2+} < Ni^{2+} < Zn^{2+} < Mn^{2+} < Cu^{2+}$. Since the Cu^{2+} shows the highest binding constant values, it forms stronger coppercarboxylate complex and thus greatly quenches the luminescence.

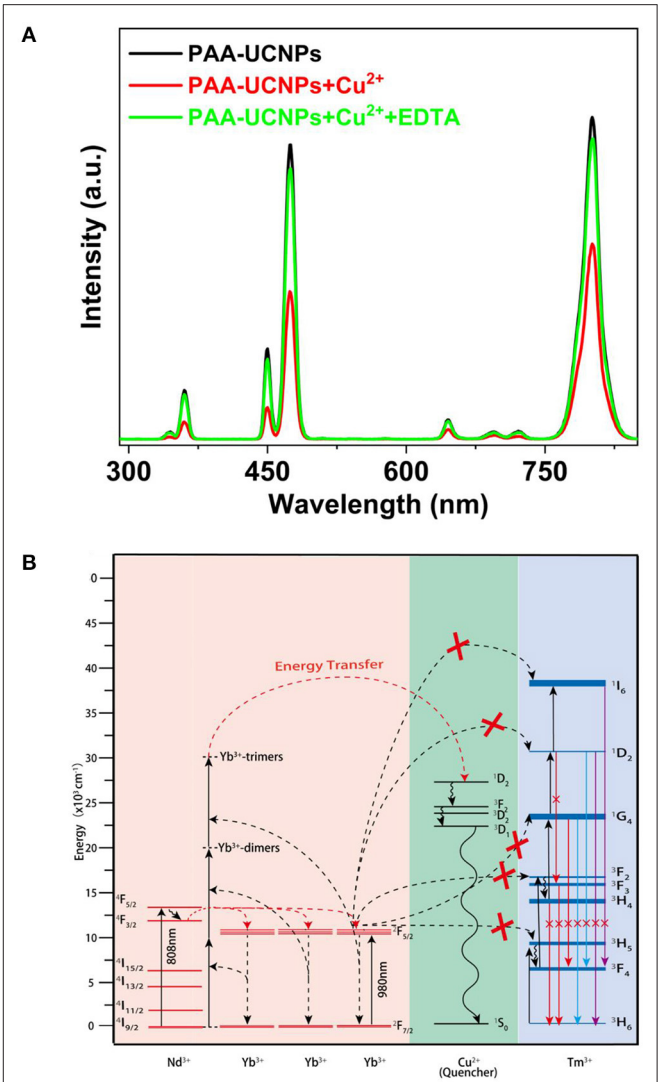

FIGURE 5 | (A) Photoluminescence spectra of PAA-$NaYb_{0.5}Nd_{0.5}F_4$@$NaYb_{0.5}Gd_{0.49}Tm_{0.01}F_4$@$NaGdF_4$ UCNPs without Cu^{2+}, with Cu^{2+} (2.0 μM), and further addition of EDTA (2.0 μM) under 980 nm laser excitation; **(B)** The proposed energy transfer mechanism between $NaYb_{0.5}Nd_{0.5}F_4$@$NaYb_{0.5}Gd_{0.49}Tm_{0.01}F_4$@$NaGdF_4$UCNPs and copper ions.

Reversibility

We also checked the reversibility of the Cu^{2+} ions detection using PAA-$NaYb_{0.5}Nd_{0.5}F_4$@$NaYb_{0.5}Gd_{0.49}Tm_{0.01}F_4$@$NaGdF_4$ UCNPs. After addition of the Cu^{2+} to the PAA-UCNPs, post copper carboxylate complex formation, EDTA was added gradually for this purpose. Upon 980 nm excitation, the emission spectra of the PAA-UCNPs before (black line) and after (red line) the Cu^{2+} addition with obvious emission intensity difference, are shown in **Figure 5A**. Upon the gradual addition of EDTA to the copper carboxylate complex, the emission intensity of the PAA-UCNPs is gradually recovered (green line) up to 90%, suggesting

the PAA-UCNPs based platform for the Cu^{2+} detection is reversible. It is also noted that the PAA-UCNPs based platform responds very quickly within a minute for both the Cu^{2+} ions to quench the emission and the EDTA solution to recover the quenched emission. We believe that the strong affinity of the Cu^{2+} toward EDTA is responsible for the dissociation of the copper carboxylate complex thereby recovering the emission intensity of the PAA-UCNPs.

Proposed Energy Transfer Mechanism

Figure 5B demonstrates the energy level diagram depicting plausible mechanism of upconversion emission quenching caused by the addition of Cu^{2+} to PAA-UCNPs. Generally, upon 980 nm excitation, the Yb^{3+} ions are excited from their $^2F_{7/2}$ ground state to the $^2F_{5/2}$ excited state, subsequently, the cooperative ET from Yb^{3+}-trimer to the different level of the Tm^{3+} produces the visible emission (Jean-Claude and Claude, 2002; Saleh et al., 2011; Wen et al., 2013; Qin et al., 2014). However, in presence of the Cu^{2+} ions, the cooperative ET from Yb^{3+}-trimer to Tm^{3+} is hampered by the quenching processes caused by Cu^{2+}, which leads to the upconversion emission quenching of the PAA-UCNPs (Saleh et al., 2011). We strongly believe that the significant quenching of the upconversion emission of PAA-UCNPs upon Cu^{2+} addition, is caused by the disturbance of the $Yb^{3+} \rightarrow Tm^{3+}$ ET by the heavy metal ion. Upon adding EDTA, the Cu^{2+} ions leave the copper carboxylate complex to bind with the EDTA because of their higher affinity toward EDTA than the PAA and thus the upconversion emission gets recovered.

CONCLUSIONS

We have developed a simple water-dispersible PAA-UCNPs based nanoplatform for the detection of Cu^{2+} ions. With increase in the Cu^{2+} concentration, the upconversion emission intensity of the PAA-UCNPs is quenched monotonically within the 0.125–3.125 μM range due to the ET between PAA-UCNPs and Cu^{2+}. The LOD for the Cu^{2+} is calculated to be 0.1 μM. It has been found that the PAA-UCNPs based nanoplatform can detect Cu^{2+} with higher sensitivity and selectivity even from the mixture of the various metal ions under 980 nm laser excitation. We believe that the PAA-UCNPs based nanoplatform under NIR excitation can be used in a wide range of practical bio-applications due to their superior characteristics such as no autofluorescence from bio-samples and interference from scattered excitation source, and high penetration depth. This makes PAA-UCNPs based nanoplatform a promising candidate for the biological applications in copper ion-related diseases i.e., in detection and diagnosis.

DATA AVAILABILITY STATEMENT

The original contributions presented in the study are included in the article/**Supplementary Material**, further inquiries can be directed to the corresponding author/s.

AUTHOR CONTRIBUTIONS

HW conceived the study. SS, HW, and XC designed the experiments. HW and DAH wrote the manuscript. SS, ZM, and GT carried out the material synthesis, characterization, and measurements. SS, HW, XC, and DAH analyzed the data. All authors contributed to the article and approved the submitted version.

FUNDING

This work was financially supported by the National Natural Science Foundation of China (Nos. 21701031 and 22075052).

SUPPLEMENTARY MATERIAL

The Supplementary Material for this article can be found online at: https://www.frontiersin.org/articles/10.3389/fchem.2020.619764/full#supplementary-material

REFERENCES

Atanassova, V. S. D., and Russeva, E. (1998). Co-precipitative pre-concentration with sodium diethyldithiocarbamate and ICP-AES determination of Se, Cu, Pb, Zn, Fe, Co, Ni, Mn, Cr and Cd in water. *Talanta* 47, 1237–1243. doi: 10.1016/S0039-9140(98)00211-2

Becker, M. V. Z. J. S., Pickhardt, C., Palomero-Gallagher, N., and Zilles, K. (2005). Imaging of copper, zinc, and other elements in thin section of human brain samples (hippocampus) by laser ablation inductively coupled plasma mass spectrometry. *Anal. Chem.* 77, 3208–3216. doi: 10.1021/ac040184q

Bu, L., Gu, T., Ma, Y., Chen, C., Tan, Y., Xie, Q., et al. (2015). Enhanced cathodic preconcentration of As(0) at Au and Pt electrodes for anodic stripping voltammetry analysis of As(III) and As(V). *J. Phys. Chem. C* 119, 11400–11409. doi: 10.1021/acs.jpcc.5b01435

Cate, D. M., Adkins, J. A., Mettakoonpitak, J., and Henry, C. S. (2015). Recent developments in paper-based microfluidic devices. *Anal. Chem.* 87, 19–41. doi: 10.1021/ac503968p

Chaiyo, S., Mehmeti, E., Zagar, K., Siangproh, W., Chailapakul, O., and Kalcher, K. (2016). Electrochemical sensors for the simultaneous determination of zinc, cadmium and lead using a nafion/ionic liquid/graphene composite modified screen-printed carbon electrode. *Anal. Chim. Acta* 918, 26–34. doi: 10.1016/j.aca.2016.03.026

Chen, G., Shen, J., Ohulchanskyy, T. Y., Patel, N. J., Kutikov, A., Li, Z., et al. (2012). (α-NaYbF4:Tm3+)/CaF2 core/shell nanoparticles with efficient near-infrared to near-infrared upconversion for high-contrast deep tissue bioimaging. *ACS Nano* 6, 8280–8287. doi: 10.1021/nn302972r

Chen, P., Miah, M. R., and Aschner, M. (2016). Metals and neurodegeneration. *F1000Res.* 5:F1000. doi: 10.12688/f1000research.7431.1

Chen, X., Jin, L., Kong, W., Sun, T., Zhang, W., Liu, X., et al. (2016). Confining energy migration in upconversion nanoparticles towards deep ultraviolet lasing. *Nat. Commun.* 7:10304. doi: 10.1038/ncomms10304

Chen, Z., Chen, H., Hu, H., Yu, M., Li, F., Zhang, Q., et al. (2008). Versatile synthesis strategy for carboxylic acid–functionalized upconverting nanophosphors as biological labels. *J. Amer. Chem. Soc.* 130, 3023–3029. doi: 10.1021/ja076151k

Dai, S., Wu, S., Duan, N., and Wang, Z. (2016). A near-infrared magnetic aptasensor for ochratoxin A based on near-infrared upconversion

nanoparticles and magnetic nanoparticles. *Talanta* 158, 246–253. doi: 10.1016/j.talanta.2016.05.063

Feng, A. L., You, M. L., Tian, L., Singamaneni, S., Liu, M., Duan, Z., et al. (2015). Distance-dependent plasmon-enhanced fluorescence of upconversion nanoparticles using polyelectrolyte multilayers as tunable spacers. *Sci. Rep*. 5:7779. doi: 10.1038/srep07779

Fu, Y., Pang, X. X., Wang, Z. Q., Chai, Q., and Ye, F. (2019). A highly sensitive and selective fluorescent probe for determination of Cu (II) and application in live cell imaging. *Spectrochim. Acta A* 208, 198–205. doi: 10.1016/j.saa.2018.10.005

Giesecke, M., Hallberg, F., Fang, Y., Stilbs, P., and Furó I. (2016). Binding of monovalent and multivalent metal cations to polyethylene oxide in methanol probed by electrophoretic and diffusion NMRJ. *Phys. Chem. B* 120, 10358–10366. doi: 10.1021/acs.jpcb.6b08923

Guo, M., Dong, P., Feng, Y., Xi, X., Shao, R., Tian, X., et al. (2017). A two-photon fluorescent probe for biological Cu (II) and PPi detection in aqueous solution and *in vivo*. *Biosens. Bioelectron*. 90, 276–282. doi: 10.1016/j.bios.2016.11.069

Han, Z. X., Zhang, X. B., Li, Z., Gong, Y. J., Wu, X. Y., Jin, Z., et al. (2010). Efficient fluorescence resonance energy transfer-based ratiometric fluorescent cellular imaging probe for Zn2+ using a rhodamine spirolactam as a trigger. *Anal. Chem*. 82, 3108–3113. doi: 10.1021/ac100376a

Helal, A., Or Rashid, M. H., Choi, C. H., and Kim, H. S. (2011). Chromogenic and fluorogenic sensing of Cu2+ based on coumarin. *Tetrahedron* 67, 2794–2802. doi: 10.1016/j.tet.2011.01.093

Homann, C., Krukewitt, L., Frenzel, F., Grauel, B., Würth, C., Resch-Genger, U., et al. (2018). NaYF4:Yb,Er/NaYF4 core/shell nanocrystals with high upconversion luminescence quantum yield. *Angew. Chem. Int. Ed*. 57, 8765–8769. doi: 10.1002/anie.201803083

Huang, X., Wang, L., Zhang, X., Yin, X., Bin, N., Zhong, F., et al. (2017). Dye-assembled nanocomposites for rapid upconversion luminescence sensing of Cu2+. *Sens. Actuat. B Chem*. 248, 1–8. doi: 10.1016/j.snb.2017.03.092

Iatridi, Z., Bokias, G., and Kallitsis, J. K. (2008). Physicochemical study of the complexation of poly(acrylic acid) with Cu2+ ions in water. *J. Appl. Polym. Sci*. 108, 769–776. doi: 10.1002/app.27757

Jean-Claude, G. B., and Claude, P. (2002). Lanthanide-containing molecular and supramolecular polymetallic functional assemblies. *Chem. Rev*. 102, 1897–1928. doi: 10.1021/cr010299j

Jiang, X., and Meng, G. (2013). A rhodamine-based sensing probe excited by upconversion NaYF4:Yb3+/Er3+ nanoparticles: the realization of simple Cu(II) detection with high sensitivity and unique selectivity. *J. Lumin*. 135, 227–231. doi: 10.1016/j.jlumin.2012.10.011

Jin, S., Zhou, L., Gu, Z., Tian, G., Yan, L., Ren, W., et al. (2013). A new near infrared photosensitizing nanoplatform containing blue-emitting up-conversion nanoparticles and hypocrellin A for photodynamic therapy of cancer cells. *Nanoscale* 5, 11910–11918. doi: 10.1039/c3nr03515h

Kenyon, A. J. (2002). Recent developments in rare-earth doped materials for optoelectronics. *Prog. Quantum Electron*. 26, 225–284. doi: 10.1016/S0079-6727(02)00014-9

Kong, W., Sun, T., Chen, B., Chen, X., Ai, F., Zhu, X., et al. (2017). A general strategy for ligand exchange on upconversion nanoparticles. *Inorg. Chem*. 56, 872–877. doi: 10.1021/acs.inorgchem.6b02479

Li, C., Liu, J., Alonso, S., Li, F., and Zhang, Y. (2012). Upconversion nanoparticles for sensitive and in-depth detection of Cu2+ ions. *Nanoscale* 4, 6065–6071. doi: 10.1039/c2nr31570j

Li, X., Wu, Y., Liu, Y., Zou, X., Yao, L., Li, F., et al. (2014). Cyclometallated ruthenium complex-modified upconversion nanophosphors for selective detection of Hg2+ ions in water. *Nanoscale* 6, 1020–1028. doi: 10.1039/C3NR05195A

Liang, T., Li, Z., Song, D., Shen, L., Zhuang, Q., and Liu, Z. (2016). Modulating the luminescence of upconversion nanoparticles with heavy metal ions: a new strategy for probe design. *Anal. Chem*. 88, 9989–9995. doi: 10.1021/acs.analchem.6b01963

Liu, J., Liu, Y., Liu, Q., Li, C., Sun, L., and Li, F. (2011). Iridium(III) complex-coated nanosystem for ratiometric upconversion luminescence bioimaging of cyanide anions. *J. Am. Chem. Soc*. 133, 15276–15279. doi: 10.1021/ja205907y

Liu, L., Xie, M. R., Fang, F., and Wu, Z. Y. (2018). Sensitive colorimetric detection of Cu2+ by simultaneous reaction and electrokinetic stacking on a paper-based analytical device. *Microchem. J*. 139, 357–362. doi: 10.1016/j.microc.2018.03.021

Liu, Q., Li, J., Yang, W., Zhang, X., Zhang, C., Labbe, C., et al. (2020). Simultaneous detection of trace Ag(I) and Cu(II) ions using homoepitaxially grown GaN micropillar electrode. *Anal. Chim. Acta* 1100, 22–30. doi: 10.1016/j.aca.2019.11.010

Liu, Y., Lu, Y., Yang, X., Zheng, X., Wen, S., Wang, F., et al. (2017). Amplified stimulated emission in upconversion nanoparticles for super-resolution nanoscopy. *Nature* 543, 229–233. doi: 10.1038/nature21366

Liu, Z., Ju, E., Liu, J., Du, Y., Li, Z., Yuan, Q., et al. (2013). Direct visualization of gastrointestinal tract with lanthanide-doped BaYbF5 upconversion nanoprobes. *Biomaterials* 34, 7444–7452. doi: 10.1016/j.biomaterials.2013.06.060

Loudet, A., and Burgess, K. (2007). BODIPY dyes and their derivatives: syntheses and spectroscopic properties. *Chem. Rev*. 107, 4891–4932. doi: 10.1021/cr078381n

Ma, C., Xu, X., Wang, F., Zhou, Z., Liu, D., Zhao, J., et al. (2017). Optimal sensitizer concentration in single upconversion nanocrystals. *Nano Lett*. 17, 2858–2864. doi: 10.1021/acs.nanolett.6b05331

Ma, H., Yang, G., Yu, L., and Zhang, P. (2008). Preparation and characterization of polyelectrolyte multilayer films containing *in-situ* synthesized nanoparticles of Cu(OH)2. *Surf. Coat. Tech*. 202, 5799–5803. doi: 10.1016/j.surfcoat.2008.05.052

Ma, Y., Huang, S., Deng, M., and Wang, L. (2014). White upconversion luminescence nanocrystals for the simultaneous and selective detection of 2, 4, 6-trinitrotoluene and 2, 4, 6-trinitrophenol. *ACS Appl. Mater. Int*. 6, 7790–7796. doi: 10.1021/am501053n

Mandel, M., and Leyte, J. C. (1964). Interaction of polymethacryhc acid and bivalent countenons IJ. *Polym. Sci*. 2, 2883–2888. doi: 10.1002/pol.1964.100020637

Ostad, M. A., Hajinia, A., and Heidari, T. (2017). A novel direct and cost effective method for fabricating paper-based microfluidic device by commercial eye pencil and its application for determining simultaneous calcium and magnesium. *Microchem. J*. 133, 545–550. doi: 10.1016/j.microc.2017.04.031

Peng, L., Zhao, Q., Wang, D., Zhai, J., Wang, P., Pang, S., et al. (2009). Ultraviolet-assisted gas sensing: a potential formaldehyde detection approach at room temperature based on zinc oxide nanorods. *Sens. Actuat. B Chem*. 136, 80–85. doi: 10.1016/j.snb.2008.10.057

Pliss, A., Ohulchanskyy, T. Y., Chen, G., Damasco, J., Bass, C. E., and Prasad, P. N. (2017). Subcellular optogenetics enacted by targeted nanotransformers of near-infrared light. *ACS Photonics* 4, 806–814. doi: 10.1021/acsphotonics.6b00475

Porasso, R. D., Benegas, J. C., and van den Hoop, M. A. G. T. (1999). Chemical and electrostatic association of various metal ions by poly(acrylic acid) and poly(methacrylic acid) as studied by potentiometry. *J. Phys. Chem. B* 103, 2361–2365. doi: 10.1021/jp9839706

Qin, W. P., Liu, Z. Y., Sin, C. N., Wu, C. F., Qin, G. S., Chen, Z., et al. (2014). Multi-ion cooperative processes in Yb3+ clusters. *Light Sci. Appl*. 3:e193. doi: 10.1038/lsa.2014.74

Saleh, S. M., Ali, R., and Wolfbeis, O. S. (2011). Quenching of the luminescence of upconverting luminescent nanoparticles by heavy metal ions. *Chem. Eur. J*. 17, 14611–14617. doi: 10.1002/chem.201101860

Sarkar, S., Chatti, M., Adusumalli, V. N., and Mahalingam, V. (2015). Highly selective and sensitive detection of Cu2+ ions using Ce(III)/Tb(III)-Doped SrF2 nanocrystals as fluorescent probe. *ACS Appl. Mater. Int*. 7, 25702–25708. doi: 10.1021/acsami.5b06730

Sarkar, S., Chatti, M., and Mahalingam, V. (2014). Highly luminescent colloidal Eu3+-doped KZnF3 nanoparticles for the selective and sensitive detection of Cu(II) ions. *Chem. Eur. J*. 20, 3311–3316. doi: 10.1002/chem.201304697

Schuetz, P., and Caruso, F. (2003). Copper-assisted weak polyelectrolyte multilayer formation on microspheres and subsequent film crosslinking. *Adv. Funct. Mater*. 13, 929–937. doi: 10.1002/adfm.200304483

Sheng, R., Wang, P., Gao, Y., Wu, Y., Liu, W., Ma, J., et al. (2008). Colorimetric test kit for Cu2+ detection. *Org. Lett*. 10, 5015–5018. doi: 10.1021/ol802117p

Sikdar, A., Roy, S., Mahto, R. B., Mukhopadhyay, S. S., Haldar, K., and Panja, S. S. (2018). Ratiometric fluorescence sensing of Cu(II): elucidation of FRET mechanism and bio-imaging application. *ChemistrySelect* 3, 13103–13109. doi: 10.1002/slct.201802818

Sonthalia, P., McGaw, E., Show, Y., and Swain, G. M. (2004). Metal ion analysis in contaminated water samples using anodic stripping voltammetry and a

nanocrystalline diamond thin-film electrode. *Anal. Chim. Acta* 522, 35–44. doi: 10.1016/j.aca.2004.06.071

Su, Q., Han, S., Xie, X., Zhu, H., Chen, H., Chen, C. K., et al. (2012). The effect of surface coating on energy migration-mediated upconversion. *J. Am. Chem. Soc.* 134, 20849–20857. doi: 10.1021/ja3111048

Tang, R., Lei, K., Chen, K., Zhao, H., and Chen, J. (2011). A rhodamine-based off–on fluorescent chemosensor for selectively sensing Cu(II) in aqueous solution. *J. Fluorescence* 21, 141–148. doi: 10.1007/s10895-010-0698-x

Tokay, F., and Bagdat, S. (2015). Determination of iron and copper in edible oils by flame atomic absorption spectrometry after liquid–liquid extraction. *J. Am. Oil Chem. Soc.* 92, 317–322. doi: 10.1007/s11746-015-2603-x

Vishal Desai, S. G. K. (2008). Role of copper in human neurological disorders. *Amer. J. Clin. Nut.* 88, 855S−858S. doi: 10.1093/ajcn/88.3.855S

Wang, F., Deng, R., Wang, J., Wang, Q., Han, Y., Zhu, H., et al. (2011). Tuning upconversion through energy migration in core–shell nanoparticles. *Nat. Mater.* 10, 968–973. doi: 10.1038/nmat3149

Wang, F., Han, Y., Wang, S., Ye, Z., Wei, L., and Xiao, L. (2019). Single-particle LRET aptasensor for the sensitive detection of aflatoxin B1 with upconversion nanoparticles. *Anal. Chem.* 91, 11856–11863. doi: 10.1021/acs.analchem.9b02599

Wang, F., Wang, J., and Liu, X. (2010). Direct evidence of a surface quenching effect on size-dependent luminescence of upconversion nanoparticles. *Angew. Chem. Int. Ed.* 49, 7456–7460. doi: 10.1002/anie.201003959

Wang, F., Zhang, C., Xue, Q., Li, H., and Xian, Y. (2017). Label-free upconversion nanoparticles-based fluorescent probes for sequential sensing of Cu2+, pyrophosphate and alkaline phosphatase activity. *Biosens. Bioelectron.* 95, 21–26. doi: 10.1016/j.bios.2017.04.010

Wang, M., Leung, K. H., Lin, S., Chan, D. S. H., Kwong, D. W. J., Leung, C. H., et al. (2014). A colorimetric chemosensor for Cu2+ ion detection based on an iridium(III) complex. *Sci. Rep.* 4:6794. doi: 10.1038/srep06794

Wang, S., Wang, X., Chen, X., Cao, X., Cao, J., Xiong, X., et al. (2016). A novel upconversion luminescence turn-on nanosensor for ratiometric detection of organophosphorus pesticides. *RSC Adv.* 6, 46317–46324. doi: 10.1039/C6RA05978C

Wang, Y., Tu, L., Zhao, J., Sun, Y., Kong, X., and Zhang, H. (2009). Upconversion luminescence of β-NaYF4:Yb3+,Er3+@β-NaYF4 core/nanoparticles: excitation power density and surface dependence. *J. Phys. Chem. C* 113, 7164–7169. doi: 10.1021/jp9003399

Wen, H., Zhu, H., Chen, X., Hung, T. F., Wang, B., Zhu, G., et al. (2013). Upconverting near-infrared light through energy management in core-shell-shell nanoparticles. *Angew. Chem. Int. Ed.* 52, 13419–13423. doi: 10.1002/anie.201306811

Wu, Y. X., Zhang, X. B., Zhang, D. L., Zhang, C. C., Li, J. B., Wu, Y., et al. (2016). Quench-shield ratiometric upconversion luminescence nanoplatform for biosensing. *Anal. Chem.* 88, 1639–1646. doi: 10.1021/acs.analchem.5b03573

Würth, C., Fischer, S., Grauel, B., Alivisatos, A. P., and Resch-Genger, U. (2018). Quantum yields, surface quenching, and passivation efficiency for ultrasmall core/shell upconverting nanoparticles. *J. Am. Chem. Soc.* 140, 4922–4928. doi: 10.1021/jacs.8b01458

Xu, Y., Li, H., Meng, X., Liu, J., Sun, L., Fan, X., et al. (2016). Rhodamine-modified upconversion nanoprobe for distinguishing Cu2+ from Hg2+ and live cell imaging. *New J. Chem.* 40, 3543–3551. doi: 10.1039/C5NJ03010B

Xu, Z., Qian, X., and Cui, J. (2005). Colorimetric and ratiometric fluorescent chemosensor with a large red-shift in emission: Cu(II)-only sensing by deprotonation of secondary amines as receptor conjugated to naphthalimide fluorophore. *Org. Lett.* 7, 3029–3032. doi: 10.1021/ol051131d

Zhan, Q., Liu, H., Wang, B., Wu, Q., Pu, R., Zhou, C., et al. (2017). Achieving high-efficiency emission depletion nanoscopy by employing cross relaxation in upconversion nanoparticles. *Nat. Commun.* 8:1058. doi: 10.1038/s41467-017-01141-y

Zhang, F., Che, R., Li, X., Yao, C., Yang, J., Shen, D., et al. (2012). Direct imaging the upconversion nanocrystal core/shell structure at the subnanometer level: shell thickness dependence in upconverting optical properties. *Nano Lett.* 12, 2852–2858. doi: 10.1021/nl300421n

Zhang, S., Yao, T., Wang, S., Feng, R., Chen, L., Zhu, V., et al. (2018). Development of an upconversion luminescence nanoparticles–based immunochromatographic assay for the rapid detection of dexamethasone in animal tissue. *Food Anal. Methods* 12, 752–760. doi: 10.1007/s12161-018-01411-5

Zhang, S., Yu, T., Sun, M., Yu, H., Zhang, Z., Wang, S., et al. (2014). Highly sensitive and selective fluorescence detection of copper (II) ion based on multi-ligand metal chelation. *Talanta* 126, 185–190. doi: 10.1016/j.talanta.2014.03.076

Zhang, Y., Xu, S., Li, X., Sun, J., Zhang, J., Zheng, H., et al. (2017). Concentration quenching of blue upconversion luminescence in Tm3+/Yb3+ co-doped Gd2(WO4)3 phosphors under 980 and 808 nm excitation. *J. Alloys Compd.* 709, 147–157. doi: 10.1016/j.jallcom.2017.03.125

Zhang, Y., Xu, S., Li, X., Zhang, J., Sun, J., Tong, L., et al. (2018). Improved LRET-based detection characters of Cu2+ using sandwich structured NaYF4@NaYF4:Er3+/Yb3+@NaYF4 nanoparticles as energy donor. *Sens. Actuat. B Chem.* 257, 829–838. doi: 10.1016/j.snb.2017.11.045

Zhao, J., Jin, D., Schartner, E. P., Lu, Y., Liu, Y., Zvyagin, A. V., et al. (2013). Single-nanocrystal sensitivity achieved by enhanced upconversion luminescence. *Nat. Nanotechnol.* 8, 729–734. doi: 10.1038/nnano.2013.171

Zhou, B., Tang, B., Zhang, C., Qin, C., Gu, Z., Ma, Y., et al. (2020). Enhancing multiphoton upconversion through interfacial energy transfer in multilayered nanoparticles. *Nat. Commun.* 11:1174. doi: 10.1038/s41467-020-14879-9

Zhou, J., Shirahata, N., Sun, H. T., 248Ghosh, B., Ogawara, M., Teng, Y., et al. (2013). Efficient dual-modal NIR-to-NIR emission of rare earth ions co-doped nanocrystals for biological fluorescence imaging. *J. Phys. Chem. Lett.* 4, 402–408. doi: 10.1021/jz302122a

Zhu, H., Chen, X., Jin, L. M., Wang, Q. J., Wang, F., and Yu, S. F. (2013). Amplified spontaneous emission and lasing from lanthanide-doped up-conversion nanocrystals. *ACS Nano* 7, 11420–11426. doi: 10.1021/nn405387t

Conflict of Interest: The authors declare that the research was conducted in the absence of any commercial or financial relationships that could be construed as a potential conflict of interest.

frontiers in Chemistry

MINI REVIEW
published: 25 January 2021
doi: 10.3389/fchem.2020.624592

Recent Advances in Developing Lanthanide Metal–Organic Frameworks for Ratiometric Fluorescent Sensing

Tianying Sun[1], *Yaobin Gao*[1], *Yangyang Du*[2], *Lei Zhou*[1]* *and Xian Chen*[2]*

[1]School of Chemical Engineering and Technology/School of Marine Sciences, Sun Yat-sen University, Zhuhai, China, [2]College of Materials Science and Engineering, Shenzhen University, Shenzhen, China

Fluorescent probes have attracted special attention in developing optical sensor systems due to their reliable and rapid fluorescent response upon reaction with the analyte. Comparing to traditional fluorescent sensing systems that employ the intensity of only a single emission, ratiometric fluorescent sensors exhibit higher sensitivity and allow fast visual screening of analytes because of quantitatively analyzing analytes through the emission intensity ratio at two or more wavelengths. Lanthanide metal–organic frameworks (LnMOFs) are highly designable multifunctional luminescent materials as lanthanide ions, organic ligands, and guest metal ions or chromophores are all potential sources for luminescence. They thus have been widely employed as ratiometric fluorescent sensors. This mini review summarized the basic concept, optical features, construction strategies, and the ratiometric fluorescent sensing mechanisms of dual-emitting LnMOFs. The review ends with a discussion on the prospects, challenges, and new direction in designing LnMOF-based ratiometric fluorescent sensors.

Keywords: lanthanide, luminescence, dual emission, ratiometric sensing, metal–organic frameworks

OPEN ACCESS

Edited by:
Qianqian Su,
Shanghai University, China

Reviewed by:
Xiaowang Liu,
Northwestern Polytechnical University, China
Qiuqiang Zhan,
South China Normal University, China

***Correspondence:**
Lei Zhou
zhoul8@mail.sysu.edu.cn
Xian Chen
x.chen87@outlook.com

Specialty section:
This article was submitted to Nanoscience, a section of the journal Frontiers in Chemistry

Received: *31 October 2020*
Accepted: *21 December 2020*
Published: *25 January 2021*

Citation:
Sun T, Gao Y, Du Y, Zhou L and Chen X (2021) Recent Advances in Developing Lanthanide Metal–Organic Frameworks for Ratiometric Fluorescent Sensing. Front. Chem. 8:624592. doi: 10.3389/fchem.2020.624592

INTRODUCTION

Fluorescent probes have attracted special attention in developing optical sensor systems due to their reliable and rapid fluorescent response upon reaction with the analyte (Vendrell et al., 2012). The strategy to develop effective fluorescent probes has become one of the hottest research areas in recent years. Various kinds of fluorescence probes based on organic dye molecules, semiconductor quantum dots (QDs) have been developed (Wu et al., 2020a; Yang et al., 2020a; Pfeifer et al., 2020). However, these probes have several limitations in detecting or sensing. For example, organic dyes suffer from several drawbacks such as poor chemical stability and rapid photobleaching, making it impossible for long-term fluorescence sensing. Compared with organic dye molecules, QDs exhibit better chemical and photostability. QDs are usually composed of heavy metals and suffer from toxicity and environmental hazards, which limit their practical applications. Lanthanide-based fluorescent probes can surpass the aforementioned inherent limitations of organic dyes or quantum dots due to their excellent properties, including low toxicity and better stability. Moreover, lanthanide luminescence features rich linelike emission bands, large Stokes shift, and high resistance to photobleaching, making the lanthanide-based luminescent materials superior in sensing applications.

Traditional fluorescent sensing system that employs the intensity of only a single emission for quantitative analysis of analytes can be difficult and might yield unreliable results. A number of analyte-independent factors such as instrumental drift, the microenvironment and local concentration variance of probes, and photobleaching of the probes, all interfere with the quantification of the analyte and lower the sensing reliability. To circumvent these drawbacks, a ratiometric approach has been adopted in the design of fluorescent sensors (Chen et al., 2020; Zhao and Li, 2020). Ratiometric fluorescent sensors allow the simultaneous measurement of emission intensities at two or more wavelengths, and their emission intensity ratio is calculated and then correlated to analytes. In particular scenarios, change in emission color output could be observed upon reaction with the analyte, allowing for fast visual screening of analytes (Chen et al., 2018; Su et al., 2018; Bigdeli et al., 2019; Zhang et al., 2020). Perceiving the variation in the color brightness is much harder than visualizing the color change. Therefore, the ratiometric fluorescence sensing method is a clear winning strategy over the traditional single emission intensity-based sensing approach.

The search for novel lanthanide-based dual- or multi-emitting materials that suitable for developing a ratiometric sensor is currently an emerging field (Yin and Yin, 2020). Lanthanide metal–organic frameworks (LnMOFs) combine the lanthanide luminescent features with the MOFs' characteristics such as high porosity, large surface-to-volume ratio, diverse structures have been proved to be a powerful candidate in sensing application (Zhang et al., 2018; Liu et al., 2019). The permanent porosity and large surface area provide the potential to effectively concentrate analytes at higher levels within MOFs (Han et al., 2012), thus improve the sensitivity. Comparing to other conventional lanthanide hybrid platforms such as lanthanide–QDs or lanthanide–dye, LnMOFs present superior emission tuning capability as lanthanide nodes, organic linkers, the ligand to metal energy transfer, all of which can be "tailor-made" or modulated (Yan, 2017; Yang et al., 2020b; Wu et al., 2020c). Moreover, the intrinsic porosity of MOFs provides a pathway to encapsulate guest materials, which may also contribute to emission. Furthermore, the host framework–guest interactions such as coordination bonds, π–π interaction, and hydrogen bonding provide excellent sensing sensitivity toward the analyte (Xu and Yan, 2017). Therefore, all these features make LnMOFs promising in developing ratiometric sensing systems.

In this mini review, we provide a general overview of the design principles of LnMOFs with multiple luminescent centers. To further discuss the details in design and the working mechanisms of these ratiometric fluorescent sensors, very recent progress in the development of LnMOFs for sensing ions, trace-water, gas and temperature, molecular decoding and biosensing will also be discussed. Our efforts here are to highlight the prospects of LnMOFs as ratiometric fluorescent sensors and briefly discuss the desired properties for future development.

The Construction of Dual-Emitting LnMOFs

The prerequisite of ratiometric assays is to generate dual or multi emission signals by one excitation. By virtue of the inherent hybrid nature, LnMOFs can mostly generate luminescent from the following component (**Figure 1A**): 1) Ligand usually conjugated organic compounds can generate emission upon excitation with UV or visible light. 2) Lanthanide metal nodes can give emission through antenna effect promoted by the ligands. 3) Lanthanide ions as guest species that incorporated into MOF structures could also yield luminescence. 4) Other chromophore guests, such as dye molecules or QDs. **Figures 1B–D** summarizes three typical scenarios by which dual emission has been generated and utilized for the construction of ratiometric sensor, namely a Ln (I)–Ln (II) bimetallic system, a Ln–Ligand system and a Ln–Chromophore system.

Ln (I)–Ln (II) Bimetallic System in LnMOFs

The traditional method of physically mixing two types of LnMOFs doped with different lanthanide ions, as illustrated in (i) of **Figure 1B**, is the most straightforward way to obtain dual emission (Chen et al., 2019). Due to the similar chemical properties of lanthanide ions, LnMOF structures can also allow for the incorporation of different types and ratios of lanthanide ions into the same host materials and thus generate characteristic emissions of each lanthanide ion at the same time ((ii) of **Figure 1B**) (Xia et al., 2017; Su et al., 2018; Ji et al., 2018; Gao et al., 2018; Li et al., 2019a; Othong et al., 2020; Zeng et al., 2020a). Once incorporated into the MOF structure, lanthanide ions can generate emission covering the spectrum region from ultraviolet to near-infrared. Among which, Eu^{3+} and Tb^{3+} ions exhibit strong red and green luminescence, respectively, that can be easily perceived by the naked eye. Therefore, Eu^{3+}/Tb^{3+} based MOFs have been widely employed for the construction of dual emission ratiometric fluorescent sensor. For example, chemical fine-tuning the Tb/Eu ratio of raw materials in the synthetic process of Tb/Eu (TATB) results in tunable dual emission from Tb^{3+} and Eu^{3+} ions (Zeng et al., 2020a). Besides serving as the metal nodes, multiple types of lanthanide ions can also be encapsulated into the pore of MOFs as emissive guest species [(iii) of **Figure 1B**] (Li et al., 2019c; Qiao et al., 2019). For instance, Tb/Eu@bio-MOF-1 material was fabricated via ion exchange between Tb^{3+} and Eu^{3+} cations into the pores of the anionic framework, also resulting in dual emission from Tb^{3+} and Eu^{3+} ions (Zhang et al., 2016b). Noted that the porous microstructure around Tb^{3+} and Eu^{3+} ions also facilitate the absorption and the transportation of analyte and therefore contribute to the effective sensing.

Ln–Ligand System in LnMOFs

Luminescent behavior of LnMOFs is highly dependent on the efficiency of the antenna effect. The perfectly matched energy levels of ligand and metal result in emission from lanthanide ions dominantly, while poor energy matching leads to almost no lanthanide emission. In the case of partial energy transfer from the ligand to lanthanide ions, both characteristic emissions from lanthanide ion and ligand can be recorded. Such dual emissive Ln–Ligand LnMOF system can be helpful in constructing ratiometric sensors once exposed to analytes (Yang et al., 2017; Yue et al., 2018; Li et al., 2019b; Yin et al., 2019). For example, Qian et al. prepared ZJU-136-$Ce_{1-x}Eu_x$ with

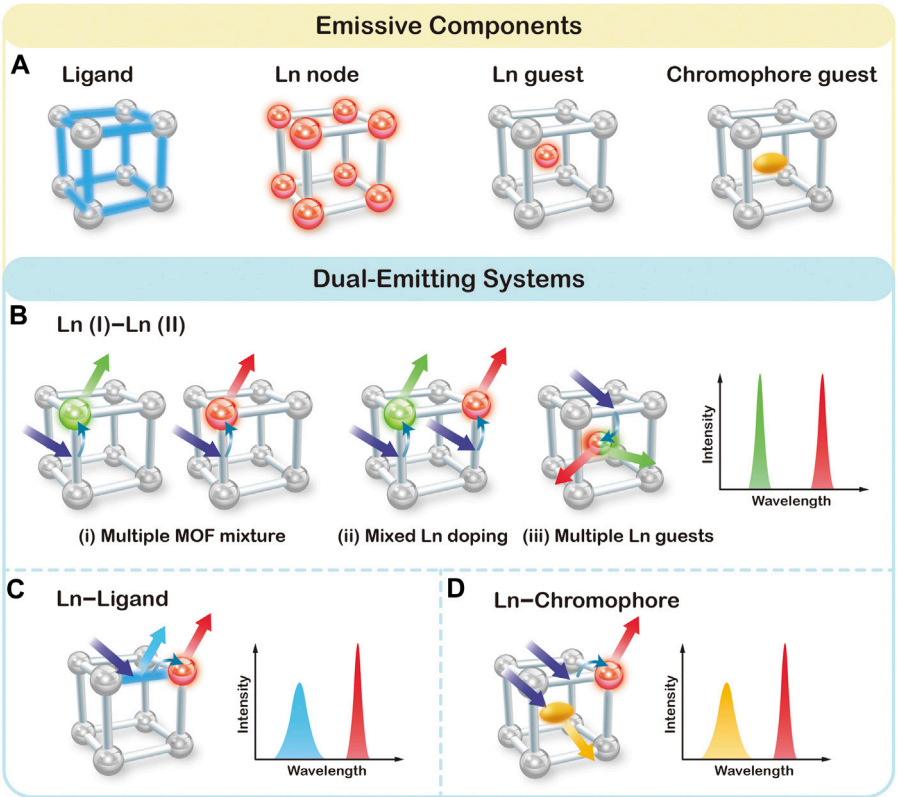

FIGURE 1 | Schematic representation of four possible emissive components **(A)**, and three typical scenarios for the construction of dual-emitting ratiometric fluorescent sensors in LnMOFs **(B–D)**.

1,1′; 4′,1″-terphenyl-2′,4,4″,5′-tetracarboxylic acid (TPTC) and Ce^{4+} and Eu^{3+} ions (Yue et al., 2018). ZJU-136-$Ce_{1-x}Eu_x$ exhibits dual emission from TPTC ligand at 390 nm and Eu^{3+} ions at 617 nm under 320 nm excitation. The introduced Ce^{4+} ions were intended to regulate the energy transfer from TPTC to Eu^{3+} ions. Due to the specific redox reaction between ascorbic acid (AA) and Ce^{4+}, the emission intensity of TPTC increased significantly with the simultaneous quenching of Eu ions. Therefore, ZJU-136-$Ce_{1-x}Eu_x$ was proved to be useful in ratiometric fluorescence sensing for AA determination.

Ln–Chromophore System in LnMOFs

MOFs possess pores and channels with highly tunable sizes and shapes. Apart from the intrinsic lanthanide luminescent from the frameworks and the encapsulated Ln^{3+} ions, there are plenty of chromophores such as metal-complex, organic dyes, QDs that can be encapsulated into MOF as chromophore guest (Cui et al., 2015; Gao et al., 2017; Hao et al., 2017; Qin and Yan, 2018; Wang et al., 2019; Yu et al., 2019). For instance, Yu and coworkers developed a water-stable RhB@Tb-dcpcpt host-guest composite by trapping the cationic rhodamine B (RhB) into the anionic framework of $[Me_2NH_2][Tb_3$ $(dcpcpt)_3(HCOO)]\cdot DMF\cdot 15H_2O$ via an ion exchange process (Yu et al., 2019). The composite exhibit dual emission from RhB and Tb ions, and therefore allows the realization of sensitive and selective detection toward ciprofloxacin and norfloxacin antibiotics via a luminescent color-changing process. Wang et al. reported a dual-emitting carbon dots@Eu-MOFs for the ratiometric fluorescent detection of Cr(VI) (Wang et al., 2019). Upon reacting with Cr(VI), the fluorescence of carbon dots was quenched while the emission intensity of Eu-MOFs remains unchanged. Therefore, the prepared composites can be employed as self-calibrated probes for Cr(VI).

Ratiometric Fluorescent Sensing Mechanisms

In a dual-emitting ratiometric fluorescent sensing system, the sensor-analyte interaction can be categorized into the following: analyte modulates by either suppressing (i) or enhancing (ii) the energy transfer from the ligand to lanthanide ions, resulting in reduced or enhanced emission from lanthanide ions. (iii) Analyte modulates the coordination interaction of lanthanide ions. (iv) Analyte modulates the Ln–Ln energy transfer. In general, dual-emitting properties of LnMOF-based sensors show a quick response once in reaction with analyte through the above-mentioned interactions. And the intensity ratio of dual emission can be calculated and then correlated to analytes. In particular scenarios, changes in output emission color can be observed, allowing for fast visual screening of analytes.

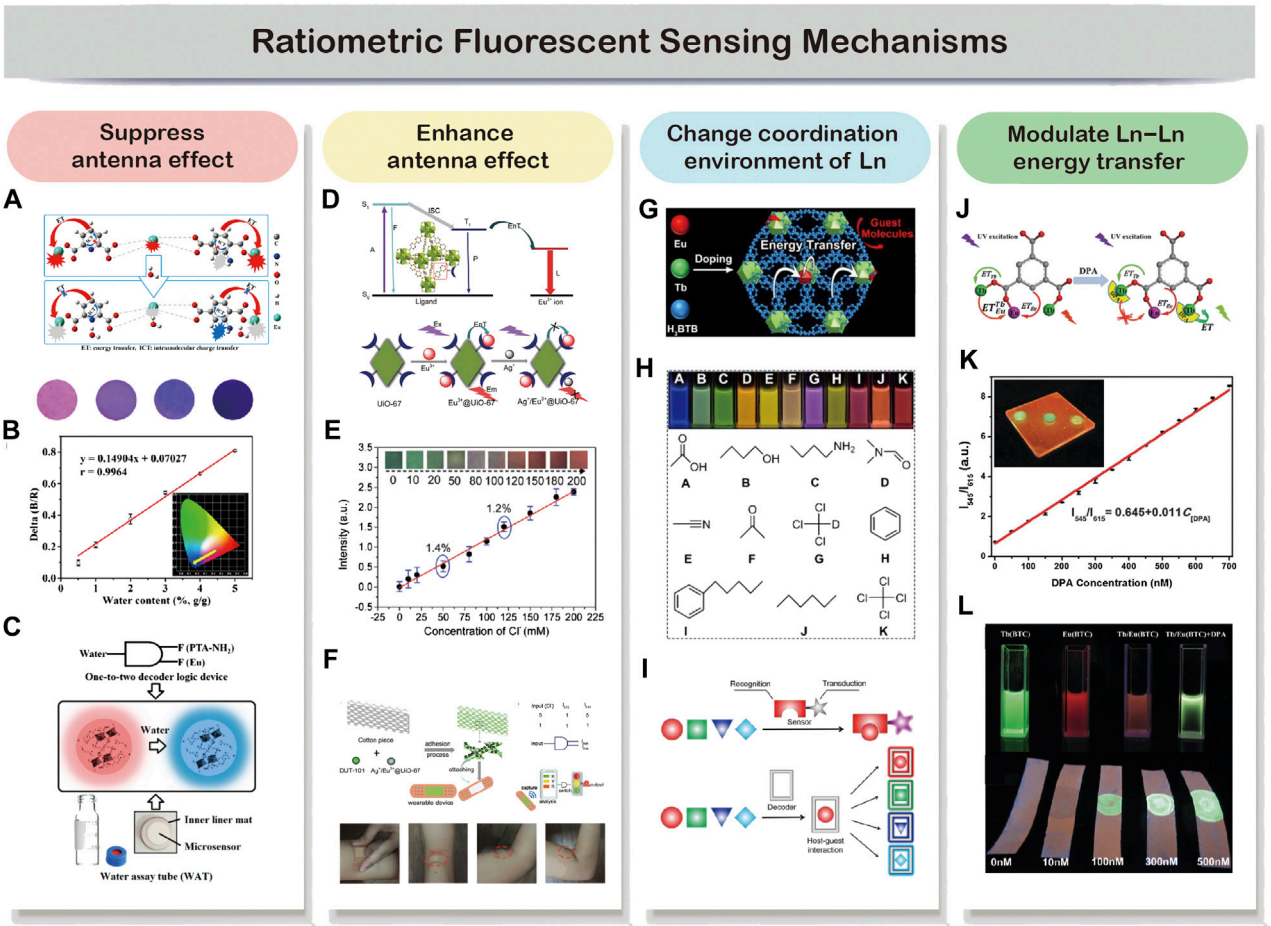

FIGURE 2 | In a dual-emitting system, analyte can be probed through the four commonly employed mechanisms. Analyte interacts with the sensor by suppressing **(A–C)** or enhancing **(D–F)** the antenna effect. Reproduced from Yu et al. (2020) with permission from American Chemical Society and Zhang et al. (2018) with permission from The Royal Society of Chemistry. The analyte may also change the coordination environment of Ln **(G,H)** or modulate the lanthanide-lanthanide energy transfer **(I,J)**. Reproduced from Zeng et al. (2020a) with permission from American Chemical Society and Zhang et al. (2016a) with permission from The Royal Society of Chemistry.

The modulation of antenna effect to quench the lanthanide luminescence is probably the most commonly employed sensing approach by LnMOFs (Cui et al., 2019; Moscoso et al., 2020; Yu et al., 2020). For example, Yu et al. (2020) developed a trace water sensor based on Eu-MOF with the mixed ligand of dipicolinic acid (DPA) and 2-aminophthalic acid (PTA-NH_2). DPA functioned as the sensitizer for Eu^{3+} ions, while PTA-NH_2 provides a second emission besides Eu^{3+}. The exposure of DPA to water leads to the occurrences of efficient intramolecular charge transfer (ICT) in DPA, which weakens the antenna effect from DPA to Eu^{3+} (**Figure 2A**). And they observed a "turn-on" blue emission of PTA-NH_2 with the water content in the MOF and a "turn-off" red emission from Eu^{3+} under 254 nm UV light excitation (**Figure 2B**). The increase of PTA-NH_2 blue emission was ascribed to the water-induced ICT fluorescence of PTA-NH_2. This ratiometric fluorescent sensor exhibits a linear and sensitive response to water in the range of 0–100% (v/v). Therefore, a one-to-two decoder logic device for water assay can be designed (**Figure 2C**). Based on this dual-emitting ratiometric sensing technique, a paper-based water microsensor was fabricated for portable, longer-term stable, and rapid sensing. In 2017, Yang et al. developed a boric acid functional Eu-MOF probe for the recognition of fluoride ion, which is also based on the suppressed antenna effect (Yang et al., 2017). The insufficient ICT from ligand to Eu^{3+} results in the dual emission from ligand at 366 nm and Eu^{3+} ions at 625 nm under 275 nm excitation. With the presence of fluoride ions, the binding of fluoride to the boron center disrupted the p_{π}–π conjugation of 5-bop and decreased the intersystem crossing efficiency, and therefore enhance the ligand emission while decreasing the Eu^{3+} emission with increased fluoride concentration. An excellent linear relationship can be observed between the intensity ratio of the dual emission and fluoride concentration in the range from 4 to 80 μM. Moreover, the boric acid exhibits a strong affinity to fluoride ions, while its interaction with other anions is relatively weak, making it perfect for fluoride selective sensing.

Reports on enhancing antenna effect resulted in "turn-on" sensing are rather few comparing to the "turn-off" mechanism discussed above (Karmakar et al., 2019; Fueyo-González et al., 2020; Min et al., 2020; Wang et al., 2020; Yue et al., 2020). However, it is obvious that "turn-on" sensors have advantages over the "turn-off" sensors, especially in the quantitative determination of an analyte in low concentration (Luo et al., 2020). For the "turn-off" sensor, the signal decrease against an already bright background makes it hard for sensitive and accurate sensing. By contrast, "turn-on" luminescent behavior can significantly enhance a weak emission or even create a new emission, reducing the likelihood of false-positive signals while providing much higher sensitivity. Yang et al. developed a "turn-on" ratiometric fluorescent sensor for H_2S by encapsulating Tb^{3+} ions within the pores of MOF [Cu(HCPOC)$_2$]n to form Tb^{3+}@Cu-MOF (Zheng et al., 2017). The composite exhibits weak Tb^{3+} emission and strong H_2CPOC ligand emission because the unsaturated electronic state of Cu^{2+} tends to have a negative effect on the energy transfer from ligand to Tb^{3+} ions. Serving as a strong electron donor, H_2S can decrease the binding energies of the metal center through its strong affinity for Cu^{2+} ions. Therefore, the luminescence of Tb^{3+} recovered as the result of the restored antenna effect between ligand and Tb^{3+}. Meanwhile, the ligand showed a slight decrease in emission with the increase of H_2S concentration. Therefore, Tb^{3+}@Cu-MOF sensor showed excellent sensitivity and selectivity toward H_2S with a linear response range from 13.25 to 1.6 mM. Another example of enhancing antenna effect-based ratiometric sensing was proposed by Xu and Yan, 2018. They developed a sweat Cl^- sensor based on Ag^+/Eu^{3+}@UiO-67 platform. As shown in **Figure 2D**, Ag^+ was deliberately introduced into the system via a Ag–N coordination bond to reduce the efficiency of the energy transfer from UiO-67 to Eu^{3+}. Upon reaction with Cl^-, the strong electronic affinity between Ag^+ and Cl^- leads to a "turn-on" luminescence of Eu^{3+}. By employing DUT-101 as a reference signal, an obvious output color shift from dark green to bright red can be observed, and a 0.1 mM Cl^- limit of detection was claimed (**Figure 2E**). They further load the two LnMOF-based sensors to a cotton piece and attach it to a band-aid for the demonstration of a wearable Cl^- monitoring device (**Figure 2F**).

Molecules with different coordination capability could cause changes in the coordination environment of lanthanide ions in MOF structures and further affect their emission (Cui et al., 2014; Zeng et al., 2020b). Based on this phenomenon, Zeng et al. developed fast and facile decoding of a broad range of molecules, including homologues, isomers, enantiomers, and deuterated isotopomers by employing Tb/Eu(BTB) as the probe (Zeng et al., 2020b). 1,3,5-benzenetrisbenzoic acid (H_3BTB) was chosen as the ligand, together with mixed Tb^{3+} and Eu^{3+}, to construct Tb/Eu(BTB) probe by a simple one-pot synthesis procedure (**Figure 2G**). Under 302 nm UV excitation, the probe exhibits red (Eu^{3+}), green (Tb^{3+}), and blue emissions (BTB) in a single host. Therefore this probe should be ideal for molecular decoding as it involves wide coverage in the visible spectral range. They found out that the ultrahigh decoding capability was realized by fine-tuning the energy transfer pathway in multiple ways, including changing the coordination environment of lanthanide ions within Tb/Eu(BTB) probe. For example, molecular with high coordination capability such as acetic acid could destroy the crystalline structure of LnMOFs and further eliminate the antenna effect. The binding of target molecules to Eu^{3+}/Tb^{3+} could change the coordination symmetry of the LnMOFs and modulate the energy of singlet or triplet excited states of BTB, affecting the energy transfer from BTB to Eu^{3+}/Tb^{3+}. As shown in **Figure 2H**, this ratiometric molecular decoding strategy enables a full-color readout and visual decoding capability. Conventional molecular decoding strategy requires a tailor-designed probe for a specific sensing target, which is time-consuming and labor-intensive. The reported probes can accommodate a diverse range of molecules, while each gives a different output signal as the result of specific host-guest interaction (**Figure 2I**). This decoding strategy allows for multiple-target differentiation by using only a single probe, significantly promoting its widespread usability.

Modulating the Ln–Ln energy transfer is a straightforward way to tune the emission ratio of two lanthanide ions and correlate with the concentration of analytes (Zhang et al., 2016a; Zhao et al., 2019; Wu et al., 2020b; Feng et al., 2020). For example, Zhang and coworkers developed a dual-emitting Tb/Eu(BTC) probe for the rapid detection of dipicolinic acid (DPA) biomarker (Zhang et al., 2016a). Since DPA can chelate with Tb^{3+}, the energy transfer from DPA to Tb^{3+} becomes dominant while the Tb-to-Eu energy transfer is interrupted (**Figure 2J**). The concentration of DPA can be linearly correlated well with the ratio I_{545}/I_{613} in the 50–700 nM concentration range with the estimated detection limit of 4.55 nM (**Figure 2K**). And the color output of Tb/Eu(BTC) sensor changes from orange-red to yellow-green after adding DPA in the solution or dropping onto test strips (**Figure 2L**). Another great example of using an analyte to modulate Ln–Ln energy transfer is for ratiometric temperature sensing (Yang et al., 2020c; Feng et al., 2020). Feng et al. developed $Eu_{0.0025}Tb_{0.9975}$-BABDC-PBMA membrane. H_2BABDC is an ideal "antenna chromophore" to sensitize both Eu^{3+} and Tb^{3+}, and therefore generate dual emission (Feng et al., 2020). They found that the intensity ratio of $^5D_4 \rightarrow {}^7F_5(Tb^{3+})/{}^5D_0 \rightarrow {}^7F_2(Eu^{3+})$ can be linear related to the temperature from 90 to 240 K. And the energy transfer from Tb^{3+} to Eu^{3+} was responsible for the unique temperature-dependent luminescent behavior. Benefiting from the tunable architectures of this probe, they then developed a free-standing and homogeneous membranous ratiometric luminescent thermometer with excellent mechanical properties. And the thermometer was tested to be stable even under harsh conditions, pushing forward the real application of LnMOF-based thermometers.

CONCLUSIONS AND PERSPECTIVE

This mini review provides a brief overview of the strategies to construct a dual-emitting LnMOF-based ratiometric fluorescent sensor. By virtue of the structural versatility, luminescent turnability, unique sensor-analyte interaction, and the possible fabrication into smart-devices make LnMOF an excellent

candidate for efficient ratiometric fluorescent sensing. This technique relies on the change in the emission intensity of two emission bands, allowing for precise, quantitative, and real-time analysis. And the direct witness of the color change by the naked eye could be a more facile way for the determination of analytes. Despite the undeniable merits of LnMOF-based ratiometric fluorescent sensors, there are still many challenges to overcome. The stability, especially the water stability of the LnMOF-based sensors, needs to be further enhanced to avoid the structural breakdown before completing the sensing in the aqueous environment or other sensing media. Most of the LnMOFs sensing experiments were still conducted in solution. The development of LnMOF films or membranes as portable devices while maintaining the original stability and ratiometric sensing capability can be meaningful during the exploration of their practical applications. The design and fabrication of LnMOFs in nanometer scale is still in their infancy. Further effort can be devoted to preparing nanostructured LnMOFs, which holds great promise in bioimaging, diagnosis, and therapy. Most of the LnMOF-based sensors are still based on the quenching mechanism. Research endeavors are preferred to devote toward the rational design of "turn-on" especially "turn-on" ratiometric fluorescent sensors.

AUTHOR CONTRIBUTIONS

All authors listed have made a substantial, direct, and intellectual contribution to the work and approved it for publication.

FUNDING

This work was supported by the National Natural Science Foundation of China (Nos. 51802198 and 51902355), the start-up Grant of Sun Yat-sen University.

REFERENCES

Bigdeli, A., Ghasemi, F., Abbasi-Moayed, S., Shahrajabian, M., Fahimi-Kashani, N., Jafarinejad, S., et al. (2019). Ratiometric fluorescent nanoprobes for visual detection: design principles and recent advances—a review. *Anal. Chim. Acta*. 1079, 30–58. doi:10.1016/j.aca.2019.06.035

Chen, D. H., Haldar, R., Neumeier, B. L., Fu, Z. H., Feldmann, C., Wöll, C., et al. (2019). Tunable emission in heteroepitaxial Ln–SURMOFs. *Adv. Funct. Mater*. 29, 1903086. doi:10.1002/adfm.201903086

Chen, D. M., Sun, C. X., Peng, Y., Zhang, N. N., Si, H. H., Liu, C. S., et al. (2018). Ratiometric fluorescence sensing and colorimetric decoding methanol by a bimetallic lanthanide–organic framework. *Sensor. Actuator. B. Chem*. 265, 104–109. doi:10.1016/j.snb.2018.03.028

Chen, L., Liu, D. H., Peng, J., Du, Q. Z., and He, H. (2020). Ratiometric fluorescence sensing of metal–organic frameworks: tactics and perspectives. *Coord. Chem. Rev*. 404, 213113. doi:10.1016/j.ccr.2019.213113

Cui, Y., Chen, F., and Yin, X. B. (2019). A ratiometric fluorescence platform based on boric-acid-functional Eu-MOF for sensitive detection of H. *Biosens. Bioelectron*. 135, 208–215. doi:10.1016/j.bios.2019.04.008

Cui, Y., Song, R., Yu, J., Liu, M., Wang, Z., Wu, C., et al. (2015). Dual-emitting MOFdye composite for ratiometric temperature sensing. *Adv. Mater. Weinheim*. 27, 1420–1425. doi:10.1002/adma.201404700

Cui, Y. J., Chen, B. L., and Qian, G. D. (2014). Lanthanide metal–organic frameworks for luminescent sensing and light-emitting applications. *Coord. Chem. Rev*. 273–274, 76–86. doi:10.1016/j.ccr.2013.10.023

Feng, T. T., Ye, Y. X., Liu, X., Cui, H., Li, Z. Q., Zhang, Y., et al. (2020). A robust mixed-lanthanide polyMOF membrane for ratiometric temperature sensing. *Angew. Chem. Int. Ed*. 59, 2–8. doi:10.1002/anie.202009765

Fueyo-González, F., Garcia-Fernandez, E., Martínez, D., Infantes, L., Orte, A., González-Vera, J. A., et al. (2020). Smart lanthanide antennas for sensing water. *ChemComm*. 56, 5484–5487. doi:10.1039/d0cc01725f

Gao, J., Li, Q., Wang, C. H., and Tan, H. L. (2017). Copper (II)-mediated fluorescence of lanthanide coordination polymers doped with carbon dots for ratiometric detection of hydrogen sulfide. *Sensor. Actuator. B. Chem*. 253, 27–33. doi:10.1016/j.snb.2017.06.092

Gao, Y. X., Yu, G., Liu, K., and Wang, B. (2018). Luminescent mixed-crystal Ln-MOF thin film for the recognition and detection of pharmaceuticals. *Sensor. Actuator. B. Chem*. 257, 931–935. doi:10.1016/j.snb.2017.10.180

Han, S. B., Hermans, T. M., Fuller, P. E., Wei, Y. H., and Grzybowski, B. A. (2012). Transport into metal–organic frameworks from solution is not purely diffusive. *Angew. Chem. Int. Ed*. 51, 2662–2666. doi:10.1002/anie.201108492

Hao, J., Liu, F. F., Liu, N., Zeng, M. L., Song, Y. H., and Wang, L. (2017). Ratiometric fluorescent detection of Cu^{2+} with carbon dots chelated Eu-based metal–organic frameworks. *Sensor. Actuator. B. Chem*. 245, 641–647. doi:10.1016/j.snb.2017.02.029

Ji, G. F., Wang, J. Z., Gao, X. C., Liu, J. J., Guan, W. H., Liu, H. T., et al. (2018). Hypersensitive self-referencing detection traces of water in ethyl alcohol by dual-emission lanthanide metal–organic frameworks. *Eur. J. Inorg. Chem*. 14, 1998–2003. doi:10.1002/ejic.201800012

Karmakar, A., Samanta, P., Dutta, S., and Ghosh, S. K. (2019). Fluorescent "turn-on" sensing based on metal-organic frameworks (MOFs). *Chem. Asian J*. 14, 4506–4519. doi:10.1002/asia.201901168

Li, B. B., Wang, W. J., Hong, Z. X., El-Sayed, E. S. M., and Yuan, D. Q. (2019a). Ratiometric fluorescence detection of trace water in an organic solvent based on bimetallic lanthanide metal–organic frameworks. *ChemComm*. 55, 6926–6929. doi:10.1039/c9cc02324k

Li, H., Han, W., Lv, R., Zhai, A., Li, X. L., Gu, W., et al. (2019b). Dual-function mixed-lanthanide metal–organic framework for ratiometric water detection in bioethanol and temperature sensing. *Anal. Chem*. 91, 2148–2154. doi:10.1021/acs.analchem.8b04690

Li, H. J., Li, Q. Q., and Xu, Z. Q. (2019c). Lanthanide cation encapsulated in a metal–organic framework as a white LED and selective naked-eye reversible HCl sensor. *J. Mater. Chem. C*. 7, 2880–2885. doi:10.1039/c8tc05956j

Liu, Y., Xie, X. Y., Cheng, C., Shao, Z. S., and Wang, H. S. (2019). Strategies to fabricate metal–organic framework(MOF)-based luminescent sensing platforms. *J. Mater. Chem. C*. 7, 10743–10763. doi:10.1039/c9tc03208h

Luo, T. Y., Das, P., White, D. L., Liu, C., Star, A., and Rosi, N. L. (2020). Luminescence "turn-on" detection of gossypol using Ln^{3+}-based metal–organic frameworks and Ln^{3+} salts. *J. Am. Chem. Soc*. 142, 2897–2904. doi:10.1021/jacs.9b11429

Min, H., Han, Z. S., Wang, M. M., Li, Y. J., Zhou, T. Z., Shi, W., et al. (2020). A water-stable terbium metal–organic framework as a highly sensitive fluorescent sensor for nitrite. *Inorg. Chem. Front*. 12, 33–39. doi:10.1039/d0qi00780c

Moscoso, F. G., Almeida, J., Sousaraei, A., Lopes-Costa, T., Silva, A. M. G., Cabanillas-Gonzalez, J., et al. (2020). A lanthanide MOF immobilized in PMMA transparent films as a selective fluorescence sensor for nitroaromatic explosive vapours. *J. Mater. Chem. C*. 8, 3626–3630. doi:10.1039/d0tc00376j

Othong, J., Boonmak, J., Kielar, F., Hadsadee, S., Jungsuttiwong, S., and Youngme, S. (2020). Self-calibrating sensor with logic gate operation for anthrax biomarker based on nanoscaled bimetallic lanthanoid MOF. *Sensor. Actuator. B. Chem*. 316, 128156. doi:10.1016/j.snb.2020.128156

Pfeifer, D., Russegger, A., Klimant, I., and Borisov, S. M. (2020). Green to red emitting BODIPY dyes for fluorescent sensing and imaging of carbon dioxide. *Sensor. Actuator. B. Chem*. 304, 127312. doi:10.1016/j.snb.2019.127312

Qiao, X. F., Han, Y. B., Tian, D., Yang, Z. C., Li, J. L., and Zhao, S. T. (2019). MOF matrix doped with rare earth ions to realize ratiometric fluorescent sensing of 2,4,6-trinitrophenol: synthesis, characterization and performance. *Sensor. Actuator. B. Chem*. 286, 1–8. doi:10.1016/j.snb.2019.01.111

Qin, S. J., and Yan, B. (2018). Dual-emissive ratiometric fluorescent probe based on Eu^{3+}/C-dots@MOF hybrids for the biomarker diaminotoluene sensing. *Sensor. Actuator. B. Chem.* 272, 510–517. doi:10.1016/j.snb.2018.06.018

Su, Y., Yu, J. H., Li, Y. B., Phua, S. F. Z., Liu, G. F., Lim, W. Q., et al. (2018). Versatile bimetallic lanthanide metal–organic frameworks for tunable emission and efficient fluorescence sensing. *Commun. Chem.* 1, 1–13. doi:10.1038/s42004-018-0016-0

Vendrell, M., Zhai, D. T., Er, J. C., and Chang, Y. T. (2012). Combinatorial strategies in fluorescent probe development. *Chem. Rev.* 112, 4391–4420. doi:10.1021/cr200355j

Wang, H., Wang, X. L., Liang, M. S., Chen, G., Kong, R. M., Xia, L., et al. (2020). A boric acid-functionalized lanthanide metal–organic framework as a fluorescence "turn-on" probe for selective monitoring of Hg^{2+} and CH_3Hg^+. *Anal. Chem.* 92, 3366–3372. doi:10.1021/acs.analchem.9b05410

Wang, Y. Y., He, J., Zheng, M. D., Qin, M. D., and Wei, W. (2019). Dual-emission of Eu based metal–organic frameworks hybrids with carbon dots for ratiometric fluorescent detection of Cr(VI). *Talanta*. 191, 519–525. doi:10.1016/j.talanta.2018.08.078

Wu, L. L., Huang, C. S., Emery, B. P., Sedgwick, A. C., Bull, S. D., He, X. P., et al. (2020a). Förster resonance energy transfer (FRET)-based small-molecule sensors and imaging agents. *Chem. Soc. Rev.* 49, 5110–5139. doi:10.1039/c9cs00318e

Wu, M. N., Zhuang, Y. X., Liu, J. B., Chen, W. W., Li, X. Y., and Xie, R. J. (2020b). Ratiometric fluorescence detection of 2,6-pyridine dicarboxylic acid with a dual-emitting lanthanide metal–organic framework (MOF). *Opt. Mater.* 106, 110006. doi:10.1016/j.optmat.2020.110006

Wu, S. Y., Min, H., Shi, W., and Cheng, P. (2020c). Multicenter metal–organic framework-based ratiometric fluorescent sensors. *Adv. Mater.* 32, 1805871. doi:10.1002/adma.201805871

Xia, T. F., Cui, Y. J., Yang, Y., and Qian, G. D. (2017). Highly stable mixed-lanthanide metal–organic frameworks for self-referencing and colorimetric luminescent pH sensing. *ChemNanoMat*. 3, 51–57. doi:10.1002/cnma.201600331

Xu, X. Y., and Yan, B. (2018). A fluorescent wearable platform for sweat Cl^- analysis and logic smart-device fabrication based on color adjustable lanthanide MOFs. *J. Mater. Chem.* 6, 1863–1869. doi:10.1039/c7tc05204a

Xu, X. Y., and Yan, B. (2017). Intelligent molecular searcher from logic computing network based on Eu(III) functionalized UMOFs for environmental monitoring. *Adv. Funct. Mater.* 27, 1700247. doi:10.1002/adfm.201700247

Yan, B. (2017). Lanthanide-functionalized metal–organic framework hybrid systems to create multiple luminescent centers for chemical sensing. *Acc. Chem. Res.* 50, 2789–2798. doi:10.1021/acs.accounts.7b00387

Yang, G. H., Zhao, J. L., Yi, S. Z., Wan, X. J., and Tang, J. N. (2020a). Biodegradable and photostable Nb_2C MXene quantum dots as promising nanofluorophores for metal ions sensing and fluorescence imaging. *Sensor. Actuator. B. Chem.* 309, 127735. doi:10.1016/j.snb.2020.127735

Yang, L., Song, Y. H., and Wang, L. (2020b). Multi-emission metal–organic framework composites for multicomponent ratiometric fluorescence sensing: recent developments and future challenges. *J. Mater. Chem. B.* 8, 3292–3315. doi:10.1039/c9tb01931f

Yang, Y., Wang, Y. Z., Feng, Y., Song, X. R., Cao, C., Zhang, G. L., et al. (2020c). Three isostructural Eu^{3+}/Tb^{3+} co-doped MOFs for wide-range ratiometric temperature sensing. *Talanta*. 208, 120354. doi:10.1016/j.talanta.2019.120354

Yang, Z. R., Wang, M. M., Wang, X. S., and Yin, X. B. (2017). Boric-acid-functional lanthanide metal–organic frameworks for selective ratiometric fluorescence detection of fluoride ions. *Anal. Chem.* 89, 1930–1936. doi:10.1021/acs.analchem.6b04421

Yin, H. Q., Wang, X. Y., and Yin, X. B. (2019). Rotation restricted emission and antenna effect in single metal–organic frameworks. *J. Am. Chem. Soc.* 141, 15166–15173. doi:10.1021/jacs.9b06755

Yin, H. Q., and Yin, X. B. (2020). Metal-organic frameworks with multiple luminescence emissions:Designs and applications. *Acc. Chem. Res.* 53, 485–495. doi:10.1021/acs.accounts.9b00575

Yu, L., Zheng, Q. T., Wang, H., Liu, C. X., Huang, X. Q., and Xiao, Y. X. (2020). Double-color lanthanide metal–organic framework based logic device and visual ratiometric fluorescence water microsensor for solid pharmaceuticals. *Anal. Chem.* 92, 1402–1408. doi:10.1021/acs.analchem.9b04575

Yu, M. K., Xie, Y., Wang, X. Y., Li, Y. X., and Li, G. M. (2019). Highly water-stable dye@Ln-MOFs for sensitive and selective detection toward antibiotics in water. *ACS Appl. Mater. Interfaces* 11, 21201–21210. doi:10.1021/acsami.9b05815

Yue, D., Huang, Y. K., Zhang, L., Jiang, K., Zhang, X., Cui, Y. J., et al. (2018). Ratiometric luminescence sensing based on a mixed Ce/Eu metal–organic framework. *J. Mater. Chem. C.* 6, 2054–2059. doi:10.1039/c7tc05309f

Yue, D., Wang, Y. Y., Chen, D., and Wang, Z. L. (2020). Solvent triggering structural changes for two terbium-based metal-organic frameworks and their photoluminescence sensing. *ChemComm.* 56, 4320–4323. doi:10.1039/d0cc00353k

Zeng, X. L., Hu, J., Zhang, M., Wang, F. L., Wu, L., and Hou, X. D. (2020a). Visual detection of fluoride anions using mixed lanthanide metal–organic frameworks with a smartphone. *Anal. Chem.* 92, 2097–2102. doi:10.1021/acs.analchem.9b04598

Zeng, X. L., Long, Z., Jiang, X. F., Zhang, Y. J., Liu, Q., Hu, J., et al. (2020b). Single bimetallic lanthanide-based metal–organic frameworks for visual decoding of a broad spectrum of molecules. *Anal. Chem.* 92, 5500–5508. doi:10.1021/acs.analchem.0c00324

Zhang, C., Li, X., Wei, W., and Chen, Z. B. (2020). Lanthanide ions as sensor elements based sensor array for colorimetric identification of antioxidants. *Sensor. Actuator. B. Chem.* 305, 127532. doi:10.1016/j.snb.2019.127532

Zhang, Y. H., Li, B., Ma, H. P., Zhang, L. M., Jiang, H., Song, H., et al. (2016a). A nanoscaled lanthanide metal–organic framework as a colorimetric fluorescence sensor for dipicolinic acid based on modulating energy transfer. *J. Mater. Chem. C.* 4, 7294–7301. doi:10.1039/c6tc01022a

Zhang, Y. H., Li, B., Ma, H. P., Zhang, L. M., and Zheng, Y. X. (2016b). Rapid and facile ratiometric detection of an anthrax biomarker by regulating energy transfer process in bio-metal–organic framework. *Biosens. Bioelectron.* 85, 287–293. doi:10.1016/j.bios.2016.05.020

Zhang, Y. M., Yuan, S., Day, G., Wang, X., Yang, X. Y., and Zhou, H. C. (2018). Luminescent sensors based on metal–organic frameworks. *Coord. Chem. Rev.* 354, 28–45. doi:10.1016/j.ccr.2017.06.007

Zhao, D., Yue, D., Jiang, K., Zhang, L., Li, C. X., and Qian, G. D. (2019). Isostructural Tb^{3+}/Eu^{3+} co-doped metal–organic framework based on pyridine-containing dicarboxylate ligands for ratiometric luminescence temperature sensing. *Inorg. Chem.* 58, 2637–2644. doi:10.1021/acs.inorgchem.8b03225

Zhao, Y. F., and Li, D. (2020). Lanthanide-functionalized metal–organic frameworks as ratiometric luminescent sensors. *J. Mater. Chem. C.* 8, 12739–12745. doi:10.1039/D0TC03430D

Zheng, X. B., Fan, R. Q., Song, Y., Wang, A. N., Xing, K., Du, X., et al. (2017). A highly sensitive turn-on ratiometric luminescent probe based on postsynthetic modification of Tb^{3+}@Cu-MOF for H_2S detection. *J. Mater. Chem. C.* 5, 9943–9951. doi:10.1039/c7tc02430d

Conflict of Interest: The authors declare that the research was conducted in the absence of any commercial or financial relationships that could be construed as a potential conflict of interest.

Advantages of publishing in Frontiers

OPEN ACCESS
Articles are free to read for greatest visibility and readership

FAST PUBLICATION
Around 90 days from submission to decision

HIGH QUALITY PEER-REVIEW
Rigorous, collaborative, and constructive peer-review

TRANSPARENT PEER-REVIEW
Editors and reviewers acknowledged by name on published articles

Frontiers
Avenue du Tribunal-Fédéral 34
1005 Lausanne | Switzerland

Visit us: www.frontiersin.org
Contact us: frontiersin.org/about/contact

REPRODUCIBILITY OF RESEARCH
Support open data and methods to enhance research reproducibility

DIGITAL PUBLISHING
Articles designed for optimal readership across devices

FOLLOW US
@frontiersin

IMPACT METRICS
Advanced article metrics track visibility across digital media

EXTENSIVE PROMOTION
Marketing and promotion of impactful research

LOOP RESEARCH NETWORK
Our network increases your article's readership